Università degli Studi di Ferrara

DOTTORATO DI RICERCA IN SCIENZE CHIMICHE

CICLO XXX

COORDINATORE: Prof. Carlo Alberto Bignozzi

Design of electron mediators for DSSC and Redox Flow Batteries and characterization of sensitized photoanodes for water splitting.

Settore Scientifico Disciplinare _____CHIM/03_____

Dottorando
Dott. Benazzi Elisabetta

Tutore
Prof. Bignozzi Carlo Alberto

Cotutore
Prof. Caramori Stefano

Anni 2014/2017

Contents

CHAPTER 1. GENERAL INTRODUCTION

1.1 Climate Change: What we can say about?

Fig.1.1 Representation of Global Warming

Earth's climate has evolved several times during history. As evidence, there have been seven cycles of glacial advance and retreat until the last ice age about 7,000 years ago. The last thaw has marked the very beginning of human civilization. So, earth has experienced climate change in the past without help from humanity. Most of these climate changes are attributed to very small variations in Earth's orbit that change the amount of solar energy our planet receives, but the current warming trend is of particular significance because most of it is human-induced and proceeds at a rate that is unprecedented in the past 1300 years (Fig.1.2) [1]. As the Earth moved out of ice ages over the past million years, the global temperature rose a total of 4 to 7 degrees Celsius over about 5,000 years. In the past century alone, the temperature has climbed 0.7 degrees Celsius, roughly ten times faster than the average rate of ice-age-recovery warming. Models predict that Earth will warm between 2 and 6 degrees Celsius in the next century and the predicted rate of warming for the next century is at least 20 times faster [2].

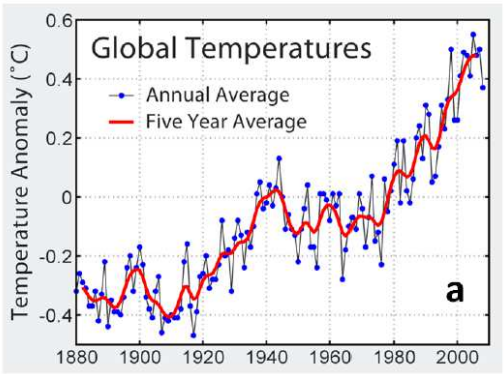

Fig.1.2 Record of global average temperature anomalies.

Climate changes cause a lot of disease for what concern environment, and it is possible to reveal a wide array of effects like as rapidly melting glaciers, destabilization of major ice sheets, increases in extreme weather, rising sea level, shifts in species ranges, and more [1]. These changes are affecting the availability and quality of water supplies, how and where food is grown, and even the very fabric of ecosystems on land and in the sea. Furthermore, the acidity of ocean water, due to the higher carbon dioxide concentration, has been increasing since the beginning of the Industrial Revolution with dramatic consequences on oceanic species. Ocean acidification is caused by the world's oceans taking in more carbon dioxide (CO_2) than they can handle subsequently increasing the acidity and decreasing the pH levels of the oceans. Estimates suggest that over twenty-two million tons of CO_2 are absorbed by the world's oceans daily and oceans are already thirty percent more acidic than they were before the industrial revolution and models suggest that by the end of this century oceans could be 150 percent more acidic [3]. The acidification of the world's oceans has a direct and dire impact on marine life, particularly on skeleton building organisms such as corals, calcifying algae and molluscs such as mussels and oysters. The rapid warming that Earth is experiencing during the last decades is due to the enhancement of Greenhouse effect [4]. The concept at the heart of Greenhouse effect is energy balance between what we can call energy that comes in and energy that goes out. There's a delicate balancing act occurring every day across the Earth, involving the radiation the planet receives from space and the radiation that's reflected out to space. It's this equilibrium of incoming and outgoing radiation that makes the Earth habitable, with an average temperature of about 59 degrees Fahrenheit (15 degrees Celsius) [5-6]. Greenhouse gasses are able to absorb part of the thermal radiation emitted by the Earth after the absorption of solar radiation. A part of thermal radiation is reflected and directed above, and another one is directed below, leading to an equilibrium for what concern Earth temperature. The more greenhouse gases you have in the atmosphere, the more heat stays on Earth. If the amount of energy from the sun and the amount of greenhouse gases in the atmosphere remains the same, then the average temperature on Earth will also be constant. But this is no longer the case. The amount of greenhouse gases in our atmosphere is the highest it has been in the last 3 million years, enhancing the greenhouse effect and making the Earth warmer than normal [7]. These greenhouse gases include water vapor, CO_2, methane (CH_4), nitrous oxide (N_2O) and other gases, according to the Environmental Protection Agency (EPA) [8]. Greenhouse gases concentration is strongly conditioned by human activities and has been rising extensively since the industrial revolution and has now reached dangerous levels leading to a rapid change of the natural greenhouse effect. Human activities such as the burning of oil, coal and gas, as well as

deforestation are the primary cause of the increased carbon dioxide concentrations in the atmosphere. Burning fossil fuels releases energy, which is most commonly turned into heat, electricity or power for transportation, producing at the same time carbon dioxide as byproduct. In 2011 fossil fuels created something like billion tonnes of carbon dioxide emission worldwide and coal is the most carbon intensive fossil fuel providing for every ton of coal burned, approximatively 2.5 tonnes of CO_2 produced [9]. Globally, economic and population growth continue to be the most important drivers of increase in CO_2 emissions from fossil fuel combustion. The contribution of population growth between 2000 and 2010 remained roughly identical to the previous three decades, while the contribution of economic growth has risen sharply. The Intergovernmental Panel on Climate Change (IPCC), which is a scientific and intergovernmental body under the auspices of United Nations dedicated to the task of providing the world with an objective, scientific view of climate changes and their political and economic impacts, stated that *"Continued emission of greenhouse gases will cause further warming and long-lasting changes in all components of the climate system, increasing the likelihood of severe, pervasive and irreversible impacts for people and ecosystems. Limiting climate change would require substantial and sustained reductions in greenhouse gas emissions which, together with adaptation, can limit climate change risks"*, and, in particular, *"Climate change will amplify existing risks and create new risks for natural and human systems. Risks are unevenly distributed and are generally greater for disadvantaged people and communities in countries at all levels of development"* [10]. IPCC recommends the necessity to limit total human-induced warming below 2°C above pre-industrial temperatures. Seems to be strictly important the development of infrastructures dedicated to energy production and distribution based on renewable, no-fossil and clean energy sources. One of the most important steps toward a sustainable life was done by 192 countries through "Kyoto Protocol", a famous international treaty which extends the 1992 United Nations Framework Convention on climate Change (UNFCCC) [11]. The protocol commits States Parties to reduce Greenhouse gas emission, in particular CO_2 emission, according to scientific consensus. More recently, Paris climate agreement was negotiated by representatives of 196 parties and adopted by consensus on 12 December 2015. In Paris agreement, each country determines, plans and regularly reports its own contribution in order to mitigate global warming. Unlike Kyoto Protocol this agreement allows for voluntary and nationally determined targets in order to support sustainable development [12]. In the end, it's is clear that both the politic and the scientific community play a fundamental role in the rescue of our planet and have the responsibility to favour employment of renewable sources.

1.2 Solar Energy: a springboard for the future

Fig.1.3 Representation of solar energy employment based on photovoltaic.

The technologic develop of our society will be driven by increasing energy demand, cost and environmental impact. Considering energy consumption which was estimated around 10^{20} joule in the world, and at the same time the need of avoiding environmental damages, an improvement toward renewable sources is required. For what concern global energy demand, fossil fuels (like as oil, coal and natural gas) are still the major resource. On the other hand, their limitations in terms of impact on human health and on environment, costs and availability on a human timescale force to invest in other power sources, such as biomass, water, geothermal, wind and solar. Renewable and low-carbon technologies are becoming increasingly cost competitive in a bigger number of countries and renewable-based power generation capacity is estimated to have increased by 128 GW in 2014, of which 37% is wind power, almost one-third solar power and more than a quarter hydropower. Furthermore, it is predicted that by 2020, renewable wind and solar resources will supply 12% of electricity in the USA and 20% in Europe [13]. For long-term employment solar is the more appealing resource: it is the ultimate sustainable energy source, providing ca. 10000 times the energy that is currently consumed worldwide. Because of its unmatched resource potential, solar energy utilization has been the subject of intense research, development, and deployment efforts that have accelerated during the past decade. Efforts have been focused on the development of photovoltaics (PVs) (see section 1.3) for production of solar electricity, on conversion of solar energy into heat, and on artificial systems that directly produce fuels from sunlight (see section 1.5). Chemistry has played a fundamental role in the design of materials and molecular systems for solar energy conversion. The employment of p-n junction silicon single-crystals solar cells demonstrates the practicality of photovoltaics but the novel approaches, which include in particular dye sensitization, organic

semiconductors and thin films offer opportunities to obtain cheaper and long-lasting systems [14]. On the other hand, it is worth to note that radiation that reaches the earth, despite is extensively distributed, presents a a low intensity and its availability depends on geography, day and night alternation, and cloud cover. Therefore, solar has to be coupled with efficient storage systems such as rechargeable batteries (see section 1.4), which are able to store and realise electric power when required [14].

1.3 Photovoltaic cells

Photovoltaic cells (PVs) generally consist of a semiconductor that can absorb solar photons above a minimum photon energy, corresponding to its band gap (see Chapter 2, Section 2.1) [14]. Indeed, sunlight contains photons with energies (hυ) that reflect the sun's surface temperature, ranging between 3.5eV (electron volt) and 0.5eV. The visible region goes from 3.0eV (violet) to 1.8eV (red), with a peak power that occurs in the yellow (2.5eV) [15].

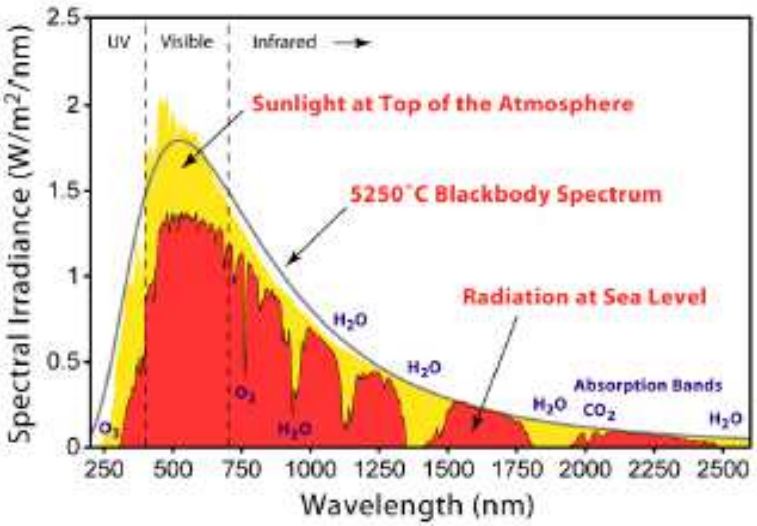

Fig.1.4 Spectral distribution of solar irradiance

Photons with energies below semiconductor band gap are transmitted, while photons with energies above the band gap are absorbed. Once light is absorbed, electrons and holes move to opposite side of the cell structure, following electrochemical potential gradients. As a consequence of the movement we can appreciate the production of a photocurrent and a photovoltage which translates in the production of electric power. The birth of the modern photovoltaic cells can be traced in 1954 with with D. Chapin, C. Fuller and G. Pearson that discovered solar cells based on p-n junctions in single crystal Silicon (Si) with an efficiency of ca 6% [16] (Fig.1.5).

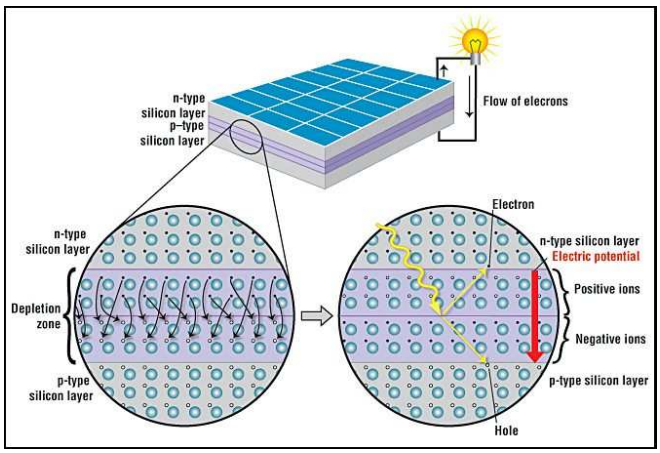

Fig.1.5 Scheme of a PV cell based on p-n junctions in Silicon

From the mid 1950s to the early 1970s, PV research and development was directed primarily towards space applications and satellite power. However, in recent years, total global PV production increased from less than 10mW_p/yr (Mega Watt peak per year) in 1980 to about 1200 MW_p/yr in 2004 and the current total global PV installed capacity is about 200 GW with a further increase foreseen for the next years [15]. Nowadays commercially available Si panels account for ~90% of total solar panel production and have an energy payback period of <2.5 years and ~16 to 21% power-conversion efficiencies [17-18]. On the other hand, in order to achieve, for example, the consumption in the United States of *ca.* 3 TW (terawatts) at *ca.*10% efficiency, would be require 140000km^2 for solar energy collection, and the materials costs with current photovoltaic technology, namely p-n junction silicon cells, would be enormous, such as *ca.* 60 trillion dollars [16]. Several efforts were done with the aim of reducing cost, including methods to integrate higher band-gap materials with Si to create a high-efficiency tandem device in a scalable, cost-effective process that is compatible with existing Si PVs [14]. Recently, in contrast to active materials based on single-crystal substrates, thin-film materials, such as cadmium telluride (CdTe), amorphous hydrogenated Si, organic PVs and organic-inorganic PVs (such has perovskites) have been explored, to reduce system installation costs [14]. Perovskites, which are formed from lead salts and organic ammonium cations, have demonstrated that extraordinary performance can be obtained using simple deposition techniques in novel material systems. However issues related to the employment of toxic materials and to instability, limit their application in large scale dispositive. For what concern all organic PVs, such as those based on composites of poly-phenylenevinylene (PPV) with a functionalized C_{60} that serves as the lightabsorber [19-20], their performances can be systematically varied by chemical control over the composition and structure of the components of the device. However, radical-related side reactions under visible and ultraviolet illumination of the organic materials that form the

active components of the device structure should compromise long-term stability and high efficiency. To date, a possible solution to avoid cost of fabrication is given by a system that, contrary to traditional photovoltaic solid-state technologies, works at molecular and nanolevel. This system, namely dye-sensitized solar cell (DSSC), is based on the interaction of a molecule (*i.e.* the dye) with, typically, a wide band gap semiconductor in contact with an electrolyte containing a redox couple (see Chapter 2, section 2.2). DSSC technology presents an efficiency range around 12% and offers the possibility to design solar cells with a large flexibility in shape, colour, and transparency. Furthermore sensitized-solar cells perform also relatively better compared with other solar cell technologies under diffuse light conditions and at higher temperature and, as a consequence, offer the possibility to be integrated into different products, opening up new commercial opportunities [21].

1.4 Energy storage

Regardless of the competitiveness on a levelized cost basis of solar electricity relative to fossil-based electricity, the value of electricity produced from an intermittent resource such as solar is not the same as the value of energy that can be provided on demand. The key to achieve a stable supply lies in the development of suitable energy storage system which is a key technology that is becoming more and more important in the energy infrastructures. Electrical energy storage technologies can be classified into three categories, namely flywheels and supercapacitors, geological storage technologies and battery storage technologies. Flywheels and supercapacitors are low-energy, high-power storage systems used for power management, but these technologies are not considered to have wide applications in transmission due to material limitations. Geological storage technologies include pumped hydro and compressed air energy storage which are large-scale, high-energy, high-power systems, capable of providing significant reserves. However, they require special terrain and have large capital investment and maintenance costs. On the other hand, battery storage technologies provide a potential solution to large-scale energy storage and act as a buffer between intermittent electricity production and customer requirements for the instant delivery of electricity power [22]. As displayed in Fig.1.6, a battery is normally made of a cathode and an anode material immersed in an electrolyte.

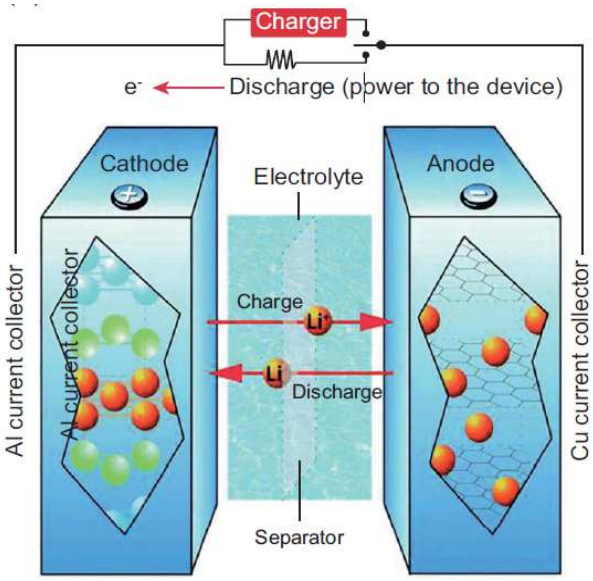

Fig.1.6 Traditional Li-ion battery made of solid electrode materials

In a typical battery energy is stored in the electrode materials, ions are shuttled between the cathode and anode through the electrolyte, while electrons are transported as electrical current through external circuits. Rechargeable batteries are commonly made of solid-state cathode and anode materials. These include lithium-ion (Li-ion) batteries, lead-acid batteries, sodium-sulfur batteries, and nickel-cadmium batteries [23-24]. Currently, because of its low cost and wide-ranging applications, the leadacid battery is the most extensively used technology in the marketplace. However, lead-acid battery technology is limited by shallow charge–discharge capacity, short cycle life and the use of hazardous lead [25]. Li-ion is the main technology currently competing with lead-acid battery for future applications. The use of lithium-ion batteries in commercial products is ever increasing; they are the popular choice in electronic devices, such as laptops and mobile phones as they have excellent life cycles and can store more energy per volume than any other portable rechargeable battery. Li-ion batteries are also seen as the best battery choice for electric vehicles. Besides, major issues associated to the use of Li-ion batteries are both the difficulty of preventing internally the battery from going into an abuse situation and their current high cost which limits their use to relatively smallscale. To date, redox flow batteries (RFBs), which contrary to solid-state batteries are based on cathode and anode contained in electrolyte reservoirs from which the electrolytes are circulated (by pumps) through an electrochemical cell, appear to offer great promise as low cost, high efficiency systems for large-scale energy storage. Indeed, for what concern large-scale energy storage in the range of 10 kW–10 MW, RFBs have cost, mobility, flexibility, depth of discharge, rapid response, and safety advantages over lithium ion batteries [26]. As an electrochemical method, redox-

flow batteries (RFBs) offer a versatile means of storing energy and furthermore the possibility of decoupling between energy storage and power delivery. Nowadays, RFBs are a focus of major early-stage R&D efforts and will be explored more deeply in Chapter 3.

1.5 Solar Fuels

Alternatively, with an appropriate process, excess solar electrical power could be stored as high-energy chemicals and utilized in existing power plants, or by secondary electricity generation in fuel cells [14]. Fuel cells (Fig.1.7) can power almost any portable application that typically uses batteries, from hand-held devices to portable generators and also our transportation, including personal vehicles, trucks and buses [31].

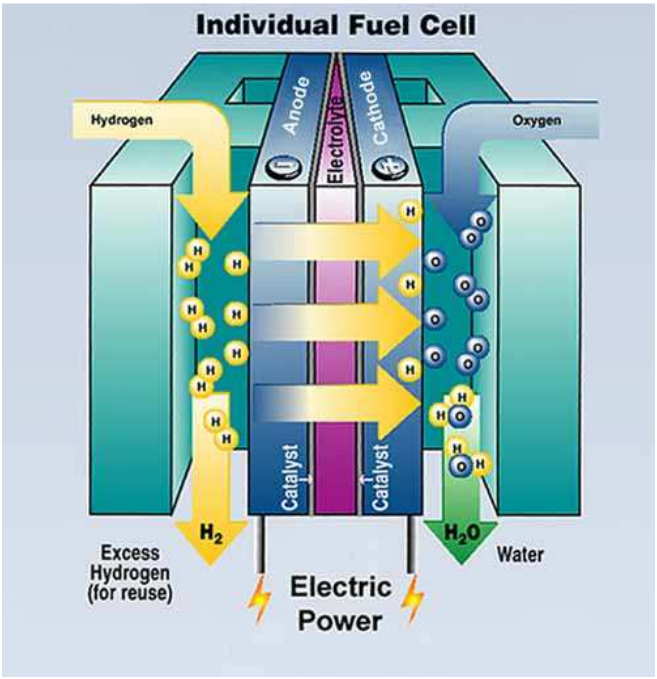

Fig.1.7 Scheme of a traditional fuel cell which employs Hydrogen as a fuel.

Generally, to refer to any scheme for capturing and storing the energy from sunlight into fuels, the term '*artificial photosynthesis'* is used, due to the inspiration given by nature [27-28]. The production of "solar fuels" should occur through water splitting [29] into oxygen and hydrogen or combination of water oxidation with carbon dioxide reduction into almost any form of reduced carbon such as carbon monoxide (CO), formaldehyde (HCHO), methanol (CH_3OH) and methane (CH_4) as ultimate goal [30]. Among solar fuels hydrogen is the most promising energy vector since is clean and powerful: the energy in 1 kg of hydrogen gas contains about the same as the energy in 1 gallon of gasoline. Furthermore, routes to solar water splitting are more straightforward than reduction of CO_2. Besides, nowadays, the majority of hydrogen (~95%) is produced from fossil fuels by natural gas

reforming and coal gasification with only a small quantity by other ways such as biomass gasification or water splitting [32]. Indeed, the development of hydrogen from natural gas is the cheapest and most common procedure to obtain hydrogen and represents 38% of the world's hydrogen production, with an approximately 80% efficiency. The limitation of this procedure is strictly connected to the byproduction of CO_2 and CO, known as greenhouse gases. Therefore, advantages in terms of using water as starting reagent and of generating only oxygen as a byproduct encourage scientific community to invest in the direct production of hydrogen from solar water electrolysis [14]. The electricity required to split water can be generated using sun in photoelectrochemical solar cells, where light is absorbed by a molecule or semiconductor, and chemical reactions occur at solid–liquid or solid–vapor interfaces. Herein, in Chapter 2, Section 2.3 we will explore photoelectrochemical systems for water splitting based on light-harvesting molecules adsorbed on wide band gap semiconductors, in contact with liquid interfaces (DSPECs) [33-34].

1.6 References

1) http://climate.nasa.gov/evidence

2) http://earthobservatory.nasa.gov/Features/GlobalWarming/page3.php

3) http://www.pmel.noaa.gov/co2/story/Ocean+Acidification

4) The Royal Society. *Climate change: A Summary of the Science*. London: The Royal Society Science Policy Centre, **2010**;

5) Le Treut, H., R. Somerville, U. Cubasch, Y. Ding, C. Mauritzen, A. Mokssit, T. Peterson and M. Prather. Historical Overview of Climate Change. In: *Climate Change 2007: The Physical Science Basis. Contribution of Working Group I to the Fourth Assessment Report of the Intergovernmental Panel on Climate Change*. Cambridge University Press, Cambridge, United Kingdom and New York, NY, USA, **2007**;

6) U.K. Met Office. *Warming: A guide to climate change*. Exeter, U.K.: Met Office Hadley Centre, **2011**;

7) R. S. W. Van De Wal, B. De Boer, L. J. Lourens, P. Köhler, R. Bintanja, *Clim. Past*. **2011**, *7*, 1459;

8) https://climate.nasa.gov/causes/

9) P. Friedlingstein1, R. M. Andrew, J. Rogelj, G. P. Peters, J. G. Canadell, R. Knutti, G. Luderer, M. R. Raupach, M. Schaeffer, D. P. van Vuuren, C. Le Quéré, *Nature Geoscience* **2014**, *7*;

10) IPCC Climate Change 2014 Synthesis Report Summary for Policymakers;

11) "7 .a Kyoto Protocol to the United Nations Framework Convention on Climate Change". *UN Treaty Database;*

12) Change, United Nations Framework Convention on Climate. "The Paris Agreement - main page". *UNFCCC.int.*;

13) International Energy Agency, *World Energy Outlook Special Report*, **2014**;

14) N. S. Lewis, *Science* **2016**, *351*, 1920;

15) G. Bergamini, S. Silvi, *Applied Photochemistry*, Lecture notes in chemistry 92, **2013**, chapter 2, pp 67-143;

16) W. Song, Z. Chen, M.K. Brennaman, J.J. Concepcion, A.O.T. Patrocinio, A. O. T., N.Y. Iha, T.J. Meyer, *Pure and Applied Chemistry* **2011**, *83*, 749;

17) J. Jean, P. R. Brown, R. L. Jaffe, T. Buonassisi, V. Bulovic, *Energy Environ. Sci.* **2015**, *8*, 1200;

18) I. S. E. Fraunhofer, *Photovoltaics Report* **2014**;

19) L. Dou et al., *Adv. Mater.* **2013**, *25*, 6642;

20) H. Hoppe, N. S. Sariciftci, *J. Mater. Res.* **2004**, *19*, 1924;

21) "*Dye sensitized solar cell market analysis by application and segment forecasts to 2022*", **2016**, http://www.grandviewresearch.com/industry-analysis/dye-sensitized-solar-cell-market;

22) X.Li, et al., *RSC Adv.,* **2012**, *2*, 10125;

23) H.L. Ferreira, R. Garde, et al., *Energy* **2013**, *53*, 288;

24) B. Dunn, H. Kamath, J.M. Tarascon, *Science* **2011**, *334*, 928;

25) C. Pillot, *The Rechargeable Battery Market and main Trends* **2014–2015**;

26) S. Eckroad, *Handbook of Energy Storage for Transmission or Distribution Applications*, Electric Power Research Institute Report 1007189, California, USA, **2002**;

27) J.Kern, G. Renger, *Photosynthesis Research* **2007**, *94*, 183;

28) Renger, G.; Renger, T. *Photosynthesis Research* **2008**, *98*, 53;

29) Y.Tachibana, L.Vayssieres, J.R. Durrant, *Nat. Photonics* **2012,** *6*, 511;

30) T. Arai, S. Sato, T. Kajino, T. Morikawa, *Energy Environ. Sci.* **2013,** *6*, 1274;

31) http://www.afdc.energy.gov/fuels/hydrogen;

32) R. J. Press, K. S. V. Santhanam, M. J. Miri, A. V. Bailey and G. A. Takac, *Introduction to Hydrogen Technology*, **2008**, John Wiley & Sons, Inc.

33) J.R. Swierk, T.E. Mallouk, *Chem. Soc. Rev.* **2013,** *42*, 2357;

34) L. Alibabaei, H.Luo, R.L. House, P.G. Hoertz, R. Lopez, T.J.Meyer, *J. Mater. Chem. A* **2013,** *1*, 4133;

CHAPTER 2. DYE-SENSITIZED SOLAR CELLS (DSSCs) and DYE-SENSITIZED PHOTOELECTROCHEMICAL CELLS (DSPECs)

DSSCs and DSPECs based on dye sensitized-semiconductor/liquid junction, which provide one of the best known chemical methods of converting solar energy into electrical energy or chemical fuels respectrively, will be the focus of this chapter. In the following, we go through the basic features of the interfaces, starting with the individual components (Section 2.1) followed by the description of the systems (Section 2.2, Section 2.3).

2.1 Description of the Interfaces

2.1.1 Semiconductor Materials

Electrochemical properties of semiconductors can be easily understood referring to band theory [1]. Because of the infinite number of atoms, we have to consider, we can discuss of the structure of this type of solids in terms of energy bands which are constituted by atomic orbitals of the individual atoms. The interactions between all the orbitals lead to spaces between electronic energies within a band so small that a band can be considered as a continuous. On the other hand, the gap between different atomic quantum states is preserved. Thus, the allowed electronic energies fall into energy bands of closely spaced levels, among which there are forbidden gaps. Energy levels of interest are the lowest (namely valence band) and the highest (namely conduction band). The properties of the band gap (i.e., the difference in energy between the upper edge of the valence band and the lower edge of the conduction band) determine the properties of the material. In insulators the energy gap is huge, the valence band is totally filled by electrons while the conduction band is empty and, as a consequence, the application of an electric field causes no motion of charge. In a conductor a filled band should overlap an empty band, so electrons can move from a band to another one freely, resulting in high conductivity. In semiconductors, there is a gap between band but it is smaller with respect to the one in insulators and electrons can be promoted thermally or optically, resulting in a conductivity smaller than the one recorded with a conductive material.

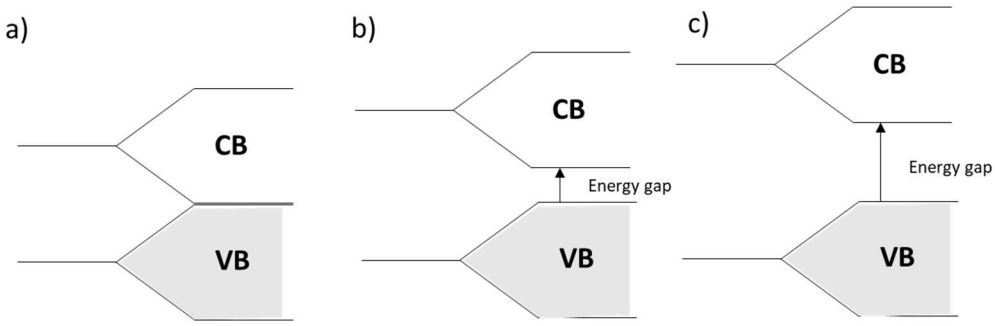

Fig.2.1 Representation of CB and VB in terms of band theory for a conductor (metal) (a), a semiconductor (b) and an insulator (c) [2].

The promotion of an electron in a semiconductor from the valence band (VB) to the conduction band (CB) leads to the generation of a vacancy, namely a hole (h^+) that is able to move through space by the transfer of one electron to the vacancy. Si (silicon) and Ge (Germanium) are prototypical examples for clarifying the basic principles of semiconductor energetics and conduction mechanisms. Classical semiconductors can be doped, i.e. the introduction of electron rich or electron deficient impurities into the semiconductor, resulting in a significant influence in their properties. For example, a small level of As in Si semiconductor introduces an extra electron per As atom. The lower orbitals in Si are filled and as a consequence the electrons in excess fill new energetic states that formed the so called donor band, close to the conduction band edge. Doping is the cause of the augmented conduction in this kind of semiconductor, likely due to the presence of more negative charge carriers (electrons). We can call this type of semiconductor *n*-type (negative) (Fig.2.2 a). On the other hand, impurities of another element like as Ga can lead to acceptor levels really near to the valence band. In this case the enhancement of conductivity is caused by holes: electrons can be easily excited and reach the energetic level close to VB, leaving a hole. The semiconductors with this kind of conduction mechanism are called *p*-type (positive) (Fig. 2.2 b).

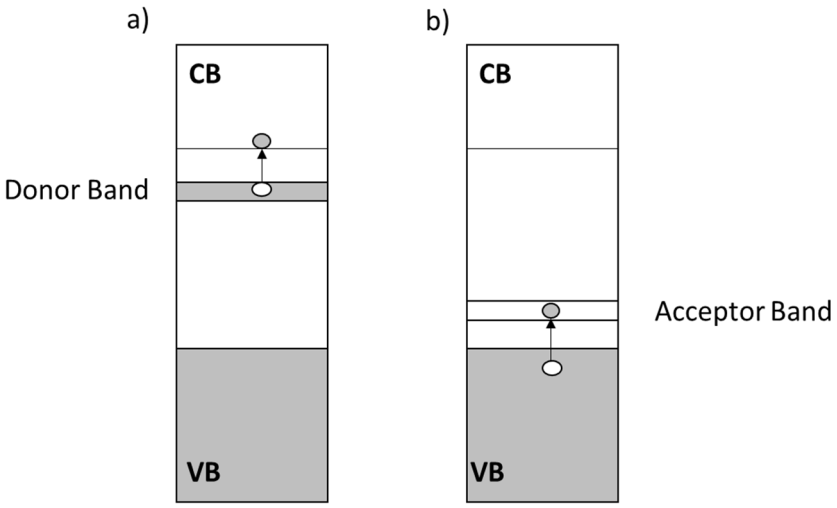

Fig.2.2 Band structure of an *n*-type semiconductor (a) and a *p*-type semiconductor (b)

In many cases impurities like as Ga or As are injected into ultrapure semiconductors in low quantity (ratio of 1 to 10^9) in order to generate *p*-type or *n*-type extrinsic semiconductors which are extremely important in solid-state electronic devices for their semiconducting properties. There are also a lot of materials that spontaneously have *n* or *p*-type character due to the presence of defects in the lattice, originating an excess or a lack of electrons inside. This is really common in the case of oxides or chalcogenides, for example Titanium dioxide (TiO_2). The stoichiometry of this semiconductor is well described by the TiO_{2-x} formula, since the presence of dangling bond leaves coordination sphere of Ti^{4+} unsaturated. The absence of oxygen in titanium dioxide crystal lattice is compensated by the presence of electrons weakly bonded that constitute donor levels near the conduction band. As a consequence, "TiO_2" can be considered a *n*-type semiconductor. Other examples of *n*-type semiconductors are WO_3, Fe_2O_3, ZnO, whereas Cu_2O and NiO present *p*-type character. All semiconductors cited above are wide band gap semiconductors, having an Energy gap (E_g) of ca. 3.0 eV, and are usually employed in photoelectrochemical devices. To discuss properly the properties of a semiconductor is really important to understand the concept connected to the so called Fermi level [1]. The Fermi Dirac equation is given by:

$$f(E) = \frac{1}{1+e^{\frac{(E-E_F)}{kT}}} \qquad \text{(Eq.2.1)}$$

Where *f*(E) is the probability that a state of energy *E* is occupied, E_F is a parameter called the Fermi energy, *k* is the Boltzmann's constant and *T* is the absolute temperature. The Fermi energy is defined as the level for which *f*(E) = ½. As a consequence, we can state that the Fermi level is a virtual energy level which have the 50% of possibility to be occupied by an electron. The Fermi energy is just the electrochemical potential, or the partial molar free

energy per electron. This result is physically understandable considering two equilibrating systems: thermodynamically we can expect that there is an exchange of particles (i.e. electrons) until their electrochemical potentials are equal; from the point of view of Fermi statistic, the transfer of electrons from one level to another fills states of lower energy in one system, emptying higher lying filled states in the other system and proceeds until the distribution over energy in the two systems match, i.e., the Fermi levels are equal. The Fermi level position distinguishes the different classes of materials, as E_F is located in the VB for metals (providing good electron conduction) and in the forbidden gap for semiconductors and insulators: for a *n*-type semiconductor the Fermi level lies between the energy level introduced by the dopant and the CB edge, and so very close to the CB, whereas in a *p*-type semiconductor it lies close to the VB. In nondegenerate semiconductors, the equilibrium Fermi level is given by [3]:

$$E_F = E_C + k \;\; T ln \frac{n_c}{N_C} \qquad \text{(Eq. 2.2)}$$

where *Ec* is the energy at the conduction band edge, *kT* is the thermal energy, n_c is the density of conduction band electrons, and N_c is the effective density of conduction band states. These values are very sensitive to the environment. For example, the position of the conduction band depends on the surface charge (dipole potential) [3]. Usually, the pH dependence of *Ec* for semiconductor films in aqueous solutions follows a Nernstian behaviour with a shift of 59 mV/pH unit due to protonation/deprotonation of surface groups [4]. Furthermore, in nonaqueous solutions, *Ec* can be widely tuned by the presence of positive ions, cations. This effect is greatest with cations possessing a large charge-to-radius ratio. Cyclic voltammetry (see Chapter 8) and spectroelectrochemical procedures (see Chapter 8) have been usually used to estimate E_c [4].

2.1.2 Electrolyte

The role of electrolytes in most electrochemical devices like electrolytic cells, fuel cells, or batteries is to serve as the medium for the transportation of charge carriers, which are in the form of ions, between a pair of electrodes, indeed, the electrolytic solution usually contains a redox couple. The electrochemical potential of electrons, or the Fermi level, for a one-electron redox couple is given by the Nernst equation and can be written as [3]:

$$E_{F,redox} = \; E^0_{F,redox} + k \;\; T \; ln(\frac{c_{ox}}{c_{red}}) \qquad \text{(Eq.2.3)}$$

where c_{ox} and c_{red} are the concentrations of the oxidized and reduced species of the redox system. Besides the Fermi energy, we also need a description of the energy states being

empty or occupied by electrons. In the energy scale, E^0_{red} corresponds to the energy position of occupied electron states and E^0_{ox} to the empty states. They differ from the Fermi level $E^0_{F,redox}$ by the so-called reorganization energy, λ, which is the energy involved in the relaxation process of the solvation shell around the reduced species following transfer of an electron to the vacuum level [5] (Fig.2.3 a).

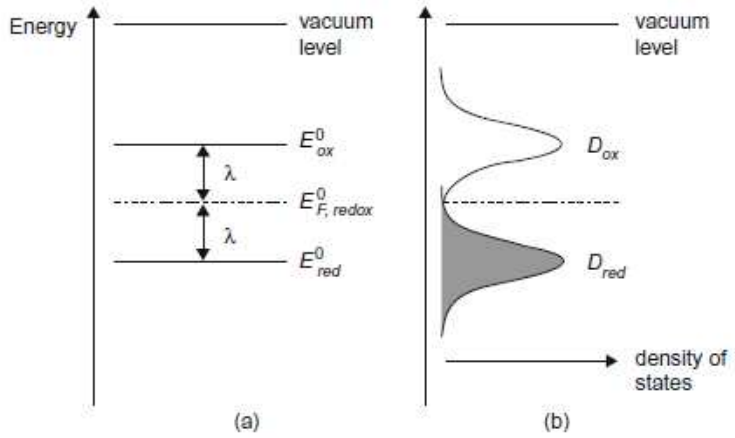

Fig.2.3 (a) Electron energies of a redox system using vacuum as a reference level. E^0_{red} = occupied states, E^0_{ox} = empty states, $E^0_{F,redox}$ = Fermi level of the redox couple. (b) Corresponding distribution functions [5].

The electron states of a redox system are not discrete energy levels but are distributed over a certain energy range due to fluctuations in the solvation shell surrounding the molecule. This is indicated by the distribution of energy states around E^0_{red} and E^0_{0x}: D_{red} is the density of occupied states represented by the reduced component of the redox system and D_{ox} the density of empty states represented by the oxidized component. Assuming a harmonic oscillation of the solvation shell, the distribution curves can be described by Gaussian functions:

$$D_{red} = D^0_{red}\, exp\left[-\frac{(E-E^0_{F,redox}-\lambda)^2}{kT\lambda}\right] \qquad \text{(Eq.2.4)}$$

$$D_{ox} = D^0_{ox} exp\left[-\frac{\left(E-E^0_{F,redox}+\lambda\right)^2}{kT\lambda}\right] \qquad \text{(Eq.2.5)}$$

Where D^0_{red} and D^0_{ox} are normalizing factors. The halfwidth of the distribution curves is given by:

$$\Delta E_{1/2} = 0.53\lambda^{1/2} eV \qquad \text{(Eq.2.6)}$$

Accordingly, the width of the distribution function depends on the reorganization energy (λ), which is a parameter of importance for the kinetics of electron-transfer processes at the oxide-dye-electrolyte interface (see Section 2.1.5).

2.1.3 Semiconductor/liquid junction properties

The interface between a semiconductor electrode and an electrolytic solution is of great interest to understand dynamics described in the present chapter. In order for the two phases to be in equilibrium, their electrochemical potentials must be the same:

$$E_F = E_{F,redox} = qV_{redox} \quad \text{(Eq.2.7)}$$

where q is the elementary charge and V_{redox} the electrochemical (redox) potential of the electrolyte. From now on, we limit the discussion to *n*-type semiconductors, keeping in mind that the inverse but analogous situation occurs with *p*-type semiconductors. For a *n*-type semiconductor with the initial Fermi level higher than the redox potential of the electrolyte, the equilibration of E_F and $E_{F,redox}$ occurs by transfer of electrons from the semiconductor to the solution. This will produce an electrical field in the solid, i.e. the so-called space charge layer (also referred to as the depletion layer since the region is depleted of majority carries). For a *n*-type semiconductor the space charge layer is positive. The electric field is represented by curvature of the conduction and the valence bands (band banding) and indicates the direction of the free carrier flow in the field (Fig.2.4). The width of the space charge layer was found to be [6]:

$$w = \sqrt{\frac{2\varepsilon\varepsilon_0(V-V_{fb})}{qN_D}} \quad \text{(Eq.2.8)}$$

Where ε is the relative dielectric constant, ε_0 the permittivity of free space, N_D the donor concentration (or dopant density), and V_{fb} and V the electrostatic potentials of the semiconductor surface and the bulk, respectively. $V - V_{fb}$ gives the band bending. While the space charge layer normally extends from a few nanometres to micrometres, the main part of the potential drops takes place in the solution within a few Angstroms of the surface in the so-called Helmholtz layer.

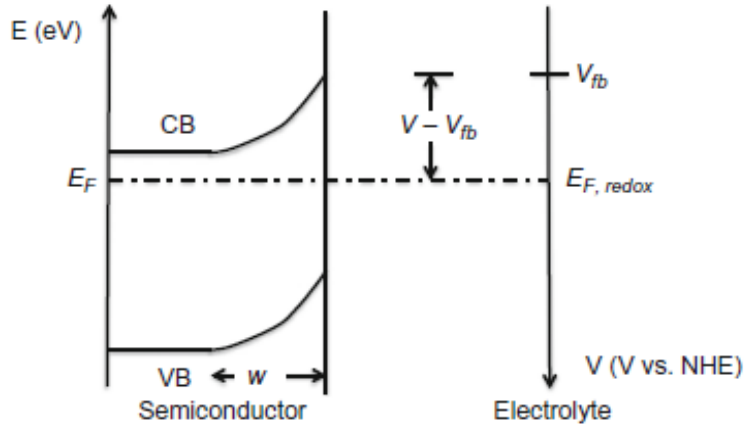

Fig.2.4 Energy-versus-distance diagram for an *n*-type semiconductor/liquid junction in equilibrium. For an *n*-type semiconductor, the space charge region, *w*, is positively charged due to depletion of conduction band electrons [3].

The development of a space charge region is fundamental for the application of semiconductor electrodes in a photoelectrochemical device: without the formation of a depletion layer, the photogenerated carriers cannot be efficiently separated and extracted from the materials and so, after their generation, recombination will take place. By tuning the external potential, it is possible to modify the space charge layer characteristics. Indeed, when a positive potential difference is applied to a *n*-type semiconductor both *w* and the band bending are increased: qualitatively, the positive applied potential increases the donor concentration in the semiconductor surface and so the potential drop in the depletion layer. On the other hand, if a negative bias is applied, the injection of electrons slowly compensates the positive holes in the space charge layer until there will be no difference at all. The potential at which the bands become flat again is the flat band potential (V_{fb}). It is worth to notice that the effect of an external field in a mesoporous semiconductor film is different compared to the discussion above for a doped compact semiconductor in which the applied potential changed the band bending. Since there is no macroscopic space charge layer formed in a mesoporous electrode, the applied potential will change the Fermi level at the back contact (conducting substrate/mesoporous oxide interface) throughout the mesoporous film with the result of a different electron concentration of the electrode compared to zero bias. The term flatband potential is therefore not appropriate for a mesoporous electrode and the term position of the conduction band edge, *Ec*, is then used [3].

2.1.4 Semiconductor/liquid junction under illumination

When a semiconductor electrode is irradiated using a light with energy greater than the Energy gap of the semiconductor, the electrode absorbs the photon energy and promote

electrons from the VB to the CB: for *n*-type semiconductors, the photoexcited electrons hardly influence the concentration of the electrons in the conduction band (because electrons are the majority charge carriers), but the number of photoproduced holes significantly increase the total concentration of holes (the minority charge carriers), in the VB. Since under the condition of photoexcitation no thermal equilibrium is established between electrons and holes in the CB and VB, the photoexcitation process has the effect to split the Fermi level of the semiconductor into two quasi-Fermi levels: the *quasi*-Fermi level of electrons (${}_n\varepsilon_F^*$) and the *quasi*-Fermi level of holes (${}_p\varepsilon_F^*$):

$$ {}_n\varepsilon_F^* = E_F + kTln\frac{n+\Delta n^*}{n} \quad \text{(Eq.2.9)} $$

$$ {}_p\varepsilon_F^* = E_F + kTln\frac{p+\Delta p^*}{p} \quad \text{(Eq.2.10)} $$

Where E_F is the Fermi level energy of the semiconductor in dark conditions, *n* and *p* are the concentration of electrons and holes in the dark and Δn and Δp are the increases in the concentration of electrons and holes produced by photoexcitation ($\Delta n = \Delta p$). For a *n*-type semiconductor, under the conditions of photoexcitation, the *quasi*-Fermi level of electrons (the majority charge carriers) remains close to the original Fermi level ($n >> \Delta n^*$), but the quasi-Fermi level of holes (minority charge carriers) shifts away from the original Fermi level, because the concentration of photoexcited holes, (Δp^*) exceeds the concentration of holes in the dark ($p << \Delta p^*$).

2.1.5 Molecular excitation and electron transfer theory

Theory of excited states and their deactivation pathways needs to be briefly described, since photoelectrochemical sensitized cells operation is based on a series of electron transfer processes that follow the sensitizer excitation by light. Upon photon absorption, a molecule, in its excited state S* can go through different decay processes to return to the ground state, such as radiative or non-radiative unimolecular decay processes, involving, respectively, the emission of the excitation energy in the form of light radiation or the transformation of electronic energy into vibrational, which is dissipated in the form of heat. Excited state can be eventually deactivated by chemical reactions. The variation during time of excited state concentration can be described by the equation reported above:

$$ \frac{-\delta[S^*]}{\delta t} = \left(k_r + k_{nr} + k_p\right)[S^*] = \sum k_i[S^*] \quad \text{(Eq.2.11)} $$

Where k_r, k_{nr}, k_p are respectively constants referred to decay processes like radiative processes, non-radiative processes and chemical reactions. Lifetime of an excitated state is defined as:

$$\tau^{S^*} = \frac{1}{\sum k_i} \quad \text{(Eq.2.12)}$$

As a consequence, the efficiency of a decay process, with respect to the others is given by:

$$\eta_i = \frac{k_i}{\sum k_i} \quad \text{(Eq.2.13)}$$

Besides, in the presence of another species B, S* excited state can react by transferring both an electron and energy, through the following reactions:

- $S^* + B \rightarrow A^+ + B^-$ Electron Transfer
- $S^* + B \rightarrow A + B^*$ Energy Transfer

Energy transfer can be seen like a non radiative transition between two electronic excited states, and in this respect kinetic constant for energy transfer can be calculated by the Fermi golden rules:

$$k_{en} = \frac{2\pi}{h}(H_{AB}^{en})^2 FC \quad \text{(Eq.2.14)}$$

Where H_{AB}^{en} is the electronic coupling between two excited states and FC is the Franck-Condon term. In this chapter, the focus is on the reaction which involves the quenching of the excited state carried out by another specie B, namely the conduction band of a semiconductor, through electron transfer. The redox properties of excited states are noticeably different from those of the fundamental state. An electronically excited molecule can be considered a new chemical entity with new thermodynamic properties: the excited state (S*) is both a better oxidizer and a better reducing agent than the corresponding ground state (S). Indeed, S* potentially has more electronic affinity and lower ionization potential than S (Fig.2.5).

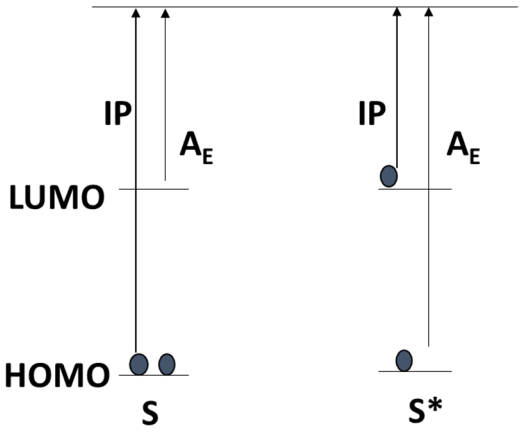

Fig.2.5 Electronic configuration of a sensitizer in the fundamental state (S) and in the excited state (S*).

If entropy differences between the excited and the fundamental state are negligible it is possible to calculate, with good approximation, the excited state redox potentials, starting from the ground state redox potentials and knowing the zero-to-zero spectroscopic energy, indicated as $E^{0\text{-}0}$, according to equations.

$$E_{S^+/S*} = E_{S^+/S} - E^{0-0} \quad \text{(Eq.2.15)}$$

$$E_{S*/S^-} = E_{S/S^-} - E^{0-0} \quad \text{(Eq.2.16)}$$

The rate constant of electron transfer can be expressed by the Marcus equation [7]:

$$k_{et} = \upsilon_N k_e e^{-\frac{\Delta G*}{kT}} \quad \text{(Eq.2.17)}$$

where k and T are the Boltzmann constant and the absolute temperature, respectively. υ_N is the nuclear frequency factor, and κ_e is the transmission coefficient, a parameter which expresses the probability of the system to evolve from the reagent to the product configuration, once the crossing of the potential energy curves along the reaction coordinate has been reached. ΔG^* is the activation energy required to switch from the transition state to the final system and it is possible to demonstrate that the trend of the potential curves associated with the two systems is parabolic. Activation energy can be estimated by the equation:

$$\Delta G^* = \frac{(\Delta G^0 + \lambda)^2}{4\lambda} \quad \text{(Eq.2.18)}$$

where ΔG° is the free energy variation accompanying the process, while λ is the reorganization energy and represents the energy necessary to transform the nuclear

configurations of the reactant and of the solvent to those of the products. λ is usually separated into inner λ_i and outer λ_o components: λ_i is due to the vibrational rearrangement consequent to the electron transfer, while λ_o is comprehensive of the repolarization of the solvation sphere. It is possible to distinguish four distinct kinetic cases, which are represented by the potential energy curves diagram of figure 2.6.

- $\Delta G° = 0$ (fig.2.6 a). The activation barrier of the process only depends on reorganization energy
- $-\lambda < \Delta G° < 0$ (fig.2.6 b). The exoergicity of the reaction results in a ΔG^* decrease and hence an increase in ration rate (normal region).
- $\Delta G° = -\lambda$ (fig.2.6 c) No activation energy is required and the rate of the reaction is maximum. In Marcus kinetic expression the exponential term is unitary and as a consequence: $k_{et} = v_N k$.
- $\Delta G° < -\lambda$ (fig.2.6 d). This is defined as inverted region. The $\Delta G°$ gradient plays against the rate of reaction.

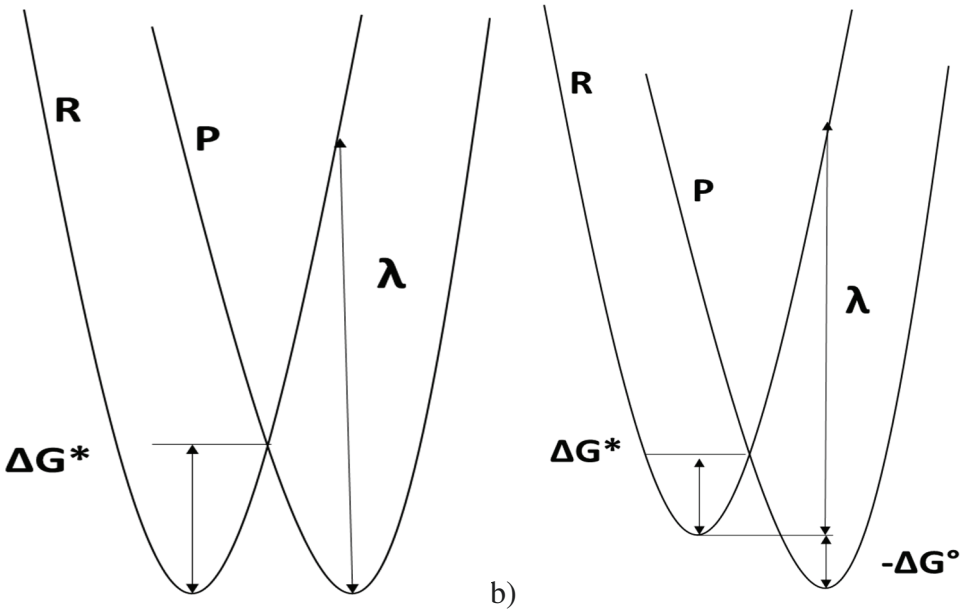

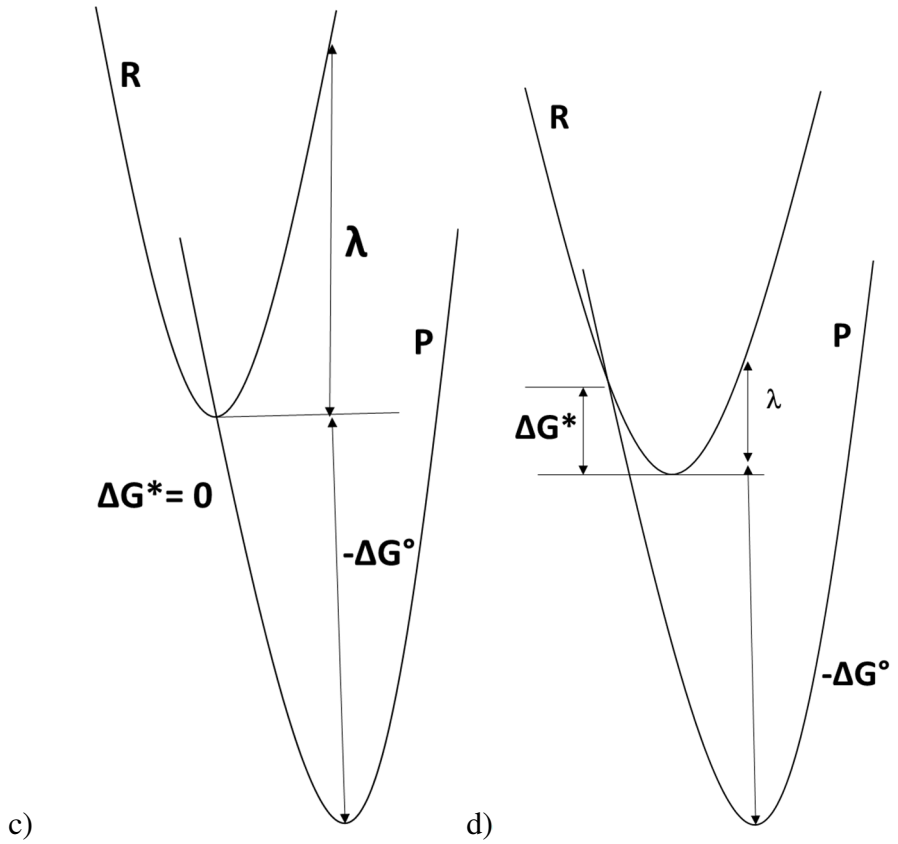

Fig.2.6 Marcus kinetics**:** a) self exchange reaction; b) normal region; c) activationless region; d) inverted region.

Marcus's theory is a classic model. Otherwise, quantization of the vibrational motions of the reactant molecules and the products is not negligible. From a quantum mechanical point of view, the electronic transfer can be discussed as a non-radiative transition from a starting vibronic state to a final one. The electron transfer rate constant turns out to be [8]:

$$k_{et} = \frac{2\pi}{\hbar}(H_{AB}^{et})^2 FCWD \qquad \text{(Eq.2.19)}$$

where *FCWD* is the Franck-Condon factor weighted for the Boltzmann population of the energy levels and H_{AB}^{et} is the electronic coupling factor between the two electronic states involved in the process, which turns out to be very important in determining the electron transfer rate.

2.2 Dye-sensitized solar cells (DSSCs)

Nowadays, Silicon is the most popular solar cell material for commercial applications because of its great abundance and an energy band gap (1.1eV at room temperature) which allows to absorb large part of the visible and NIR solar radiation. Silicon solar cells are made of two layers of semiconductor material, which are doped in order to polarize the junction

(p-n junction) [9]. When a photon having enough energy is absorbed, an electron is excited from the valence into the conduction band, leaving a positively charged hole. This effect provides a potential difference across the junction of the two differently doped silicon layers, which acts separating the carriers and inducing a current flow through the external circuit. In contrast to these types of systems, where the semiconductor assumes both the tasks of light absorption and charge carrier transport, in dye sensitized solar cells (DSSC) the two functions are separated. Light is absorbed by a sensitizer molecule, which is a metalorganic or an organic molecule with a high molar extinction coefficient, anchored to the surface of a wide band-gap semiconductor, while charge separation takes place via photoinduced electron injection from the dye into the conduction band of the solid. As previously reported, wide-band gap semiconductors such as TiO_2, SnO_2, $SrTiO_3$, ZnO and so on, have a separation between the energy levels of the valence band and the conduction band of the order of 3eV, which means that the electron-hole pairs (e^--h^+) can be generated, upon photoexcitation, by a radiation of wavelength below 400nm, at the limit between the visible and the UV spectra. In order to extend the spectral sensitivity of these materials towards low energy photons, "molecular sensitization" seems to be a valid solution. When the excited state energy level of the sensitizer is higher with respect to the bottom of the conduction band, an electron can be injected without thermal activation barrier into the semiconductor, leaving the sensitizer in its one electron oxidized form. While, when the excited state is lower in energy with respect to the top of the valence band electron transfer (formally a hole transfer) between the semiconductor and the sensitizer can take place leaving the molecule in its one electron reduced form [10].

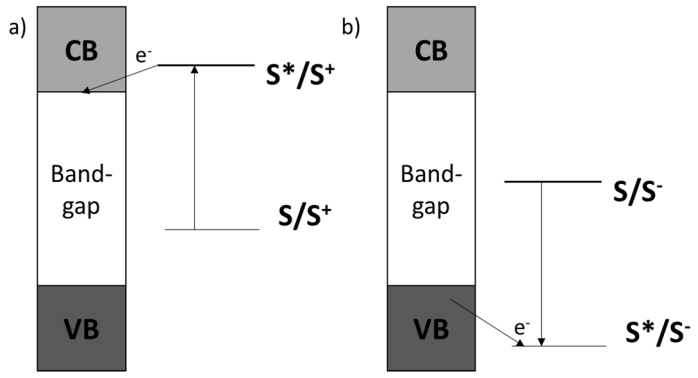

Fig.2.7 Sensitized charge injection: (a) electron injection (oxidative quenching), (b) hole injection (reductive quenching).

Dye can be physically or chemically bonded on semiconductor surface, with this latter case preferred to guarantee a more efficient charge transfer. Electron injection and sensitization are the fundamental mechanisms of photoelectrochemical solar cells. The principle of dye

sensitization of semiconductors can be traced back to the end of 1960s [11], however the efficiencies obtained with single crystals substrates were too low due to the poor light absorption of the adsorbed monolayer of dye molecules. The "Bob Beamon like" increase in efficiency for DSSC type solar cells reported in the famous 1991 Nature paper by O'Regan and Graetzel was bewildering [12]: the use of a mesoporous semiconductor (Fig.2.9) electrode with a high internal surface area leads to a paradigm shift in the fields of photoelectrochemistry and photovoltaics in general. The working principle of a DSSC is schematized in Fig.2.8 where the main electron transfer processes are indicated by numbers 1-7 [13].

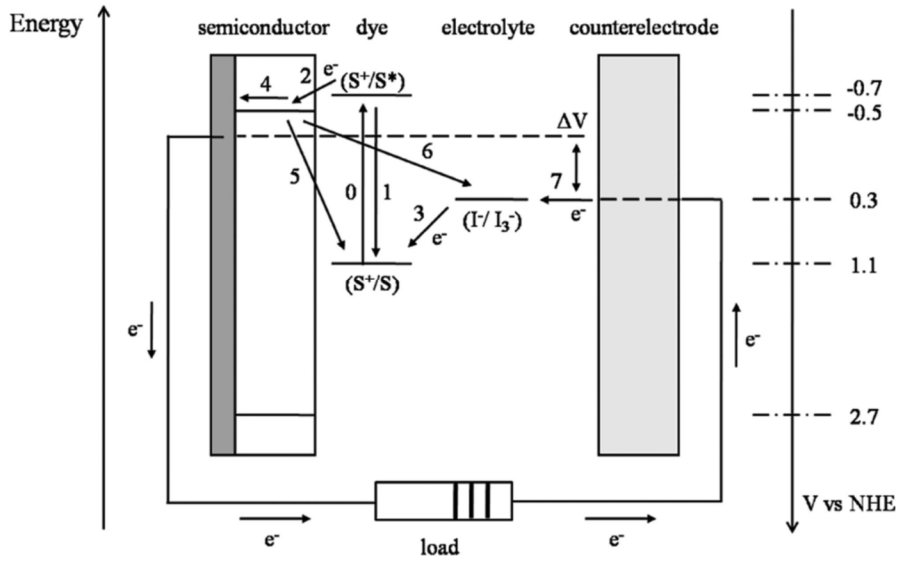

Fig.2.8 Simple energy level diagram for a DSSC. The basic electron transfer processes are indicated by numbers (1-7). The potentials for a DSSC based on the N3 dye, TiO_2, and the I^-/I_3^- redox couple are shown [13].

The device is constituted by two different electrodes, the photoanode and the counter electrode with an electrolyte in between. Both electrodes are usually constituted by a glass covered on one side with a transparent conductive layer of Fluorine doped tin oxide (FTO) or Indium tin oxide (ITO). Surface electrical resistivity of few ohms (*ca.* 18) can be easily obtained while preserving a good optical transmission over the whole visible and near infrared spectrum. For what concern the photoanode, the transparent conductive film is covered by a thin film (8-10μm) of mesoporous semiconductor oxide, usually TiO_2 which is a chemically inert, nontoxic and cheap material, obtained by several sol-gel procedures including drop casting, spin coating, dip coating, spraying, and simple doctor blade technique [14]. The porosity is 50-60%. Once deposited, the film is sintered at 500C° to establish electronic conduction (Fig.2.9). Generally, several crystal forms of TiO_2 occur naturally: rutile, anatase, and brookite. Rutile is the thermodynamically most stable form but

anatase is the preferred structure in DSSCs, because it has a larger bandgap (3.2 vs 3.0 eV for rutile) and a higher conduction band edge energy, *E*c [13].

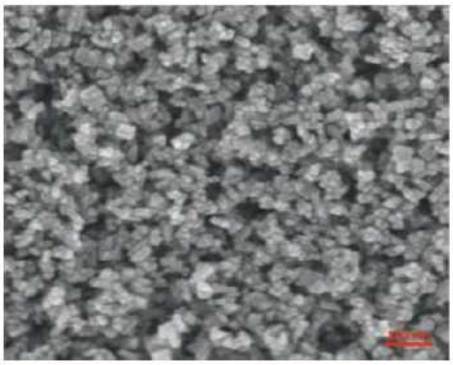

Fig.2.9 SEM image of the surface of a mesoporous TiO_2 film prepared from 18NR-T colloidal paste (Aldrich), after sintering.

Dye coverage of semiconductor nanoparticles is generally obtained by immersion of the sintered film in a bath of the sensitizer and sensitizers are usually designed to have functional groups such as -COOH, -PO_3H, -R(CN)(COOH) for stable adsorption onto the semiconductor substrate. The presence of an acidic functional group allows the formation of a stable bond with titanium dioxide and promotes a strong electronic coupling between the π^* orbital of the binder and the CB semiconductor band. The photoanode is in contact with an electrolytic solution containing a redox couple dissolved in a non-viscous solvent. The redox couple must satisfy some characteristics like the ability to reduce quantitatively the sensitizer. A huge variety of redox mediators has been studied, and the most common redox couple is the I^-/I_3^- couple [15]. Furthermore, generally the counter electrode is a transparent conductive film usually covered with clusters of platinum which have a catalytic effect. In recent years really efficient new materials were employed as counter electrodes such as an electrodeposited polymer, namely PEDOT (poly-(3,4-ethylenedioxythiophene)) [16]. The complete photoelectrochemical cycle of the device can be outlined as follows and the main processes are shown in Fig.2.8 [13]: the dye absorbs photons and as a consequence reaches the excited state (S*), followed by electron injection in the conduction band of the semiconductor in a time-scale of femtoseconds (Fig. 2.8 reactions 0, 2); injected electrons move through the metal oxide film reaching the electron collectors of the photoanode (Fig.1.8 reaction 4) and oxidized sensitizer (S^+) is reduced by the reduced form of the redox mediator, usually I^- ion, (Fig.2.8 reaction 3) meanwhile electrons injected flow in the external circuit where electric work is produced and migrate to the counter electrode in order to reduce the oxidized form of the redox mediator (Fig.2.8 reaction 7) [13]. The entire cycle

consists in the quantum conversion of photons to electrons. Besides the desired pathway of the electron transfer processes (reactions 2, 3, 4, and 7) described above, there are loss reactions (1, 5, and 6) as indicated in Fig.2.8. Reaction 1 is direct recombination of the excited dye reflected by the excited state lifetime. Recombination of injected electrons in the TiO_2 with either oxidized dyes or acceptors in the electrolyte are numbered as 5 and 6, respectively [13]. All of these electron transfer processes taking place at the oxide/dye/electrolyte interface need to be understood and mastered to improve our ability to identify predictive materials and optimized structure/function relationships. It is worth to notice that at the very beginning all the processes will be analysed taking as example the most common electron redox mediator, the I^-/I_3^- couple.

- *Electron Injection and Excited State Decay*

$$S^* + TiO_2 \rightarrow S^+ + (e^-, TiO_2)$$ **Electron injection** (Fig.2.8, reaction 2)

One of the most astounding findings in DSSC research is the ultrafast injection from the excited dye in the TiO_2 conduction band (Fig.2.8 reaction 2). Although the detailed mechanism of the injection process is still under debate, it is generally accepted that a fast femtosecond component is observed for the most common types of sensitizers directly attached to an oxide surface [17-20]. The injection can take place from various states in the thermal relaxation pathway, that is, Franck-Condon singlet injection, thermally relaxed excited-state singlet injection, or intersystem crossing to the triplet state followed by injection. Charge injection efficiency is given by [13]:

$$\phi_{inj} = \frac{k_{inj}}{k_{inj} + \frac{1}{\tau}} \qquad \text{(Eq.2.20)}$$

Where k_{inj} is the charge injection rate constant and τ is the sensitizer lifetime in the absence of charge injection (i.e. the excited dye decay through radiative and non radiative processes), which lies in the ns-μs time domain. To achieve a satisfactory value of ϕ_{inj} the value of k_{inj} should be at least 100 time higher with respect to $\frac{1}{\tau}$, which implies that electron injection should occur in picoseconds or faster times. Normally, techniques such as femtosecond transient absorption spectroscopy (see Chapter 8) are used to determine the kinetics of the injection process by measuring the absorption changes associated with the formation of the dye cation [21].

- *Regeneration of the Oxidized Dyes*

$$2S^+ + 3I^- \rightarrow 2S + I_3^-$$ **Sensitizer regeneration** (Fig.2.8 reaction 3)

The interception of the oxidized dye by the electron donor, in the present case I^-, falls in the microsecond time domain. A lower limit for the regeneration time is given by diffusion-limited kinetics. In non-viscous electrolytes, the diffusion rate constant, k_{diff}, is in the range of 10^9-10^{10} M^{-1} s^{-1}. As a consequence, for an electron donor concentration in electrolyte concentration >0.1 M, a lower limit for the regeneration time ((k_{diff} × donor concentration)$^{-1}$) of some nanoseconds is calculated [27-29]. It is useful to define the regeneration efficiency,ϕ_{reg}, which gives the probability that an oxidized dye is regenerated by an electron donor in the electrolyte rather than by recombination with an electron in the TiO_2 [13]:

$$\phi_{reg} = \frac{k_{reg}}{k_{reg}+k_{rec}} \qquad \text{(Eq.2.21)}$$

Where, k_{reg} is the rate constant for regeneration, and k_{rec} is the (pseudo-) first-order rate constant for electron-oxidized dye recombination. For many types of sensitizer, very high values, approaching unity, have been found with iodide. Upon reduction of the oxidized dye, the diiodide radical. $I_2^{-\bullet}$[22-24], is formed, which is subsequently converted into triiodide. The reduction of the oxidized sensitizer (S^+) by iodide follows most likely the following reaction mechanism [27]:

$$S^+ + I^- \rightarrow S \cdots I$$

$$(S \cdots I) + I^- \rightarrow (S \cdots I_2^{-\cdot})$$

$$(S \cdots I_2^{-\cdot}) \rightarrow S + I_2^{-\cdot}$$

$$2I_2^{-\cdot} \rightarrow I_3^- + I^-$$

Evidence for the formation of intermediate dye-iodide complexes was pointed out by several groups with different kind of dyes [22-24]. Furthermore, fast regeneration kinetics are also found for the one electron redox mediators based on Cobalt complexes [25-26].

- *Electron Transport through the Mesoporous Oxide Film*

The mesoporous semiconductor electrode consists of numerous interconnected nanocrystals. Because these particles typically are not electronically doped [30] and surrounded by ions in the electrolyte, they will not have an internal electrical field and will not display any significant band bending. So, the gradient in photoinjected electron concentration appears to be the main driving force for transport in the mesoporous TiO_2 film, that is, electron transport occurs by diffusion [31-32]. The electrons in the mesoporous TiO_2 are charge compensated by ions in the electrolyte and, as a consequence, the diffusion processes of electrons and ions

will be coupled through a weak electric field. The measured electron diffusion could be described by the ambipolar diffusion model [33-34]:

$$D_{amb} = \frac{p+n}{p/D_n + n/D_p} \qquad \text{(Eq.2.22)}$$

Where D_{amb} is the ambipolar diffusion coefficient, n and p are the concentrations of negative and positive charge carriers (corresponding to electron and cation concentration in the DSSC), and Dp and Dn are the diffusion coefficients of positive and negative charge carriers.

- *Recombination of Electrons in the Semiconductor with Oxidized Dyes or Electrolyte Species.*

$$S^+ + (e^-, TiO_2) \rightarrow S \qquad \textbf{Back electron transfer} \text{ (Fig.2.8 reaction 5)}$$

$$I_3^- + 2(e^-, TiO_2) \rightarrow 3I^- \qquad \textbf{Electron capture from mediator} \text{ (Fig.2.8, reaction 6)}$$

Photoinjected electrons should escape from any recombination process in order to have a unit charge efficiency at the photoelectrode back contact. The two major waste processes in DSSC are due to (i) back electron transfer, at the semiconductor-electrolyte interface, between electrons in the conduction band and the oxidized dye molecules (reaction 5), and (ii) reduction of the electron mediator at the semiconductor nanoparticles surface (reaction 6). The electron transfer from nanocrystalline TiO_2 to oxidized dye molecules proceeds over a time scale from nano- to milliseconds and does not follow simple first-order kinetics, depending on several factors [35-38]. The large driving force and small reorganization energy of the back reaction places the process in the Marcus inverted region as confirmed by the observation that the recombination rate is almost temperature independent and insensitive to the surrounding of the coated film [39]. On the other hand, the application of a potential to the mesoporous TiO_2 electrode has a strong effect on the recombination kinetics and when the electron concentration in the TiO_2 particles is increased, a strong rise in recombination kinetics is found [40]. Under working conditions, electron concentration in the TiO_2 particles is rather high, and recombination kinetics competes with dye regeneration. Recombination of electrons in TiO_2 with acceptors in the electrolyte is normally referred to as the electron lifetime and could be estimated by measuring transient response of the open circuit potential (Voc) [41-42]. The steady-state value of Voc provides also information on the recombination, indeed under illumination at open circuit, the net rate of electron injection from dyes into the mesoporous oxide is balanced by the net rate of electron transfer to electron acceptors. In this case, recombination kinetics may be dominated by the electron trapping-detrapping mechanism in the TiO_2 [43]. It is worth to notice that in

most studies, it is assumed that only recombination of electrons with acceptors in the electrolyte occurs, as oxidized molecules are very rapidly regenerated.

- *Transport of the Redox Mediator and Reactions at the Counter Electrode.*

$$I_3^- + 2e^- \rightarrow 3I^-$$ **Electron donor regeneration** (Fig.2.8 reaction7)

Transport of the redox mediator between the electrodes is mainly driven by diffusion, since typical redox electrolytes have a high conductivity and ionic strength so that the influence of the electric field and transport by migration is negligible. The mass transport is governed by the diffusion impedance (see Chapter 8) (R_D), which depends on the diffusion coefficient and concentration of the redox mediator and on the distance between the electrodes [44]. The counter electrode must be catalytically active to ensure rapid electron donor regeneration and low overpotential. The charge transfer reaction at the counter electrode leads to a series resistance in the DSSC, namely the charge transfer resistance at the electrolyte/counter electrode interface (R_{CE}). Usually, Pt is a suitable catalyst to reduce iodide, while for redox mediators based on metal complexes is preferred a PEDOT based material.

2.2.1 Solar Cell efficiency

Since a DSSC is a quantum converter, the efficiency of the conversion process is expressed in terms of the ratio between the number of electrons flowing in the external circuit and the number of photons, striking at the photoanode. This efficiency is always referred as incident photon-to-current conversion efficiency (IPCE). In terms of measurable quantities IPCE value is given by the following equation:

$$IPCE\ (\lambda) = \frac{n_e}{n_{hv}} = \frac{hc}{e}\frac{J}{\lambda P(\lambda)} \qquad \text{(Eq.2.23)}$$

Where, h is the Planck's constant expressed in joul×second, c is the speed of light in vacuo (ms^{-1}), e is the electron charge (C), J is the photocurrent density (Am^{-2}), and $P(\lambda)$ is the radiant power density at the wavelength λ. A plot of IPCE as a function of wavelength is called action spectrum. Alternatively quantum efficiency can be expressed by the product of three terms related to the key steps of the device working principle and obtainable by Current-Voltage measurements:

$$IPCE = LHE\ (\lambda)\phi_{inj}\eta \qquad \text{(Eq.2.24)}$$

Where LHE is the light harvesting efficiency, ϕ_{inj} is the electron injection quantum yield and η is the efficiency of electron collection at the photoanode. Light harvesting efficiency

is the fraction of incident light that is absorbed by the dye-coated mesoporous film. Due to the small size of the semiconductor nanoparticles, light scattering is almost negligible, and the transparency is sufficiently high that Beer-Lambert law can be applied:

$$LHE = 1 - 10^{-A} \quad \text{(Eq.2.25)}$$

Where A is the absorbance of the film due to dye molecule, given by:

$$A = 1000\varepsilon ct \quad \text{(Eq.2.26)}$$

With ε molar absorptivity of the dye ($mol^{-1}lcm^{-1}$),c dye concentration ($molcm^{-3}$), t film thickness (cm) and 1000 (cm^3l^{-1}) volume conversion factor. Typical values for the volume concentration of dye molecules are in the range of 10^{-4} $molcm^{-3}$ and the maximum extinction coefficient for a large class of sensitizers is in the range of (1-2) $10^4 mol^{-1}lcm^{-1}$, this means that for a 10 μm (10^{-3} cm) film the term LHE is in excess of 90%. ϕ_{inj} was extensively described above. η is the global efficiency of the device, namely the ratio between the maximum electric power delivered by the cell at optimum load and the optical power of the irradiating source, which is expressed as Air Mass 1.5 (AM 1.5) and is the solar power per square meter received by the earth at average latitudes at high noon on a cloudless day. The global efficiency is given by the formula:

$$\eta = \frac{V_{oc} J_{ph} FF}{P_s} \quad \text{(Eq.2.27)}$$

Where V_{oc} is the open circuit voltage, J_{ph} is the short circuit integrated photocurrent density (Am^{-2}), FF is the cell fill factor and P_s is the total optical power density at the cell surface (Wm^{-2}). The short photocurrent density is a quantity that can be estimated by measuring the current-voltage characteristics of a cell under simulated solar light by recording short circuit photocurrent (I_{ph}) and dividing for the solar cell active area. I_{ph} is the largest current obtainable from the device and represents the current across the cell in the condition of zero voltage applied. Alternatively, J_{ph} can be calculated by the integration of Eq.2.23 with respect to λ:

$$J_{ph} = \frac{e}{hc} \int IPCE(\lambda)\, \lambda\, P(\lambda) d\lambda \quad \text{(Eq.2.28)}$$

When the net current through the device reaches zero, the potential value detected during current-voltage measurements corresponds to the maximum voltage available from a solar cell, which is called open circuit voltage (V_{OC}). The maximum open circuit voltage attainable in this kind of devices is given by the energetic difference between the *quasi*-Fermi level of the solid under illumination and the Nerst potential of the redox couple in the electrolyte.

However, this limitation has not been realized and V_{oc} is in general much smaller. It is worth to note that it is limited by electron tunnelling through the solid to acceptors at the interface or in the electrolyte. For an *n*-type semiconductor in a regenerative cell, V_{oc} is equal to:

$$V_{OC} = \frac{kT}{e_s} \ln\left(\frac{Iinj}{n} \sum ki[A]i\right) \quad \text{(Eq.2.29)}$$

Where *Iinj* is the electron injection flux, *n* is the concentration of electrons in TiO_2 and the summation is for all the electron transfer rates to acceptors. This parameter as a marked influence on solar cell efficiency and is governed by charge recombination between conduction band electrons and the oxidized electron mediator. Fill factor values can be obtained by measuring the current-voltage characteristics and determines the maximum power extractable from a solar cell. It is defined as the ratio between the maximum electric work produced at the optimum load and the product of open circuit voltage and short circuit current:

$$FF = \frac{(JV)_{MAX}}{J_{ph} V_{oc}} \quad \text{(Eq.2.30)}$$

All these parameters determine cell efficiency. A global efficiency of 14% has been recently reported for a state of the art DSSC, making these types of devices really competitive with solar cells based on amorphous silicon [45].

2.2.2 Molecular Sensitizers for DSSCs

Considerable work is now directed towards the optimization of organic sensitizers and of natural sensitizers extracted from plants, besides transition metal complexes are still playing a major role in DSSC development, since many of the most efficient and most stable dye sensitizers are constituted by Ru(II) complexes displaying intense metal to ligand charge transfer (MLCT) transitions. N3 dye (namely $[Ru(H_2dcb)_2(NCS)_2]$, where H_2dcb is the 4,4'-dicarboxy-2,2'-bipyridine) is one of the first dyes reported by the Graetzel's group and is still playing the major role in dye sensitizer devices [46]. It is a rare example of a molecule able to satisfy several of the requirements that an efficient sensitizer has to fulfil: (i) a broad and strong absorption, preferably extending from the visible to the near-infrared; (ii) minimal deactivation of its excited state through the emission of light or heat; (iii) a firm, irreversible adsorption (chemisorption) to the semiconductor's surface and a strong electronic coupling between its excited state and the semiconductor conduction band; (iv) chemical stability in the ground as well as in the excited and oxidized states; (v) negative enough excited state oxidation potential in order to bring out an effective electron injection; and (vi) ground state

oxidation potential positive enough to provide the driving force for oxidizing the electron mediator [47-53]. In about 20 years of work the most significative improvement have been obtained with dyes similar to N3, by modifying the ancillary ligands or the degree of protonation at the polypyridine ligands which provide the binding site for TiO_2. For example, N719, obtained by changing the number of acidic protons of N3, renders an impressive η of 11.2%[54]. Furthermore, by replacing one of the dcbpy ligands in N3 with a modified 2,2' -bipyridine ligand in order to block the electrolyte from interacting with the surface and to absorb more light, a series of dyes such as C101 and C106 were designed, reaching an efficiency up to 11% [55]. While there are a number of fundamentally new approaches to dye design that have recently emerged based on the paradigmatic N3, one that has gained attention is the substitution of the monodentate NCS ligands with anionic cyclometalating C^N ligands [56-58]. These chelating ligands have the potential to circumvent degradation pathways and optimize the light-harvesting capacity of DSSC dye. An important finding for this approach was provided in 2009 when Graetzel and his co-workers reported an efficiency near to 10% for a cyclometalated Ru based complex (YE05) which avoids the employ of the labile Ru-NCS bond [59]. The high efficiency is ascribed to the suitable reduction potential for YE05 that results in a larger thermodynamic driving force for dye regeneration. Moreover, Ru-1 (Fig.2.10) with strong electron-withdrawing $-CF_3$ groups installed on the phenyl ring of the bipyridine and the two -COOH groups on one of the dcbpy ligands being replaced by 2-hexylthiophene units can extend the absorption spectrum down to 600 nm. This paradigm provides the unique opportunity to control the thermodynamic position of the HOMO energy level and a way of manipulating the thermodynamic driving force for the regeneration of the photooxidized Ru(II) dye. Nevertheless, the lack of absorption in the red region of the visible spectrum has prompted research to synthesized sensitizers that absorb visible light of all colours. The so called black dye [tri(isothiocyanato)(2,2';6',2''-terpyridyl-4,4',4''-tricarboxylic acid)ruthenium(II)] has been found to have near-IR photo response up to 920nm [60]. The use for black dye of the terpyridyl ligand, with its low-lying π* molecular orbitals, gives an impressive panchromatic absorption associated with the stabilization of the "hole" at the Ru(III) centre due to the electron-donating ligand, resulting in an overall efficiency of 10.4%. However, the extension of the spectral response to the near IR is gained at the expense of shifting the excited state to lower energy from where injection into TiO_2 conduction band can no longer occur and the challenge to further optimize devices still remains.

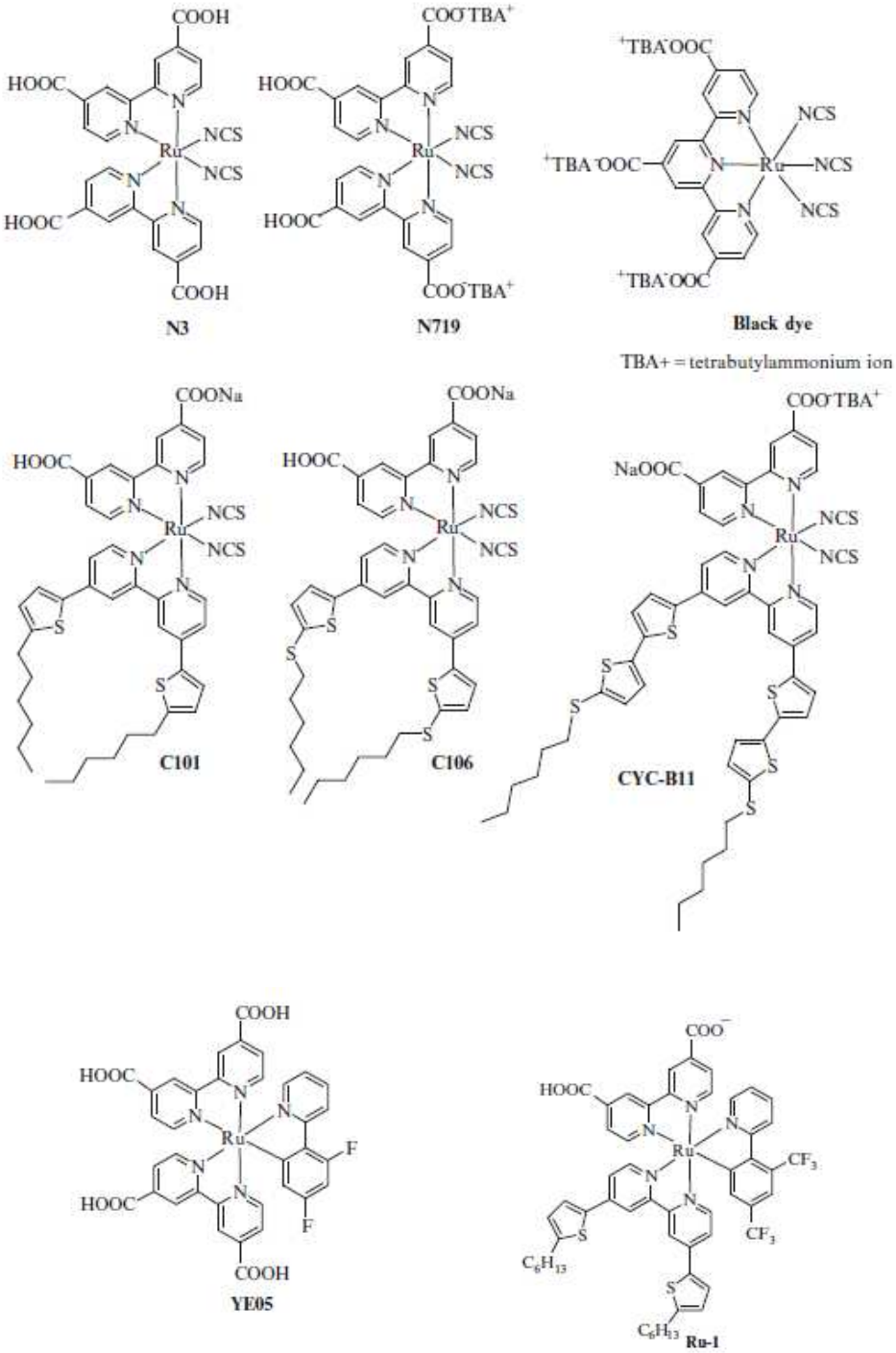

Fig.2.10 Ruthenium based dyes for the employment in DSSCs.

Moreover, the high cost and scarcity of ruthenium have necessitated the consideration of other options. As a consequence, an increasing attention is devoted to donor-acceptor organic dyes and to tetrapyrrolic macrocycles, namely porphyrins. Porphyrins are an obvious choice as a class of simple, robust, efficient, and economically viable photosensitizers due to their well-known role as light absorbers and charge separators in natural photosynthetic systems. This class of sensitizers will be well described in **Chapter 5**. For what concern,

donor-acceptor organic dyes (Fig.2.11), although many, if not all, of these species do not contain metals, their most promising application is in association with electron transfer mediators based on coordination compounds. In general, the photoconversion efficiencies observed with these dyes are lower (≤10%) in comparison with the ruthenium based sensitizers, but they have advantageous features such as high molar extinction coefficient and tunable absorptions achieved through variation of the molecular structure which typically consists of the donor–π(spacer)–acceptor (D–π–A) architecture [61-63]. The most successful donor units are represented by functionalized triarylamine moieties, first introduced by the Yanagida's group [64], which are characterized by chemical and photochemical stability due to charge delocalization in the aryl substituents, while carboxylic acid or cyanoacrylic acid moieties are usually the electron acceptors, serving also as anchoring groups for attachment to the TiO_2 surface [65]. In Fig.2.11 is represented a screening of organic dyes based on these functional groups. The efficiency (~3%) of the simple dye 1 (Fig.2.11) can be easily improved by extending conjugation, employing a vynil group, resulting in a red shift of the absorption spectrum (absorption onset 600 nm), paralleled by an increase in efficiency up to 5.1% [66]. The parallel inhibition of charge recombination between conduction band electrons and the oxidized electron mediator is also expected to enhance the electron collection efficiency. For example, the insertion of a phenyl ring in the acceptor unit of dye 5 results is a sevenfold increase of the efficiency with respect to dye 4 [67]. This effect can be widely explained by the increased twisting angle between the phenyl ring of the acceptor unit and the conjugated donor in the oxidized dye, decoupling the photogenerated hole from the TiO_2 surface and slowing down over five times the charge recombination process. This was further elegantly demonstrated by the Ko group [68] which realized the new type of organic sensitizer 6, incorporating a planar amine with long alkyl chain units which screen the semiconductor surface from the electron acceptors present in the electrolyte, yielding to an efficiency near to 9%.

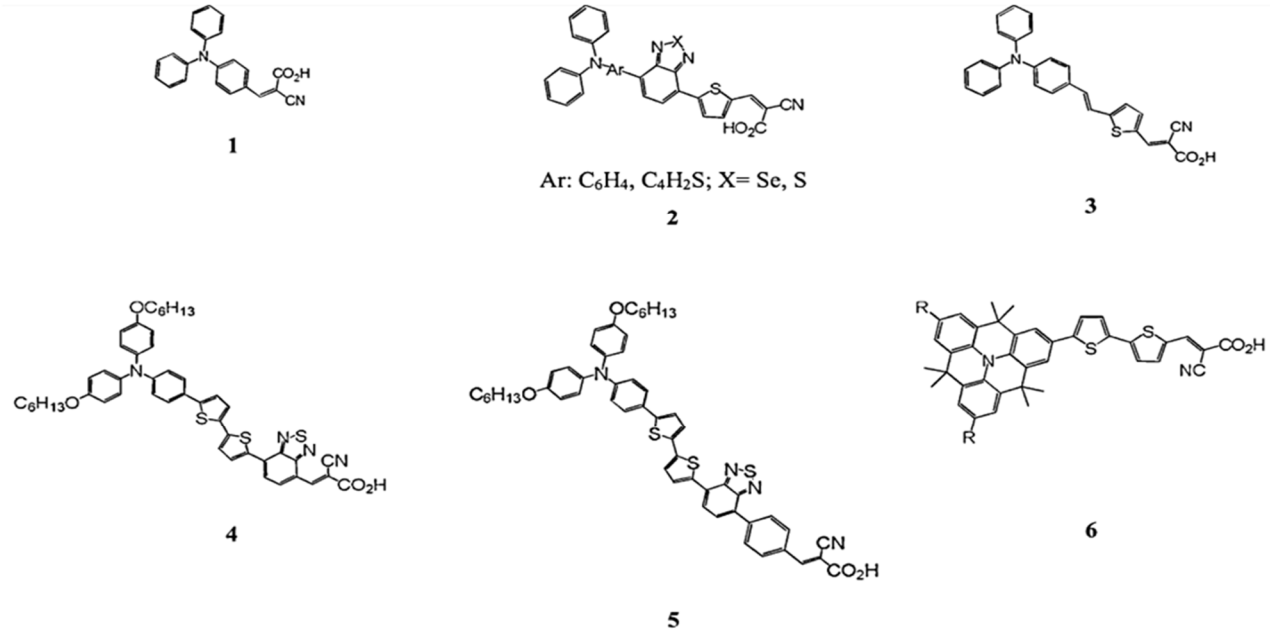

Fig.2.11 Donor-Acceptor organic dyes for the employment in DSSCs**.**

These examples underline how a careful design of organic dye structures can lead to the complete control over the interfacial charge separation processes, boosting cell efficiencies. In particular in **Chapter 4** will be employed two interesting hindered organic dyes with high molar extinction coefficients [69-71].

2.2.3 Electron Mediators for DSSCs

Typical electronic mediators can be divided into three different categories: liquid electrolytes, quasi-solid electrolytes, and solid-state conductors [72-74]. The focus of this thesis is given to liquid electrolytes, in which the redox couple involved in charge carries transport is dissolved in non-viscous organic solvents. As previously reported, the ubiquitous combination of I^- and I_3^- is the most common redox couple and appears very hard to replace; in the presence of a reasonable driving force (*ca.* 0.2 eV), I^- allows for a fast regeneration of most dyes, intercepting them on a sub-microsecond time scale [75-76], whereas the reduction of I_2 and I_3^- is a complex multi-step reaction which, according to some authors, involves a first dissociation of I_3^- in I^- and I_2, a subsequent reduction of I_2 to I_2^- followed by the rate limiting dismutation of two I_2^- to give I^- and I_3^- [77-78]. As a consequence, the electronic recapture involving I_3^- is kinetically slow onto TiO_2 surface and, under short circuit conditions, most of electrons survive the transit through the mesoporous titania film without undergoing disadvantageous recombination processes. Thus, the I_3^-/I^- couple appears to have ideal kinetic properties which lead to an "asymmetric behaviour" at the basis of the efficient functioning of the DSSC: the forward electron donation by I^- is a facile

monoelectronic process which ensures an efficient dye recovery, while the reduction of I_3^- appears to be largely inefficient allowing for a minimization of the interfacial back recombination. On the other hand, the I_3^-/I^- redox couple has a list of regrettable characteristics which limits its practical use as a relay electrolyte: (1) I_2 in equilibrium with I_3^- is volatile, complicating long term cell sealing; (2) I_3^- is darkly coloured and limits the light harvesting efficiency of the dye, (3) I_3^-/I^- redox potential is not ideally positioned for many sensitizers, leading to a significant loss in the maximum open circuit potential and (4) I_3^-/I^- is corrosive and will corrode most metals, posing a serious problem for the use of metal grid collectors necessary for scaling up the solar cells to large areas [79]. Due to all these limitations the search for new electron transfer mediators potentially capable of replacing the triiodide/iodide couple seems to be necessary. However, the use of alternative redox couples as electron mediators has been addressed, so far, by a limited number of research groups, but, the development of redox shuttles based on transition metal complexes has been central for achieving promising results. The research has been triggered by the fact that the electrochemical properties of coordination compounds can be easily tuned through a rational choice of the metal and an appropriate design of the coordination sphere and that their electrochemical response is sensitive to the electrodic material. The choice and design of the redox couples have been done by considering inexpensive and available metals like the elements of the first transition row and easily synthesizable ligands. To date, octahedral Co(II)/(III) polypyridine complexes represent the most successful examples of electron transfer mediators based on coordination compounds. The Co(II)/(III) couple is usually characterized by a high inner sphere reorganization energy associated to the electron transfer, essentially due to the involvement of a metal centred e_g redox orbital with antibonding characteristics: the spin forbidden change from high spin Co(II) $t_{2g}^5e_g^2$ to low spin Co(III) t_{2g}^6 may also contribute to explain the typically low self-exchange rate constants observed in the case of many cobalt complexes, which disfavoured recombination processes [80]. Co(II)-bis-[2,6- bis(1'-butylbenzimidazol-2'-yl)pyridine] (dbbip) was the first couple to be employed in DSSCs by Graetzel group in 2001 [25]. The redox potential of the couple $[Co(III)(dbbip)_2]^{3+}/[Co(II)(dbbip)_2]^{2+}$ was found to be comparable with that of the I_3^-/I^- couple and the efficiencies appeared to rival the triiodide/iodide performances in terms of IPCE and global cell efficiency. Encouraging was also the weak coloration of the complex which exhibited a moderate absorption in the visible region which allowed for the preparation of concentrated solutions without a serious competition in light absorption with the sensitizer. One of the limitations of Co(II) benzimidazol complexes is their availability related to a multi-step synthetic procedure for the ligand. In this aim a wide class of

polypyridine, which can be easily produced by mixing the corresponding salt with the appropriate easily synthesizable ligand, was explored (Fig.2.12) [81].

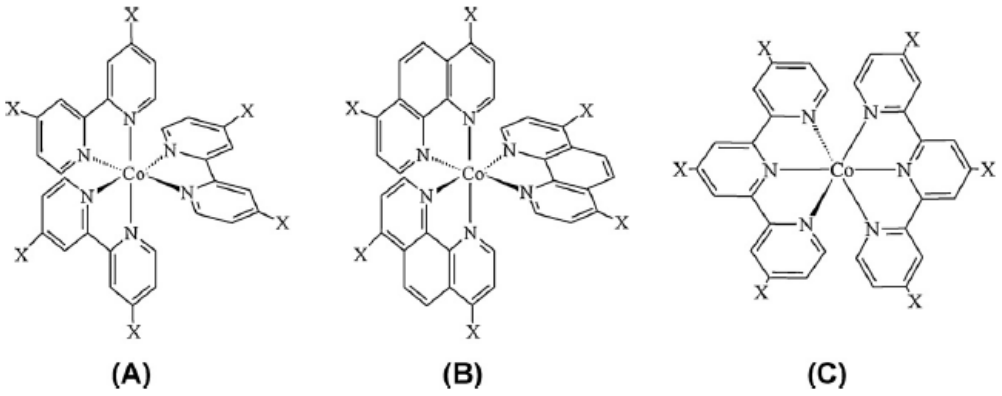

Fig.2.12 Structure of polypyridilic Co(II) complexes: (A) X = *tert*-butyl (dtb), methyl (dmb), H (bpy). (B) X = H (phen). (C) X = *tert*-butyl (ttt), ethyl (tet).

IPCE of ($[Co(dtb)_3]^{2+}/[Co(dtb)_3]^{3+}$) (dtb = 4,4'-di-*tert*-butyl-2,2'-bipyridine) redox couple in conjunction with a Ruthenium based dye was found to be ~60% [82]. It is worth to notice that, generally, cobalt complexes of unsubstituted and methyl-substituted bipyridine or terpyridine ligands were poor electron transfer mediators with respect to tertiary butyl substituted ones, which are more sterically hindered disfavouring recombination. The observed substituent effect can be explained by a reduced electron recapture induced by the presence of bulky substituents which decrease the electronic coupling and hence the tunnelling probability which varies exponentially with the distance between the wavefunctions of the electron donor (free or trapped electrons in the TiO_2) and acceptor (d type orbitals contracted on Co(III) centres) [82]. Despite progresses, the absolute efficiencies of triiodide/ iodide mediated solar cells were difficult to approach with the most typical bis-NCS dyes (such as N3), however under certain circumstances, when associated to specific dye structures, non corrosive electron mediators revealed interesting electron transfer dynamics and improved electron collection efficiencies over the conventional triiodide/iodide couple, indicating that the direction followed was correct. In particular with hindered organic dyes, cobalt complexes reached efficiencies up to 14% [83-84]. On the other hand, polypyridine Cobalt couples present some issues related to mass transport limitation, due to the slow diffusion of the species between the electrodes and especially inside the pores of dye-sensitized TiO_2 [85], which is particularly evident in the case of highly sterically hindered complexes, like $[Co(dtb)_3]^{2+/3+}$, and related to long-term stability trend if compared to the traditional iodide/triiodide redox couple. Hence, the search for efficient and robust redox shuttles has been extended to other first row coordination

complexes based on Cu(I) [86], Ni(III) [87] and Fe(II) [88] complexes. Cu(I)/(II) couples were among the first to be considered, since are usually characterized by slow electron transfer kinetics which could guarantee inefficient electron recapture processes without the needed of bulky substituent. The electron transfer processes involving Cu(I)/(II) couples are slow due to a large inner sphere reorganizational contribution because the electron transfer is associated to a significant change in the preferred coordination geometry, from tetrahedral Cu(I) to tetragonal Cu(II). If the electron transfer is too slow, a low efficiency in dye regeneration is expected and in order to optimize the electron transfer properties of the redox shuttles the coordination sphere of the complex has to be rationally designed. A perfect compromise was found in nature in the structure associated to blue copper proteins which show tetrahedrally distorted geometries intermediate between Cu(I) and Cu(II). As a consequence, blue copper model complexes with a distorted tetrahedral geometry have been recently employed as efficient electron transfer mediators for DSSCs (Fig.2.13) [89].

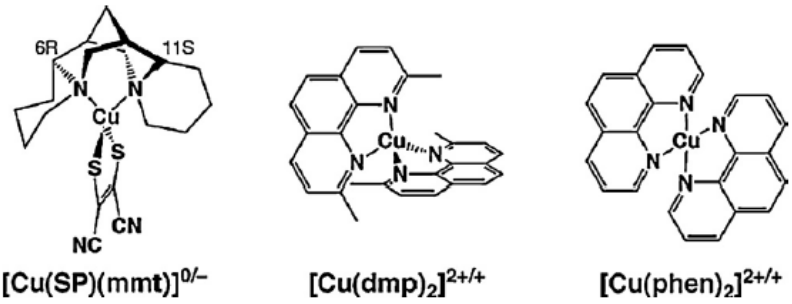

Fig.2.13 Structure of distorted tetrahedral copper complexes. SP is sparteine, mmt is maleonitriledithiolato, dmp is 2,9 dimethyl-1,10 phenanthroline, phen is 1,10 phenantroline.

In **Chapter 5** the possibility of coupling blue copper model complexes with sterically hindered porphyrins will be explored. Three different copper redox mediators were tested, among which one is the $[Cu(dmp)_2]^{2+/+}$ couple, already tested in DSSCs, and the others, more hindered, were synthetized in order to augment the electron transfer kinetics. It is worth to notice that all the copper couples, taken into account, present a higher redox potential with respect to iodide/triiodide, allowing to obtain enhanced open circuit voltages.

Furthermore, in **Chapter 4** new redox couples based on Mn(II) and Mn(III) complexes are reported, which are the first Manganese based redox mediators tested in a DSSC except for the $[Mn(acac)]^{3+}/[Mn(acac)]^{4+}$ couple reported by Udo Bach [90]. In the chapter several passivation techniques were employed to reduce recombination processes. At first, 4-*tert*-butyl-pyridine (TBT), which gives a negative shift of the TiO_2 conduction band and reduced interfacial recombination losses, was added to electrolytic solution. Subsequently, the

photoanode was passivated by modifying with layers made by insulating polymers like polysilanes.

2.3 Dye sensitized photoelectochemial cells (DPECs)

As previously reported, a new method of storage is to borrow the design of nature, in which chemical bonds are broken and formed to produce solar fuels in an artificial photosynthesis process [91-98]. In natural photosynthesis, the anodic charge of the wireless current is used at the oxygen-evolving complex to oxidize water to oxygen, with the concomitant release of four protons. The cathodic charge of the wireless current is captured by Photosystem I to reduce the protons to ‘‘hydrogen’’ with the reduced hydrogen equivalents stored through the conversion of NADP to NADPH. Thus, the overall primary events of photosynthesis store sunlight by the rearrangement of the chemical bonds of water, to form oxygen and Nature’s form of hydrogen. The search for high-tech strategies for realizing an efficient artificial photosynthetic device represents a challenging multidisciplinary task which, at present, is still in its infancy. As regards the water splitting reaction, wide band gap semiconductors (SCs), have been extensively used (Fig.2.14) [99-100]. The absorption of suitable photons by the semiconductor (1,2) leads to the formation of electrons and holes (3) that, depending on their potential, are able to perform the cathodic and anodic reactions respectively (4), after being transferred to the solution directly from the semiconductor surface or after the extraction through an external circuit (Fig.2.14).

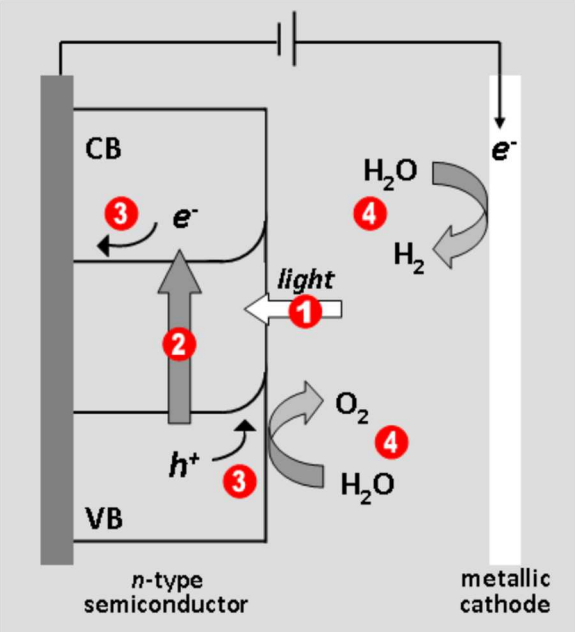

Fig.2.14 Scheme of the relevant processes involved in the solar water splitting process using a *n*-type semiconductor as a photoanode connected to a metallic cathode. The different steps (1 to 4) are detailed in the text.

For the application of a semiconductor in a photoelectrochemical device, different requirements must be considered. It has to be stable in aqueous solutions under photoirradiation and gas evolution condition, moreover, the band gap should be large enough to overcome the 1.23 eV required by the water splitting reaction (considering kinetic limitations, some overpotential is necessary and band gap of 1.6 – 2 eV is the best compromise):

$2H^+ + 2e^- \rightarrow H_2$ $\quad E^0 = 0$ V vs. NHE

$2H_2O \rightarrow O_2 + 4H^+ + 4e^-$ $\quad E^0 = 1.23$ V vs. NHE

The edge of the valence band has to be more positive than the oxidation potential of water to produce O_2 as well as the conduction band edge has to be more negative than the reduction potential of water to produce H_2. In fig.2.15 are shown the most common semiconductors and are reported the energy levels associated to their valence and conduction bands.

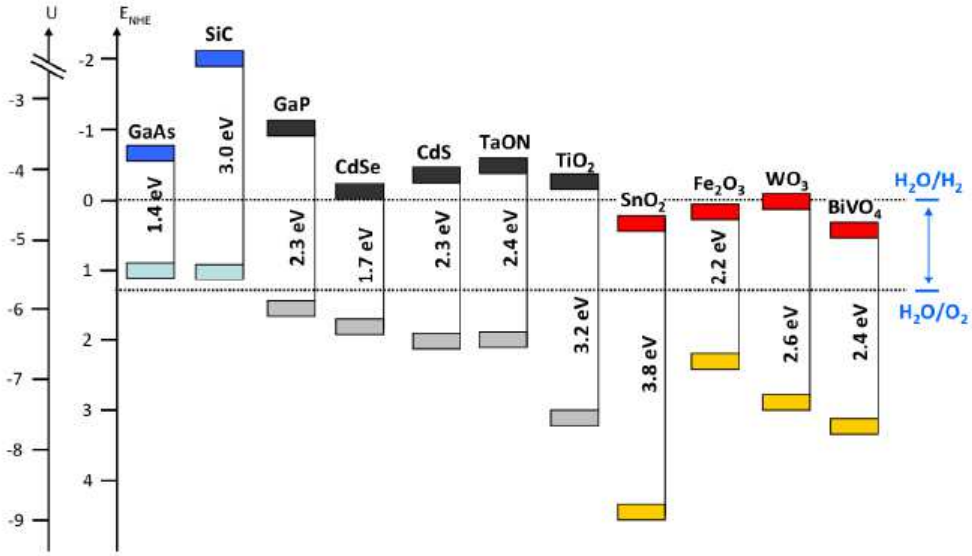

Fig.2.15 Energy levels of Conduction and Valence band edges of a selection of semiconductors relative to the reversible oxidation and reduction potentials of water (at pH = 0), reported as dashed lines. The energy scale is referred both to Normal Hydrogen Electrode and to the vacuum.

In 1972, Fujishima and Honda firstly reported photoelectrolysis of water using a TiO_2 electrode illuminated with UV light [102]. By the way, the large band gap makes the TiO_2 and in general all the semiconductors unable to absorb visible photons, and so their utilization of the solar spectrum is poor. As a consequence, inspired by DSSC technology, the scientific community has focused the attention on devices based on the interfacing of molecular sensitizer adsorbed on a semiconductor surface in contact with an electrolytic

solution in order to achieve a better light harvesting [103-105]. A molecular photosynthetic device must satisfy several key points, such as:

1. Light absorption resulting in the formation of a molecular excited state, as previously seen in DSSC technology, with appropriate energetics
2. Electron-transfer quenching of the excited state of the molecule
3. Spatially directed electron/proton transfer driven by free energy gradients, to give stored oxidative and reductive equivalents
4. Catalysis of water oxidation and H^+ reduction, in order to boost the efficiency by competing with energy wasting charge recombination

The so-called Dye-sensitized photoelectrochemical cell (DSPEC) can be thought of as a hybrid of the Fujishima-Honda cell and the Grätzel cell (Fig.2.16):

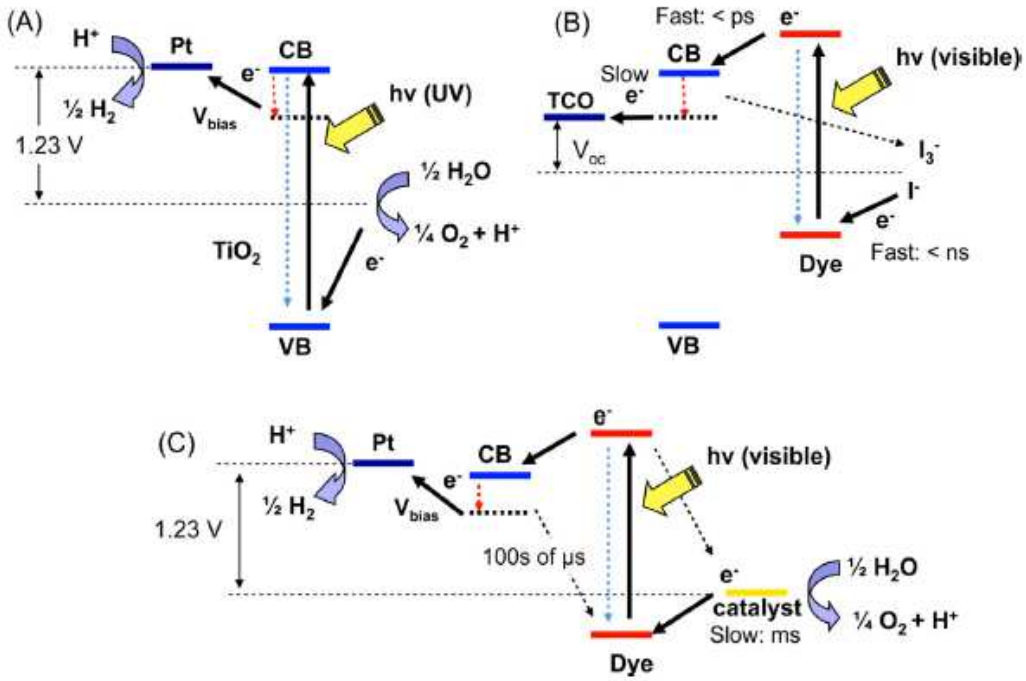

Fig.2.16 Electrochemical potential diagrams for (a) Fujishima-Honda, (b) Grätzel, and (c) water-splitting dye-sensitized solar cells. Solid lines indicate forward electron transfer pathways. Charge recombination pathways are shown as dashed lines [106].

In the water-splitting version, an aqueous electrolyte is used, and a catalyst for the oxygen evolution reaction (WOC) replaces the iodide/triiodide redox shuttle in the DSSC. The characteristics of the semiconductor employed in DSPEC establish the direction of the electron flow through the cell. In their most common configuration (Fig.2.17) DSPECs are built with transparent *n*-type semiconductors, and electron flow, like in DSSC, results from charge injection in their empty conduction band by the sensitizer. An example of a device of this type is reported in fig.2.17 and includes a light absorber (Dye), which upon excitation

and electron injection into the semiconductor conduction band starts a sequence of electron transfer events that activate redox catalysts for water oxidation (WOC). The charge carriers (electrons and holes) are separated into different phases, the solid phase collects electrons and the holes are transiently confined in the molecular assembly bound at the surface of the material. Oxygen is evolved at the dye-sensitized photoanode and water is reduced to hydrogen at a dark catalytic cathode: following photoinjection of electrons by dye molecules, holes diffuse across the surface to reach the catalyst and to be finally transferred to H_2O which is the electron source for regenerating the oxidized dye. The electrons then percolate through the semiconductor films until they find their way into an external circuit before being used to reduce protons to hydrogen at a counter-electrode. The regeneration of reduced dye molecules occurs in competition with charge recombination and electron scavenging by the oxidized catalyst.

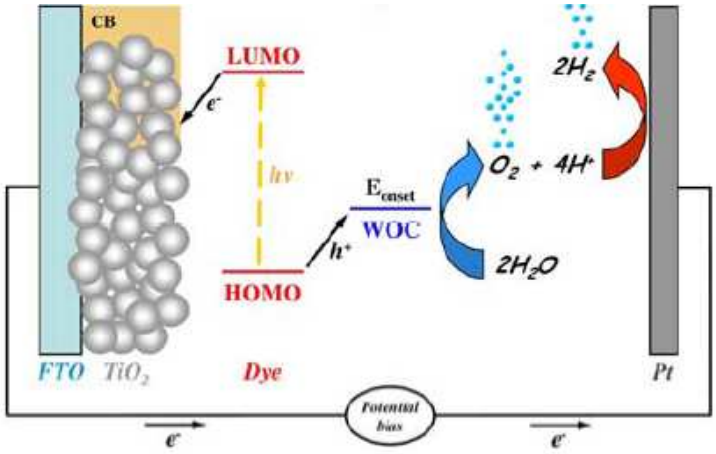

Fig.2.17 Principles of operation of *n*-type DSPECs for water splitting. TiO_2 is taken here as common examples of *n*-type semiconductor. Semiconductor electrode is connected to a catalytic dark counter electrode (platinum wire in the example) [2].

It is worth to notice that the overall processes are separated into half-reactions (i.e water oxidation and hydrogen production) occurring at the separate compartments of the Dye-sensitized photoelectrochemical cell. The semiconductor is usually deposited on a charge collector (FTO), as a thin film consisting of a 20-40 nm nanoparticles and of the thickness of 3-5 µm. In a *n*-type dye-sensitized photoelectrochemical cell, the *quasi*-Fermi level (which is in equilibrium with the Fermi level of the dark cathode) of the semiconductor is the key factor that determines the thermodynamic of the cell, indeed to observe hydrogen evolution without externally applied potential bias, the *quasi*-Fermi level of the semiconductor must be more negative than the formal potential for hydrogen evolution ($E°(H^+/H_2)$ = 0 V vs NHE). As shown in fig.2.18, when the Fermi level of the cathode, in equilibrium with the *quasi*-Fermi level of the semiconductor, is too much negative to ensure

H^+ reduction, a positive bias has to be applied to the semiconductor electrode. The application of the voltage will raise the Fermi level of the cathode having opposite polarity, activating the charge transfer. As a first approximation, the redox levels of the surface bound sensitizing species are not affected by the applied bias.

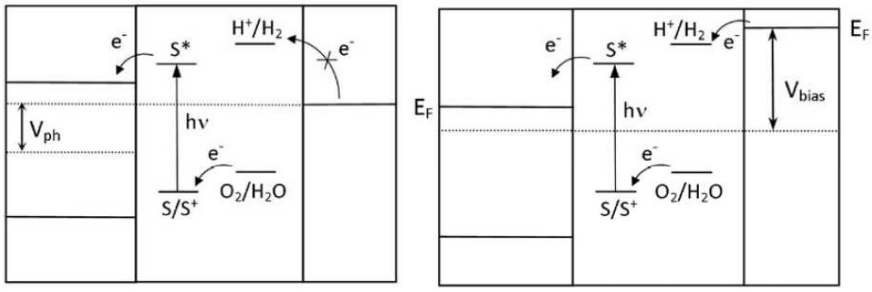

Fig.2.18 Energy level diagram for a sensitized *n*-type semiconductor used as a photoanode in DSPEC for water splitting with a single photoactive junction. S/S^+ represents the redox level of the oxidized sensitizer/catalyst assembly. Here the *quasi*-Fermi level (dotted line) of the *n*-type material is approximated with the flat band potential of the semiconductor, as commonly accepted [2].

When the application of an additional bias is required, the efficiency of the cell has to consider the energy loss due to the need of bias application, according to Eq.2.31:

$$ABPE = \frac{[J(mA/cm^2)\times(E^0_{fuel}-V_{bias})(V)]\eta}{P(\frac{mW}{cm^2})} \qquad \text{(Eq.2.31)}$$

Where *J* is the photocurrent density produced at a given voltage (V_{bias}) under the incident solar power (P), *ABPE* is the applied bias photon to current efficiency, η is the faradaic efficiency and E^0_{fuel} is the standard potential for the fuel forming reaction (E^0_{fuel} = 1.23V in the case of water splitting reaction) [2,107]. Alternatively, other possible DSPEC configuration is possible, where the photoelectrochemical events are driven by hole transfer at the photocathode. This kind of device is called *p*-type DSPEC, which operates in an inverted configuration with respect to the already described *n*-type DSPEC (Fig.2.17). The dye upon excitation, injects a hole into the conduction band of the selected semiconductor which has to be a *p*-type, such as NiO. The injected hole diffuses to the back contact of the conducting substrate while the reduced dye is restored to its ground state by delivering an electron to the oxidized component in the electrolyte, resulting in hydrogen evolution. The coupling of the dye with a catalyst to boost H^+ reduction efficiency (HEC), should be necessary also in this case (Fig.2.19).

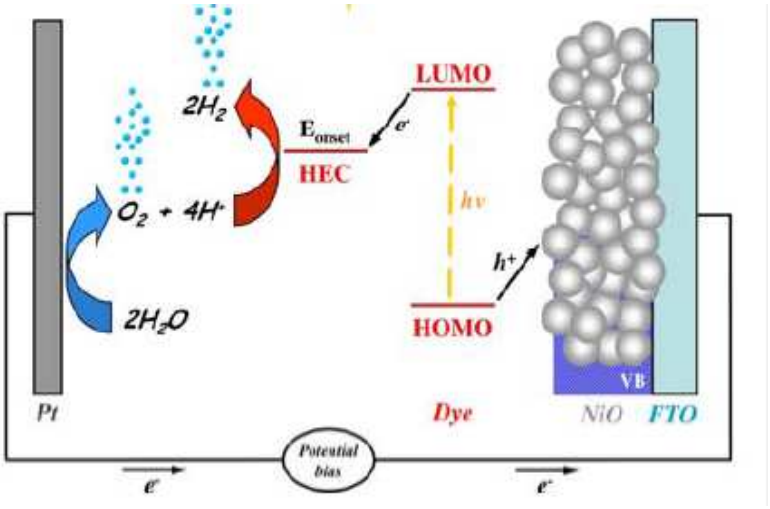

Fig.2.19 Principles of operation of *p*-type DSPECs for water splitting. NiO is taken here as common example of *p*-type semiconductor. Semiconductor electrode is connected to a catalytic dark counter electrode (platinum wire in the example) [2].

It is worth to notice that solar fuel production is a complex matter, where several subsystems must cooperate in order to drive with success the fuel forming reaction, minimizing the recombination events. The current approach is to project a DSPEC with separate p-n junctions which sum their respective photovoltages and try to optimize the separate interfaces, which can be later assembled together in an unassisted photoelectrochemical device [108-109]. The major bottleneck in the design of efficient and durable water splitting cells is the catalytic four-electron oxidation of water which is typically slow (millisecond timescale) (Fig.2.20) because of the weak driving force for the reaction. Indeed, while the millisecond turnover rates of the best water oxidation catalysts are adequate to sustain water electrolysis, they are too slow to compete effectively with back electron transfer to the oxidized dye on the 100 s of microseconds timescale (Fig.2.20) [106]. Low quantum yields for water splitting – typically 1–2% – are a consequence of the fast kinetics of charge recombination, which competes effectively with the catalytic oxidation of water. Rapid back electron transfer is the dominant kinetic pathway in dye-sensitized photoanodes and is the primary reason for their low quantum yield. Since the introduction of the water splitting dye cell in 2009 [105], much of the effort in re-design of the photoanode has focused on improving the quantum yield by slowing down back electron transfer and/or accelerating the water oxidation process.

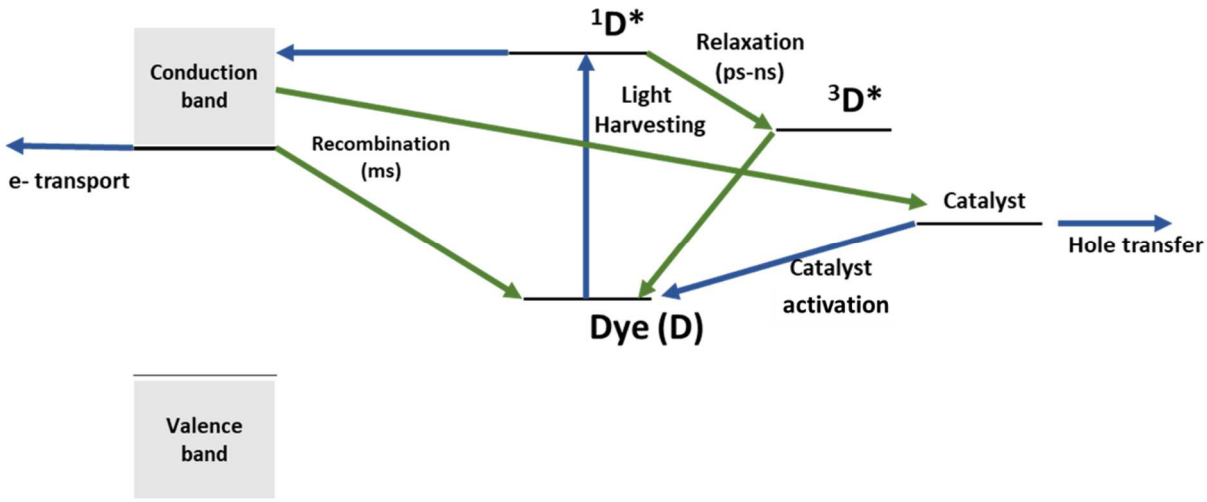

Fig.2.20 Examples of physical processes relevant for the dye-sensitized fuel forming reactions at an *n*-type interface. Blue arrows indicate the desired electron flow, instead green arrows indicate the energy wasting deactivation and recombination events.

2.3.1 Molecular sensitizers for *n*-DSPECs

Because of its importance in aqueous electrochemical systems, the catalytic four-electron oxidation of water to oxygen has been well studied and many different sensitizers and catalysts have been developed [110]. The ideal dye should absorb a significant fraction of visible spectrum, convert all absorbed photons to electron–hole pairs, bind persistently to the surface, and have the appropriate redox potential to drive the catalytic oxidation of water at a catalyst [110]. As reported above, functional water-splitting systems require more energy than the 1.23 V stored in the products. Otherwise, most of the dyes that have sufficiently negative excited state redox potentials to transfer an electron to common semiconductors and are sufficiently oxidizing to accept electrons from water catalyst absorb in the blue part of the visible spectrum. To date, most studies of dye-sensitized photoanodes have employed $[Ru(bpy)_3]^{2+}$ derivatives functionalized with carboxylic acid or phosphonic acid groups and high potential porphyrins, which have a long history in studies of light-driven electron transfer reactions and in conventional dye-sensitized solar cells [110]. In $[Ru(bpy)_3]^{2+}$ derivatives, the major visible absorption is a metal-to-ligand charge transfer (MLCT) band with an absorbance maximum around 450–470 nm and with a high molar absorsorbivity (around 1-2 × 10^4 $M^{-1}cm^{-1}$). Absorption of a photon initially produces a singlet state, which undergoes intersystem crossing within ~300 fs to give a predominantly triplet MLCT state [111]. In this kind of dye/semiconductor system the rapid decay to the triplet state, which is several hundred mV lower in energy than the singlet state, is the first energy loss within the cell [112]. However, as the return of the excited electron to the ground state is spin-forbidden, the triplet MLCT state lifetime is sufficiently long-lived for a

diffusional encounter with an electron donor or acceptor in solution(~600 ns) [113]. Most importantly, the internal quantum yield for formation of the MLCT excited state is nearly unity, meaning that virtually all excited sensitizer molecules can participate in electron transfer reactions and electron injection into the most common wide-band gap semiconductors from both the lowest singlet (^{1}MLCT) and triplet (^{3}MLCT) states is thermodynamically feasible (Fig.2.21) [114].

Another attractive quality of ruthenium tris(bipyridyl) derivatives is the possibility of including multiple functionalities into the three ligands: spectroscopic and electrochemical properties can be optimized by substituting the chromophoric ligands with different electron donating or electron withdrawing functional groups, in addition to phosphonic and carboxylic acid attachment functionalities [115-116]. The lowest excited state of ruthenium tris(bipyridyl) derivate sensitizers, $Ru^{II}L_3$, is best described in terms of a ligand-localized state, $Ru^{III}L_2(L^-)$ [117]. Because the electron localizes on one bipyridine ligand, the excited state of the sensitizers mirrors the electrochemical and spectroscopic properties of the free reduced ligand. Upon excitation, the excited electron hops rapidly (<15 ps) between ligands and thermally equilibrates to reside primarily on the most readily reduced, that is the most electron-deficient, ligand. The excited state oxidation potential can be made more positive by adding an electron-deficient ligand or more negative by adding electron-rich ligands [118]. Furthermore, by using a combination of σ-donor and π-acceptor effects, the ground state oxidation potential can also be shifted. Broadly considered, a more electrondeficient ligand donates less electron density via σ-donation giving a higher nuclear charge on the metal centre and therefore, stabilizing the dπ orbitals. Back-bonding between the dp and π* orbitals of the ligands results in further stabilization of the dπ orbitals [119]. The net effect is that complexes with ligands that are more readily reduced exhibit more positive oxidation potentials. In the context of watersplitting, electron injection into a semiconductor electrode can be accelerated by making the ligand bound to the electrode the most electron-withdrawing. Along the same lines, an increased reduction potential to drive a WOC can be generated by using more easily reduced ligands. Of course, this strategy also leads to more positive excited state potentials, which can affect the efficiency of electron injection.

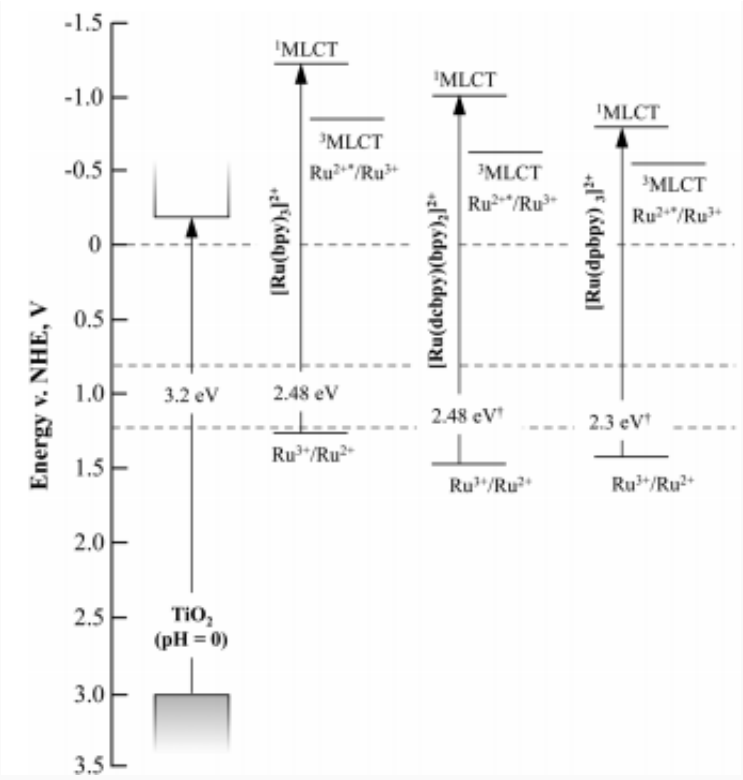

Fig.2.21 Plot of ground state, singlet, and triplet redox potentials versus the conduction and valence bands of TiO_2. $[Ru(bpy)_3]^{2+}$ (bpy = 2,2' -bipyridine); $[Ru(dcbpy)(bpy)_2]^{2+}$ (dcbpy = 4,4' -dicarboxy-2,2' -bipyridine); $[Ru(dpbpy)_3]^{2+}$ (dpbpy = 4,4' -diphosphonic-2,2' -bipyridine) [110];

Organic dyes are a viable alternative to metal complexes to avoid the use of rare earth metals. Moreover, their π-π* transition exhibit a very high extinction coefficient, ten times higher than the one associated to MLCT transitions ($10^5 M^{-1}cm^{-1}$). Among the wide libraries of organic species, porphyrins have been studied by the photochemical community as light harvesters in donor-acceptor dyads for a long time. Porphyrins are strongly absorbing with intense Soret bands ($\varepsilon \sim 10^5$ M^{-1} cm^{-1}) in the blue part of the visible spectrum and Q-bands ($\varepsilon \sim 10^4$) in the green to red [120-122]. The singlet (S_0) ground state of porphyrins tends to be more oxidizing with respect to Ru(II) complexes, and electron injection into semiconductor conduction band is typically only favourable from the S_2 and S_1 excited states. On the contrary, the triplet has too much positive energy to promote an efficient injection [2]. To date, high potential porphyrins have been proposed as suitable light harvesters for molecular water splitting. Electron-withdrawing pentafluorophenyl groups can be incorporated at the *meso*-carbon of a zinc-prophyrin to induce an electron deficiency that leads to a positive shift in the ground state oxidation potential of the complex. Consequently, the holes remaining on a high potential photooxidized porphyrin are thermodynamically capable of driving water oxidation. Moore et al. [123] demonstrated visible light water-splitting via the co-deposition

of a high potential porphyrin zinc 5-(4-carbomethoxyphenyl)-15-(4- carboxyphenyl)-10,20-bis-(pentafluorophenyl) porphyrin(ZnBPFP) (Fig.2.22) and iridium WOC onto a TiO_2 electrode.

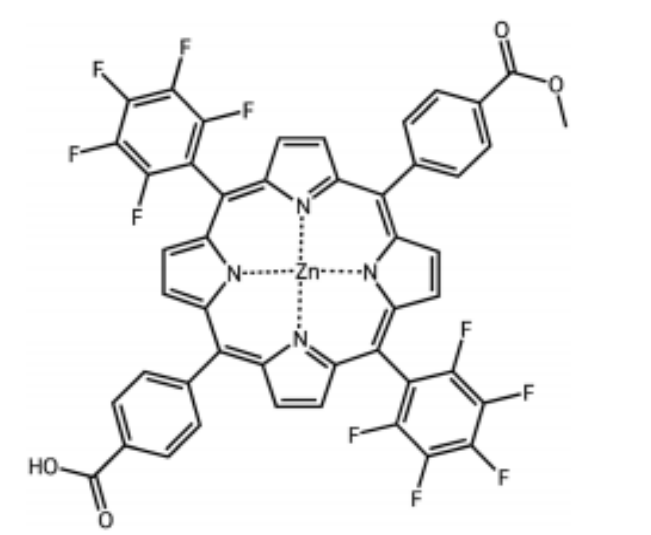

Fig.2.22 Zinc 5-(4-carbomethoxyphenyl)-15-(4-carboxyphenyl)-1',2,-bis-(pentafluorophenyl)porphyrin (ZnBPFP).

In both ruthenium complexes and porphyrins, the electronic coupling of the sensitizer with the substrate should be established through the formation of covalent bonds. Carboxylic and phosphonic are the most used anchoring group for the attachment of molecular specie to metal oxides. In particular, carboxylic acids are the most frequently used linking groups, and provide strong electronic coupling for ultra-fast electron injection from the dye excited state. However, photoanodes for water splitting necessarily operate in solutions that contain water, and are often used with aqueous buffer solutions, making hydrolysis of the carboxylic acid–metal bond a significant problem. Under the aqueous conditions, phosphonate linkers provide a more robust linkage to the oxide surface [124-125], but recent work by Hanson et al. [126-127] has shown that the photodesorption of phosphonate-bond dyes in water is accelerated in the presence of oxygen, possibly because of the generation of superoxide ions by back electron transfer from the semiconductor. In order to solve problems associated to dye desorption both in strong acidic and basic solutions, to date, organic perylens were employed as dye sensitizer for water splitting photoanodes. Perylens are a class of sensitizers that adsorb onto the surface of semiconductor materials by hydrophobic/*pi*-stacking interactions without any specific anchoring site and, as a consequence, do not suffer the hydrolytic cleavage of the covalent link [128]. Most importantly, in their common design, perylens present high oxidation potentials, resulting compatible with the activation of many

WOCs reported in literature such as Iridium oxide, Ruthenium oxide and polioxometalates [129-130]. On the contrary, their redox potentials preclude injection in many semiconductors, for example the most common TiO_2 [128]. Hence, in **Chapter 7** of the present thesis will be described the possibility to couple a dicationic perylene [(N,N'-bis(2-(trimethylammonium)ethylene) perylene 3,4,9,10-tetracarboxylic acid *bis*-mide) $(PF_6)_2$] [128] with SnO_2 semiconductor and the corresponding Antimony doped (SnO_2:Sb) semiconductor, in order to build an efficient photoanode for water splitting reaction. The employment of SnO_2 based semiconductor would reduce the photovoltage of the cell, given by the difference between the potentials of the O_2/H_2O couple and the Fermi level of the semiconductor, but at the same time it would also lower the driving force for back electron transfer. Furthermore, SnO_2 has higher electrical conductivity and mobility with respect to TiO_2. Indeed, unlike TiO_2, the density of trap states in SnO_2 is significantly lower, resulting in an electron diffusion coefficient of two orders of magnitude greater than in TiO_2. Bergeron et al. [131] have already demonstrated the viability of this approach using ruthenium sensitizers on SnO_2 with excited state potentials too positive for electron injection into TiO_2.

2.4 References

1) N.B. Hannay, N. B., *Semiconductors*; Reinhold Publishing Corporation: New York, **1959**;

2) G. Bergamini, S. Silvi, *Applied Photochemistry*, Lecture notes in chemistry 92, **2013**, chapter 2, pp 67-143;

3) H. Hagfeldt, et.al., *Dye-Sensitized Photoelectrochemical Cells*, Practical Handbook of Photovoltaics, **2012**;

4) S. Ardo, G.J. Meyer, *Chem. Soc. Rev.* **2009**, *38*, 115;

5) R. Memming, *Prog. Surf. Sci.* **1984**, *17*, 7;

6) W.W. Gartner, *Phys. Rev.* **1959**, *116*, 84;

7) J.R. Bolton, M. Archer, *Advances in Chemistry,* **1991**, *228*, chapter 2, pp 7-23;

8) C.A. Bignozzi, J.R. Schoonover, F. Scandola, *Molecular Level Artificial Photosynthetic Materials*, **1997**, John Wiley & Sons: New York;

9) N. S. Lewis, *Science* **2016**, *351*, 1920;

10) J. Desilvestro, M. Graetzel, L. Kavan, J. Moser, J. Augustynski, *Journal of the American Chemical Society* **1985**, *107*, 2988;

11) H. Gerischer, H. Tributsch, *Berichte der Bunsengesellschaft für physikalische Chemie* **1968**, *72*, 437;

12) B. O'Regan, M. Gratzel, *Nature* **1991**, *353*, 737;

13) A. Hagfeldt, G. Boschloo, L. Sun, L. Kloo, H. Pettersson, *Chem. Rev.* **2010**, *110*, 6595;

14) A. Heglein, *Chem.Rev.* **1989**, *89*, 1861;

15) M. Graetzel, et al. *Chem. Commun.* **2008**, 2635;

16) S. Carli, E. Busatto, S. Caramori, et al., *J. Phys. Chem. C.* **2013**, *117*, 5142;

17) R.J. Ellingson, N.H. Ghosh, S. Ferrere, A.J. Nozik, T.Q. Lian, *J. Phys. Chem. B* **1999**, *103*, 3110;

18) G. Ramakrishna, D.A. Jose, D.K. Kumar, A. Das, D.K. Palit, H.N. Ghosh, *J. Phys. Chem. B* **2005**, *109*, 15445;

19) D. Kuang, S. Ito, B. Wenger, C. Klein, J-E. Moser, R. Humphry-Baker, S.M. Zakeeruddin, M. Graetzel, *J. Am. Chem. Soc.* **2006**, *128*, 4146;

20) G. Benko, J. Kallioinen, J.E.I Korppi-Tommola, A.P. Yartsev, V. Sundstrom, *J. Am. Chem. Soc.* **2002**, *124*, 489;

21) N.A. Anderson, T.Q. Lian, *Annu. Re*V. *Phys. Chem.* **2005**, *56*, 491;

22) A.F. Nogueira, M.A.D. Paoli, I. Montanari, R. Monkhouse, J. Nelson, J.R. Durrant, *J. Phys. Chem. B* **2001**, *105*, 7517;

23) I. Montanari, J. Nelson, J.R. Durrant, *J. Phys. Chem. B* **2002**, *106*, 12203;

24) C. Bauer, G. Boschloo, F. Mukhtar, A. Hagfeldt, *J. Phys. Chem. B* **2002**, *106*, 12693;

25) H. Nusbaumer, J.E. Moser, S.M. Zakeeruddin, M.K. Nazeeruddin, M. Grätzel, *J. Phys. Chem. B* **2001**, 105, 10461;

26) H. Nusbaumer, S.M. Zakeeruddin, J.-E. Moser, M. Graetzel, *Chem.sEur. J.* **2003**, 9, 3756;

27) J.N. Clifford, E. Palomares, M.K. Nazeeruddin, M. Gra¨tzel, J.R. Durrant, *J. Phys. Chem. C* **2007**, *111*, 6561;

28) D. Kuciauskas, M.S. Freund, H.B. Gray, J.R. Winkler, N.S Lewis, *J. Phys. Chem. B* **2001**, 105, 392;

29) S.N. Mori, W. Kubo, T. Kanzaki, N. Masaki, Y. Wada, S. Yanagida, *J. Phys. Chem. C* **2007**, 111, 3522;

30) G.K. Boschloo, A. Goossens, J. Schoonman, *J. Electrochem. Soc.* **1997**, *144*, 1311;

31) B. O'Regan, J. Moser, M. Anderson, M. Gra¨tzel, *J. Phys. Chem.* **1990**, *94*, 8720;

32) A. Hagfeldt, et.al, *J. Phys. Chem.* **1994**, *98*, 5552;

33) N. Kopidakis, E.A. Schiff, N.G. Park, J. van de Lagemaat, A.J. Frank, *J. Phys. Chem. B* **2000**, *104*, 3930;

34) A. Hagfeldt, et.al., *Sol. Energy Mater. Sol. Cells* **2002**, *73*, 411;

35) G.M., Hasselmann, G.J. Meyer, *J. Phys. Chem. B* **1999**, *103*, 7671;

36) J.N. Clifford, E. Palomares, M.K. Nazeeruddin, M. Graetzel, J. Nelson, X. Li, N.J, Long, J.R. Durrant, *J. Am. Chem. Soc.* **2004**, *126*, 5225;

37) S.A. Haque, Y. Tachibana, R.L. Willis, J.E. Moser, M. Graetzel, R. David, J.R. Durrant, *J. Phys. Chem. B* **2000**, *104*, 538;

38) Y. Tachibana, J.E. Moser, M. Graetzel, D.R. Klug, J.T. Durrant, J. R. *J. Phys. Chem.* **1996**, *100*, 20056;

39) J.E. Moser, M. Graetzel, *Chem. Phys.* **1993**, *176*, 493;

40) S.G. Yan, J.T. Hupp, *J. Phys. Chem.* **1996**, *100*, 6867;

41) S.Y. Huang, et al., *J. Phys. Chem. B* **1997**, *101*, 8139;

42) A. Zaban, M. Greenshtein, J. Bisquert, *ChemPhysChem* **2003**, *4*, 859;

43) L.M. Peter, *J. Phys. Chem. C* **2007**, *111*, 6601;

44) A. Hauch, A. Georg, *Electrochim. Acta* **2001**, *46*, 3457;

45) K. Kakiage, et al., Chem. Commun. **2015**, *51*, 15894;

46) M.K. Nazeeruddin, A. Kay, I. Rodicio, R. Humphry-Baker, E. Mueller, P. Liska, N. Vlachopoulos, M. Graetzel, *J. Am. Chem. Soc.***1993,** 115, 6382;

47) A. Hagfedlt, M. Graetzel, *Chem. Rev. 95* (1995) 49.

48) R. Argazzi, N.Y.M. Iha, F. Zabri, F. Odobel, C.A. Bignozzi, *Coord. Chem. Rev.* **2004**, *248*, 1299;

49) M.K. Nazeeruddin, S.M. Zakeeruddin, J.-J. Lagref, P. Liska, P. Comte, C. Barolo, G. Viscardi, K. Schenk, M. Graetzel, *Coord. Chem. Rev.* **2004**, 1317;

50) A. Sarto Polo, M.K. Itokazu, N.Y.M. Iha, *Coord. Chem. Rev.* **2004**, *248*, 1343;

51) G.J. Meyer, *Inorg. Chem.* **2005**, *44*, 6852;

52) N. Robertson, *Angew. Chem. Int. Ed.* **2006**, 45, 2338;

53) P. Xie, F. Guo, *Curr. Org. Chem.* **2007**, *11*, 1272;

54) M.K. Nazeeruddin, F. De Angelis, S. Fantacci, A. Selloni, G. Viscardi, P. Liska, S. Ito S, B. Takeru, M. Graetzel, *J Am Chem Soc* **2005**, *127*, 16835;

55) G.B. Paolo, C.D.R. Kiyoshi, B.D. Koivisto, C.P. Berlinguette, *Coord Chem Rev* **2012**, *256*, 1438;

56) P.G. Bomben, T.J. Gordon, E. Schott, C.P. Berlinguette, *Angew. Chem. Int. Ed.* **2011**, *50*, 10682;

57) P.G. Bomben, K.C.D Robson, P.A. Sedach, C.P Berlinguette, *Inorg. Chem.,* **2009**, *48,* 9631;

58) C.C. Chou, K.L. Wu, Y. Chi, et al., *Angew. Chem. Int. Ed.* **2011**, *50*, 2054;

59) T. Bessho, E. Yoneda, J.H. Yum, M. Guglielmi, I. Tavernelli, H. Imai, U. Rothlisberger, M.K. Nazeeruddin, M. Graetzel, *J. Am. Chem. Soc*., **2009**, *131*, 5930;

60) M.K. Nazeeruddin, P. Pechy, T. Renouard, S.M. Zakeeruddin, R. Humphry-Baker, P. Comte,

P. Liska, L. Cevey, E. Costa, V. Shklover, L. Spiccia, G.B. Deacon, C.A. Bignozzi, M. Graetzel, *J. Am. Chem. Soc*. **2011**, *123*, 1613;

61) A. Hagfeldt, G. Boschloo, L. Sun, L. Kloo, H. Pettersson, *Chem. Rev.* **2010**, *110*, 6595;

62) Y. Ooyama, Y. Harima, *Eur. J. Org. Chem.* **2009**, 2903;

63) A. Mishra, M.K.R. Fischer, P. Bauerle, *Angew. Chem. Int. Ed.* **2009**, *48*, 2474;

64) T. Kitamura, M. Ikeda, K. Shigaki, T. Inoue, N.A. Anderson, X. Ai, T.Q. Lian, S. Yanagida, *Chem. Mater*. **2006**, *16*, 1806;

65) K. Hara, M. Kurasighe, S. Ito, A. Shinpo, S. Suga, K. Sayama, H. Arakawa, *Chem. Commun.* **2003**, 252;

66) D.P. Hagberg, T. Edvinsson, T. Marinado, G. Boschloo, A. Hagfedlt, L.C. Sun, *Chem. Commun.* **2006**, *21*, 2245;

67) S. Haid, M. Marszalek, A. Mishra, M. Wielopolski, J. Teuscher, J.E. Moser, R.H. Baker, S.M. Zakeeruddin, M. Graetzel, P. Bauerl, *Adv. Funct. Mater.* **2012**, *22*, 1291;

68) K. Do, D. Kim, N. Cho, S. Paek, K. Song, J. Ko, *Org. Lett*. **2012**, *14*, 222;

69) S. M. Feldt, E. A. Gibson, E. Gabrielsson, L. Sun, G. Boschloo, A. Hagfedlt, *J. Am. Chem. Soc.,* **2010,** *132*, 16714;

70) H.N. Tsao, C. Yi, T. Moehl, J. H. Yum, S.M. Zakeeruddin, M.K. Nazeeruddin, M. Graetzel, *ChemSusChem* **2011,** *4*, 591;
71) Kashif, M. K.; Axelson, J. C.; Duffy, N. W.; Forsyth, C. M.; Chang, C. J.; Long, J. R.; Spiccia, L.; Bach, U. *J. Am. Chem. Soc.* **2012**, *134*, 16646;
72) M. Gorlov, L. Kloo, *Dalton Trans*. **2008**, 2655;
73) J. Wu, Z. Lan, S. Hao, P. Li, J. Lin, M. Huang, L. Fang, Y. Huang, *Pure Appl. Chem.* **2008**, *80*, 2241;
74) B. Li.; L. Wang, B. Kang, P. Wang, Y. Qiu, *Sol. Energy Mater. Sol. Cells* **2006**, *90*, 549;
75) T.A. Heimer, E.J. Heiweil, C.A. Bignozzi, G.J. Meyer, *J. Phys. Chem. A* **2000**, 104, 4256;
76) I. Montanari, J. Nelson, J.R. Durrant, *J. Phys. Chem. B* **2002**, *106*, 12203;
77) G. Schlichthorl, S.Y. Huang, J. Sprague, A.J. Frank, *J. Phys. Chem. B* **1997**, *101*, 8141;
78) S.Y. Huang, G. Schlichthorl, A.J. Nozik, M. Graetzel, A.J. Frank, *J. Phys. Chem. B* **1997**, *101*, 2576;
79) M. Toivola, F. Ahlskog, P. Lund, *Sol. Energ. Mat. Sol. Cells* **2006**, *90*, 2881;
80) T.J. Meyer, H. Taube, in: G. Wilkinson (Ed.), *Comprehensive Coordination Chemistry: The Synthesis, Reactions, Properties and Applications of Coordination Compounds*, vol. 1, Pergamon Press, Oxford, U.K., **1987**, p. 331;
81) S.A. Sapp, C.M. Elliott, C. Contado, S. Caramori, C.A. Bignozzi, *J. Am. Chem. Soc.* **2002**, *124*, 11215;
82) C.A. Bignozzi, et.al., *Coordination Chemistry Reviews;* **2013**, *257*, 1472;
83) S.M. Feldt, E.A. Gibson, E. Gabrielsson, L. Sun, G. Boschloo, A. Hagfedlt, *J. Am. Chem. Soc.* **2010**, *132*, 16714;
84) H.K. Tsao, C. Yi, T. Moehl, J.-H. Yum, S.M. Zakeeruddin, M.K. Nazeeruddin, M. Graetzel, *ChemSusChem* **2011**, *4*, 591;
85) J.J. Nelson, T.J. Amick, C.M. Elliott, *J. Phys. Chem. C,* **2008**, *112*, 18255;
86) M. Brugnati, S. Caramori, S. Cazzanti, L. Marchini, R. Argazzi, C.A. Bignozzi, *Int. J. Photoenergy* **2007**, *1*, 80756;
87) T.C. Li, A.M. Spokoyny, C. She, O.K. Farha, C.A. Mirkin, T.J. Marks, T.J. Hupp, *J. Am. Chem. Soc.* **2010**, *132*, 4580;
88) T. Daeneke, T.-H. Kwon, A.B. Holmes, N.W. Duffy, U. Bach, L. Spiccia, Nat. Chem. **2011**, *3*, 211;
89) Y. Bai, Q. Yu, N. Cai, Y. Wang, M. Zhang, P. Wang, *Chem. Commun.* **2011**, *47*, 4376;
90) I. R. Perera, A. Gupta, W. Xiang, T. Daeneke, U. Bach, R. A. Evans, C. A. Ohlin and L. Spiccia, *Phys. Chem. Chem. Phys.*, **2014**, *16*, 12021;

91) J. Kern, G. Renger, *Photosynthesis Research* **2007**, *94*, 183;
92) G. Renger, T. Renger, *Photosynthesis Research* **2008**, *98*, 53;
93) T.J. Meyer, M.H.V. Huynh, H.H. Thorp, *Angewandte Chemie International Edition* **2007**, *46*, 5284;
94) J.P. McEvoy, G.W. Brudvig, *Chemical Reviews* **2006**, *106*, 4455;
95) H. Dau, I. Zaharieva, *Accounts of Chemical Research* **2009**, *42*, 1861;
96) G.W. Brudvig, *Philosophical Transactions of the Royal Society of London B: Biological Sciences* **2008**, *363*, 1211;
97) J. Barber, B. Andersson, *Nature* **1994**, *370*, 31;
98) J. Barber, *Biochemical Society Transactions* **2006**, *34*, 619;
99) X. Chen, S.S. Mao, *Chem. Rev.* **2007,** *107*, 2891;
100) C.A. Bignozzi, S. Caramori, V. Cristino, R. Argazzi, L. Meda, A. Tacca, *Chem. Soc. Rev.* **2013,** *42*, 2228;
101) A. Fujishima and K. Honda, *Nature* **1972**, *238*, 37;
102) J.R. Swierk, T.E. Mallouk, *Chem. Soc. Rev.* **2013,** *42*, 2357;
103) L. Alibabaei, H. Luo, R.L. House, P.G. Hoertz, R. Lopez, T.J. Meyer,. *J. Mater. Chem. A* **2013,** *1*, 4133;
104) Z. Yu, F. Li, L. Sun, *Energy Environ. Sci.* **2015,** *8* (3), 760-775;
105) A. Mishra, M. Fischer, P. Bäuerle, *Angew. Chem. Int. Ed.* **2009,** *48*, 2474;
106) E. Mallouk et al., *Nano Today* **2017**, *14*, 42;
107) Z. Chen, T.F. Jaramillo, T.G. Deutsch, A. Kleiman-Shwarsctein, A.J. Forman, N. Gaillard, R. Garland, K. Takanabe, C. Heske, M. Sunkara, E.W. McFarland, K. Domen, E.L. Miller, J.A. Turner, H.N. Dinh, *Journal of Materials Research* **2010**, *25*, 3;
108) L. Hammarström, *Accounts of Chemical Research* **2015**, *48*, 840;
109) F. Li, K. Fan, B. Xu, E. Gabrielsson, Q. Daniel, L. Li, L. Sun, *Journal of the American Chemical Society* **2015**, *137*, 9153;
110) E. Mallouk et al., *Chem. Soc. Rev.*, **2013**,*42*, 2357;
111) N. Damrauer, G. Cerullo, A. Yeh, T. Boussie, C. Shank and J. McCusker, Science, **1997**, *275*, 54;
112) E. M. Kober and T. J. Meyer, *Inorg. Chem.,* **1982**, *21*, 3967;
113) J. V. Caspar and T. J. Meyer, *Inorg. Chem.*, **1983**, *22*, 2444;
114) J. Demas and D. Taylor, *Inorg. Chem.*, **1979**, *18*, 3177;
115) E. Bae, W. Choi, J. Park, H. S. Shin, S. B. Kim and J. S. Lee, *J. Phys. Chem. B,* **2004**, *108*, 14093;
116) H. Park, E. Bae, J.-J. Lee, J. Park and W. Choi, J. *Phys. Chem. B*, **2006**, *110*, 8740;

117) D. P. Rillema, G. Allen, T. J. Meyer and D. Conrad, *Inorg. Chem.*, 1983, *22*, 1617;
118) C. M. Elliott and E. J. Hershenhart, *J. Am. Chem. Soc.*, **1982**, *104*, 7519;
119) D. P. Rillema, G. Allen, T. J. Meyer and D. Conrad, *Inorg. Chem.,* **1983**, *22*, 1617;
120) P. A. Christensen, A. Harriman, G. Porter and P. Neta, *J. Chem. Soc., Faraday Trans. 2*, **1984**, *80*, 1451;
121) A. Harriman, G. S. Nahor, S. Mosseri and P. Neta, *J. Chem. Soc., Faraday Trans. 1*, *1988*, *84*, 2821;
122) K. Kalyanasundaram and M. Neumann-Spallart, *J. Phys. Chem.,* **1982**, *86*, 5163;
123) G. F. Moore, J. D. Blakemore, R. L. Milot, J. F. Hull, H.-E. Song, L. Cai, C. A. Schmuttenmaer, R. H. Crabtree and G. W. Brudvig, *Energy Environ. Sci.,* **2011**, *4*, 2389;
124) E. Bae, W. Choi, J. Park, H. S. Shin, S. B. Kim and J. S. Lee, *J. Phys. Chem. B*, **2004**, *108*, 14093;
125) H. Park, E. Bae, J.-J. Lee, J. Park and W. Choi, *J. Phys. Chem. B*, **2006**, *110*, 8740;
126) K. Hanson, M. K. Brennaman, H. Luo, C. R. K. Glasson, J. J. Concepcion, W. Song and T. J. Meyer, *ACS Appl. Mater. Interfaces*, **2012**, *4*, 1462;
127) K. Hanson, M. K. Brennaman, A. Ito, H. Luo, W. Song, K. A. Parker, R. Ghosh, M. R. Norris, C. R. K. Glasson, J. J. Concepcion, R. Lopez and T. J. Meyer, *J. Phys. Chem. C*, **2012**, *116*, 14837;
128) F. Ronconi, Z. Syrgiannis, A. Bonasera, M. Prato, R. Argazzi, S. Caramori, V. Cristino, C.A. Bignozzi, *J. Am. Chem. Soc.* **2015,** *137*, 4630;
129) C.C. McCrory, S. Jung, J.C. Peters, T.F. Jaramillo, *J. Am. Chem. Soc.* **2013,** *135*, 16977;
130) A. Llobet, *Molecular water oxidation catalysis*. John Wiley & Sons: 2014;
131) B. V. Bergeron, A. Marton, G. Oskam and G. J. Meyer, *J. Phys. Chem. B*, **2005**, *109*, 937;

CHAPTER 3. REDOX FLOW BATTERIES

The stationary electrochemical energy storage is an interesting field for what concerns renewable energy development. To this aim, liquid flow-batteries look promising devices since their architecture offers the advantage to decouple the power rating (cell stack size) from the energy capacity (tank size), and could be sized for both domestic and industrial applications ranging from kW to MW size [1-2]. In these conditions their limitations, namely low energy density, relatively large volume, poor portability, are relatively unimportant. Their fundamental operation is relatively undemanding: in the charge phase the current generated by the solar power plant converts two redox couples in their respective oxidized and reduced form, which are stored in separate compartments. In the discharge phase, the battery operates the reverse reaction, *i.e.* the reduced and oxidized forms are restored to their initial state supplying current to the external load [1]. Indeed, in a typical RFB the cathode and anode materials are made of electrolyte solutions (i.e. catholytes and anolytes). As shown in Fig.3.1, electrolytes at the anode and cathode sides are pumped through porous electrodes located at each side in a cell stack, where they are separated by a membrane or a porous separator to prevent mixing and to guarantee cross-transport of nonactive species (*i.e.*, H^+, Cl^-) [3].

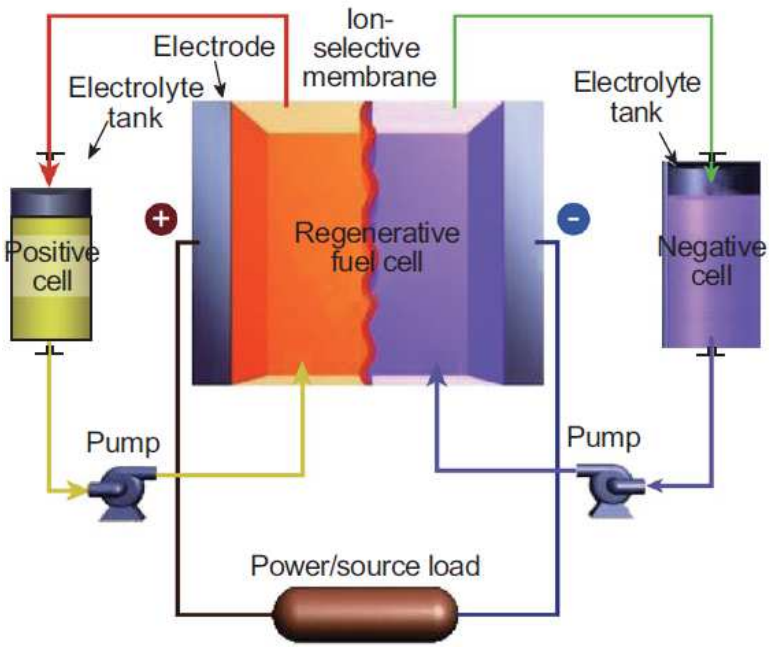

Fig.3.1 Schematic illustrating the general structure of a typical redox-flow battery

Practical applications tend to require high currents and voltages. To meet this, many unit cells can be stacked in electrical series to increase the voltage and the stacks can be electrically connected in parallel to yield high currents [1]. A typical unit cell of a flow battery stack is illustrated in Fig.3.2. Rubber gasket seals and steel tie-bolts are normally used to compress the cell stack in order to avoid electrolyte leakages. Metallic end-plates, such as aluminium and copper, can be used as current conductors to provide electrical conductivity. Turbulence promoters can be employed in the compartment to increase the mass transport and exchange of electroactive species. Since the electroactive species used in RFBs are often highly oxidizing, no metallic component should be in contact with the electrolytes. Chemically resistant polymers, such as polytetrafluoroethylene (PTFE), ethylene-polypropylene-diene (EPPD), polyvinylchloride (PVC), polyvinylidene (PVDF) and acrylics (Perspex1) are the typical materials for producing the battery components (excluding the metallic end-plate and the electrode catalysts). The electrodes are usually three-dimensional carbon-based electrodes, including carbon cloth [4], carbon paper [5] and carbon felts [6]. An ideal electrode material should provide a high electrical conductivity, good mechanical properties, strong chemical resistance, be of reasonable price and have a long cycle life in highly oxidizing media. As a consequence, carbon-based electrodes are more common than their metallic counterparts, as they do not undergo dissolution or formation of oxide during chemical oxidation. Indeed, metal ions from the metallic electrodes can dissolve into the electrolyte during discharge and corrosion, which could lead to unstable redox potentials and disturb the chemistry of the RFBs. The membrane is typically an ion exchange membrane, which is produced from polymeric materials with pore diameters of ~20 A° [7]. An ideal membrane should prevent mixing of the electrolytes and the direct chemical reaction of active species or chemical products, such as electrodeposits from the positive and negative electrolytes, which can result in energy losses [8-9]. Moreover, to minimize resistance and power loss, the membrane is required to have a high ionic conductivity. In aqueous electrolyte, ion-exchange membranes are designed to conduct positively charged ions (*i.e.* H^+ or Na^+) or negatively charged ions (*i.e.* Cl^-, NO_3^- or SO_4^{2-}) by means of cationic or anionic exchange membranes, respectively. Due to the high conductivity and good chemical stability in the oxidizing electrolyte, perfluorinated membranes have been commonly used in RFBs, such as the commercially available Nafion®, Flemion®, Fumapem®, Aciplex® and Dow® [10]. The development of ion-exchange membranes for aqueous RFB has been reviewed by Li et al. [11] and they concluded that the Nafion cationic exchange membrane, although expensive, is still the most used.

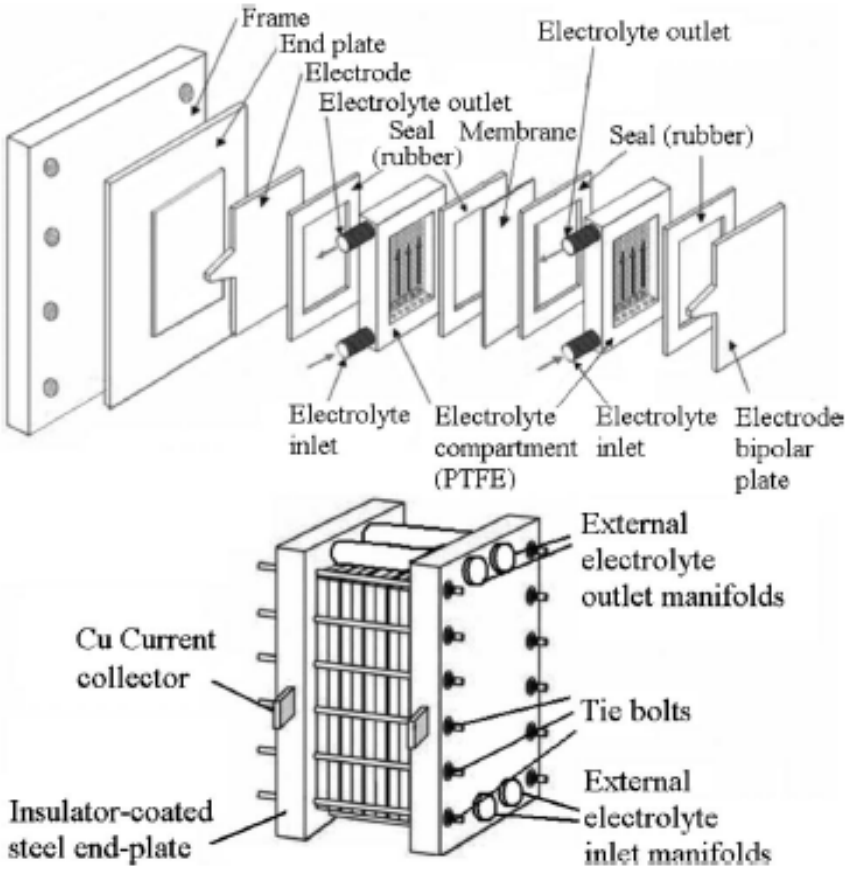

Fig.3.2 Components of a cell stack [1].

3.1 Aqueous Redox Flow Batteries

Because of good safety characteristics, aqueous systems have attracted widespread interest. Among aqueous RFBs, the vanadium redox battery (VRFB), which was pioneered at The University of NewSouthWales by M. Skyllas-Kazacos [12], and employs vanadium redox couples in sulfuric acid in both half-cells, is now moving towards commercialization in a wide range of stationary applications [13]. The negative half-cell employs V^{2+} /V^{3+} (hypovanadous/vanadous ion) redox couple whereas the positive half-cell uses VO^{2+}/ VO_2^{+} (vanadyl/vanadic ion) redox couple. Generally, vanadium solutions of compositions corresponding to different negative and positive half-cell electrolyte are prepared by the electrolysis of vanadyl sulphate solutions in H_2SO_4 supporting electrolyte. 2M vanadium in 5M total sulphates is often selected as the preferred electrolyte composition for the VRB [14]. With a standard electrode potential (E^o) of approximately +1.00 V versus the standard hydrogen electrode (SHE), the characteristic reaction of the vanadium battery at the positive electrode is as follows:

$$VO^{2+} + H_2O \rightarrow VO_2^{+} + 2H^{+} + e^{-} \qquad \text{(Charge)}$$

$$VO_2^+ + 2H^+ + e^- \rightarrow VO^{2+} + H_2O \quad \text{(Discharge)}$$

While, the reversible reaction at the negative electrode involves V(II) and V(III) species and has a standard potential of −0.26V versus SHE:

$$V^{3+} + e^- \longrightarrow V^{2+} \quad \text{(Charge)}$$

$$V^{2+} \longrightarrow V^{3+} + e^- \quad \text{(Discharge)}$$

As a consequence, the theoretical (thermodynamic) standard cell voltage for the overall reaction is +1.26 V. It is worth to notice that the hypovanadous, vanadous, vanadyl and vanadic ions can be identified during operation of the cell by their colouration: violet, green, blue and light yellow, corresponding to soluble vanadium species in the (II), (III), (IV) and (V) oxidation states, respectively. The concentration of vanadium ions is a determinant factor to increase the energy capacity and is determined by the solubility of each of the V(II), V(III), V(IV) and V(V) ions, this being a function of temperature and sulfuric acid concentration [15]. In the case of the V(II), V(III) and V(IV) oxidation states, the solubility increases with increasing temperature and decreasing acid concentration. The reverse is true however, for the V(V) oxidation state which undergoes thermal precipitation at temperatures above 40 °C. Taking into account that during continuous operation of the VRFB, higher operating temperatures are most likely to be experienced due to resistance losses which heat up the solutions, the stability of the positive half-cell electrolyte at elevated temperatures is the most critical parameter to be controlled if high vanadium concentrations are to be employed. Recently, a study in which the maximum concentration to operate in a VRFB was evaluate for both the anolyte and the catholyte was reported [15]. In particular, a concentration of about 3.5M V(V) solution in 5–6 M total sulphate/bisulphate concentration appears to be the limiting concentration to be able to remain in the hydraulic flow region and with further increase in V(V) concentration viscosity increases rapidly. Moreover, it was concluded that a 3M V(V) solution in 6M total sulphate/bisulphate may be suitable for the VRFB up to a temperature of about 40 ◦C. It is worth to note that increasing the vanadium concentration to 3M will allow a 50% increase in the energy density compared with the standard 2M solution. The advantages possessed by VRFB can be summarized as follows: (i) VRFB employs the same electrolyte solution in both half-cells, thereby eliminating cross-contamination and electrolyte maintenance problems; (ii) does not require a catalyst for each electrode reaction since the relatively fast kinetics of the vanadium redox couples allow high charge and voltage efficiencies to be obtained; (iii) can be over-charged and deeply discharged, within the limits of the capacity of the electrolytes, as well as being cycled from

any state of charge or discharge, without permanent damage to the cell or electrolytes and (iv) employs vanadium electrolytes with long-life, reducing replacement costs and minimizing waste [16]. For practical applications, however, the VRFB system faces several challenges: (i) despite the above reported efforts to improve the solubility of vanadium, the stability of vanadium ions is determined by many influential factors [17-19] (*i.e.* solution temperature, the concentration of supporting electrolyte, additives), hence low energy density still remains a major challenge for the VRFB system; (ii) the highly oxidizing nature of V(V), which is also a cancerogenic agent, is another challenge in VRFB, since it can cause degradation of the ion-exchange membrane and of the positive electrode material [20]; (iii) Air oxidation of the V(II) ions in the negative half-cell should cause an imbalance between the positive and negative electroactive species and a subsequent loss of capacity. In the light of the above, scientific community focused the attention on the research of alternative aqueous RFB systems, like as bromine-polysulphide battery. The bromine-polysulphide RFB employs NaBr electrolyte in the positive half-cell and Na_2S_4 electrolyte in the negative half-cell [21]. During the charging process, Br^- ions are oxidized to Br_2 and complexed as Br_3^- ions at the positive electrode while the sulphur, present as the soluble polysulphide S_4^{2-} anion, is reduced to sulphide S_2^{2-} ions at the negative electrode. During discharge, the sulphide ion is the reducing agent and the tribromide ion the oxidizing species. The electrode reactions are complex, especially at the negative electrode but may be simplified as follows. At the negative electrode:

$$S_4^{2-} + 2e^- \rightarrow 2S_2^{2-} \qquad \text{(Charge)}$$

$$2S_2^{2-} \rightarrow S_4^{2-} + 2e^- \qquad \text{(Discharge)}$$

At the positive electrode:

$$3Br^- \rightarrow Br_3^- + 2e^- \qquad \text{(Charge)}$$

$$Br_3{}^- + 2e^- \rightarrow 3Br^- \qquad \text{(Discharge)}$$

In contrast to other systems using bromide salts, no complexing agent is required. The open-circuit cell voltage (see Section 3.3) is reported to be 1.74 V in a fully charged state and 1.5 V at a 50% state of charge when operated at 25 °C in 1 M NaBr and 2 M Na_2S_4 [22]. On the other hand, there are a number of technical challenges facing the bromine-polysulphide technology: (i) there is a risk of cross-contamination of the electrolytes due to cross-over of the ionic species through the membrane; (ii) the system encountered the problem of the

build-up of sulphur species either on the electrodes or membrane and therefore over extended cycling there is a net loss of sulphur from the system; (iii) the mixing of the electrolytes can generate heat and toxic gases such as Br_2 and H_2S [16]. An alternative approach in aqueous redox flow battery concerns the employment of organic species. In 2014, the Aziz group [23] and Narayanan group [24] opened the way to this application and proposed the use of a water-soluble, metal-free organic redox couple (*i.e.* quinone-based) in RFBs. Quinone derivatives are attractive because of their low cost with respect to vanadium and their availability from biological processes. The Aziz group chose 9,10-anthraquinone-2,7-disulfonic acid (AQDS) and bromine as anode active material and cathode active material respectively, while the Narayanan group presented an all-quinone based RFB where a solution of 1,2-benzoquinone- 3,5-disulfonic acid (BQDS) and a solution of anthraquinone-2-sulfonic acid (AQS) acted as catholytes and anolytes, respectively. The results on quinone systems suggest that other water-soluble organic molecules should be studied, particularly those that can be produced from natural products [25]. On the other hand, all aqueous RFBs have the same limitation, connected to the narrow electrochemical window of water (~1.23V). Indeed, when the cell is overcharged, the side reactions of hydrogen and oxygen evolution can occur at the negative and positive electrodes, respectively:

$$2H^+ + e^- \rightarrow H_2 \qquad \text{(Negative electrode)}$$

$$2H_2O \rightarrow O_2 + 4H^+ + 4e^- \qquad \text{(Positive electrode)}$$

Gas evolution should be minimised because it can interrupt the electrolyte flow, lead to changes in the pH, increase the cell resistance and, in the case of oxygen evolution, oxidize the carbon electrode (positive half-cell)[16]. Furthermore, since the energy density of a RFB is proportional to both cell voltage and solubility of redox couples (see Section 3.3), the energy density of aqueous RFBs is fundamentally limited.

3.2 Non-aqueous Redox Flow Batteries

Some recent efforts have shifted to developing non-aqueous RFBs to achieve high energy densities due to the wider electrochemical windows (*i.e.* over 5V) of organic solvents, such as acetonitrile, propylene carbonate, dichloromethane and tetrahydrofuran [26]. In general, non-aqueous RFBs employ acetonitrile as organic solvent besides its low boiling point, since has a low viscosity, a high dielectric constant and good compatibility with supporting electrolytes (i.e. tetraethylammonium tetrafluoroborate, $TEABF_4$, Lithium triflate, LiOTf) [27]. A key challenge in battery electrolyte development is to determine the optimal combination of viscosity and dielectric constant to achieve moderate ionic conductivity,

indeed ohmic overpotentials in the solutions, which are the major causes for low energy efficiency, arise from the low conductivity of the electrolyte. The basic concept of non-aqueous RFBs was first proposed by Singh [28]. Then, Matsuda et al. [29] first developed an experimental non-aqueous RFB based on tris(bipyridine)ruthenium(II) tetrafluoroborate complex $[Ru(bpy)_3(BF_4)_2]$ in acetonitrile (AcN) with $TEABF_4$ as supporting electrolyte(Fig.3.3). The expected open circuit voltage (OCV) of this system is approximately 2.6 V, which is higher than those of most aqueous RFBs. However, Ruthenium is a really expensive metal, and the searching for cheaper alternative has attracted attention in recent years. Thompson and co-workers studied three redox systems: vanadium acetylacetonate $[V(acac)_3]$ [30], chromium acetylacetonate $[Cr(acac)_3]$ [31], and manganese acetylacetonate $[Mn(acac)_3]$ [32] (Fig.3.3). However, it was found that the structures of these metal–ligand complexes can undergo dramatic changes as a result of gain or loss of electrons. Indeed, in a study of cyclic voltammogram for $[V(acac)]_3$ in acetonitrile, three redox couples showed redox potential around –1.8, 0.5, and 0.8 V vs. Ag/Ag^+, respectively. The two first redox couples are from the disproportionation of $[V(acac)]_3$, but the third redox couple with an adverse effect on the system has not been unambiguously assigned. As the kinetics of this redox reaction is much less reversible than those related to the disproportionation of $[V(acac)_3]$, the loss of redox-active species in the electrolyte could occur, leading to low coulombic efficiencies (see Section 3.3). Similarly, a side reaction of $[Cr(acac)_3]$ and of $[Mn(acac)_3]$ was found in their application in a lab. scale non-aqueous RFB.

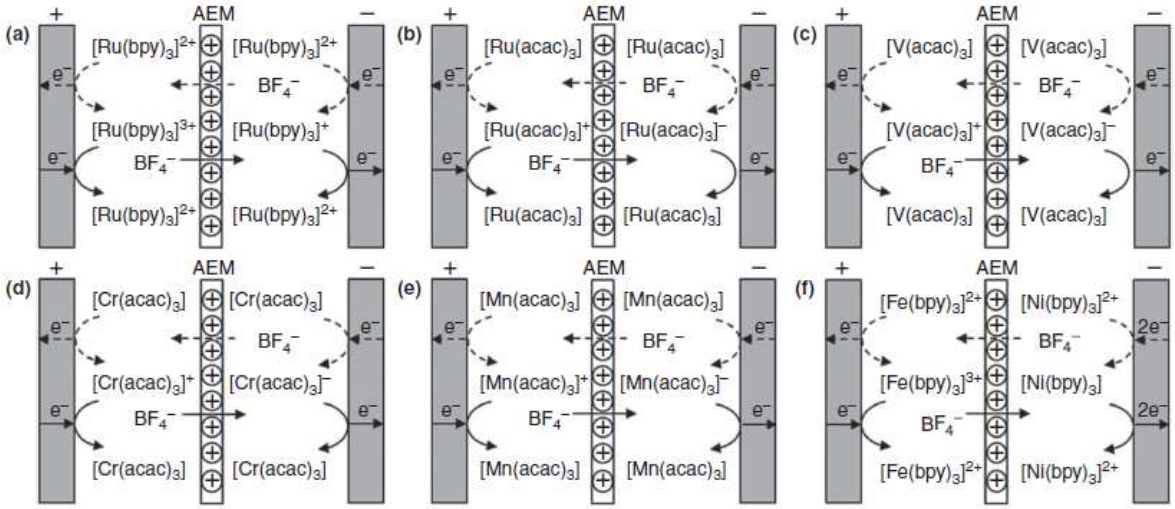

Fig.3.3 Non-aqueous RFB cells: (a) ruthenium bipyridine, (b) ruthenium acetylacetonate, (c) vanadium acetylacetonate, (d) chromium acetylacetonate, (e) manganese acetylacetonate, (f) iron bipyridine/nickel bipyridine.

However, Kim et al. [33] developed a non-aqueous RFBs based on tri(2,2'-bipyridine) nickel(II) tetrafluoroborate [$Ni(bpy)_3(BF4)_2$] as negative couple and tri(2,2'-bipyridine) iron(II) tetrafluoroborate [$Fe(bpy)_3(BF_4)_2$] (Fig. 3.3) as positive couple in propylene carbonate, obtaining coulombic and energy efficiencies near to 90%. This result encourages other groups to follow the same approach. Recently, new redox couples based on polypyridine ligands were explored, and the metals used to construct non-aqueous RFB pairs include especially Fe and Co [34-38]. Armstrong et al. [34] projected a single species redox flow battery employing a new class of cobalt(II) complexes with "tunable" tridentate azole-pyridine type ligands (Fig.3.4). Four structures were synthesised to customise the electrochemistry of the complexes, in order to increase the cell potential.

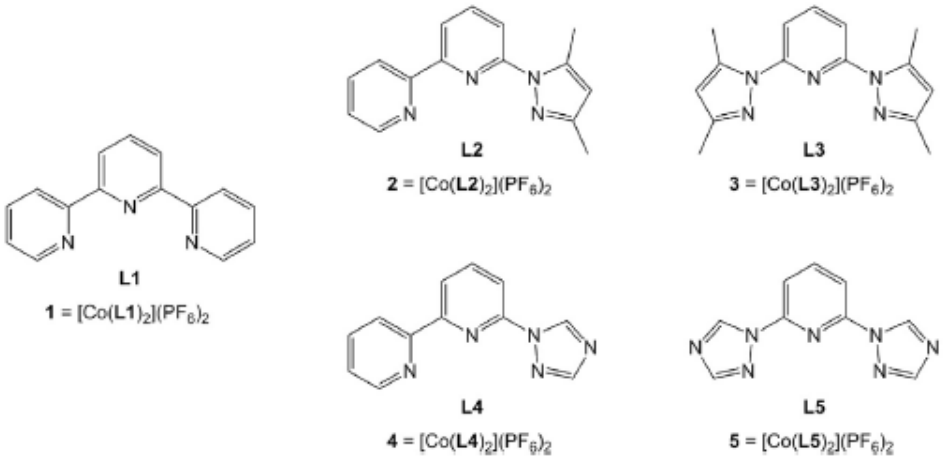

Fig.3.4 Tridentate azole-pyridine type ligands.

The one-electron reaction at the positive electrode is as follows:

$$[Co(II)(L)_2](PF_6)_2 \rightarrow [Co(III)(L)_2](PF_6)_3 + e^- \quad \text{(Charge)}$$

$$[Co(III)(L)_2](PF_6)_3 + e^- \rightarrow [Co(II)(L)_2](PF_6)_2 \quad \text{(Discharge)}$$

While, at the negative electrode:

$$[Co(II)(L)_2](PF_6)_2 + e^- \rightarrow [Co(I)(L)_2](PF_6) \quad \text{(Charge)}$$

$$[Co(I)(L)_2](PF_6) \rightarrow [Co(I)(L)_2](PF_6)_2 + e^- \quad \text{(Discharge)}$$

The open circuit voltage that can be obtained is in the range of 1.06-2.17 V, depending on the structure of the complex and the redox couples utilized. Similarly, Xing et al. [36] developed a redox flow battery employing tris(1,10-phenanthroline) complexes of iron(II) and cobalt(II). The $[Fe(phen)_3]^{2+/3+}$and $[Co(phen)_3]^{+/2+}$ (phen = 1,10-phenanthroline) redox

couples were used as the positive and negative active materials, respectively, in an electrolyte consisting of $TEAPF_6$ and acetonitrile. At the positive electrode:

$$[Fe(II)(phen)_3](PF_6)_2 \longrightarrow [Fe(III)(phen)_3](PF_6)_3 + e^- \quad \text{(Charge)}$$

$$[Fe(III)(phen)_3](PF_6)_3 + e^- \longrightarrow [Fe(II)(phen)_3](PF_6)_2 \quad \text{(Discharge)}$$

At the negative electrode:

$$[Co(II)(phen)_3](PF_6)_2 + e^- \longrightarrow [Co(I)(phen)_3](PF_6) \quad \text{(Charge)}$$

$$[Co(I)(phen)_3](PF_6) \longrightarrow [Co(II)(phen)_3](PF_6)_2 + e^- \quad \text{(Discharge)}$$

The open circuit voltage that can be reached is *ca.* 2V. Besides, in both the examples dealing with cobalt and iron complexes reported above, mostly very diluted (from 0.001 up to 0.01 M) redox couple concentrations were used for the tests in a lab. scale RFB. These conditions are quite far from the real device application. Consequently, inspired by recent works, we synthetized and explored several Iron and cobalt complexes based on polypyridine ligands, with the aim of finding promising candidates for application in high voltage non-aqueous RFBs (**Chapter 6**). Then, we preliminary test the most promising compounds in a lab. scale flow cell at concentration suitable for the employment in a real Redox Flow Batteries. It is worth to notice that reversibility and stability of redox active species are the major challenges in the development of non-aqueous RFBs. The rates of the electrochemical reactions must be rapid on carbon based electrodes, since high rates of reaction and favourable thermodynamics at low values of polarisation during charge and discharge lead to high coulombic, voltaic and energy efficiencies. As a consequence, compounds were selected by considering the electrochemical response of the iron and cobalt couples on carbon-felt based electrodes.

3.3 Redox Flow Battery Parameters

- *Open Circuit Voltage (OCV)*

Open-circuit voltage is the difference of electrical potential between the two terminals of the device when disconnected from any circuit and it can be calculated using equilibrium thermodynamics. For electrochemical systems, such as RFBs, the equilibrium potential at a single redox electrode is predicted using the Nernst equation, which describes the potential difference between the electrolyte and the electrode when there is no net reaction inside the cell, and is defined as follows:

$$E = E^0 + \frac{RT}{nF}\ln\left(\frac{c_{ox}}{c_{red}} \times \frac{\gamma_{ox}}{\gamma_{red}}\right) \quad \text{(Eq.3.1)}$$

where E is the potential difference, and E^0 is the standard reduction potential, calculated using the thermodynamic properties of the global reactions at the given electrode. R is the universal gas constant, T is the absolute temperature, n is the number of equivalents transferred per mole of species reduced or oxidized and F is Faraday's constant. The subscripts *ox* and *red* represent the oxidized and reduced species, respectively. The term, c, represents the ionic concentration, and γ is defined as the activity coefficient of the species, which represents the deviation of an ion from ideal reactivity due to interionic interactions within the solution. However, in a general RFB, the liquid electrolytes are typically well-circulated, yielding negligible interactions among the ions. Therefore, it is reasonable to assume that the activity coefficient (γ) for all species is equivalent to one. The open circuit voltage (OCV) of a RFB cell could be defined as the difference between the equilibrium potentials at each electrode, where the positive and negative electrode potentials depend on the general global reactions given as follows:

$$A^m \rightleftarrows A^{(m+n)} + ne^- \quad \text{(Positive electrode)}$$

$$C^{(b-n)} + ne^- \rightleftarrows C^b \quad \text{(Negative electrode)}$$

$$OCV = E^+ - E^- = E^0 + \frac{RT}{nF}\ln\left[\frac{A^{(m+n)} \times C^b}{C^{(b-n)} \times A^m}\right] \quad \text{(Eq.3.2)}$$

where the superscripts '+' and '−' represent the positive and negative half-cells, and the total standard reduction potential (E^0) is the difference between the positive (E_0^+) and negative (E_0^-) standard reduction potentials. The OCV is commonly determined by cyclic voltammetry experiments, and resulting voltammograms can be also analysed to estimate the redox reversibility in qualitative/quantitative manner. When a net current is flowing through the cell, the equilibrium conditions are not met anymore and the cell potential (V_{cell}) is now given by the difference between the open circuit potential (OCV) and the internal losses (V_{loss});

$$V_{cell} = OCV - V_{loss} \quad \text{(Eq.3.3)}$$

These losses are often called overpotentials and represent the energy needed to force the redox reaction to proceed at the required rate:

$$V_{loss} = \eta_{act} + \eta_{conc} + \eta_{ohm} + \eta_{ion} \quad \text{(Eq.3.4)}$$

Where the activation η_{act} and the concentration η_{conc} overpotentials are electrode phenomena and are respectively associated with the energy required to initiate a charge transfer and with concentration differences between the bulk solution and the electrode surface. While, the ohmic losses η_{ohm} occur in the electrodes, the bipolar plates and the collector plates and the ionic losses η_{ion} occur in the electrolytes and the membranes. Energy density that can be reached by a redox flow battery is a function of the cell voltage(V_{cell}) and concentration of the active species (C_{active}), as follows [34]:

$$\hat{E} \approx n\, V_{cell} C_{active} F/2 \qquad \text{(Eq.3.5)}$$

Where F is the Faraday constant and n is the number of electrons exchanged during the reactions.

- *Efficiency*

A RFB converts chemical energy stored in the electrolytes into a discharge electronic current $I = I_{discharge}$ at a voltage $V = V_{discharge}$ for a time $\Delta t = \Delta t_{discharge}$, and, subsequently, restores the chemical energy by the application of a charging current I_{charge} at a voltage V_{charge} over a time Δt_{charge}. Efficiencies are parameters used to assess the performance of storage systems. The energy efficiency η_{energy} is the ratio of the energy furnished by the battery during the discharge to the energy supplied during the charge:

$$\eta_{energy} = \frac{\int_0^{\Delta t} P_{discharge}\, dt}{\int_0^{\Delta t} |P_{\ charge}| dt} \qquad \text{(Eq.3.6)}$$

While, the coulombic efficiency $\eta_{coulombic}$ is a measure of the ratio of the charge withdrawn from the system $Q_{discharge}$ during the discharge to the charge Q_{charge} supplied during the charge:

$$\eta_{coulombic} = \frac{Q_{discharge}}{Q\ charge} = \frac{\int_0^{\Delta t} I_{discharge}\, dt}{\int_0^{\Delta t} |I_{\ charge}| dt} \qquad \text{(Eq.3.7)}$$

The voltaic efficiency $\eta_{voltaic}$ is ganerally defined for a charge and discharge cycle at constant current. It is a measure of the ohmic and polarisation losses during the cycling and it can be calculated by the ratio of the integral of the cell potential during the discharge $V_{discharge}$ to that of the potential V_{charge} during the charge:

$$\eta_{voltaic} = \frac{\int_0^{\Delta t} V_{discharge}\, dt}{\int_0^{\Delta t} |V_{\ charge}| dt} \qquad \text{(Eq.3.8)}$$

3.4 References.

1) Q. Huang, W. Huang, Y. Kim, *Chempluschem* **2015**, *80*,312;

2) G. Kear, A.A. Shah, F.C. Walsh, *Int. J. Energy. Res.* **2012**, *36*, 1105;

3) J.Liu, B. Lin, *National Science Review* **2015**, *4*, 91;

4) N. Akira, K. Hiroko and N. Ken, *Denki Kagaku oyobi Kogyo ButsuriKagaku*, **1993**, *61*, 1442;

5) D. S. Aaron, Q. Liu, Z. Tang, G. M. Grim, A. B. Papandrew, A.Turhan, T. A. Zawodzinski and M. M. Mench, *J. Power Sources*, **2012**, *206*, 450;

6) M. Skyllas-Kazacos and F. Grossmith, *J. Electrochem. Soc*., **1987,** *134*, 2950;

7) P. Arora and Z. Zhang, *Chem. Rev*., **2004**, *104*, 4419;

8) G. J. Hwang and H. Ohya, *J. Membr. Sci*., **1997**, 132, 55;

9) D. G. Oei, *J. Appl. Electrochem*., **1985**, *15*, 231;

10) W. Grot, *Fluorinated ionomers, ed. William Andrew Inc*., **2008**, Vol. 978, pp. 10;

11) X. F. Li, H. M. Zhang, Z. S. Mai, H. Z. Zhang, I. Vankelecom, *Energy Environ. Sci*., **2011**, *4*, 1147;

12) E. Sum and M. Skyllas-Kazacos, *J. Power Sources*, **1985**, *15*, 179;

13) E. Wesoff, J.S. John, Largest capacity Flow Battery in North America and EU is on-line and commissioned. http://www.greentechmedia.com/ articles/read/Largest-Capacity-Flow-Battery-in-NorthAmerica-and-EU-is-Online-and-Commiss;

14) M. Skyllas-Kazacos, M. Kazacos, *Journal of Power Source,s* **2011**, *196*, 8822;

15) F. Rahman, M. Skyllas-Kazacos*, Journal of Power Sources* **2009***, 189,* 1212;

16) C.Walsh et.al. *RSC Advances*, **2012**, *2*, 10125;

17) F. Rahman and M. Skyllas-Kazacos, *J. Power Sources*, **1998**, *72,* 105;

18) M. Skyllas-Kazacos, C. Peng and M. Cheng, *Electrochem. Solid-State Lett*., **1999**, *2*, 121;

19) F. Rahman and M. Skyllas-Kazacos, *J. Power Sources*, **2009**, *189*, 1212;

20) M. Skyllas-Kazacos, M. H. Chakrabarti, S. A. Hajimolana, F. S. Mjalli and M. Saleem, *J. Electrochem. Soc*., **2011**, *158*, R55;

21) C. Ponce de Leo´n, A. Frı´as-Ferrer, J. Gonza´lez-Garcı´a, D. A. Sza´nto and F. C. Walsh, *J. Power Sources*, **2006**, *160*, 716;

22) R. J. Remick and P. G. P. Ang, US 1984/4485154, 27 Nov 1984, 1984.

23) B. Huskinson, M.P.Marshak, C. Suh et al. *Nature* **2014**, *505*, 195;

24) B.Yang, L. Hoober-Burkhardt, F. Wang et al. *J Electrochem Soc* **2014**, *161*, A1371;

25) T. Janoschka, N. Martin, U. Martin et al. *Nature* **2015**, *527*, 78;

26) X. Liang, Z.Y. Wen, Y. Liu, H. Zhang, J. Jin, M.F. Wu, X.W. Wu, *J Power Sources* **2012**, *206*, 409;

27) K.Gong. et al. *Energy Environ. Sci.*, **2015** ,*8*, 3515;

28) P. Singh, *J Power Sources* **1984**, *11*, 135;

29) Y. Matsuda, K. Tanaka, M. Okada, Y. Takasu, M. Morita, T. Matsumura- Inoue, *J Appl. Electrochem*. **1988**, *18*, 909;

30) Q. Liu Q, A.E.S. Sleightholme, A.A. Shinkle, Y. Li, L.T. Thompson, *Electrochem Commun* **2009**, *11*, 2312;

31) Q.H. Liu, A.aA. Shinkle, Y.D. Li, C.W. Monroe, L.T. Thompson, A.E.S. Sleightholme AES *Electrochem Commun* **2010**, *12*, 1634;

32) A.E.S. Sleightholme, A.A. Shinkle, Q.H. Liu, Y.D. Li, C.W. Monroe, L.T. Thompson, *J Power Sources* **2011**, *196*, 5742;

33) J.H. Kim, K.J. Kim, M.S. Park, N.J. Lee, U. Hwang, H. Kim, Y.J. Kim YJ, *Electrochem Commun* **2011**, *13*, 997;

34) C.G. Armstrong, K.E. Toghill, J. *Power Sources* **2017**, *349*, 121;

35) X. Xing, D. Zhang, Y. Li, *J. Power Sources* **2015**, *279*, 205;

36) X. Xing, Y. Zhao, Y. Li, *J. Power Sources* **2015**, *293*, 778;

37) Yu Ding et al., *Energy Environ. Sci.* **2017**, *10*, 491;

CHAPTER 4. ON THE STABILITY OF MANGANESE COMPLEXES AS REDOX MEDIATORS IN DSSCs.

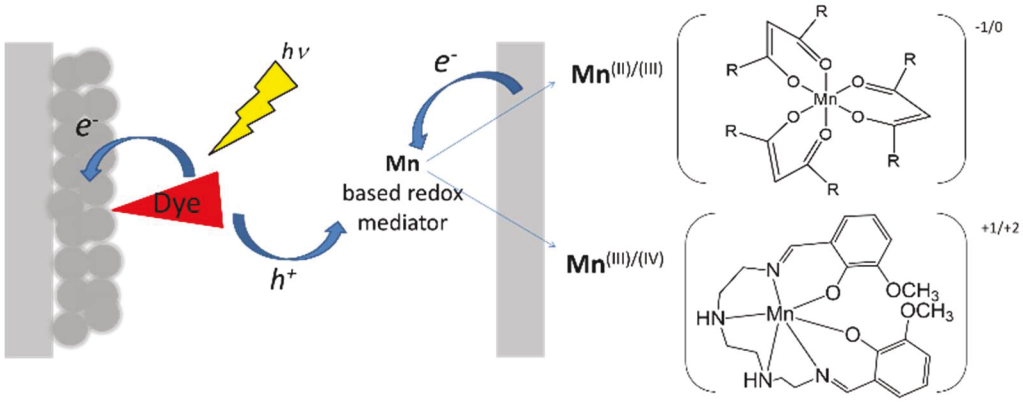

Fig.4.1 Scheme of a DSSC constituted by an organic dye and redox mediators based on manganese complexes.

In the present Chapter the photoelectrochemical properties and stability of dye sensitized solar cells containing Mn(β-diketonato)$_3$ complexes, [Mn^{III}(acac)$_3$] **1** (acac = acetylacetonate), [Mn^{III}(CF2)$_3$] **2** (CF2 = 4,4'-difluoro-1-phenylbutanate-1,3-dione), [Mn^{III}(dbm)$_3$] **3** (dbm = dibenzoylmethanate), [Mn^{II}(CF2)$_3$]TBA (TBA = tetrabutylammonium) **4** and [Mn^{II}(dbm)$_3$]TBA **5**, have been evaluated. At room temperature, the complexes undergo ligand exchange with 4-*tert*-butyl-pyridine (TBP), an additive commonly used in solar devices to reduce charge recombination at the photoanode. An increased device stability was achieved by using the Z907 dye and passivating the photoanode with short chain siloxanes. It was also found that the Mn(II)/(III) couple is involved in the dye regeneration process, instead of Mn(III)/(IV) ($E_{1/2}$ > 1V Vs SCE), previously indicated in the literature. In addition, a new Manganese encapsulating complex [Mn(L1)]OTf (where L1= (3-methoxy-sal-(N-1,4,7,10) and OTf= trifluoromethansulfonate anion)**6**, which is stable in TBP, was synthetized and tested in dye sensitized solar cell devices.

4.1 Introduction

As previously reported, with the milestone paper of Grätzel and O'Regan, Dye-Sensitized Solar Cells (DSSCs) have emerged as a realistic solution for harnessing the energy of the Sun and converting it into electricity [1]. An impressive amount of work has been carried out in order to improve the photoconversion efficiency (PCE), trying to optimize the sensitizer, and, in the last few years, the redox mediators [2-3]. Until recently, the most

efficient DSSCs were based on polypyridyl ruthenium complexes as dye and the iodide/triiodide couple (I^-/I_3^-) as electrolyte [4]. I_3^-/I^- redox couple is an ideal candidate to balance the dual kinetic constraint of fast dye regeneration and slow charge recombination. However, this redox couple has a list of undesirable chemical properties, such as a too negative redox potential, a darkly colouring of I_3^- limiting the light harvesting efficiency of the dye, corrosiveness and volatility of I_2 in equilibrium with I_3^- complicating long-term cell sealing and therefore hampering long-term stability [5-6]. Starting from 2000 the search for alternative electron mediators has become an active field of research, exploring the properties of redox tunable transition metal complexes based on Fe(III)/(II) [7-8], Co(III)/(II) [9-10], Ni(IV)/(III)[11] and Cu(II)/(I) [12-13], as well as on organic molecules like TEMPO [14], and thiolate/disulfide [15]. It was observed that when used in conjunction with specific dye architectures, some of these redox couples allowed to obtain considerably high solar cell efficiencies [16-17]. In particular, the most promising $Co^{2+/3+}$ complexes have addressed some of the problems related to the employment of the I^-/I_3^- couple, since they are outer-sphere one-electron redox systems with low molar extinction coefficients and more positive and tunable redox potentials, affording large V_{OC} [18-19]. Nevertheless, $Co^{2+/3+}$ complexes bring some issues associated with their stability and slow mass transport in the electrolyte solution. Among first row transition metals, Manganese can be considered interesting candidate for the variety of accessible redox states, low toxicity and abundance. The first example of application was reported in 2014 by Spiccia et al., which focused on DSSCs containing the commercially available $[Mn(acac)_3]^{0/+1}$ (acac = acetylacetonate) in conjunction with MK2 organic dye, (Fig.4.2), reporting an energy conversion efficiency of 4.4% [20].

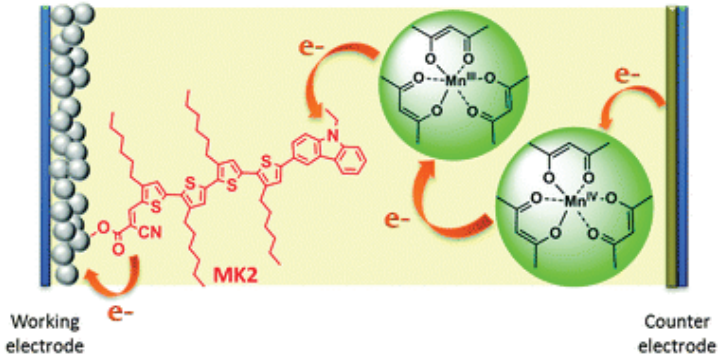

Fig.4.2 Scheme of a DSSC which employs new $[Mn(acac)_3]$ redox mediator in conjunction with MK2 dye [20]

Following that report a series of tris-(β-diketonato) manganese complexes (Fig.4.3), namely $[Mn^{III}(CF2)_3]$ **2** (CF2 = 4,4'-difluoro-1-phenylbutanate-1,3-dione), $[Mn^{III}(dbm)_3]$ **3** (dbm =

dibenzoylmethanate), have been prepared with the aim of comparing their properties to $[Mn^{III}(acac)_3]$ **1**. Complex **2** was synthesized to boost V_{OC} thanks to its more positive potential due to the presence of electron withdrawing groups, and complex **3** was synthesized in order to enhance stability through the presence of bulky substituents. The study revealed that Mn(III)/(II) is the relevant redox couple involved in dye regeneration process and for this reason the corresponding Mn(II) complexes $[Mn^{II}(CF2)_3]$TBA **4** and $[Mn^{II}(dbm)_3]$TBA **5** (TBA = tetrabutylammonium) were synthesized (Fig.4.3). The corresponding Mn(II) complex with unsubstituted ligands $[Mn^{II}(acac)_3]$TBA was not stable and oxidized after exposure to air, consequently it was not characterized in the present work. In addition, the study showed that all species are unstable, at room temperature, with respect to ligand exchange with 4-*tert*-butyl-pyridine (TBP), an additive normally used to reduce charge recombination [21]. A new Manganese complex $[Mn^{III}(L1)]$OTf (where L1= (3-methoxy-sal-(N-1,4,7,10)) **6** with an encapsulating ligand was studied to improve stability of the device.

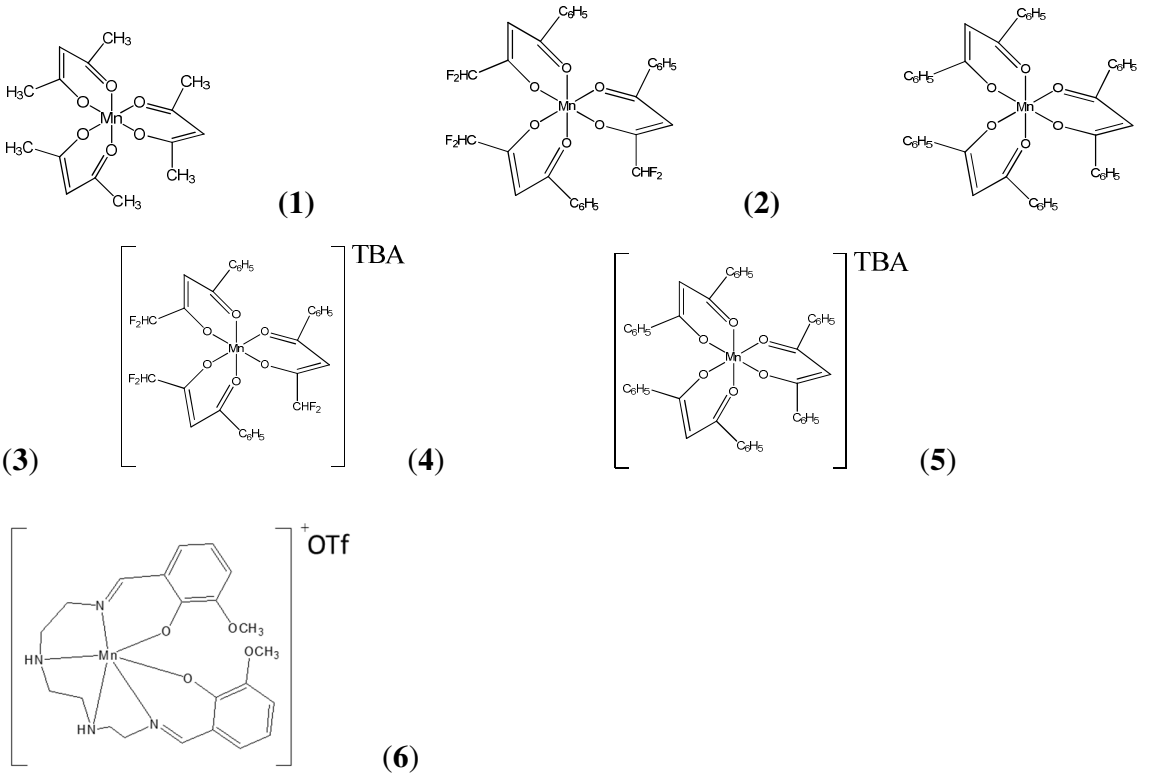

Fig.4.3 Mn complexes

4.2 Experimental Section

4.2.1. Materials and Methods

All chemicals were Sigma Aldrich products and were used as received. Conductive FTO (fluorine tin oxide) TEC8, 2.3 mm thick substrates (Pilkington) were carefully cleaned by several washings in ethanol, acetone, and Alconox followed by annealing at 450 °C in air before use. TiO_2 colloidal paste (DSC 18NR-T) was purchased from Dyesol. Mass spectrometry was performed in ESI mode with a Finningan LCQ Duo Ion Trap (Capillary Temp: 250 °C, Infusion flow rate: 18 μL/min, Sheath gas flow rate: 20 AU), or with a Waters Micromass ZQ 2000 (Cone Temperature 110°C and desolvation Temperature of 130°C, Capillary voltage 2.30 KV, Cone Voltage 20 V, Extractor Voltage 3V and RF Lens Voltage 0.3V, Flow rate 295 L/hr) under positive/negative mode acquisition. Cyclic Voltammetry plots were collected in a standard three-electrode cell with an Autolab PGSTAT302N potentiostat at a scan rate of 100 mV s^{-1} with a standard calomel electrode (SCE) as reference (Amel), a Pt wire as auxiliary (Sigma-Aldrich), and a glassy carbon as working electrode. Absorption spectra were collected with a JASCO V-570 UV–Vis spectrophotometer.

4.2.2. Synthesis of Mn(III) acetylacetonate complexes.

A stirred solution of Manganese(III) acetate dihydrate ($Mn(CH_3COO)_3 \times 2H_2O$) (0.74 mmol) in toluene (25 mL) was treated with an excess of the ligand (CF2 or dbm) (4.93 mmol). The mixture was heated under stirring for 6 hours, cooled to room temperature and the solvent was removed with a rotavapor. The residue was dissolved in the minimum amount of diethyl ether and *n*-hexane was added until a green to brown solid separated. After several hours the precipitate was filtrated under vacuum and washed several times with *n*-hexane. Yields were in the range of 50÷60%. **2**: *m/z* (ESI): 449 $[Mn(CF2)_2]^+$ calculated for $C_{30}H_{21}F_6MnO_6$: 646.2; ε_{560} (M^{-1} cm^{-1}): 216. **3**: *m/z* (ESI): 501 $[Mn(dbm)_2]^+$ calculated for $C_{45}H_{33}MnO_6$: 724.2; ε_{560} (M^{-1} cm^{-1}): 170.

*4.2.3 Synthesis of **4**.*

A stirred solution of Manganese(II) acetate tetrahydrate ($Mn(CH_3COO)_2 \times 4H_2O$) (1 mmol) in methanol (25 mL) and tetrabutylammonium hexafluorophosphate ($TBAPF_6$) (1 mmol) was treated, at room temperature, with a solution of CF2 (3 mmol) in the minimum amount of methanol. The yellow/orange solid was separated by filtration under vacuum and washed several times with cold methanol. Yield was in the order of 50%. *m/z* (ESI): 646 $[Mn(CF2)_3]^-$ calculated for $C_{30}H_{21}F_6MnO_6$: 646.2; ε_{450} (M^{-1} cm^{-1}): 370.

*4.2.4 Synthesis of **5**.*

Dbm (3 mmol) was added to a stirred solution of tetrabutylammonium hydroxide (TBAOH) (3 mmol, 30% mol in methanol) in methanol (25 mL). The stirred solution was treated, at room temperature, with a Manganese(II) chloride hexahydrate ($MnCl_2 \times 6H_2O$) (1 mmol) dissolved in the minimum amount of methanol. The yellow/orange solid was separated by filtration under vacuum and washed several times with cold methanol. Yield was in the order of 60%. *m/z* (ESI): 724 $[Mn(dbm)_3]^-$; calculated for $C_{45}H_{33}MnO_6$:724.2; ε_{450} (M^{-1} cm^{-1}): 273.

*4.2.5 Synthesis of **6**.*

Complex **6** was synthesized following a procedure reported in literature [22]: to an ethanol solution containing 2 mmol of o-vanillin was added 1 mmol of triethylenetetramine. The yellow solution was brought to reflux for 20 min and then cooled to room temperature (r.t.), followed by the dropwise addition of 1 mmol of Manganese (II) triflate hexahydrate ($Mn(OTf)_2 \times 6H_2O$) dissolved in ethanol. The resulting brownish black solution was heated up to 60°C for 30 min and the final product was obtained by evaporation under vacuum. **6** was purified by dissolving the solid in a minimum amount of acetonitrile, followed by precipitation with diethyl ether. The yield was in the order of 80%. *m/z* (ESI): 467 $[Mn(L1)]^+$; ε_{412} (M^{-1} cm^{-1}): 247.

4.2.6 Preparation of Solar cells.

A compact TiO_2 blocking underlayer was prepared by spin-coating a 0.3 M titanium tetraisopropoxide solution in 1-butanol (1000 rpm for 10 s, 2000 rpm for 20 s) onto FTO substrates. Then the substrates were heated at 500 °C for 15 min. The blocking underlayer was applied to limit recombination rates of the injected electrons with the electrolyte at the highly conductive FTO interface. Mesoporous titania films (ca. 6 μm thick) were prepared by blading a commercial 400-nm nanoparticle colloidal TiO_2 paste on FTO electrodes. After the TiO_2 deposition, the electrodes were heated up to 500°C, following a programmed temperature ramping: 25−120 °C (10 min), 120−450 °C (30 min), 450 °C (20 min), 450−500 °C (10 min), 500 °C (10 min). The sintering process regulates parameters such as the contact between interconnected nanoparticles and their coordination in the porous TiO_2 network, enhancing the film conductivity. The resulting transparent films were immersed in a 0.4 M Titanium tetrachloride ($TiCl_4$) solution for 12 hours, in order to improve the active area, owing to the $TiCl_4$ hydrolysis on the TiO_2 substrate. In the end the electrodes were rinsed with water and heated at 450 °C for 30 minutes

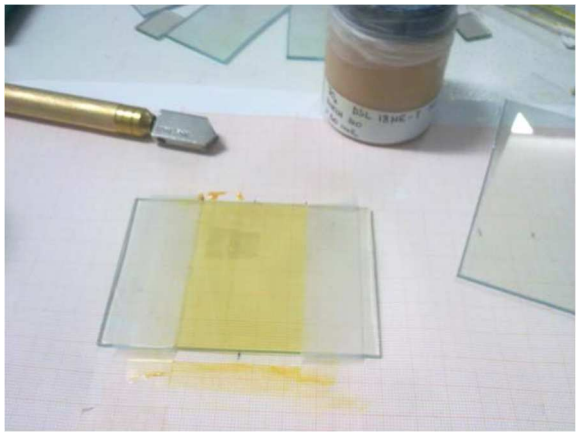

Fig.4.4 TiO_2 photoanodes preparation with FTO conductive glass.

Finally, the photoanodes were immersed in a 0.2 mM solution of MK2 [25] (Fig.4.5 a) in a 1:1 toluene/acetonitrile mixture, in a 0.5mM solution of D35 [24] (Fig.4.5 b) or in a 0.3 mM solution of Z907 [23] (Fig.4.5 c) in ethanol for 24 hours at room temperature.

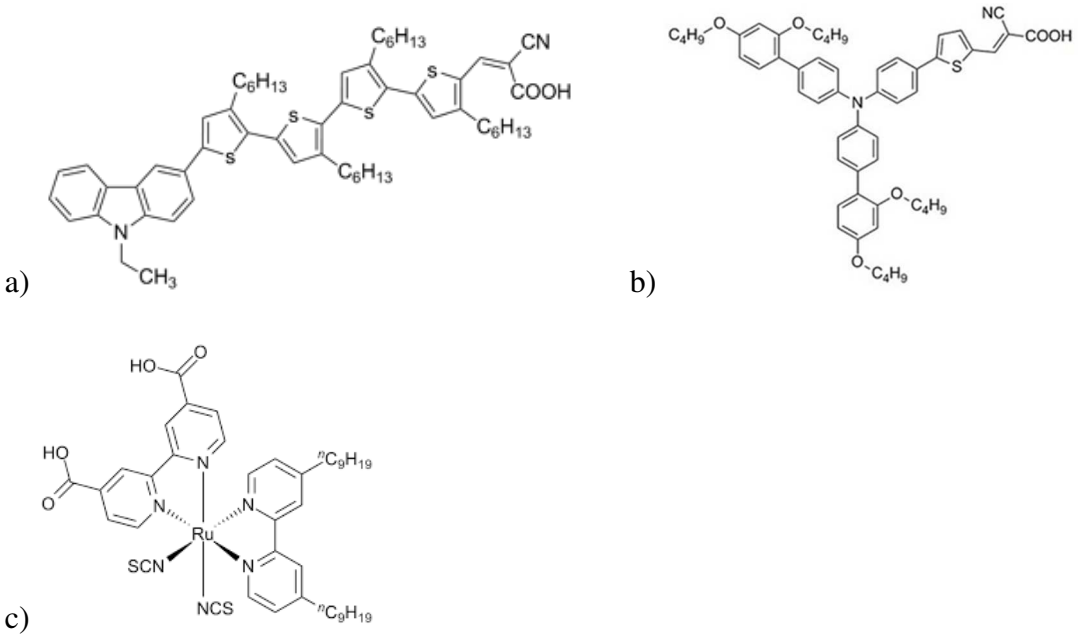

Fig.4.5 a) Dye MK2; b) Dye D35; c) Dye Z907

After the adsorption of Z907 dye overnight, photoanodes were immersed in a 10^{-3}M solution of (3-Aminopropyl)triethoxysilane (APTS) in toluene at 60°C for 1h, in order to post functionalize TiO_2 surface with short chain siloxanes that were found to successfully screen the semiconductor surface from electron acceptors in the electrolyte [26]. Solar cells were assembled by holding the sensitized photoanode and a PEDOT-modified FTO counter electrode together with metallic clamps and by using a 25 μm thick spacer (Surlyn®-DuPont). PEDOT (poly(3,4-ethilenedioxythiophene)) counter electrodes were prepared by

electrodeposition on FTO glasses through cyclic voltammetry technique, scanning 2 times from 0 to 1,7 V vs SCE at 20 mV/s in a 10^{-2} M 3,4-ethylenedioxythiophene (EDOT) /0.1 M Lithium perchlorate ($LiClO_4$) acetonitrile solution [27].

4.2.7 Solar Cell Characterization.

Current−voltage measurements were performed with an Autolab PGSTAT302N potentiostat at a scan rate of 10 mV s^{-1} by linear sweep voltammetry (LSV). Cell performances were evaluated under AM 1.5G illumination (ABET sun simulator). Electrochemical impedance spectroscopy (EIS) of **5**, **4** mediated solar cells under AM 1.5G was recorded with an Autolab PGSTAT302N potentiostat by using a 10mV sinusoidal perturbation in the 10^5–10^{-2} Hz frequency range. The DC potential was sampled along the ascending branch of the J-V curve with an interval of 20 mV starting from V_{OC}. Impedance data were analyzed using commercially available Z-View software and were fitted with the simplified equivalent electric circuit reported in Scheme 4.1, where the R2-CPE1 mesh describes the TiO_2/electrolyte electrochemical interface (see Chapter 8), Ws1 represents the short Warburg diffusion element and R3-CPE2 stands for the counter electrode/electrolyte interface (R_{CE}). The non-ideal capacitances of the electrochemical interfaces are described by constant phase elements (CPE) with exponents in the range 0.95±0.05. Typical maximum errors from fits were <10 %.

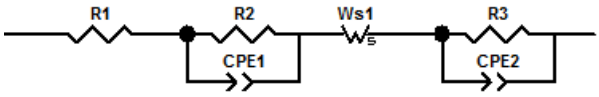

Scheme 4.1: electric model used to fit experimental EIS data.

TiO_2 charge transfer and chemical capacitance weere plotted against the voltage drop occurring at the TiO_2 interface (V_{TiO2}) calculated by $V_{TiO2} = V_{app}$-IR and $R = R_S + R_{CE} + R_D$ where R_S, R_{CE}, and R_D are the ohmic, counter electrode charge transfer, and diffusional resistances respectively and I is the photocurrent recorded at the given voltage V_{app}.

4.2.8 Stability tests.

Stability tests were carried out in acetonitrile solutions containing 0.1 M $LiClO_4$ and a 0.15 M concentration of the selected Mn complex, either $[Mn^{III}(acac)_3]$ **1** or $[Mn^{III}(CF2)_3]$ **2**, or $[Mn^{III}(L1)]OTf$ **6**. In the case of $[Mn^{III}(dbm)_3)]$ **3** (0.13 M) DMF/0.1 M $LiClO_4$ was used. Each solution was treated with an excess of TBP (3.3 equivalents). The resulting solutions were stored in the dark at room temperature. Spectra were recorded by diluting the mother

solutions with acetonitrile to a nominal final concentration of 1.2×10^{-4} M of the initial Mn complex.

4.2.9 Crystallization of complexes.

Dark-green crystals of *fac*-[Mn(CF2)$_3$] **2** were obtained by slow evaporation of the solvent from a 0.15M solution in AcN. Yellow/orange crystals spontaneously separated by the electrolyte solution after two weeks or 24 hours for *trans*-[Mn^{III}(acac)$_2$TBP$_2$]ClO$_4$ and *trans*-[Mn^{II}(CF2)$_2$TBP$_2$]^0 respectively.

4.2.10 Crystallography.

The crystal data of compounds *fac*-[Mn(CF$_2$)$_3$] **2**, *trans*-[Mn^{III}(acac)$_2$-TBP$_2$]ClO$_4$ and *trans*-[Mn^{II}(CF2)$_2$TBP$_2$]^0 were collected at room temperature using a Nonius Kappa CCD diffractometer with graphite monochromated Mo-Ka radiation. The data sets were integrated with the Denzo-SMN package [28] and corrected for Lorentz, polarization and absorption effects (SORTAV) [29]. The structures were solved by direct methods using the SIR9746 system of programs and refined using full-matrix least-squares with all non-hydrogen atoms anisotropically and hydrogens included on calculated positions, riding on their carrier atoms. All calculations were performed using SHELXL-97 [30] and PARST [31] implemented in the WINGX [32] system of programs. The figures have been drawn using the program ORTEP.50. The crystal data are given in the Appendix A.

4.3. Results and Discussion

Tris-(β-diketonato) Mn(III) complexes are generally prepared by treatment of an aqueous solution of potassium permanganate with acetylacetone, following a procedure reported in literature [35-36]. Attempts to prepare **2** and **3,** in high yields, with this method however failed and the two complexes were obtained by treating a solution of Mn(III) acetate with an excess of the respective ligand in hot toluene. The divalent manganese complexes **4** and **5** were easily prepared in high yields by mixing the appropriate ligand with a Mn^{II} precursor in methanol at room temperature. All products were characterized by ESI mass, UV/Vis spectroscopy and cyclic voltammetry. The *fac*-[Mn(CF2)$_3$] **2** complex was crystallized in the trigonal *R-3* space group with the central Mn(III) on the crystallographic special position *3*, therefore displays a C_3 symmetry where the three equivalent CF2 ligands exhibit Mn1-O1 and Mn1-O2 distances of 1.978(2) and 1.995(2) Å, respectively (Fig.4.6, Table A1a and b, Appendix A). The complex, which shows a slight distorted octahedral geometry, does not display the typical Jahn-Teller distortion reported for **1** and **3** [36-37].

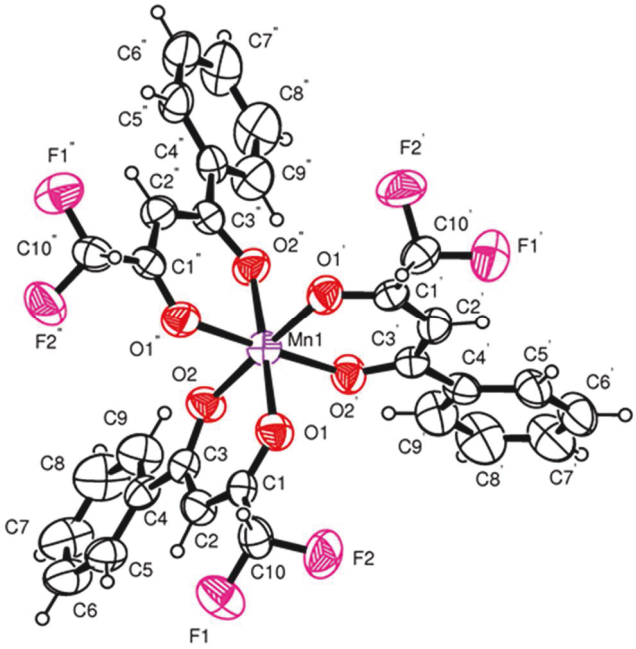

Fig.4.6 ORTEP drawing of **2**

Mass characterization of the commercially available $[Mn^{III}(acac)_3]$ **1** has previously been performed by electron ionization (EI) [38], matrix-assisted laser desorption/ionization time-of-flight mass spectrometry (MALDI-TOFMS) [39] and electrospray ionization ESI [40]. Generally manganese(III) tris(acetylacetonato) exhibits the same dominant fragmentation, namely, the loss of a single ligand yielding the base peak $[Mn(acac)_2]^+$. The ESI spectrum of the commercial $[Mn^{III}(acac)_3]$ **1** obtained in our conditions is reported in Figure A1a (Appendix A). As expected, the main peak is relative to $[Mn(acac)_2]^+$ (*m/z* = 253), but it can be observed also the solvent-complex $[Mn(acac)_2AcN]^+$ (AcN = acetonitrile) (*m/z* = 274), the molecular cationic radical $[Mn(acac)_3]^{\bullet+}$ (*m/z* = 352) and the sodium adduct $[Mn(acac)_3 + Na]^+$ (*m/z* = 375). A similar fragmentation pattern was observed for **3** (Fig.A1c, appendix A). ESI mass of Mn(II) complexes **4** and **5** was detected in negative ion mode, showing the molecular anions $[Mn(CF2)_3]^-$ and $[Mn(dmb)_3]^-$ as the most intense signals (Fig.A1d, e, Appendix A). The electronic absorption spectra of Mn(III) and Mn(II) complexes (Fig.4.7), show the typical d-d transitions at wavelengths > 450 nm, with maximum molar extinction coefficients of ca 250 M^{-1} cm^{-1} for Mn (III) and 400 M^{-1} cm^{-1} for Mn(II) species.

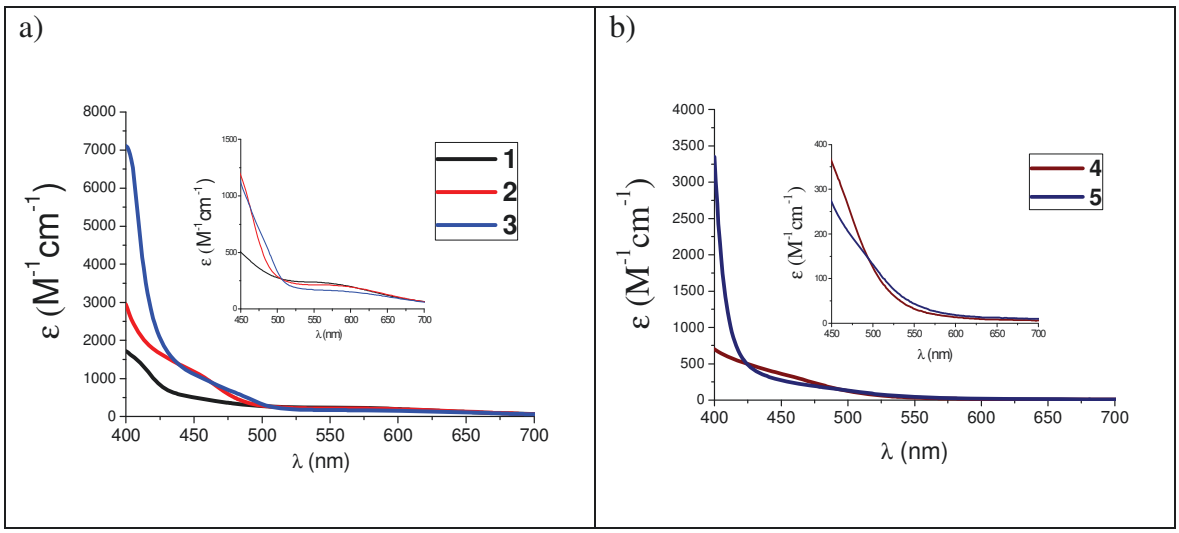

Fig.4.7 Visible spectra of a) **1**,**2**,**3**,**6** and b) **4**,**5** complexes.

The electrochemistry of Mn complexes **1**, **2**, **3** has been studied by cyclic voltammetry (CV). CVs were collected by employing a glassy carbon as working electrode (WE), a Pt wire as counter electrode (CE) and a saturated calomel electrode as reference (SCE). Relevant voltammetric data are reported in Fig.4.8 and in Table 4.1.

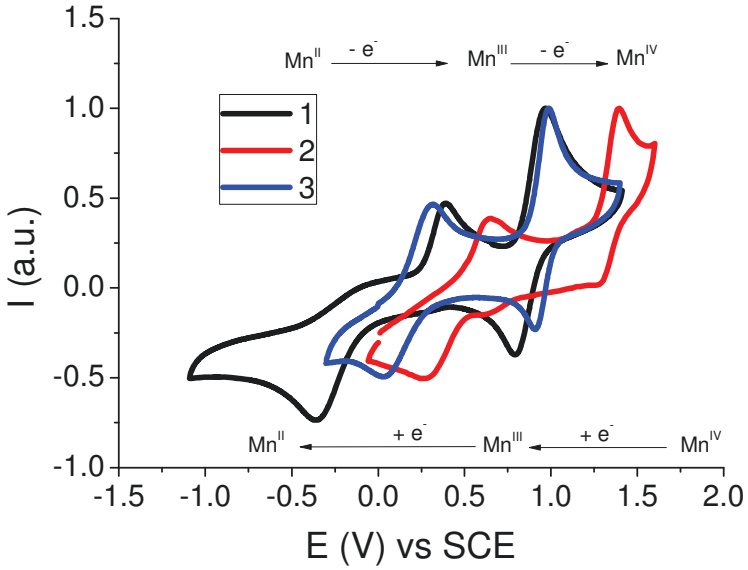

Fig.4.8 CV of **1**, **2**, **3** in 0.1M $LiClO_4$/AcN solution (scan rate 100mVs^{-1}).

All acetylacetonate CVs are characterized by two redox waves corresponding to the oxidation of Mn(III) to Mn(IV), with $E_{1/2}$ in the range of +0.8 to +1.4 V vs SCE, and to the reduction of Mn(III) to Mn(II) in the potential range of 0 to 0.5 V vs SCE. The latter process of **1** and **2** is electrochemically irreversible, showing a large peak indicating a huge inner sphere contribution to electron transfer, which is a consequence of the lack of ligand field stabilization for the Mn(II) high spin d^5 configuration; while the (IV)/(III) process is *quasi-*

reversible with a ΔE of 180 and 110mV respectively [41]. On the contrary, complex **3** presents a reversible ((IV)/(III)) and a *quasi*-reversible ((III)/(II)) processes which indicate its faster kinetic on glassy carbon, probably due to steric hindrance associated to six phenyl substituents which minimize reorganization energy.

Table 4.1. Relevant data obtained from CV analysis of **1**, **2**, **3** (potentials are referred to SCE).

	$Mn^{II} \rightarrow Mn^{III}$				$Mn^{III} \rightarrow Mn^{IV}$			
	E_{pc} (V)	E_{pa} (V)	ΔE (mV)	$E_{1/2}$ (V)	E_{pc} (V)	E_{pa} (V)	ΔE (mV)	$E_{1/2}$ (V)
1	-0.37	0.39	760	0.01	0.79	0.97	180	0.88
2	0.26	0.64	380	0.45	1.28	1.39	110	1.33
3	0.00	0.139	139	0.07	0.93	0.99	60	0.96

A preliminary analysis was carried out by recording (Current-voltage) *J-V* plots of MK2 sensitized solar cells containing **1** and **2** as redox mediators in AcN solution. Complex **3** was only slightly soluble in AcN, preventing the comparison with the other two mediators at concentration levels of the order of 0.15 M. Furthermore, the use of an alternative solvent like as Dimethylformamide (DMF), was prevented by the fast desorption phenomenon of MK2 dye in the presence of this solvent. For these reasons, MK2 sensitized solar cells were only tested with the redox mediators **1** and **2** in the presence (Fig.4.9 A, B) and in the absence (Fig.4.9 C, D) of TBP additive which guarantees a negative shift of the semiconductor *quasi*-Fermi level and a decreased recombination rate between photoinjected electrons and the oxidized form of the electron mediators. We would like to point out that extremely high recombination was detected in the absence of photoanode passivation and almost no photocurrent and photovoltage were recorded in DSSCs containing Mn(IV)/(III) species without adding TBP (Fig.4.9 C, D). While, in presence of TBP, overall efficiencies η% of the order of 2.36(**1**) and 2.72(**2**) were obtained. Corresponding short circuit photocurrent densities (J_{sc}), open circuit voltages (V_{OC}) and fill factors (FF) are reported in Table 4.2.

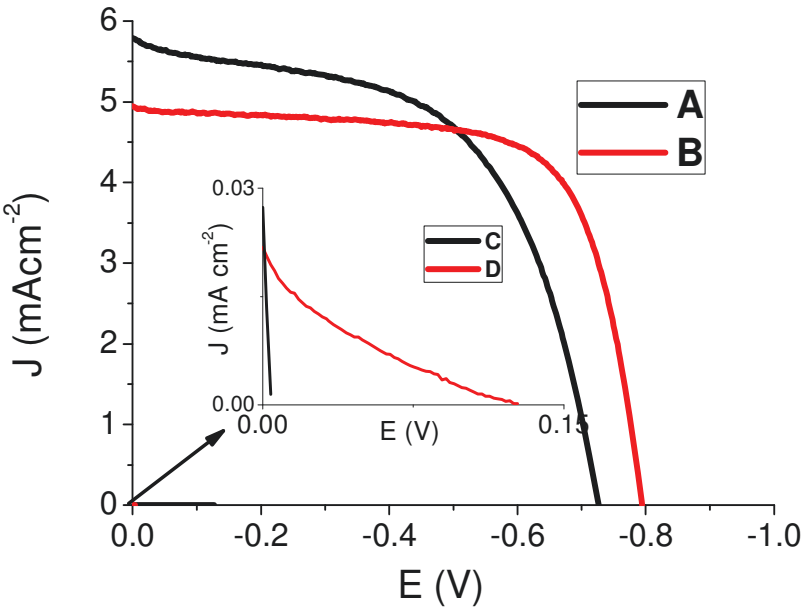

Fig.4.9 J-V plots of A- 0.165M **1**; B- 0.165M **2** in 0.1M LiOTf/AcN, 0.5M TBP, 0.015M $NOBF_4$ and C- 0.165M **1**; D- 0.165M **2** in 0.1M LiOTf/AcN, 0.015M $NOBF_4$.

Table 4.2 Relevant photoelectrochemical data obtained from the J-V plots reported in Figure 4.9 Electrolyte composition: 0.165M **1** or **2** , 0.5M TBP, 0.1M LiOTf, 0.015M $NOBF_4$ in AcN.

	J_{sc} (mA cm^{-2})	**V_{OC} (V)**	**FF**	**η%**
1	5.69	0.73	0.57	2.36
2	4.95	0.80	0.69	2.72

In general, depending on the dye, both redox couples Mn(III)/(II) and Mn(IV)/(III) can be involved in the regeneration process. In conjunction with MK2 dye, Spiccia et al. [20] indicated Mn(III) as responsible for dye regeneration, but this is in contrast with the thermodynamic of the bimolecular electron transfer process. ΔG values can be obtained from the redox potentials according to:

$$\Delta G = -ne\left[E_{1/2}\left(\frac{S^+}{S}\right) - E_{1/2}\left(\frac{M^{ox}}{M^{red}}\right)\right] \qquad \text{(Eq.4.1)}$$

where n is the number of electrons transferred, e is the elemental charge of the electron, $E_{1/2}\left(\frac{S^+}{S}\right)$ and $E_{1/2}\left(\frac{M^{ox}}{M^{red}}\right)$ are the redox potentials of the sensitizer and redox mediator,

respectively. As reported previously, and supported by literature reports [41-44], the redox potentials for the couples $[Mn^{III/IV}(acac)_3]^{0/+1}$, $[Mn^{III/IV}(CF2)_3]^{0/+1}$ and $[Mn^{III/IV}(dbm)_3]^{0/+1}$ are +1.12V, +1.57V and +1.20V (vs NHE) respectively, with the dye exhibiting a reversible $[MK2]^{0/+1}$ process at +1.12V Vs NHE as shown in Fig.4.10. Furthermore, considering the redox potential for MK2 adsorbed on TiO_2, which spans from +0.89 V [45], to +0.96 V [46] vs NHE, it appears that the Mn(III)/(IV) redox couples cannot easily be involved in dye regeneration. From the redox potential (V, vs NHE) of the couples $[Mn^{II/III}(acac)_3]^{-1/0}$ (+0.24), $[Mn^{II/III}(CF2)_3]^{-1/0}$ (+0.69) and $[Mn^{II/III}(dbm)_3]^{-1/0}$ (+0.41) driving forces for dye regeneration of 0.88 eV, 0.43 eV and 0.71 eV can be estimated, indicating that Mn(II) should be the best candidate to effectively reduce the oxidized MK2 dye during cell operation.

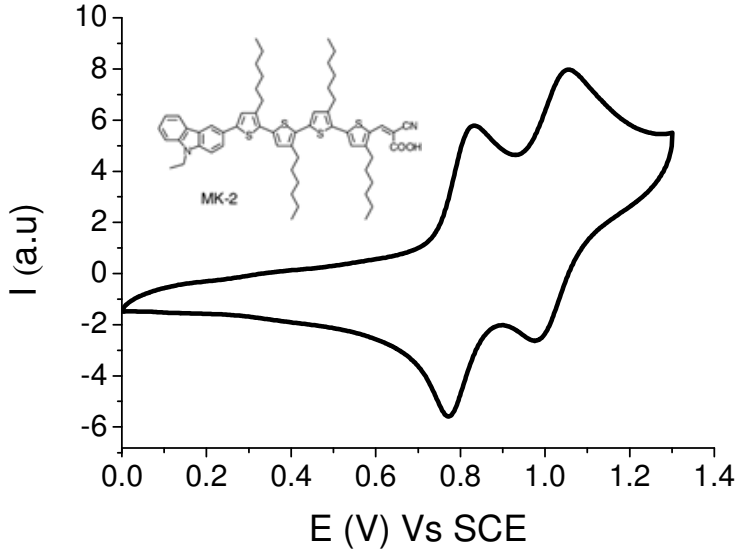

Fig.4.10: CV of MK2 in 0.1M $LiClO_4$/AcN solution at scan rate 100 mV s^{-1}.

The attribution of the ability to regenerate MK2 dye to Mn(II) can also justify absence of photocurrent without TBP, since, at the very beginning, the presence of the concentrated Mn(III) complex, namely the oxidized form of the active redox couple, boosts recombination. After the addition of TBP, the performances are satisfying, as reported in Table 4.2, but to reach steady state **1** and **2** based cells need to be cycled to generate in situ the Mn(II) form by reduction of Mn(III) at the counter electrode of the cell. Nevertheless, at the same time, in steady state irradiation experiments with the reported TBP containing electrolyte composition we observed a considerable decay of the photoelectrochemical performances after reaching the steady state. Even in dark conditions at RT, solutions of Mn(II) or of Mn(III) complexes, in the presence of TBP, showed spectral changes indicating modifications of the solution composition, which in the case of **1** were almost complete after

48 h (Fig.4.11). In neat AcN no appreciable changes of the electronic absorption spectra were observed for **1**, **2, 3,** while for the reduced **4** and **5**, the spectral variations were consistent with oxidation to the corresponding Mn(III) species.

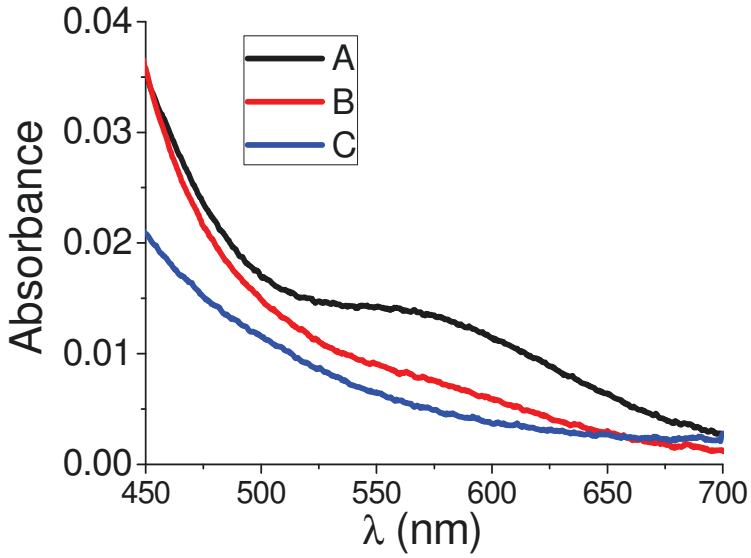

Fig.4.11: Spectral changes of a 0.15M **1** solution in 0.1M $LiClO_4$ AcN upon 0.5M TBP addition at A- t_0, B- after 24 h and C- after 48 h.

ESI mass spectra revealed that addition of TBP to $[Mn(acac)_3]$ **1** in AcN solution caused an almost immediate appearance of a new peak at *m/z* = 387 which best fits with the $[Mn(acac)_2TBP]^+$ fragmentation adduct. Except for intensity variations, the ESI profile remained almost unchanged even after 24 hours with the most important peaks relative to the species $[Mn(acac)_2]^+$ (*m/z* = 253), $[Mn(acac)_2ACN]^+$ (*m/z* = 294) and to the species $[Mn(acac)_2TBP]^+$ (Fig.A2a, Appendix A). The ability of TBP in coordinating the Mn center was confirmed by X-ray structure on the crystals which were spontaneously separated from the AcN solution of **1** and **2** containing TBP. Figure 4.12 shows the structure of *trans*-$[Mn^{III}(acac)_2TBP_2]ClO_4$ and *trans*-$[Mn^{II}(CF2)_2TBP_2]^0$, where, in the latter case, the higher oxidation potential due to the fluorinated ligand, stabilizes Mn(II) in the complex; the corresponding crystallographic data are reported in Tables A2a, b and A3a, b (Appendix A).

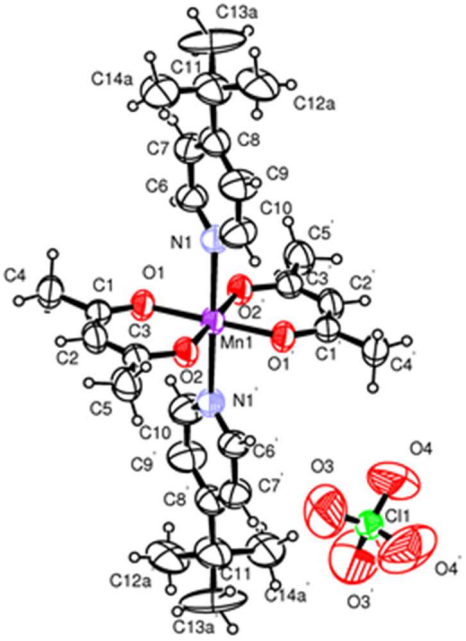

a)

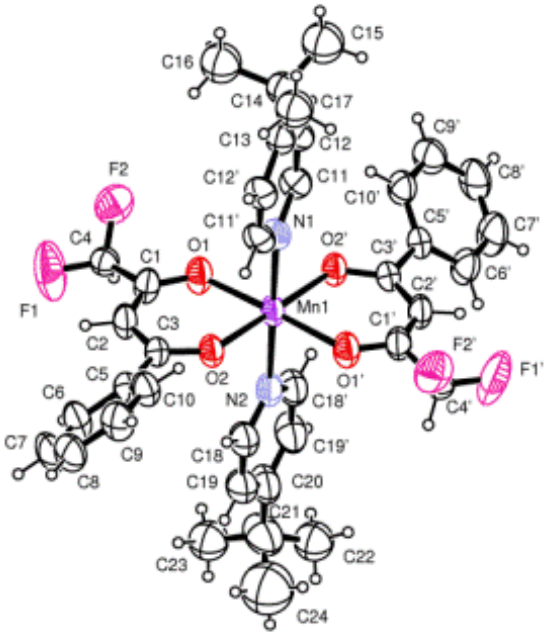

b)

Fig.4.12 ORTEP plot of (a) $[Mn(acac)_2TBP_2]ClO_4$ and (b) $[Mn^{II}(CF2)_2TBP_2]^0$

A similar behaviour was observed for compound **3**, but in this case, it was not possible to obtain crystals of the TBP containing complex. The ESI profile confirms the same decomposition pattern observed for **1** and **2**, with *m/z* = 636 which best fits with the $[Mn(dbm)_2TBP]^+$ fragmentation adduct (Fig.A2 b, Appendix A). Attempts to employ benzimidazole derivatives led to similar electrolyte instability [47]. In order to improve the

electrolyte stability and to suppress at the same time the dark current without using nitrogen based Lewis bases as TiO_2 passivating agents, we performed a series of experiments by using APTS silanized photoanodes [26], sensitized with the dye cis-Ru(H_2dcbpy)(dnbpy)$(NCS)_2$ (Z907, where the ligand H_2dcbpy is 4,4'-dicarboxylic acid-2,2'-bipyridine and dnbpy is 4,4'-dinonyl-2,2'-bipyridine), in the presence of the redox mediators **4** and **5**, which are the supposed species really active in DSSC, and of the corresponding oxidized forms **2** and **3**. Contrary to MK2 sensitized photoanodes [48], Z907 ones were found to exhibit a good a stability following trialkoxysilane post-treatments and Z907 was thus the dye considered for this study. TiO_2 post functionalization with short chain siloxanes successfully screened the semiconductor surface from electron acceptors in the electrolyte by acting mainly through sterical blocking against neutral Mn(III) complexes. Sealed DSSCs based on Mn(II) mediators showed an appreciable response, despite the absence of basic additives, reaching quickly the steady state (Fig.4.13A,B), corresponding to overall efficiencies of 2.62% and 1.48% for $[Mn^{II/III}(CF2)_3]^{-1/0}$ (**4**/**2**) and $[Mn^{II/III}(dbm)_3]^{-1/0}$ (**5**/**3**) respectively. From Figure 4.13 it can be appreciated that the manganese complexes under investigation produce similar open circuit voltages despite variations in $E_{1/2}$ of the order of 400 mV ($E_{1/2}$ = 0.45 V vs SCE for **4** and 0.07 V vs SCE for **5**), suggesting that *Voc* is mainly controlled by recombination at the photoanode. It can be observed that the Mn(III) based mediators **2** and **3** reach respectable efficiencies in DSSC (Fig.4.13 B,C), but such performances are only achieved after hundred potential cycles (Fig.4.14) in LSV mode at 10 mV/s, necessary to accumulate Mn(II). This corroborates the indication that Mn(II) is the active species in the dye regeneration process in these types of manganese based electrolytes. 0.3 M Mn(II) approaches the solubility limit of the **4** and **5** species in the selected solvents (AcN, DMF/AcN 1/1). Tests carried out with 0.15 M Mn(II) lead to halved photocurrent densities with respect to the curves reported in Fig. 4.13 at least with acetonitrile solvent. On the other hand, the dependence of the photocurrent on the concentration is much less pronounced in the more viscous electrolytes containing DMF.

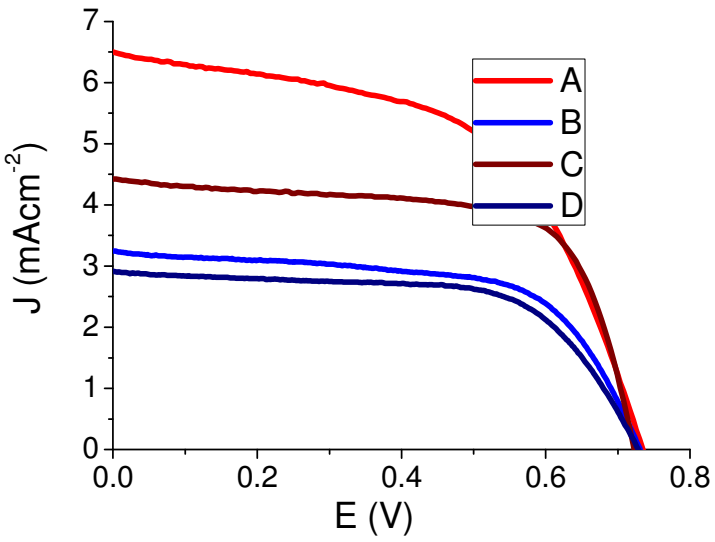

Fig.4.13 Z907/APTS sensitized DSSCs. Electrolyte composition: (A) 0.3/0.03 M $[Mn^{II/III}(CF2)_3]^{-1/0}$ (**4**/**2**), 0.1 M LiOTf, AcN; (B) 0.3/0.03 M $[Mn^{II/III}(dbm)_3]^{-1/0}$ (**5**/**3**), 0.1 M LiOTf, AcN/DMF 1:1 vol; (C) 0.15 M $[Mn^{III}(CF2)_3]^{0}$ (**2**), 0.1 M LiOTf, AcN; (D) 0.13 M $[Mn^{III}(dbm)_3]^{0}$ (**3**), 0.1 M LiOTf, DMF.

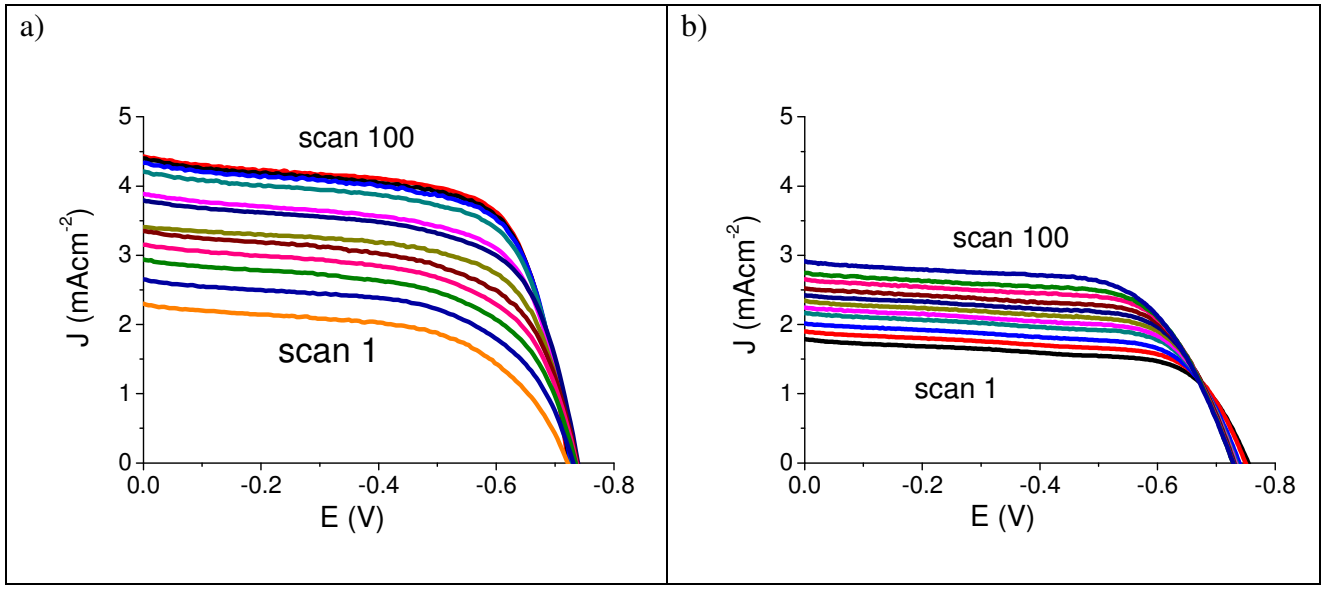

Fig.4.14 Z907/APTS sensitized DSSCs. Electrolyte composition: a) **2** in 0.1M LiOTf AcN; b) 0.13M **3** in 0.1M LiOTf DMF.

A more depth study through Electronic Impedance spectroscopy (ESI), in order to separate charge transfer from diffusional contribution and to evaluate recombination, was carried out in the new Mn(II) electrolytes $[Mn^{II/III}(CF2)_3]^{-1/0}$ (**4**/**2**) and $[Mn^{II/III}(dbm)_3]^{-1/0}$ (**5**/**3**). EIS investigation shows a higher charge transfer resistance of **5**/**3** with respect to **4**/**2**. This indication is corroborated by the log R_{CT} vs log C_{μ} characteristic (Fig.4.15 c) where it can be observed that even at comparable chemical capacitance (*i.e.* density of occupied states)

of the TiO_2 (*ca.* 2×10^{-4} F) the charge transfer resistance in the presence of **5**/**3** is about one order of magnitude larger than that observed in the presence of **4**/**2**. Further, the analysis of the log C_μ vs V_{TiO_2} behavior (fig.4.15 b) points out a substantial negative shift (*ca.* 300 mV) of the conduction band edge of the TiO_2 in the presence of **5**/**3**. These two effects provide a good explanation of the unexpectedly very similar open circuit voltages observed with the **5**/**3** and **4**/**2** redox couples, whose redox potentials, *i.e.* the Fermi level of the counter electrode, differ by *ca.* 400 mV. In **5**/**3** the less positive potential is counterbalanced at the TiO_2/electrolyte interface by a slower electron recapture rate by Mn(III) and by a *ca.* 300 mV negative voltage offset of the lower conduction band edge. The more positive conduction band edge observed with the fluorinated manganese (II) mediator could be explained by the higher surface dipole induced by the interaction of the more polar **4**/**2** mediator with the semiconductor surface. We note that the lower photocurrent observed with **5**/**3** can be either due to a reduction in the charge injection rate by the sensitizer, due to the decreased driving force following the negative shift of the conduction band edge, but also to a higher diffusional resistance, caused by the use of a more viscous electrolyte composed of a mixture of AcN and DMF, as can be appreciated by the large diffusional loop in Nyquist plots (Fig.4.16)**.**

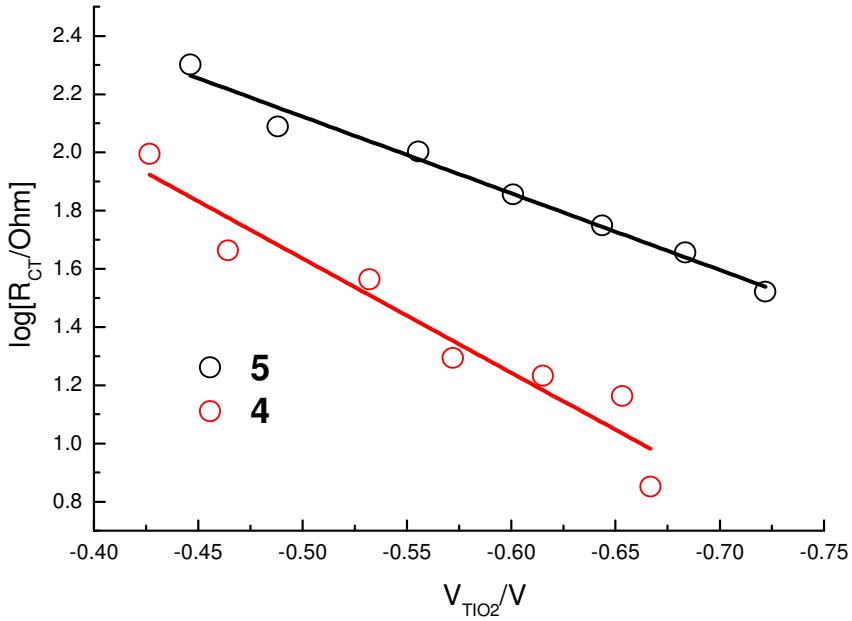

a)

b)

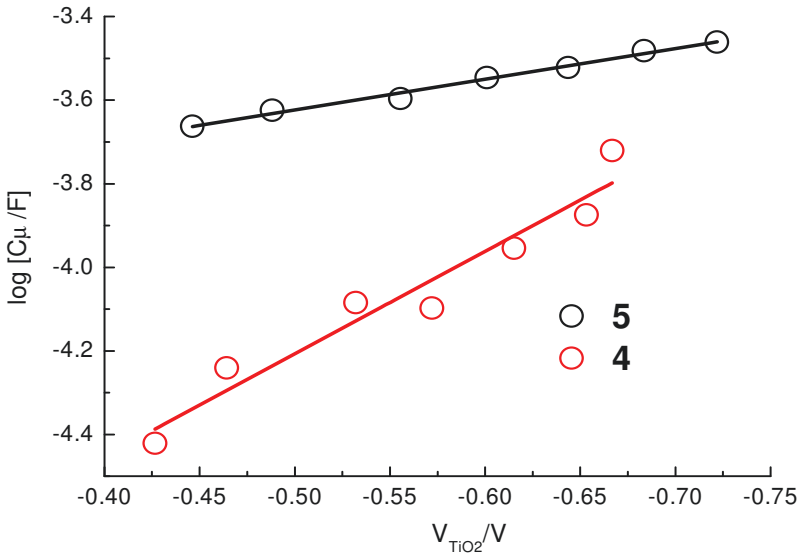

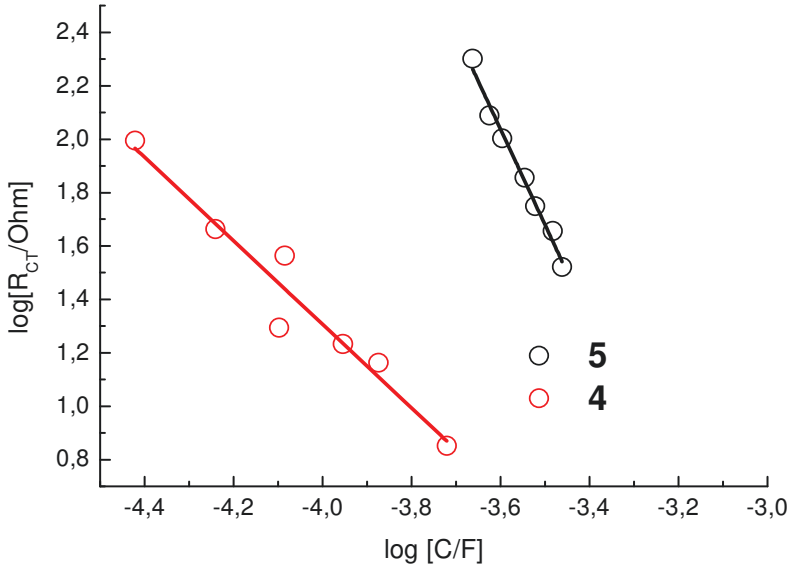

c)

Fig.4.15 TiO_2 charge transfer resistance (R_{CT}) and chemical capacitance (C_μ extracted from EIS under illumination. a) log R_{CT} vs V_{TiO_2}; b) logC_μ vs V_{TiO_2}; c) log R_{CT} vs logC_μ .

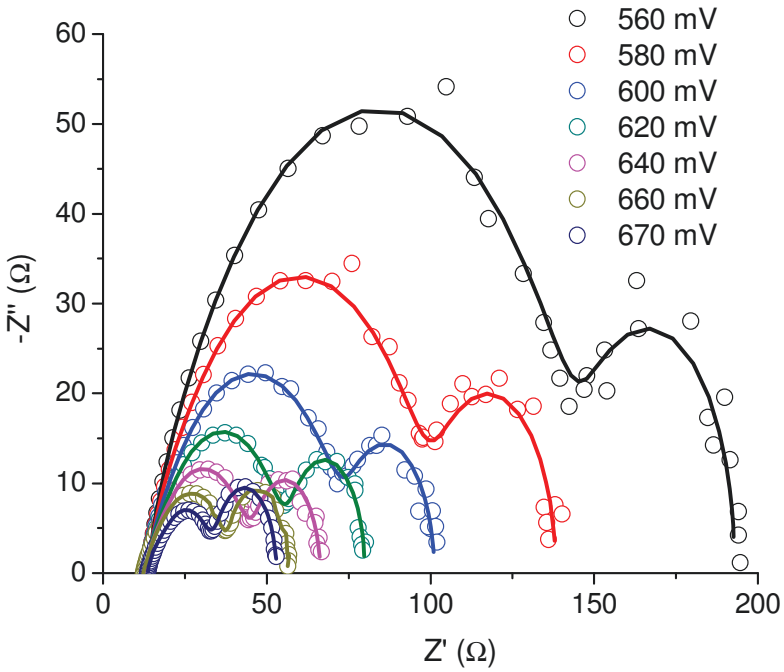

a)

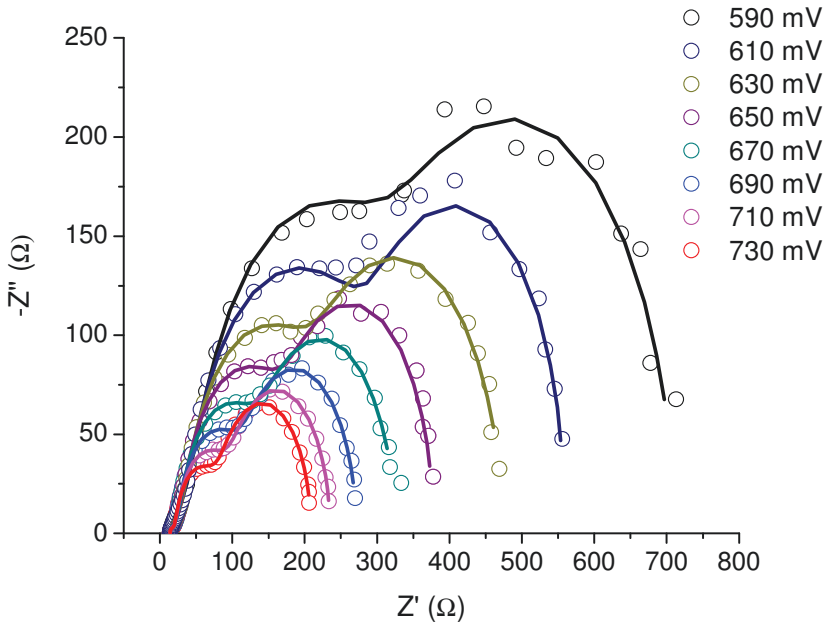

b)

Fig.4.16 Nyquist plots for Z907 sensitized DSSCs, post treated with APTS and assembled with PEDOT coated counter electrodes based on: a) 0.3/0.03M $[Mn^{II/III}(CF2)_3]^{-1/0}$ (**4/2**) in AcN + 0.1 M LiOTf; ;b) 0.3/0.03M $[Mn^{II/III}(dbm)_3]^{-1/0}$ (**5/3**) in AcN/DMF 1:1 + 0.1 M LiOTf. AM 1.5G illumination. Circles indicate experimental data points, continuous lines of the same color are fits to the relevant experimental data.

We would like to point out that Z907 may not be the best dye to be used in conjunction with the investigated electron mediators and higher efficiencies can be reached by employing a sterically hindered organic dye [49], with a stable binding group in the presence of siloxanes. Usually organic dyes present more intense optical absorption with respect to Ruthenium based ones and should allow the use of thinner TiO_2 layers resulting in a further reduction of recombination events. An easier solution to enhance efficiency could be the employment of Mn complexes with chelating ligands, which allow an improvement of stability in the presence of Lewis bases based additives. A proper example is complex **6**, with the encapsulating ligand L1= 3-methoxy-sal-N-1,4,7,10, which is easy to synthesize in high yield. The compound was characterized by ESI mass, UV/Vis spectroscopy and cyclic voltammetry. CV (Fig.4.17) shows two redox waves corresponding to the oxidation of Mn(III) to Mn(IV), with $E_{1/2}$ of 0.6V and to the reduction of Mn(III) to Mn(II) with $E_{1/2}$ = -0.06V (Table 4.3). Both processes are *quasi*-reversible with a ΔE of 70mV and 190mV for the (III)/(II) and the (IV)/(III) process, respectively. We would like to point out that in the present case Mn(IV)/(III) redox potential is suitable for the employ in conjunction with MK2 dye: from the redox potential (V, vs NHE) of the couple $[Mn^{III/IV}(L1)]^{+1/+2}$ (+0.84), driving force for dye regeneration of *ca.* 0.3 eV can be estimated, indicating that Mn(III) should be the candidate to effectively reduce the oxidized MK2 dye during cell operation.

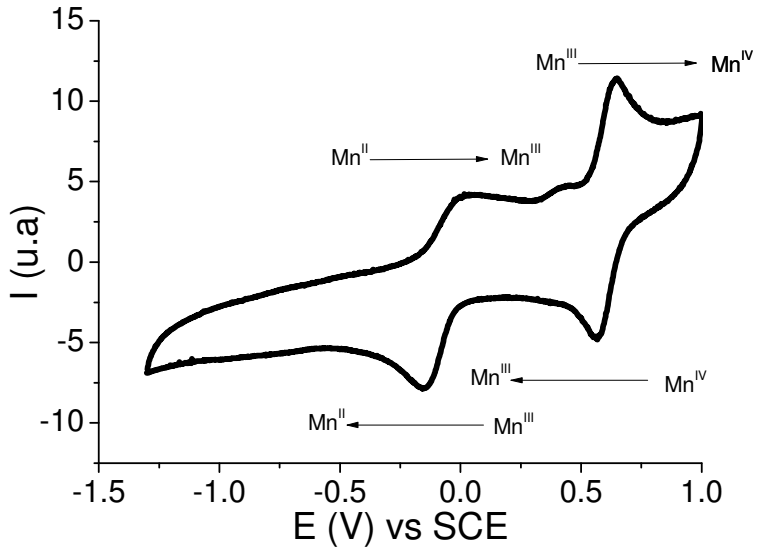

Fig.4.17 CV of **6** in 0.1M $LiClO_4$/AcN solution at scan rate 100 mV s^{-1}, WE glassy carbon, CE Pt wire.

Table 4.3 Relevant data obtained from CV analysis of **6** (potentials are referred to SCE).

	$Mn^{III} \rightarrow Mn^{IV}$				$Mn^{II} \rightarrow Mn^{III}$			
6	E_{pa} (V)	E_{pc} (V)	ΔE (mV)	$E_{1/2}$ (V)	E_{pa} (V)	E_{pc} (V)	ΔE (mV)	$E_{1/2}$ (V)
	0.64	0.57	70	0.60	0.04	-0.15	190	-0.06

Furthermore, tests carried out in order to evaluate the stability of **6** in presence of TBP demonstrate that there is no evidence of formation of TBP adducts. In dark conditions at RT, solution of Mn(III) complex, in the presence of TBP, did not show appreciable spectral changes (Fig.4.18). At the same time, the only peak detected during ESI experiment, before and after the addition of TBP, is related to $[MnL1]^+$ (*m/z* = 467) (Fig.A3 a,b, Appendix A).

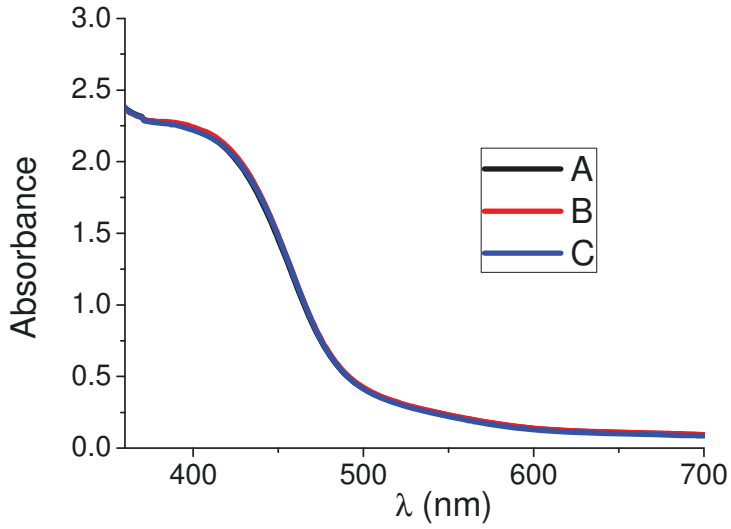

Fig.4.18 Visible spectrum of a 0.15M **6** solution in 0.1M $LiClO_4$ AcN upon 0.5M TBP addition at A- t_0, B- after 6 h and C- after 18 h.

The *J-V* plot of a MK2 sensitized solar cell, containing **6** as redox mediator in AcN, is reported in Fig. 4.19 a. It is worth to notice that an efficiency (η%) of *ca* 2.4% was recorded for $[Mn^{III/IV}(L1)]^{+1/+2}$**6**, which can be compared to the one obtained for $[Mn^{III/IV}(acac)_3]^{0/+1}$**1**

and $[Mn^{III/IV}(CF2)_3]^{0/+1}$ **2** (Fig.4.19 a) in the same conditions. Moreover, the efficiency of the device containing $[Mn^{III/IV}(L1)]^{+1/+2}$**6** redox couple does not decrease with time upon repeated cyclings contrary to the one monitored for acetylacetonate Mn(III) complexes which decays significantly once they reach the steady state(Fig.4.19 b).

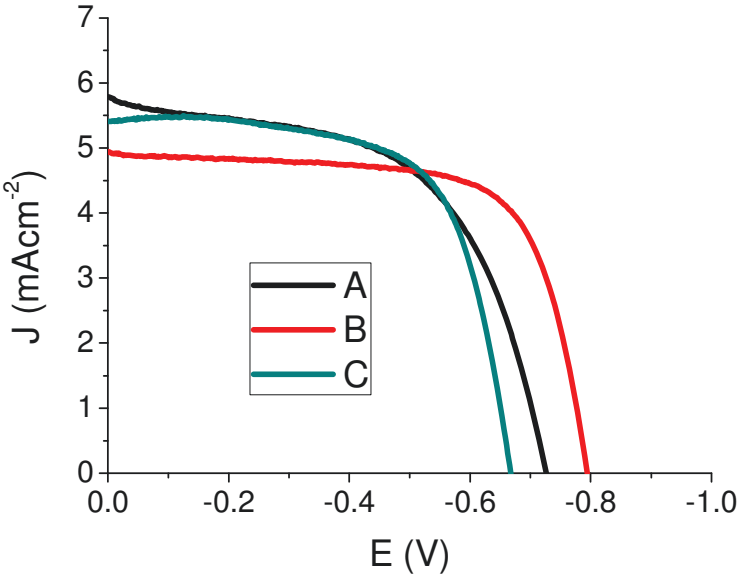

a)

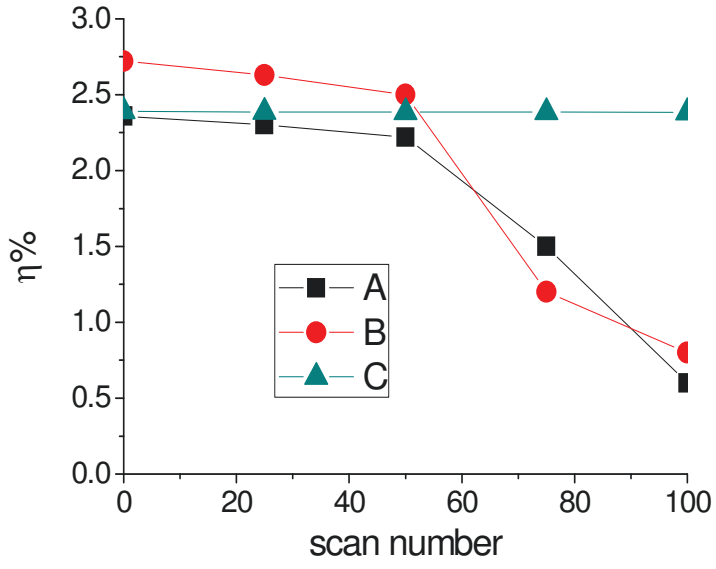

b)

Fig.4.19 a) J-V plots of A- 0.165M **1** in 0.1M LiOTf AcN, 0.5M TBP, 0.015M $NOBF_4$; B- 0.165M **2** in 0.1M LiOTf AcN, 0.5M TBP, 0.015M $NOBF_4$; C- 0.165M **6** in 0.1M LiOTf AcN, 0.5M TBP, 0.015M $NOBF_4$. b) Efficiency (η%) vs scan number of A- 0.165M **1** in 0.1M LiOTf AcN, 0.5M TBP, 0.015M $NOBF_4$; B- 0.165M **2** in 0.1M LiOTf AcN, 0.5M TBP, 0.015M $NOBF_4$; C- 0.165M **6** in 0.1M LiOTf AcN, 0.5M TBP, 0.015M $NOBF_4$.

The overall efficiency was improved by employing D35 organic dye in conjunction with **6**, reaching an efficiency corresponding to 3.1%, which is higher with respect to the ones obtained with all the tris-(β-diketonato) complexes in our conditions.

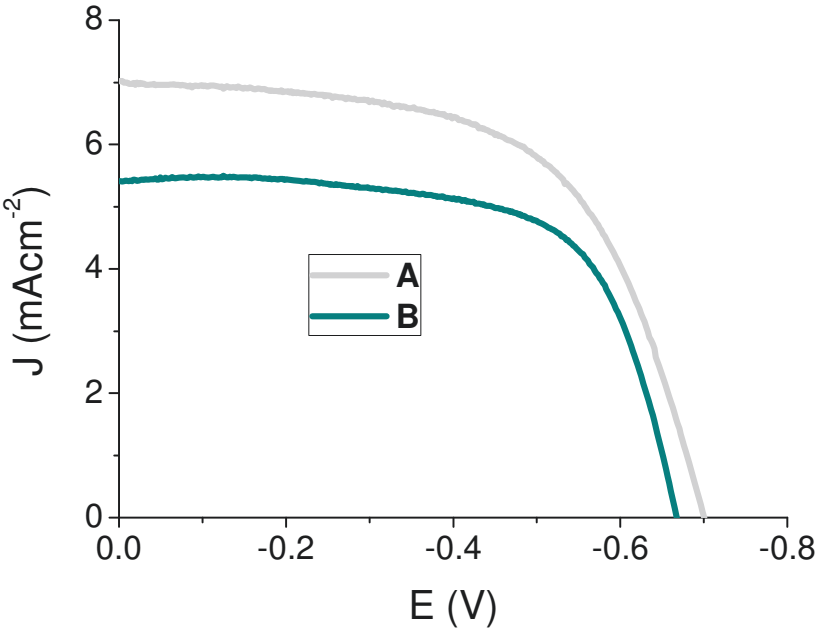

Fig.4.20 J-V plots of 0.165M **6** in 0.1M LiOTf AcN, 0.5M TBP, 0.015M $NOBF_4$ in conjunction with A- D35; B- MK-2

Table 4.4 Relevant photoelectrochemical data obtained from the J-V plots reported in Fig.4.20 Electrolyte composition: 0.165M **6** ,0.5M TBP, 0.1M LiOTf, 0.015M $NOBF_4$ in AcN.

Mn complex	**Dye**	**J_{sc} mA cm^{-2}**	**V_{OC} V**	**FF**	**η%**
6	**D35**	7.1	0.7	0.62	3.1
6	**MK2**	5.41	0.68	0.65	2.38

4.4 Conclusions

This study indicates that tris(β-diketonate)Mn complexes can operate with reasonable efficiency only in the presence of basic additives like TBP, tasked to the suppression of charge recombination at the TiO_2/electrolyte interface. However, under these conditions these Mn redox mediators are chemically unstable due to coordination of the basic nitrogen, leading to the formation *trans*-TBP substituted derivatives, as demonstrated by the crystal structure of the reaction products. In order to obtain solar devices with an increased stability, the presence of basic additives was avoided and TiO_2 passivation was achieved by co-adsorption of short chain siloxanes, acting as steric barrier against electron recapture by oxidized manganese species. Finally, the combined analysis of the electrochemical and photoelectrochemical properties revealed that Mn(III)/(II) is the redox couple involved in the dye regeneration process. To date, the results obtained with tris(β-diketonate)Mn complexes have still been unsatisfactory with respect to other alternative metal based redox mediators, but it can be foreseen that the use of a Manganese complex with an encapsulating ligand, compatible with an appropriate organic dye may lead to better DSSC performances.

4.5 References

1) B. O'Regan, M. Graetzel, *Nature* **1991**, *353*, 737;

2) J.Wu, Z. Lan, J. Lin, M. Huang, Y.Huang, L.Fan, G. Luo, *Chem. Rev.* **2015**, *115*, 2136;

3) C.A Bignozzi, R.Argazzi, R. Boaretto, E.Busatto, S. Carli, F. Ronconi, S. Caramori, *Coord. Chem. Rev.* **2012**, *257*, 1472;

4) H. Ozawa, Y. Okuyama, H. Arakawa, *ChemPhysChem*, **2014**, *15*, 1201;

5)H.Nusbaumer, S.M. Zakeeruddin, J.E. Moser, M. Graetzel, *Chem. Eur. J.* **2003**, *9*, 3756;

6) Toivola, M.; Ahlskog, F.; Lund, P. *Sol. Energ. Mat. Sol. Cells* **2006**, *90*, 2881;

7) S. Caramori, J. Husson, M. Beley, C.A. Bignozzi, R. Argazzi, P. Gros, C. *Chem. Eur. J.* **2010**, *16*, 2611;

8) B.A. Gregg, F. Pichot, S, Ferrere, C.L. Fields, *J. Phys. Chem. B* **2001**, *105*, 1422;

9) S.A. Sapp, C.M. Elliott, C.Contado, S. Caramori, C.A. Bignozzi, *J. Am. Chem. Soc.* **2002**, *124*, 11215;

10) H. Nusbaumer, J.E. Moser, S.M. Zakeeruddin , M.K. Nazeeruddin, M. Graetzel, *J. Phys. Chem. B* **2001**, *105*, 10461;

11) T.C. Li, A.M. Spokoyny, C. She, O.K. Farha, C.A. Mirkin, T.J. Marks, T.J. Hupp, *J. Am. Chem. Soc.* **2010**, *132*, 4580;

12) S.W.Y. Hattori, S.Yanagida, S.Fukuzumi, *J. Am. Chem. Soc.* **2005**, *127*, 9648;

13) Y.Bai, Q.Yu, N. Cai, Y. Wang, M. Zhang, P. Wang, *Chem. Commun.* **2011**, *47*, 4376;

14) Z. Zhang, P. Chen, T.N. Murakami, S.M. Zakeeruddin, M. Graetzel, *Adv. Funct. Mater.* **2008**, *18*, 341;

15) M. Wang, N. Chamberland, L. Breau, J.E. Moser, R. Humphry-Baker, B. Marsan, S.M. Zakeeruddin, M. Graetzel, *Nat. Chem.* **2010**, *2*, 385;

16) S.M. Feldt, E.A. Gibson, E. Gabrielsson, L. Sun, G. Boschloo, A. Hagfeldt, A. *J. Am. Chem. Soc.* **2010**, *132*, 16714;

17) T. Daeneke, T.H. Kwon, A.B. Holmes, N.W. Duffy, U. Bach, L. Spiccia, *Nat. Chem.* **2011**, *3*, 211;

18) T.W. Hamann, *Dalton Trans.* **2012**, *41*, 3111;

19) L. Giribabu, R. Bolligarla, M. Panigrahi, *Chem. Rec.* **2015**, *15*, 760;

20) I. R. Perera, A. Gupta, W. Xiang, T. Daeneke, U. Bach, R. A. Evans, C. A. Ohlin and L. Spiccia, *Phys. Chem. Chem. Phys.*, **2014**, *16*, 12021;

21) M. Nazeeruddin, A. Kay, I. Rodicio, R. Humpbry-Baker, E. Miiller, P. Liska, N. Vlachopoulos, M. Gratzel, *J. Am. Chem. Soc.* **1993**, *115*, 6382;

22) A. Panja, et al., *Inorganica Chimica Acta* **2003**, *351*, 27;

23) P. Wang, S.M. Zakeeruddin, I. Exnar, M. Gra¨tzel, *Chem. Commun.* **2002**, 2972;

24) H.N. Tsao , C. Yi , T. Moehl, J. H. Yum, S.M. Zakeeruddin, M.K. Nazeeruddin, M. Graetzel , *ChemSusChem* **2011,** *4*, 591;

25) M.K. Kashif, J.C. Axelson, N.W. Duffy, C.M. Forsyth, C.J. Chang, J.R. Long, L. Spiccia, U. Bach*, J. Am. Chem. Soc.* **2012**, *134,* 16646;

26) S. Carli, L. Casarin, S. Caramori, R. Boaretto, E. Busatto, R. Argazzi and C. A. Bignozzi, *Polyhedron*, **2014**, *82*, 173;

27) S. Carli, E. Busatto, S. Caramori, R. Boaretto, R. Argazzi, C. J. Timpson and C. A. Bignozzi, *J. Phys. Chem. C*, **2013**, *117*, 5142;

28) Z. Otwinowski , W. Minor, *Methods Enzymol.*, **1997**, *276*, 307;

29) R. H. Blessing, *Acta Crystallogr.*, *Sect. A: Found. Crystallogr.*, **1995**, *51*, 33;

30) A. Altomare, M. C. Burla, M. Camalli, G. L. Cascarano, C. Giacovazzo, A. Guagliardi, A. G. Moliterni, G. Polidori and R. Spagna, *J. Appl. Crystallogr.,* **1999**, *32*, 115;

31) G. M. Sheldrick, *Program for Crystal Structure Refinement*, University of Gottingen, Germany, **1997**;

32) M. Nardelli, *J. Appl. Crystallogr.*, **1995**, *28*, 659;

33) L. J. Farrugia, *J. Appl. Crystallogr.*, **1999**, *32*, 837;

34) M. N. Burnett and C. K. Johnson, *ORTEP III, Report ORNL-6895*, Oak Ridge National Laboratory, Oak Ridge, TN, **1996**;

35) M. N. Bhattacharjee, M. K. Chaudhuri, D. T. Khathing, *J. Chem. Soc., Dalton Trans.*, **1982**, 669; 36) S. Geremia, N. Demitri, *J. Chem. Educ.*, **2005**, *82*, 460;

37) R. Freitag, T. J. Muller and J. Conradie, *J. Chem. Crystallogr.*, **2014**, *45*, 352;

38) G. M. Bancroft, C. Reichert and J. B. Westmore, *Inorg. Chem.*, **1968**, *7*, 870;

39) M. F. Wyatt, S. Havard, B. K. Stein and A. G. Brenton, *Rapid Commun. Mass Spectrom.,* **2008**, *22*, 11;

40) W. Henderson and J. S. McIndoe, *Mass Spectrometry of Inorganic and Organometallic Compounds: Tools – Techniques – Tips, John Wiley & Sons*, **2005**;

41) R. Freitag and J. Conradie, *Electrochim. Acta*, **2015**, *158*, 418;

42) T. Paczes´niak, P. Błoniarz, K. Rydel and A. Sobkowiak, *Electroanalysis*, **2007**, *9*, 945;

43) A. M. Bond, R. I. Martin and S. A. F. Master, *Inorg. Chem.,* **1975**, *14*, 1432;

44) S. A. Richert, P. K. S. Tsang and D. T. Sawyer, *Inorg. Chem.,* **1989**, *28,* 2471;

45) T. Daeneke, A. J. Mozer, Y. Uemura, S. Makuta, M. Fekete, Y. Tachibana, N. Koumura, U. Bach and L. Spiccia, *J. Am. Chem. Soc.*, **2012**, *134*, 16925;

46) Z. S. Wang, N. Koumura, Y. Cui, M. Takahashi, H. Sekiguchi, A. Mori, T. Kubo, A. Furube and H. Kohjiro, *Chem. Mater.,* **2008**, *20*, 3993;

47) H. Kusama and H. Arakawa, *J. Photochem. Photobiol., A*, **2004**, *162*, 441;

48) M. Mba, M. D'Acunzo, P. Salice, M. Maggini, S. Caramori, A. Campana, A. Aliprandi, R. Argazzi, S. Carli and C. A. Bignozzi, *J. Phys. Chem. C*, **2013**, *117*, 19885;

49) K. Kakiage, Y. Aoyama, T. Yano, T. Otsuka, T. Kyomen, M. Unno and M. Hanaya, *Chem. Commun*., **2014**, *50*, 6379;

CHAPTER 5. COUPLING OF ZINC PORPHYRIN DYES AND COPPER ELECTROLYTES FOR THE EMPLOYMENT IN DSSCs

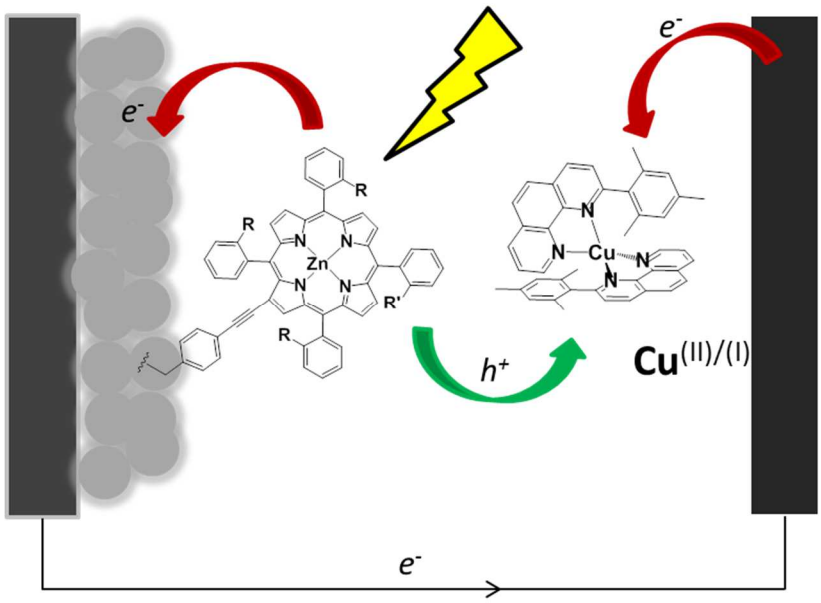

Fig.5.1 Scheme of a Dye Sensitized solar cell base on β-substituted porphyrin dye in conjunction with Copper redox mediator.

One of the most environmentally friendly solutions in the field of solar cells can be given by the employment of β-substituted Zn^{2+} porphyrins in conjunction with copper mediators. In this work is presented a new copper mediator which reaches performance able to overcome the ones reached with iodide/triiodide and Co(III)/(II) reference couples.

5.1 Introduction

Despite the progress in DSSCs field during recent years, the coupling of ruthenium based dyes and redox couple I_3^-/I^- seems to still reach best performance in DSSCs [1]. On the other hand, the searching for free-Ruthenium dyes is becoming extremely important to avoid cost and environmental issue. Among organic sensitizers, tetrapyrrolic macrocycles whose basic design may lead to a class of simple, robust, efficient and economically viable sensitizers have become more and more interesting [2]. Porphyrins are an obvious choice, due to their well-known role as light absorbers and charge separators in natural photosynthetic systems. Furthermore, their oxidation potentials in both ground state (*ca.* 1V vs SCE) and excited state oxidation (*ca.* -1V vs SCE) match perfectly with most redox shuttles employed in DSSCs and the conduction band of TiO_2, respectively. On the other hand, in order to operate successfully as DSSC sensitizers, the basic porphyrin structure has to undergo important

modifications oriented to tune and optimize the excited state characteristics. In particular, to obtain almost quantitative quantum yields of charge injection it is important to establish a strong electronic coupling between the excited state and the acceptor band of the TiO_2. To satisfy this characteristic the linkage group is usually constituted by either a carboxylic group or a cyanoacetic group and the functionalization with anchoring groups could be obtained either at the *meso* position (1,2) or at the β-(3,4) position of the pyrrole, without largely affecting the resulting properties [3]. β-substituted design can offer some advantages over *meso* substituted porphyrin, resulting in a better shielding of the TiO_2 surface, reducing back recombination [4]. The first step towards the affirmation of porphyrins in DSSC was done in 1993 by Grätzel and Kay, by working on chlorophylls and related porphyrin derivatives. They reported a η value of 2.6% for a TiO_2 electrode sensitized with Cumesoporphine IX [5].

Durrant *et al.* attributed low efficiencies recorded at the dye aggregation on TiO_2 surface [6]. Palomares *et al.* [7] demonstrated that by introducing alkyl-hydrophobic substituents on *meso*-phenylporphin, it was inhibited not only the formation of molecular aggregates but also the recombination between the electrons injected into the conduction band of TiO_2 and the electrolyte. Studies about kinetics of electronic recombination processes at the variation of structural characteristics of a common porphyrinic nucleus proved that when the position and size of the substituents is appropriate to cover the space between the absorbed dye and the semiconductor surface, the dye acts as a physical obstacle to the approach of the electrolyte, by avoiding recombination. Furthermore, the introduction of an electro-donating group lead to the increase in the charge transfer character, which is beneficial to increase excited state directionality by shifting the electron density of the excited state on the electron withdrawing group linked to the titania surface. Thus, the incorporation of both donor and acceptor, namely the liking group, moieties into the porphyrin macrocycle lead to a successful design resulting in higher power conversion efficiencies in the presence of chenodeoxycholic acid and triiodide/iodide electrolyte [8]. Recently efficiencies up to *ca.* 13%, higher than those obtained with the most efficient Ru complexes, were reached by combining *meso*-disubstituted push-pull Zn^{2+} diarylporphyrins with tris(bipyridine) cobalt electrolytes which allow to significantly increase the open-circuit voltage (V_{OC}) with respect to the traditional I^-/I_3^- couple [9]. On the other hand, for what concern synthetically less demanding β-substituted Zn^{2+} tetraaryl porphyrins, their effect has never been tested with a metal-complex redox mediator. In this work a β-substituted Zn^{2+} tetraaryl **D1** porphyrin, bearing ortho-dodecyloxy chains, in order to reduce recombination, was employed [10]. We explored the possibility to combine an efficient β-substituted porphyrin with

environmentally friendly metal-complex redox mediators like Copper based ones. The choice of Copper instead of the famous Cobalt is attributable to several reasons among which the lower reorganization energy of Cu(II)/Cu(I) complexes with tetragonal distorted geometry (intermediate between the 4-coordinated tetrahedral one preferred by Cu(I) and the 5- or 6-coordinated tetragonal one for Cu(II)) with respect to Co(III)/Co(II) characterized by really large internal reorganization energy between high-spin d^7 and low-spin d^6 states [11]. Furthermore, both Cobalt and Copper complexes present easily tunable redox potentials which can be adapted to enhance the open circuit voltage (V_{OC}), contrary to iodide/triiodide couple. In view of the above, **D1** porphyrin was tested in conjunction with a new copper based redox couple, $[Cu(2\text{-mesityl-}1,10\text{-phenanthroline})_2]^{+/2+}$ (**1/2**), which was designed with the aim of improving V_{OC} with respect to the well-known performing couple $[Cu(2\text{-mesityl-}4,7\text{-dimethyl-}1,10\text{-phenanthroline})_2]^{+/2+}$(**3/4**) [12]. 2,9-dimethyl-1,10-phenanthroline Copper complex [13] (**5/6**) was studied as reference, as well as I^-/I_3^- and $[Co(dtb)_3]^{2+/3+}$ (dtb = 4,4'-di-*tert*-butyl-2,2'-bipyridine) [14] redox couples. The effect of the anchoring group was studied by combining the best redox shuttle, namely the new one, with **D2** dye. Copper redox mediators **1**-**6** were synthesized and characterized by D. Roberto group, while **D1** and **D2** porphyrins by M. Pizzotti group at the University of Milan.

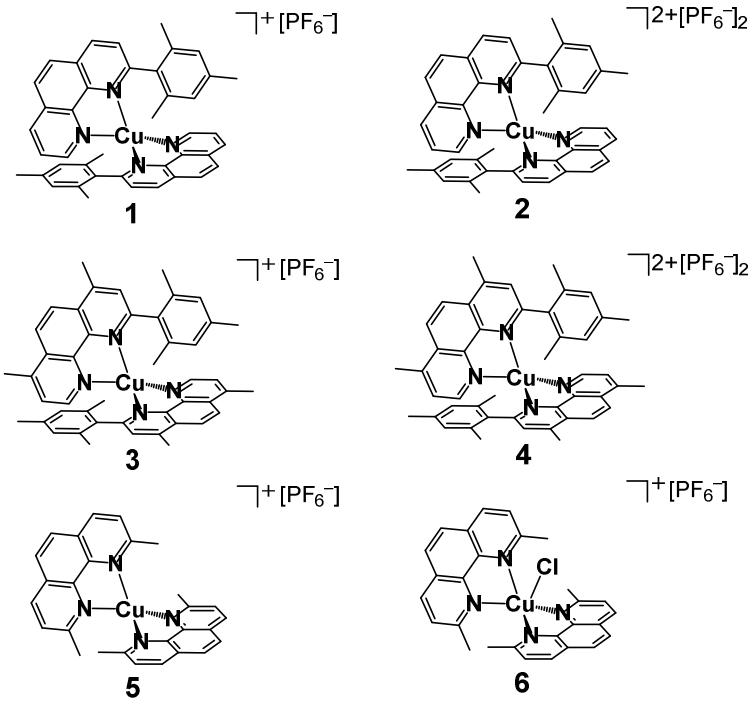

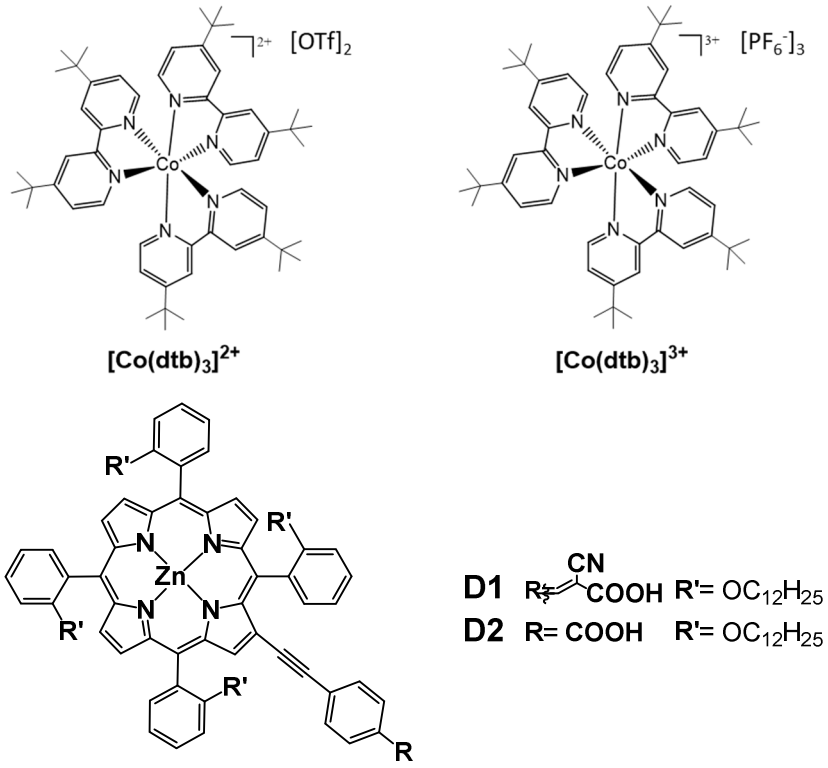

Fig.5.2 Chemical structure of the three couples of copper-based redox mediators(**1**-**6**), of cobalt-based couple and of the two tetraaryl Zn^{2+} porphyrin dyes (**D1**,**D2**).

5.2. Experimental Section

5.2.1 Materials and Methods

All reagents and solvents were purchased by Sigma-Aldrich and used without further purification, except Et_3N (freshly distilled over KOH). 4,7-(di-methyl)-1,10-phenanthroline was purchased by Alfa Aesar. Reactions requiring anhydrous conditions were performed under argon. Conductive FTO (fluorine tin oxide) TEC8, 2.3 mm thick substrates (Pilkington) were carefully cleaned by several washings in ethanol, acetone, and Alconox followed by annealing at 450 °C in air before use. TiO_2 colloidal paste (DSC 18NR-T) was purchased from Dyesol. Glassware has been flame-dried under vacuum before use when necessary. Microwave assisted reactions were performed using a Milestone MicroSYNTH instrument. Thin layer chromatography, TLC, was carried out with pre-coated Merck F_{254} neutral aluminium oxide 60 plates. Liquid chromatography was carried out with neutral aluminium oxide (Brockmann grade II, Alfa Aesar) or silica gel (Geduran Si 60, 63-200 μm, Merck). ^{1}H-NMR, ^{13}C-NMR, ^{19}F-NMR and ^{31}P-NMR spectra were recorded at T = 300 K on a Bruker Avance- DRX-400 or 300 instrument. Chemical shifts (δ) of spectra were expressed in ppm relative to Me_4Si (for ^{1}H and ^{13}C), $CFCl_3$ (for ^{19}F) and H_3PO_4 (for ^{31}P)

reference compounds. Signals were abbreviated as s, singlet; d, doublet; dd, doublet of doublets; t, triplet; q, quartet; sept, septet; m, multiplet. Mass spectra, MS, were obtained with a FT-ICR Mass Spectrometer APEX II & Xmass software (Bruker Daltonics) 4.7 Magnet and Autospec Fission Spectrometer (FAB ionization) or with a Thermo-Finnigan apparatus with a Ion Trap analyzer (positive mode) and an electrospray ionization source (ESI) using a LCQ-Advantage instrument. Elemental analysis was carried out with a Perkin-Elmer CHN 2400 instrument. Electronic absorption spectra were recorded at room temperature in THF or acetonitrile solution, using a Shimadzu UV3600 spectrophotometer and quartz *cuvettes* with 1 cm optical path length. Photoluminescence experiments were carried out at room temperature, in THF solution after N_2 bubbling for 120 s. Photoluminescence quantum yields (Φ) were measured with a C11347 Quantaurus - QY Absolute Photoluminescence Quantum Yield Spectrometer (Hamamatsu Photonics K.K), equipped with a 150 W Xenon lamp, an integrating sphere and a multi-channel detector. Steady state emission and excitation spectra and photoluminescence lifetimes (τ) were obtained with a FLS 980 spectrofluorimeter (Edinburg Instrument Ltd.). Stationary absorption characterization of copper redox mediators was carried out by D.Roberto group at the University of Milan, while stationary absorption/emission characterization of porphyrin dyes was carried out by M.Pizzotti group at the University of Milan.

5.2.2 Synthesis of ligand 2-mesityl-1,10-phenanthroline (L).

Ligand L was prepared by following a literature procedure [28]. 19.2 mmol of 2-bromo-mesitylene were dissolved in degassed dry Et_2O and cooled at –78°C under an Ar atmosphere. Then, 42.2 mmol of *tert*-butyl lithium were carefully dropped. When the addition was completed the stirred solution was maintained at –78°C for 30 minutes and then it was warmed up to r.t. over 30 minutes. A white solid precipitated and was filtered under Ar, washed with some Et_2O and dissolved, under Ar, in 20 mL of dry toluene. The white solution was dropped into a flask, filled with argon, containing a stirred solution of 1,10-phenanthroline (12.6 mmol) dissolved in 260 mL of degassed dry toluene cooled to 0 °C. The solution gradually turned dark. After 20 minutes the reaction mixture was allowed to warm at r.t. and stirred overnight. The mixture was quenched with water and the organic solution was separated. The aqueous layer was washed with dichloromethane. The organic phases obtained were dried with Na_2SO_4, filtered into a flask containing activated manganese dioxide (403 mmol) and stirred at r.t. overnight. The mixture was filtrated, and the solvent was evaporated at reduced pressure. The product was purified by liquid chromatography on

neutral Al_2O_3 through a gradient elution (from CH_2Cl_2/toluene 7:3 to pure CH_2Cl_2). Pure L was obtained as a white/yellow solid. Yield was 40%.

^{1}H-NMR (400 MHz, $CDCl_3$) δ(ppm): 9.28 (dd, J_2 = 4.4 Hz, J_3 = 1.6 Hz, 1H), 8.39 (dd, J_2 = 8.0 Hz, J_3 = 1.6 Hz, 1H), 8.33 (d, J_2 = 8.2 Hz, 1H), 7.95 (d, J_2 = 8.8 Hz, 1H), 7.88 (d, J_2 = 8.8 Hz, 1H), 7.71 (dd, J_2 = 8.0 Hz, J_3 = 4.4 Hz, 1H), 7.57 (d, J_2 = 8.2 Hz, 1H), 6.89 (s, 2H), 2.36 (s, 3H), 1.97 (s, 6H).

*5.2.3 Synthesis of complex **1***

Copper (I) iodide (CuI) (0.366 mmol) was added to a stirred solution of the ligand L (0.751 mmol) dissolved in 20 mL of acetonitrile, under Argon atmosphere. The solution was stirred at room temperature for *ca.* 30 minutes. The solvent was eliminated under reduced pressure and the light red solid was dissolved in the minimum amount of a 1:2 mixture H_2O/EtOH under vigorous stirring. After the addition of 2.3eq. of sodium hexafluorophosphate ($NaPF_6$) a red solid precipitated. The solid was filtered, washed with H_2O and Et_2O and, finally, dried under vacuum for some hours, until a red powder of compound **1** was obtained. Yield was 85%.

^{1}H-NMR (300 MHz, CD_3CN) δ(ppm): 9.03 (dd, J_2 = 4.8 Hz, J_3 = 1.3 Hz, 2H), 8.62-8.57 (m, 4H), 8.11 (d, J_2 = 9 Hz, 2H), 8.06 (d, J_2 = 9 Hz, 2H), 7.88 (dd, J_2 = 8.2 Hz, J_3 = 4.8 Hz, 2H), 7.59 (d, J_2 = 8.2 Hz, 2H), 6.12 (s, 2H), 5.79 (s, 2H), 1.94 (s, 6H), 1.69 (s, 6H), 1.00 (s, 6H); ^{13}C-NMR APT (75 MHz, CD_3CN) δ(ppm): 158.7 (C), 149.4 (CH), 144.1 (C), 143.9 (C), 137.8 (CH), 137.5 (C), 136.5 (CH), 135.9 (C), 135.1 (C), 133.4 (C), 129.6 (C), 128.4 (CH), 127.9 (C), 126.9 (3CH), 126.7 (CH), 126.0 (CH), 20.3 (CH_3), 19.7 (CH_3), 19.1 (CH_3); ^{19}F-NMR (282 MHz, CD_3CN) δ(ppm): –73.2 (d, J_{F-P}= 704 Hz, 6F); ^{31}P-NMR (121 MHz, CD_3CN) δ(ppm): –144.0 (sept, J_{P-F}= 704 Hz, 1P). ε_{451} (M cm^{-1}): 4000 (Fig.5.3).

*5.2.4 Synthesis of complex **2**, and **4***

The two complexes were synthesized by employing a described procedure [12], here described for **2**. 0.050 mmol of Copper (II) sulphate ($CuSO_4 \times 5H_2O$) were added to 0.100 mmol of 2-mesityl-1,10-phenanthroline in 6 mL of acetonitrile. The light green solution was stirred at room temperature for 1 hour and then was concentrated under reduced pressure. EtOH was added to completely dissolve the green solid and the addition of 0.210 mmol of $NaPF_6$ (35 mg, 0.210 mmol) lead to the precipitation of a light green solid in 1 mL of H_2O. The suspension was lead stirring for 2 hours. The product was collected by filtration, washed with H_2O and Et_2O and, finally, dried under vacuum for some hours. Complex **2** resulted as

a light green powder. Yield was 72%. *m/z* (ESI): 659.47. (659.22 calculated). ε_{696} (M cm^{-1}): 3100 (Fig.5.3).

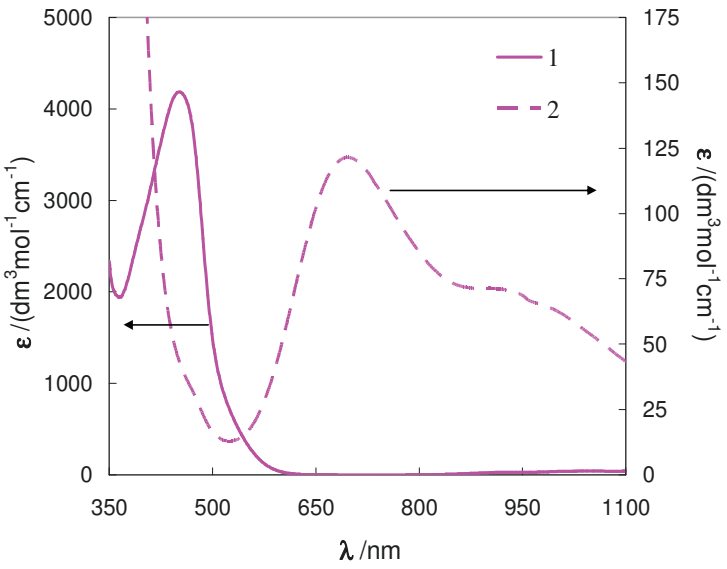

Fig.5.3 Absorption spectra of the new complexes **1** and **2** in acetonitrile. (Data recorded by D.Roberto group at the University of Milan)

*5.2.5 Synthesis of complexes **3, 5***

3 and **5** were synthesized according to the same procedure described for **1**, adding 2-mesityl-4,7-dimethyl-1-10-phenanthroline, prepared as previously reported, or commercially available 2,9-dimethyl-1,10-phenanthroline as ligand, respectively [14]. Yields were in the range of 80÷90%.

3: ^{1}H-NMR (300 MHz, CD_3CN) δ(ppm): 8.82 (d, J_2 = 3.6 Hz, 2H), 8.28 (d, J_2 = 6.9 Hz, 2H), 8.24 (d, J_2 = 6.9 Hz, 2H), 7.68 (d, J_2 = 3.6 Hz, 2H), 7.41 (s, 2H), 6.19 (s, 2H), 5.81 (s, 2H), 2.91 (s, 6H), 2.85 (s, 6H), 1.94 (s, 6H), 1.68 (s, 6H), 1.04 (s, 6H); ^{19}F-NMR (282 MHz) δ(ppm): –73.2 (d, $J_{F\text{-}P}$= 704 Hz, 6F); ^{31}P-NMR (121 MHz) δ(ppm): –144.0 (sept, $J_{P\text{-}F}$= 704 Hz, 1P). **5**: ^{1}H-NMR (300 MHz, CD_3CN) δ(ppm): 8.59 (d, J_2 = 8.2 Hz, 4H), 8.11 (s, 4H), 7.84 (d, J_2 = 8.2 Hz, 4H), 2.43 (s, 12H); ^{19}F-NMR (282 MHz) δ(ppm): –73.2 (d, $J_{F\text{-}P}$= 704 Hz, 6F); ^{31}P-NMR (121 MHz) δ(ppm): – 144.0 (sept, $J_{P\text{-}F}$= 704 Hz, 1P).

*5.2.6 Synthesis of complex **6***

The penta-coordinated complex **6** was synthesized as reported in literature [15] and obtained as a bright green powder in 76 % yield.

5.2.7 Synthesis of $[Co(dtb)_3][OTf]_2$ complex

$[Co(dtb)_3][OTf]_2$ was synthesized by a simple procedure reported in literature [14] as follows: 2.8mmol of Cobalt (II) triflate haxahydrate ($[Co(H_2O)_6](OTf)_2$) salt were mixed with 8.4mmol of 4,4'-di-*tert*-butylpyridine in methanol. The solution was stirred for 15 minutes, and the final product was obtained by solvent evaporation under vacuum. The complex was purified by dissolving the solid in a minimum amount of acetonitrile and then by precipitation in EtO_2 as a light-yellow powder. Yield was *ca.* 90%.

5.2.8 Synthesis of $[Co(dtb)_3][PF_6]_3$ complex

The complex $[Co(dtb)_3](PF_6)_3$ was prepared by oxidizing the corresponding Co(II) species with a stoichiometric amount of Br_2 in acetonitrile solution under stirring for 1 h at room temperature. After removing the solvent by rotary evaporation, the yellowish solid was dissolved in water, and an excess of ammonium hexafluorophosphate (NH_4PF_6) was added. The precipitate was collected by filtration, washed with water and diethyl ether, and dried to finally obtain a yellow powder. Yield was *ca.* 90%. ^{1}H-NMR spectroscopy confirmed the purity and the symmetry of the complex.

^{1}H-NMR (400 MHz, CD_3CN) δ(ppm): 8.66 (d, 6 H), 7.7 (dd, 6 H), 7.1 (d, 6 H), 1.5 (s, 54 H).

*5.2.9 Synthesis of **D1** and **D2** porphyrins*

D1 was prepared following a literature procedure [10]. **D2** ([2-(4'-Carboxyphenylethynyl)-5,10,15,20-tetrakis(2-dodecyloxyphenyl)porphyrinate]Zn^{II}) was prepared by mixing 736.3 μmol of 4-ethynylbenzoic acid, 14.7 μmol of Tatrakis(triphenylphosphine)palladium(0) ($Pd(PPh_3)_4$) and 147.3 μmol of [2-bromo-5,10,15,20-tetrakis(2-dodecyloxyphenyl)porphyrinate]Zn^{II} (1 equiv.) in a mixture of anhydrous DMF and Et_3N that was de-aerated with three freeze-pump-thaw cycles at about -96°C, using a bath of liquid nitrogen and acetone. Then solution was warmed to room temperature and 22.1 mmol of Copper Iodide (CuI) were added and after a bubbling of nitrogen for 15 min, the reaction was heated at 120 °C in a microwave cavity for 1 h. The solvents were removed in vacuo and the product was dissolved in CH_2Cl_2 again and washed with H_2O acidified with phosphoric acid (H_3PO_4). The organic phase was dried over anhydrous Sodium sulphate (Na_2SO_4), filtered and concentrated. The crude product was purified by column chromatography on silica (CH_2Cl_2/MeOH 97.5:2.5 gradient to 95:5). Yield was about 50.6 %. ^{1}H-NMR (400.1 MHz, $CDCl_3$) δ, ppm: 9.20 (1H, m), 8.78 (6H, m), 8.01 (4H, m), 7.74 (3H, m), 7.54 (5H, m), 7.34 (7H, m), 7.23 (1H, m), 3.89 (8H, m), 1.40-0.5 (92H, m);

Elemental analysis calculated (%) for $C_{101}H_{128}N_4O_6Zn$: C 77.79, H 8.27, N 3.59; found C 77.56, H 8.29, N 3.58; m/z (ESI): ca1c. for $C_{101}H_{128}N_4O_6Zn$ 1556, found 1557 $[M+H]^+$.

5.2.10 Electrochemical characterization

Cyclic voltammetry (CV) and electrochemical impedance spectroscopy (EIS) for the electrochemical characterization of complexes were performed with a potentiostat/galvanostat PGSTAT302N in a three-electrode cell with tetrabutylammonium hexafluorophosphate ($TBAPF_6$, ≥98.0 %, Sigma-Aldrich) acting as supporting electrolyte. The working solution was well deareated by bubbling nitrogen before each measure starts and blowing it over the surface of the solution during the scans. Teflon-embedded glassy carbon electrodes, GC (geometric surface area 0.071 cm^2, purchased by Metrohm and Amel), were used as working electrode in combination with a platinum wire as counter electrode and a saturated calomel electrode, SCE, as reference one.

The recorded potentials were referred to the redox couple $Fc^+|Fc$ (ferricenium/ferrocene) added as external standard (*ca.* $1 \cdot 10^{-3}$ M). In order to calculate diffusion coefficients of Copper complexes, CVs were performed at different sweep potentials (0.02-2 V s^{-1}) and an instrumental compensation of the resistance was carefully performed in order to minimize the ohmic drop between the working and reference electrode. The determination of redox potential of electrolytes was carried out with the same setup, recording CV of a Fc solution at 0.2 V s^{-1} (see below for more details). EIS spectra of Cu complexes were recorded superimposing to a continuous potential bias set at the half-wave potential ($E_{1/2}$) a sinusoidal alternating potential signal of 0.01 V amplitude and frequency ranging from $1 \cdot 10^4$ to $1 \cdot 10^{-1}$ Hz. Sixty logarithmically distributed single sine frequencies were employed for recording each spectrum. NOVA 1.10 software was used to validate EIS data and to fit them with a Randles-type equivalent circuit to estimate the charge transfer resistance (R_{CT}) at the electrolyte/electrode interface. Electrochemical characterization was performed by D.Roberto group at the University of Milan.

5.2.11 Preparation of Solar Cells.

A compact TiO_2 blocking underlayer was prepared by spin-coating a 0.3 M titanium tetraisopropoxide solution in 1-butanol (1000 rpm for 10 s, 2000 rpm for 20 s) onto FTO substrates. Then the substrates were heated to 500 °C for 15 min. The blocking underlayer was applied to limit recombination rates of the injected electrons with the electrolyte at the highly conductive FTO interface.

Mesoporous titania films (ca. 6 μm thick) were prepared by blading a commercial 400-nm nanoparticle colloidal TiO_2 paste on FTO electrodes. After the TiO_2 deposition, the electrodes were heated up to 500°C, following a programmed temperature ramping: 25−120 °C (10 min), 120−450 °C (30 min), 450 °C (20 min), 450−500 °C (10 min), 500 °C (10 min). The sintering process regulates parameters such as the contact between interconnected nanoparticles and their coordination in the porous TiO_2 network, enhancing the film conductivity.

The resulting transparent films were immersed in a 0.4 M Titanium tetrachloride ($TiCl_4$) solution for 12 hours, in order to improve the active area, owing to the $TiCl_4$ hydrolysis on the TiO_2 substrate.

In the end the electrodes were rinsed with water and heated to 450 °C for 30 minutes. Once cooled, the electrodes were immersed in a 0.2 mM solution of the dye (**D1** and **D2**) in ethanol/tetrahydrofuran 9:1, containing chenodeoxycholic acid 1 mM.

PEDOT (poly(3,4-ethilenedioxythiophene)) counter electrodes [17] were prepared by electrodeposition on FTO glasses through cyclic voltammetry technique, scanning 2 times from 0 to 1,7 V vs SCE at 20 mV/s in a 10^{-2} M 3,4-ethylenedioxythiophene (EDOT) /0.1 M Lithium perchlorate ($LiClO_4$) acetonitrile solution.

The PEDOT-modified FTO electrodes were then thoroughly washed with fresh acetonitrile and dried in air.

Solar cells were finally assembled by sealing the sensitized photoanode and a PEDOT-modified FTO counter electrode through a mask of 25 μm ionomer resin (Surlyn®, DuPontTM), properly pressed and warmed. Electrolyte was injected by a syringe through one of two holes pre-drilled on the counter electrode.

5.2.12. Solar Cell Characterization.

Current−voltage measurements at a scan rate of 10 mV s^{-1} and electrochemical impedance spectroscopy (EIS) were performed with a PGSTAT302N potentiostat equipped with a frequency response analyzer module and controlled by NOVA or GPES software (Metrohm Autolab). Cell performances were evaluated under 100 mW cm^{-2} AM 1.5 illumination (ABET sun simulator). EIS spectra were recorded by using a 10 mV sinusoidal perturbation in the 10^5–10^{-2} Hz frequency range. The DC potential was sampled along the ascending branch of the J-V curve with an interval of 20 mV starting from V_{OC}. Impedance data were analysed using commercially available Z-View software and were fitted with the simplified equivalent electric circuit reported in Scheme 5.1, where the R2-CPE1 mesh describes the TiO_2/electrolyte electrochemical interface (R_{CT}), Ws represents the short Warburg diffusion

element and R3-CPE2 stands for the counter electrode/electrolyte interface (R_{CE}). The non-ideal capacitances of the electrochemical interfaces are described by constant phase elements (CPE) with exponents in the range 0.95±0.05. Typical maximum errors from fits were <10 %.

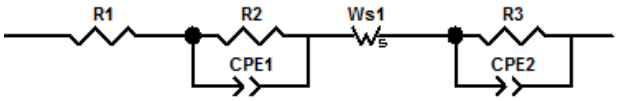

Scheme 5.1: Electric model used to fit experimental EIS data.

IPCE spectra were collected with a custom-built apparatus comprising an Applied Photophysics Monochromator, a 175 W Xe source (Luxtel) and various optical elements [18]. Photocurrents were measured with an Agilent 34301 A multimeter while incident irradiance was provided by a calibrated silicon photodiode (OSD 100 7Q). Spectra were determined in sandwich DSSCs under short circuit conditions (i.e. without applying an external potential bias) by sampling the visible spectrum (400-800 nm) at 20 nm intervals with a spectral bandwidth of 10 nm.

5.2.13 Electrolyte formulation

Electrolytes were all formulated using acetonitrile as solvent, 0.1 M lithium triflate (LiOTf) and 0.25 M 4-*tert*-butyl pyridine (TBP) as additives. A 10:1 molar ratio was chosen for reduced and oxidized species of each redox couple, respectively. Thus, copper electrolytes (**1**/**2**-El, **3**/**4**-El and **5**/**6**-El, where El means electrolyte), were prepared dissolving the redox couple (0.17 M Cu^{+} /0.017 M Cu^{2+}) in acetonitrile with 0.1 M lithium trifluoromethanesulfonate as supporting salt and 0.25 M 4-*tert*-butylpyridine as additive to improve the V_{OC} of the devices. Control electrolytes I^{-}/I_3^{-}-El and Cobalt-El were prepared with a comparable amount of electroactive species: 0.17 M I^{-} (0.024 M LiI + 0.146 1-methyl-3-propylimidazolium iodide)/0.017 M I_2 and 0.17 M $[Co(dtb)_3]^{2+}$/0.017 M $[Co(dtb)_3]^{3+}$, respectively

5.2.14 Transient absorption spectroscopy measurements

Transient absorption spectroscopy, TAS, was performed with an apparatus described in Chapter 8[19] by using the 532 nm harmonic of a nanosecond Nd:YAG laser (Continuum Surelite II). A typical pulse energy of 2 mJ cm^{-2} was used. A 532 nm notch filter prevented laser light from reaching the photomultiplier, whereas a 420 nm cut-off filter, placed in front

of the white light probe beam prevented direct TiO_2 excitation. From 10 to 30 laser shots, at a frequency of 0.2 Hz were averaged to reach a good S/N ratio. The photoelectrodes were prepared by doctor-blading TiO_2 18NR-T paste on FTO substrates. After a programmed ramp heating up to 500°C the $TiClO_4$ treatment was applied, by immersing the electrodes in a 0.4 M aqueous solution overnight, after which they were heated at 450°C for 30 minutes. Once cooled, the electrodes were immersed in a 0.2 mM solution of the dye **D1** in an ethanol/tetrahydrofuran 9:1 mixture overnight for the sensitization.

TAS was carried out on **D1**-sensitized transparent TiO_2 films in contact with an acetonitrile 0.1M LiOTf solution (blank) and with the electron donating electrolytes in acetonitrile 0.1M LiOTf, by drawing the solution by capillarity inside the chamber constituted by a FTO slide pressed against the TiO_2 photoanode.

Regeneration efficiency was calculated by applying the formula:

$$\eta = \frac{k'_{reg}}{k'_{reg} + k'_{rec}} \qquad \text{(Eq.5.1)}$$

where the first order recombination, k'_{rec}, and pseudo-first order regeneration, k'_{reg}, rate constants were obtained by fitting the experimental decay curves with a biexponential function:

$$y = A_1 \exp\left(-\frac{x}{t_1}\right) + A_2 \exp\left(-\frac{x}{t_2}\right) + y_0 \qquad \text{(Eq.5.2)}$$

following the equation:

$$k' = \left(\frac{A_1 t_1^{\,2} + A_2 t_2^{\,2}}{A_1 t_1 + A_2 t_2}\right)^{-1} \qquad \text{(Eq.5.3)}$$

The following solutions were tested:

- 0.1M LiOTf in acetonitrile (blank)
- 0.146M 1-methyl-3-propylimidazolium iodide, 0.024M LiI, in acetonitrile ($\mathbf{I^-}$)
- 0.17M $[Co(dtb)_3](OTf)_2$, 0.1 M LiOTf , in acetonitrile (**Cobalt**)
- 0.17 M **1**, 0.1 M LiOTf , in acetonitrile (**1**)
- 0.17 M **3**, 0.1 M LiOTf , in acetonitrile (**3**)
- 0.17 M **5**, 0.1 M LiOTf , in acetonitrile (**5**)

5.2.15 Determination of redox potentials of electrolytes

The redox potential of the electrolytes, E_{redox}, was experimentally determined through three-electrode voltammetric measurements recording a cyclic voltammogram of a solution

containing *ca.* 0.001 M Fc dissolved in acetonitrile with 0.1 M tetrabutylammonium hexafluorophosphate as supporting salt. A glassy carbon electrode was employed as working electrode, a platinum wire as counter electrode and an electrode filled with the tested electrolyte as reference electrode. The redox reference electrode was prepared by filling a small glass tube ending with a porous frit (assuring the electric contact) with about 100 µl of the solution then employed in DSSC, and tipping in it a well-polished platinum wire. After each measurement the wire was rinsed with fresh acetonitrile and deionised water, then tipped for some minutes in concentrated HNO_3, abundantly rinsed with water, then sonicated in water and finely dried.

In this way the half-wave potential of $Fc^+|Fc$, $E_{1/2,Fc+/Fc}$, was detected respect to the E_{redox} of the tested electrolyte.

5.2.16 Thin layer cell study

Slow scan rate cyclic voltammetry (10mV/s) was carried out with an Autolab PGSTAT302N potentiostat, employing PEDOT electrodes to study **1**/**2**-El in symmetric (i.e. two identical electrodes) thin layer dummy cells having active area of 0.25 cm^2 sealed with a 25 µm inter-electrode spacing (Surlyn®, DuPontTM). PEDOT films were electrodeposited on FTO as previously reported.

5.3. Results and Discussion

Among Copper complexes, **3**, **5** and the equivalent oxidized **4**, **6** forms are known and obtained by a procedure reported in literature [12-13]. On the other hand, complex **1** and its oxidized form **2** are new and can be obtained by mixing copper salts with the appropriate ligand. **D2** porphyrin is new as well and was synthesized following the same procedure that was adopted for the already reported **D1** [10]. The difference between the two porphyrins is attributable only to the anchoring group, which is a cyanoacryl one in **D1** and a carboxyl in **D2**. For what concern the energetics, the two porphyrins are almost identical and the absorption and emission properties of the new porphyrin dye **D2** are similar to those previously reported for **D1** [10] (Table5.1)

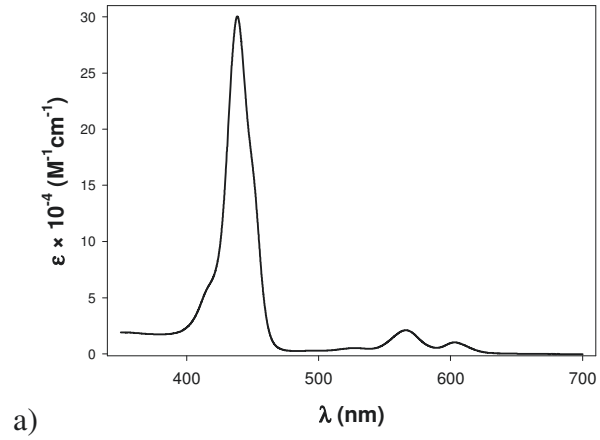

a)

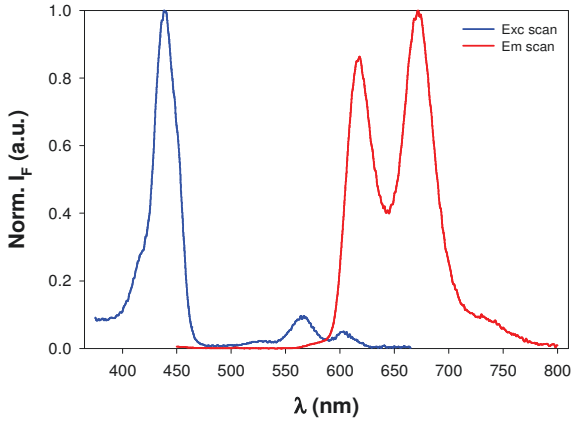

b)

Fig.5.4 a) Absorption spectrum of Zn^{2+}-porphyrin **D2** in THF solution; **b)** Excitation (λ_{em}: 672 nm) and emission (λ_{exc}: 438 nm) spectra of **D2** in THF solution. (Data recorded by M.Pizzotti group at the University of Milan)

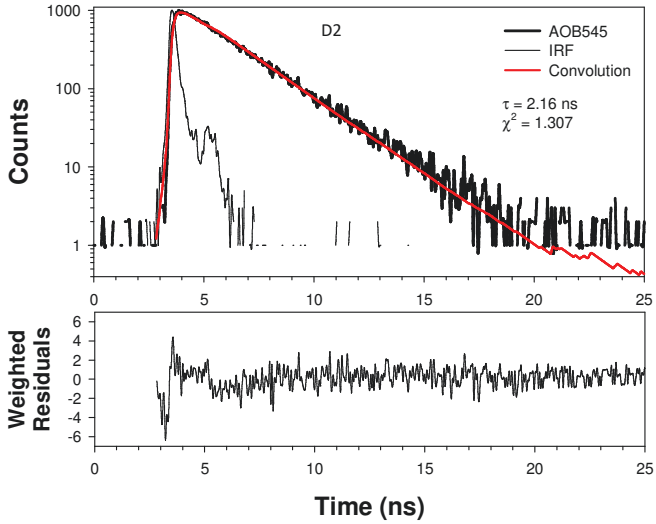

Figure 5.5 Fluorescence decay of **D2**, bold black line (λ_{exc} 445nm; λ_{em} 617 nm). Instrument response function (IRF) and convolution fit black line and red line respectively. Weighted

residuals are shown under the decay curves. (Data recorded by M.Pizzotti group at the University of Milan)

Table 5.1 Absorption and emission data of **D1** and **D2**. Photoluminescence quantum yields (Φ), photoluminescence lifetimes (τ). [b] Reference 10.

Dye	λ_B (nm)	λ_Q (nm)	λ_{ex} (nm)	λ_{em} (nm)	Φ (%)	τ (ns)
D1[b]	438	566 604	439	616 671	3.8	2.38
D2	438	566 604	438	617 672	4.0	2.16

Furthermore, **D2** dye is characterized by two subsequent reversible oxidation processes (Fig.5.6) centred on the porphyrinic core like those reported for **D1** (Table 5.2). The excited state half-wave potential for both porphyrins calculated from Eq.5.4 is in very good agreement with the ground-state $E_{1/2,\,IRd}$ directly estimated by CV (Table5.2).

$$E_{1/2}(S^*/S^+) = -\left(\frac{U_{0-0}}{e} - E_{1/2,IOx}\right) \qquad \text{(Eq.5.4)}$$

Where e is the unitary charge and $U_{0\text{-}0}$ the 0-0 transition energy, estimated as $U_{0-0} = hc / \lambda_{cross}$ by the wavelength at the cross point (λ_{cross}) between normalized absorption and emission spectrum.

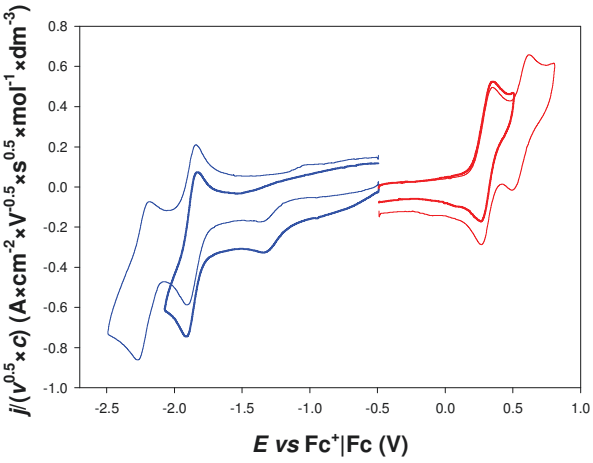

Fig.5.6 CV patterns of **D2** on glassy carbon electrode, in N,N'-dimethylformamide with 0.1 M $TBAPF_6$, at 0.2 Vs^{-1}.

Table 5.2 [a]Some electrochemical parameters of **D1** and **D2** sensitizers in solution recorded from cyclic voltammetry, CV, in N,N'-dimethylformamide with tetrabutylammonium perchlorate 0.1M.
[b] Reference 10.

Dye	$E_{1/2,I\ Ox}$ *vs* $Fc^+|Fc$ (V)[a]	$E_{1/2,I\ Rd}$ *vs* $Fc^+|Fc$ (V) [a]	$U_{0\text{-}0}$ (eV)	$E_{1/2}(S^*/S^+)$ *vs* $Fc^+|Fc$ (V)
D1[b]	0.29	–1.83	2.11	–1.82
D2	0.31	–1.87	2.12	–1.81

In order to get a deeper inside of the electrochemical properties of the redox mediators, cyclic voltammetry (CV) measurements and electrochemical impedance spectroscopy (EIS) were carried out. The half-wave potential calculated from cyclic voltammetry referred to complex **1** is more positive with respect to the one recorded for **3**, consistent to the absence of electron donating methyl groups in 4,7 positions of the phenanthrolines. Actually all the half-wave potentials of copper complexes are higher than $[Co(dtb)_3](OTf)_2$. For this reason, we can expect open circuit voltages reasonably greater for this class of mediators. Advantages of employing Copper couples seem to be substantial also in terms of kinetic and mass transport. The apparent diffusion coefficients (D_{red}) of the Co(III)/Co(II) and Cu(II)/Cu(I) species were estimated from cyclic voltammetry measurements and calculated from the Randles-Sevcik equation [20] (Eq.5.5), by plotting the anodic peak current (i_{pa}) vs scan rate ($v^{1/2}$).

$$I_{pa} = (3.01 \times 10^5)\, n^{3/2}\, \alpha^{1/2}\, A D_{red}^{1/2}\, v^{1/2}\, C \qquad \text{(Eq.5.5)}$$

Where n represents the number of exchanged electrons, C the bulk concentration of the electroactive species, A the electrode surface area, and D_{red} the diffusion coefficient of the complexes when using anodic peak current. Diffusion coefficients (Table5.3) calculated for Copper mediators are comparable, while the one referred to Cobalt complex is a half, probably due to the presence of six bulky *tert*-butyl substituents in the ligand sphere. Kinetic properties of the couples were investigated by electrochemical impedance spectroscopy by employing glassy carbon electrodes as working electrodes and recording impedance of all complexes at the half-wave potential. Data were fitted with a Randles-type equivalent circuit to estimate the charge transfer resistance, R_{CT}, at the electrolyte/electrode interface in order to calculate heterogenous rate constants (k_{heter}), according to Eq 5.6.

$$k_{heter} = \frac{i_0}{FC_{Rd}} = \frac{RT}{F^2 R_{CT} C_{Rd}} \qquad \text{(Eq.5.6)}$$

where i_0 is the exchange current density, F the Faraday constant, C_{Rd} the concentration of the reduced complex (in mol cm^{-3}), R is the gas constant, T the absolute temperature. Electron transfer is faster regarding copper complexes (Table5.3). The reason of this

behaviour should be found in Copper coordination sphere: the hindered phenanthroline ligands can minimize geometry modification of Copper complexes during electron transfer, lowering the kinetic barrier.

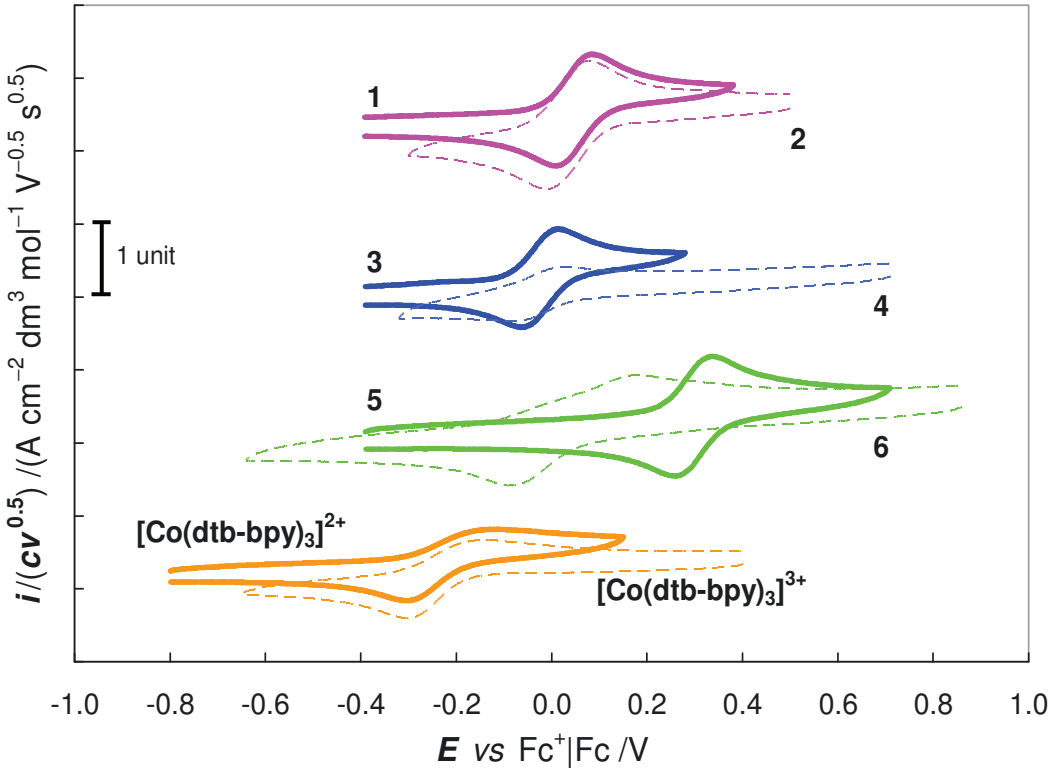

Fig.5.7 Cyclovoltammetric (CV) patterns of Cu-based redox mediators, **1**-**6**, and $[Co(dtb)_3](OTf)_2$ in acetonitrile with 0.1 M $TBAPF_6$.

Table 5.3 Half-wave potential, $E_{1/2}$, heterogeneous rate constant, k_{heter}, and apparent diffusion coefficient, D_{Red}, of the reduced form of redox couples employed in the formulation of electrolytes for DSSCs.

Complex	$E_{1/2}$ ***vs*** **Fc^+|Fc (V)**	k_{heter} **(cm s^{-1})**	D_{Red} **(cm^2 s^{-1})**
1	0.06	$9.1 \cdot 10^{-3}$	$8 \cdot 10^{-6}$
3	–0.02	$6.9 \cdot 10^{-3}$	$7 \cdot 10^{-6}$
5	0.30	$2.0 \cdot 10^{-2}$	$1.04 \cdot 10^{-5}$
$[Co(dtb)_3]^{2+}$	–0.21	$1.10 \cdot 10^{-3}$	$3.9 \cdot 10^{-6}$

From CV and EIS analysis in a three-electrode cell, it is clear that copper complexes are promising candidates for the employment in dye sensitized solar cell, also with respect to the $[Co(dtb)_3]^{2+/3+}$ based couple. Results of the investigated thin film (ca. 6 μm) transparent DSSCs are presented in Table 5.4. The formulation of Copper based electrolytes was studied in order to obtain the higher solubility with these mediators, adding the oxidized form to

improve fill factor (FF) and to reach quickly the steady state. Copper electrolytes were prepared by dissolving the redox couple (0.17M Cu^{+}/0.017M Cu^{2+}) in acetonitrile with 0.1 M LiOTf as supporting salt and 0.25 M 4-*tert*-butylpyridine (TBP) as additive to improve the V_{OC} of the devices. For sake of comparison, reference electrolytes based on cobalt, $[Co(dtb)3]^{2+/3+}$-El, and iodine/triiodine, I^{-}/I_3^{-}-El, were not optimized but prepared in identical way, to evidence intrinsic differences among the tested cells avoiding effects simply due to the mismatch of the electrolyte compositions and the mediator concentrations. From data recorded in DSSCs we can appreciate that the new electrolyte **1**/**2**-El presents the higher efficiency (η), mostly due to its high open circuit voltage (*Voc*) which is inferior only to the one reached with the Cu reference electrolyte **5**/**6**-El. Furthermore, we would like to point out that despite **5/6**-El presents the higher *Voc* its η is substantially lower than the one reported for **3/4**-El, confirming previous reports [12]. Incident photon–to-current conversion efficiency curves are in total agreement with data extrapolated from J-V measurements (Fig.5.8, bottom), with the only exception of **1/2**- El which shows a IPCE lower than the one recorded for Cobalt based electrolyte and I^{-}/I_3^{-}-El. The phenomenon is attributable to the light-harvesting competition of **1**/**2** -El with **D1** porphyrin at 460 nm where phenanthroline copper complexes have their maximum absorption (Fig.5.3). On the other hand, at wavelength >550nm IPCE curves related to **1**/**2** -El are superimposable to curves related to Cobalt-El and I^{-}/I_3^{-}-El.

Table 5.4 Photoelectrochemical performances of DSSCs. Data are referred to at least two replicates.

Dye	**Electrolyte**	**j_{SC} (mA cm^{-2})**	**V_{OC} (V)**	**FF**	**η %**
D1	**1/2-El**	5.9±0.1	0.81±0.01	0.77±0.01	3.7±0.1
D1	**3/4-El**	5.6±0.5	0.68±0.04	0.77±0.05	2.9±0.4
D1	**5/6-El**	3.5±0.2	0.86±0.05	0.70±0.03	2.1±0.2
D1	**Cobalt–El**	8.0±0.2	0.58±0.02	0.63±0.05	2.9±0.2
D1	**I^{-}/I_3^{-}-El**	8.6±0.1	0.60±0.01	0.66±0.02	3.4±0.1
D2	**1/2-El**	4.8±0.3	0.75±0.03	0.74±0.04	2.7±0.3

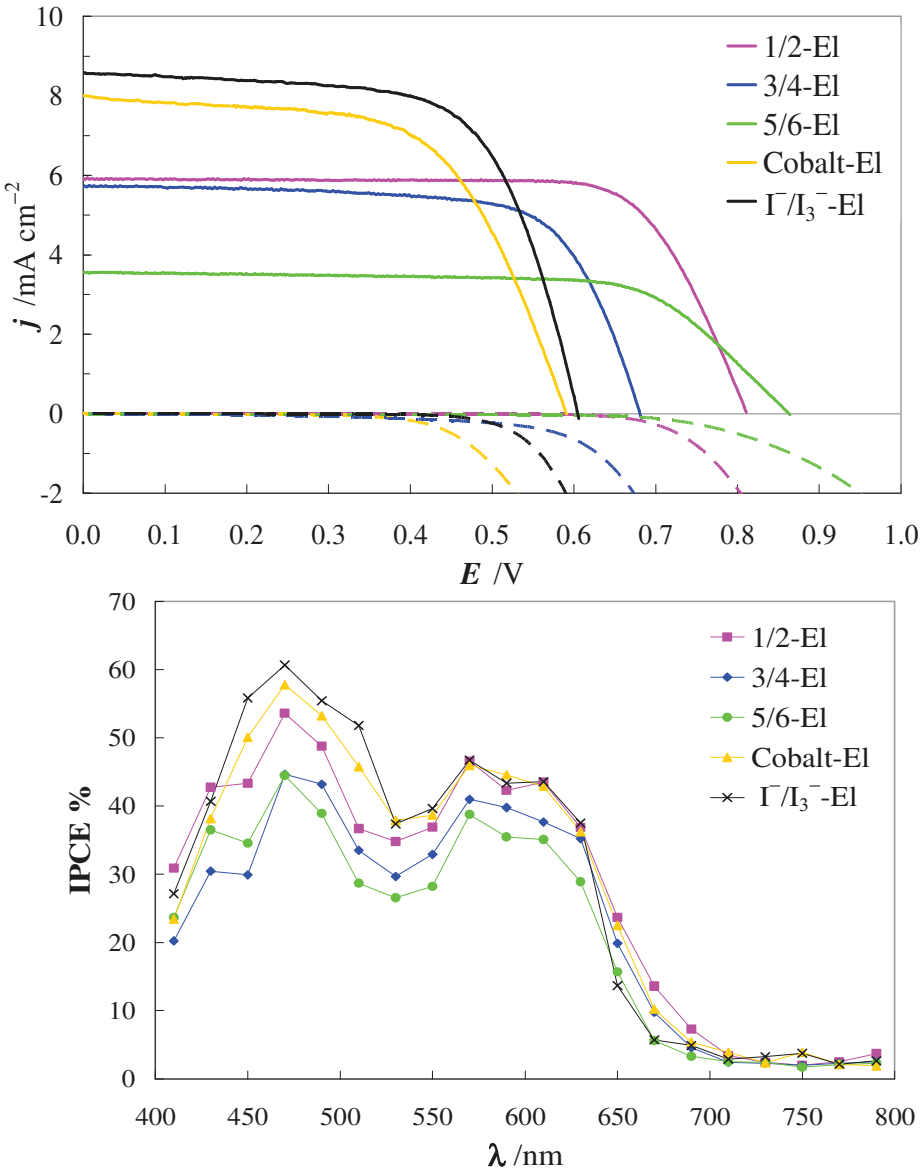

Fig.5.8. Top: current-voltage curves under 100 mW cm^{-2} AM 1.5G illumination (solid lines) and in dark (dashed lines) of **D1**-sensitized DSSCs. Bottom: photoaction spectra of the devices.

Transient absorption spectroscopy (TAS) was recorded to evaluate the kinetic of dye regeneration to have a deeper insight of the dynamics that govern trends in DSSCs. In general, all the monoelectronic couples based on coordination metal complexes exhibit, at comparable concentration, nearly unitary dye regeneration efficiencies (91-85%, Table 5.5) and are superior to the equimolar iodide based electrolyte (71%). The best regeneration was found with **3/4-El** and **5/6-**El.

Table 5.5 Parameter fitted by dye recovery traces for pseudo-first order regeneration kinetic constants, k'_{reg}, and for dye regeneration efficiency, η_{reg}, for **D1**-sensitized TiO_2 anodes. Apparent recombination constant, k'_{rec}, was estimated to be $2.9 \cdot 10^4$ s^{-1} from a blank solution (AcN + LiOTf 0.1M).

Electron donor	k'_{reg} (s^{-1})	η_{reg} %
0.17 M **1**	$1.63 \cdot 10^5$	85
0.17 M **3**	$2.88 \cdot 10^5$	91
0.17 M **5**	$2.99 \cdot 10^5$	91
0.17 M $[Co(dtb)_3]^{2+}$ (**Cobalt**)	$1.71 \cdot 10^5$	85
0.17 M I^-	$7.25 \cdot 10^4$	71

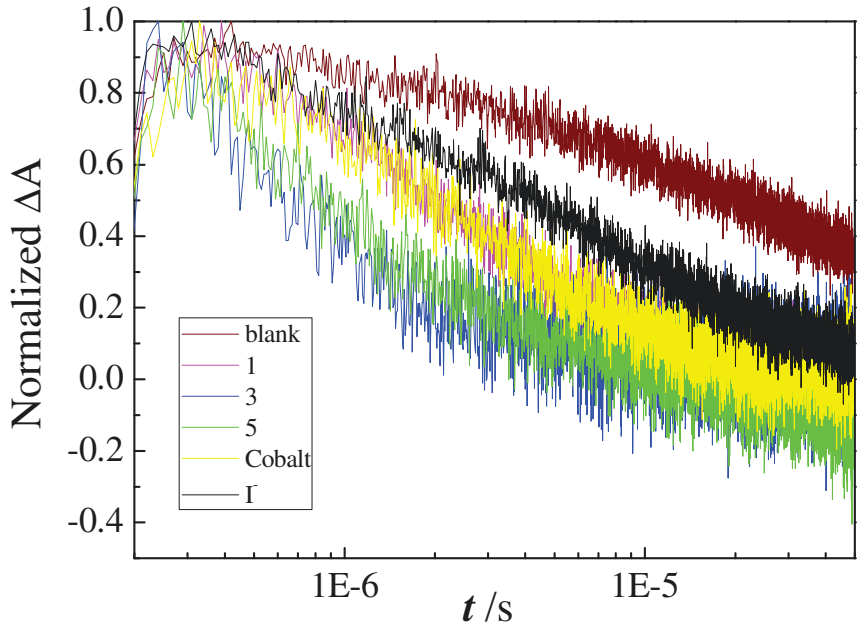

Fig.5.9: Dye recovery traces of transparent **D1**-sensitized TiO_2 anode by 0.17 M solution of electron donor **1**, **3**, **5**, $[Co(dtb)_3]^{2+}$ (**Cobalt**), I^- and by a blank solution.

TAS measurement does not explain the lower incident photon-to-current conversion efficiency generated by **5/6**- El, which in purely theoretical terms has the best percentage photopotential conversion (Table 5.6), presenting the strongest oxidative power of all the investigated electrolytes.

E_{redox} of all the electrolytes employed in DSSCs was calculated, by referring to $Fc^+|Fc$. The half-wave potential of $Fc^+|Fc$, $E_{1/2,Fc+/Fc}$, was detected respect to the E_{redox} of the tested electrolytes; hence the redox potential of the electrolyte corresponds to $E_{redox} = -E_{1/2,Fc+/Fc}$. The corresponding energy of their Fermi level, $U_{F,redox}$, was calculated by the equation 5.7:

$$U_{F,redox} = -e(E_{redox} + 4.8) \qquad \text{(Eq.5.7)}$$

where e=1 C and 4.8V stands for the recommended redox potential of the ferrocenium/ferrocene couple *versus* vacuum [21]. The Fermi-level energy ($U_{F,redox}$) of **5**/**6** was found to be –4.76 eV as reported in Table 5.6, demonstrating its higher oxidative power with respect to the other couples. Consequently, in order to gain a major characterization of devices and of mechanisms that govern their efficiency, Electrochemical Impedance Spectroscopy (EIS) was carried out on **D1**-sensitized solar cells in conjunction with all the redox couples. In Fig.5.10 are reported Nyquist plots for copper based electrolytes. Lifetime of electrons in the TiO_2 (Fig.5.11 a) and conduction band energy (U_{CB}) were calculated from EIS analysis. The first was estimated by the product of recombination resistance at TiO_2/electrolyte interface (R_{CT}) and chemical capacitance (C_μ). The second one was estimated according to the following equation [22]:

$$n_{CB} = N_{CB}\exp\left(\frac{U_{Fn}-U_{CB}}{kT}\right) \quad \text{(Eq.5.8)}$$

with k the Boltzmann constant, T the absolute temperature, N_{CB} the density of state calculated as:

$$N_{CB} = 2\left(\frac{m_e^* kT}{2\pi\hbar^2}\right)^{3/2} \quad \text{(Eq.5.9)}$$

(where $m_e^*=2.3m_e$ was selected as the effective mass of an electron) and n_{CB} the concentration of conduction band electrons calculated according to:

$$n_{CB} = k\ \ TC_\mu/e^2 \quad \text{(Eq.5.10)}$$

(with e the elementary charge) which was estimated from the chemical capacitance of TiO_2 film (C_μ) at V_{OC} under full sunlight illumination, obtained by EIS fitting (Fig.5.11 b). U_{Fn}, namely *quasi*-Fermi level of TiO_2 at open circuit, was evaluated as $U_{Fn} = U_{F,redox} + eV_{OC}$.

5/**6**-El was found to be the redox couple with the longest lifetime (τ) for electrons in TiO_2, resulting in the narrowest gap between the conduction band energy (U_{CB}) and the quasi-Fermi level of TiO_2 (U_{Fn}) within the explored series(Table 5.6, Fig.5.11 a). As a consequence, its low efficiency cannot be attributed neither to a poorer dye regeneration (Table 5.5) nor to any recombination phenomena. It could be attributed to limitations due to mass-transport. As reported in a previous work [13], diffusional resistance is the main resistive contribution for what concern **5**/**6**-El (Fig.5.11 d, e) and is a drawback that could explain the low photocurrent and fill factor observed for the DSSC based on such electrolyte. While, if we consider **1**/**2** couple, namely the best electrolyte tested in the present work, its efficiency is attributable to thermodynamic reasons. Regarding electron lifetime in TiO_2 (Fig.5.11 a), dye regeneration constants (Table.5.5) and total resistance (R_{tot}) (Fig.5.11 c), **D1**-sensitized DSSCs, filled with **1**/**2**-El, present a similar behaviour with respect to cells filled with Cobalt electrolyte and **3**/**4** electrolyte, but **1**/**2**-El has a more positive redox

potential (Table 5.6) which leads to an increase of the V_{OC} from 0.58 V, for Cobalt–El**,** and 0.68 V, for **3/4 -**El, to 0.81 V. In agreement with this thermodynamic explanation, similar U_{CB}–U_{Fn} values were obtained (Table 5.6), suggesting comparable charges in the two cells and hence comparable rate of recombination

Table 5.6 E_{redox}, $U_{F,redox}$, U_{Fn}, and U_{CB}, at open circuit potential of **D1**-DSSCs.

Electrolyte	E_{redox} *vs* Fc^+|Fc (V)	$U_{F,redox}$ (eV)	U_{Fn} (eV)	U_{CB} (eV)	U_{CB}–U_{Fn} (eV)	**photopotential conversion %**[f]
1/2-El	–0.10	–4.70	-3.89	–3.38	0.51	61
3/4-El	–0.20	–4.60	-3.92	–3.42	0.50	58
5/6-El	–0.04	–4.76	-3.90	–3.45	0.45	66
Cobalt–El	–0.28	–4.52	-3.94	–3.44	0.50	54
I^-/I_3^--El	–0.32	–4.48	-3.88	–3.40	0.48	55

[f] Calculated comparing the generated photopotential V_{OC} respect to the theoretical maximum photopotential (U_{CB}–$U_{F,redox}$)/e.

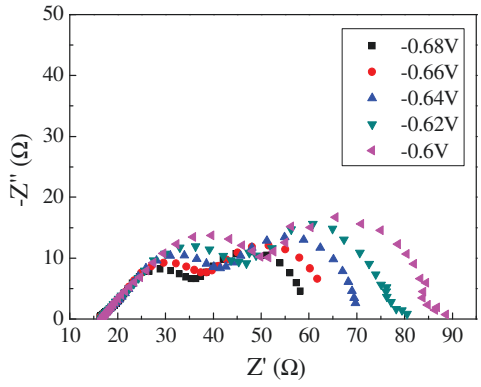

a)

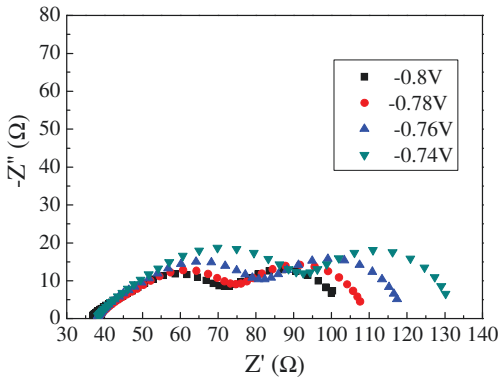

b)

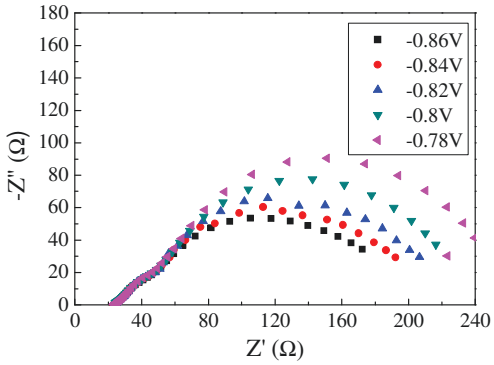

c)

Fig.5.10 Nyquist plots for **D1** sensitized DSSC based on: a) **3/4** -El, b) **1/2** -El, c) **5/6** –El

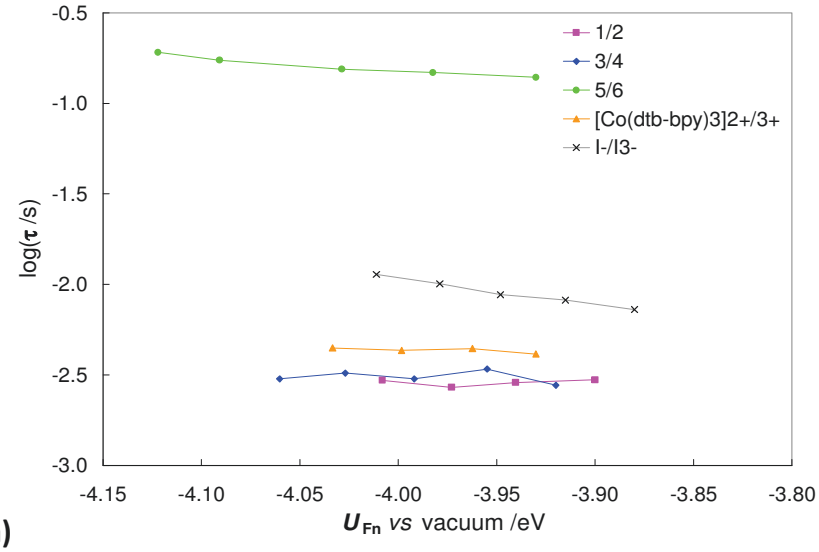

a)

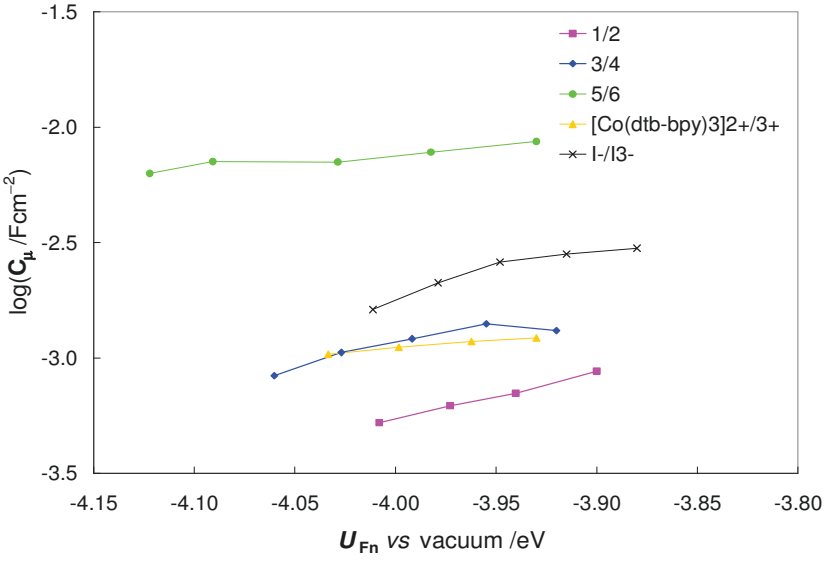

b)

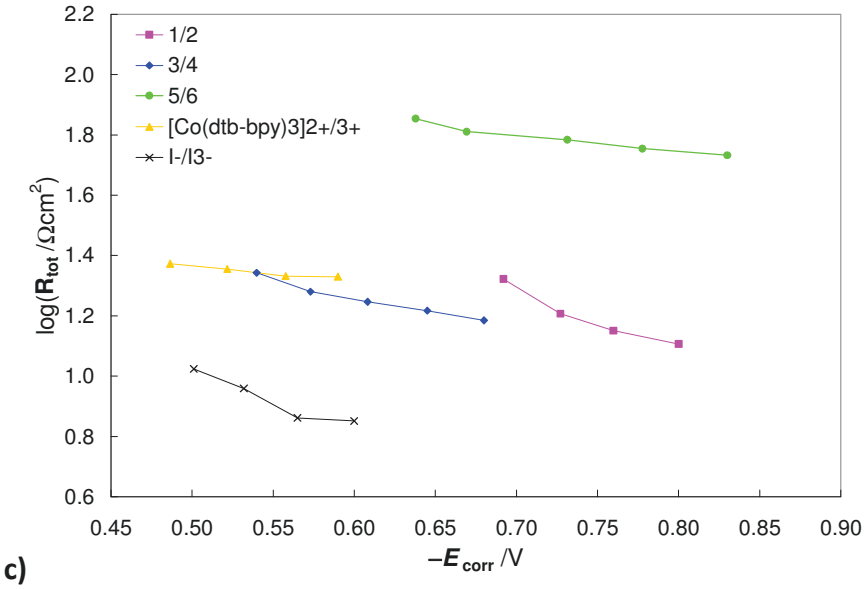

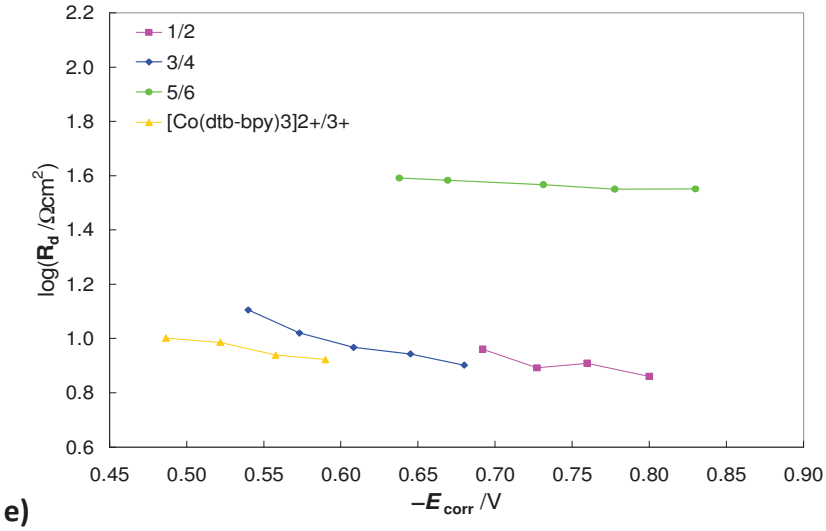

Fig.5.11 a) electron lifetime $\tau = R_{CT}C_{\mu}$ and **b)** C_{μ} chemical capacitane as a function of electron Fermi level in TiO_2, U_{Fn}; **c)** total resistance R_{tot} and **d)** diffusional resistance R_d as a function of corrected bias potential E_{corr}

The most promising redox couple, *i.e* **1/2**, was tested in PEDOT-PEDOT symmetric thin layer dummy cell in order to try-out its stability upon electrochemical cycles. No loss in electroactivity nor appearance of electroactive decomposition byproducts were observed upon repeated cyclings, confirming the stability of **1**/**2**-El response on substrates based on cathode material even under concentrations suitable for the application in a dye sensitized solar cell (Fig.5.12). Similar stability tests conducted on **3/4** and **5/6** copper redox couples are reported in literature [12], showing a lower cathodic response for what concern **5/6** couple [12].

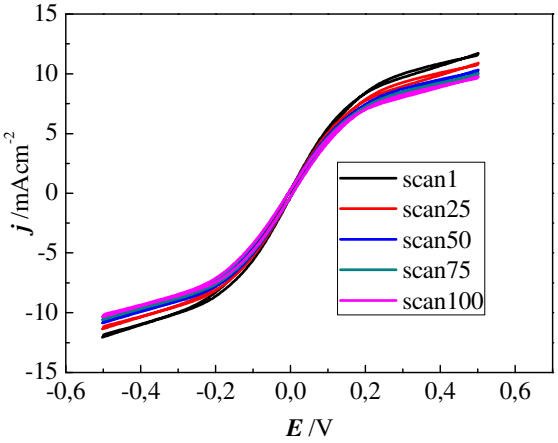

Fig.5.12: Stability test of **1**/**2**-El by scanning potential up to 100-times in symmetrical PEDOT/PEDOT dummy cell.

Furthermore, to gain a major understanding of **1**/**2** couple behaviour, the new electrolyte was tested with the **D2** Zn^{2+} porphyrin. Comparison with **D1** is reported in Fig.5.13. The constantly lower IPCE (Fig.5.13) together with the lower j_{sc} point towards a sluggish electron injection, notwithstanding the comparable energy of the $S^*|S^+$ excited state ($E_{1/2}(S^*|S^+$ = –1.82 and –1.81 V for **D1** and **D2**, respectively; Table 5.2). This behaviuor can reasonably be explained by an energy increase of the conduction band edge with **D2**, leading to a lower driving force for the electron injection, attributable to the different nature of the anchoring group, being the electrolyte exactly the same.

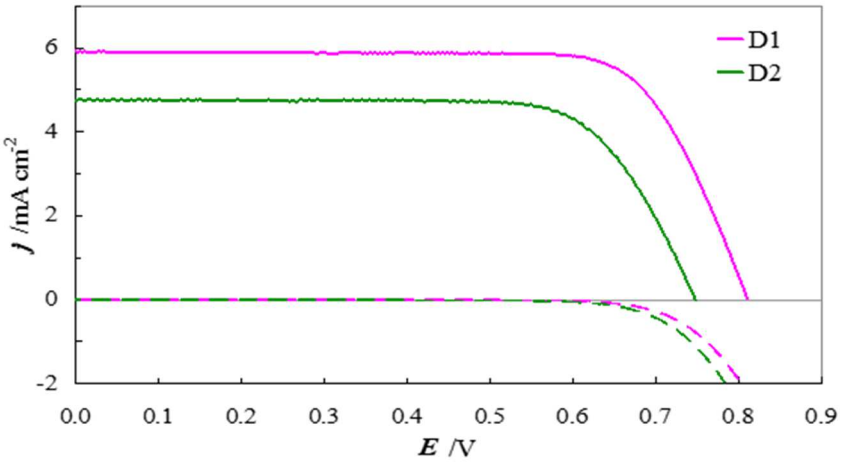

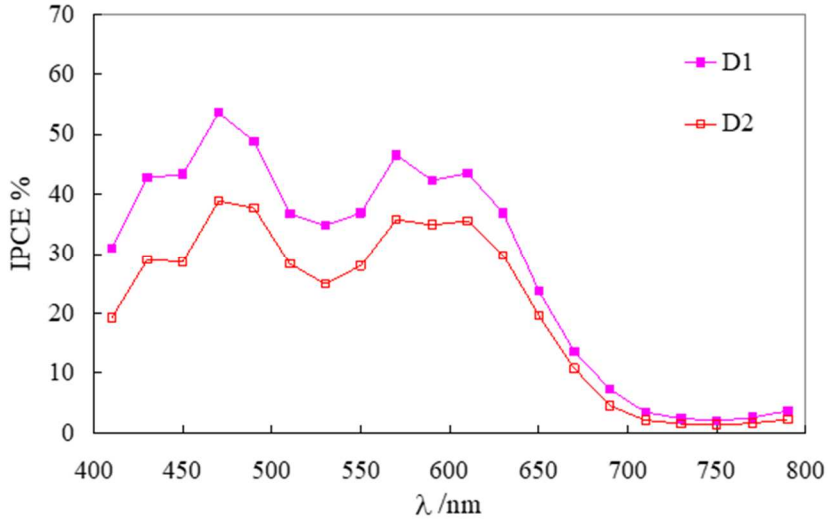

Fig.5.13 Top: current-voltage curve under 100 mW cm^{-2} AM 1.5G illumination of **D2**-sensitized DSSCs, filled with **1**/**2**-El. For sake of comparison **D1**-sensitized cell is also reported. Bottom: Photoaction spectra of the devices.

5.4. Conclusions

In conclusion this work has shown the great potential of Cu complexes that can be coupled with one of the most efficient classes of sensitizers, Zn^{2+} porphyrins in transparent solar cells. The new $[Cu(2\text{-mesityl-}1,10\text{-phenanthroline})_2]^{+/2+}$ **1/2** couple is particularly efficient when combined with **D1**, reaching a remarkable 75% increase of η with respect to the **5/6** Cu-reference thanks to a better diffusional behaviour. Removal of the electron releasing methyl groups from the positions 4,7 of the phenanthroline leads to an improvement of cell efficiency due to a quite high V_{OC}. Moreover, as a result of a more oxidizing $U_{F,redox}$, **1/2-**El overcomes $[Co(dtb)_3]^{2+/3+}$ and I^-/I_3^- reference couples. Remarkably, Cu^+ complexes are efficient electron donors toward **D1**, reaching dye regeneration constants up to 4-fold faster than I^-, in equimolar conditions (Table 5.5). Thus, combination of β-substituted tetraaryl Zn^{2+} porphyrin dyes with copper-based redox mediators represents a novel route to low cost, environmental friendly DSSCs. This first report opens the way to new promising prospects through which optimization of electrolyte composition, copper complex solubility, photoanode architecture and exploitation of other Zn^{2+}-porphyrins will surely result in a net improvement of DSSCs efficiencies.

5. 5 References

1) M. Graetzel, et al. *Chem. Commun.* **2008**, 2635;

2) S.L. Wu, et al. *Energy Environ. Sci.* **2010**, 3, 949;

3) C.W. Lee, et al. *Chem. Eur. J.* **2009***,* 15, 1403;

4) G. Di Carlo, S. Caramori, et al. *ACS Applied Mater. Interf.* **2014***,* 6, 15841;

5) M. Graetzel, et al. *J. Phys. Chem.* **1993**, 97, 6272;

6) J.R. Durrant, et al. *J. Phys. Chem. B* **2000**, *104* (6), pp 1198;

7) E.J. Palomares, *Mater. Chem.* **2008**, *18*, 1652;

8) J. Bisquert, et al. *J. Phys. Chem. C* **2011**, *115*, 10898;

9) M. Graetzel, et al. *Angew. Chem.* **2014**, *126*, 3017;

10) A. Covezzi, A. Orbelli Biroli, at al. *Chem. Commun*. **2016**, *52*, 12642;

11) D.L. Jameson, et al. *Inorganica Chimica Acta* **2000**, *307*, 7;

12) M. Magni, R. Giannuzzi, et al. *Inorg Chem*. **2016**, *55*, 5245;

13) M. Freitag, et al. *J. Phys. Chem. C* **2016**, *120*, 9595;.

14) S. Caramori, et al. *J. Am. Chem. Soc.* **2002**, *124*, 11215;

15) A. Colombo, C. Dragonetti, et al. *ACS Appl. Mater. Interfaces* **2014**, *6*, 13945;

16) Y. Bai, At al. *Chem. Commun*. **2011,** *47*, 4376;

17) S. Carli, et al. *J. Phys. Chem. C*, **2013**, *117*, 5142;

18) F. Ronconi, et al. *Dalton Trans*. **2016,** *45*, 14109;

19) M. Mba, et al. *J. Phys. Chem. C* **2013**, *117,* 19885;

20) F. Ghamouss, R. Pitson, F. Odobel et al., *Electrochimica Acta* **2010**, *55*, 6517;

21) S. Trasatti, *Pure & Appl. Chem.* **1986**, *58*, 955-966;

22) D. Mandal, T. Hamann, *ACS Appl. Mater. Interfaces* **2016,** *8,* 419;

CHAPTER 6. ELECTROCHEMICAL CHARACTERIZATION OF POLYPYRIDINE IRON (II) AND COBALT (II) COMPLEXES FOR NON-ACQUEOUS REDOX FLOW BATTERIES.

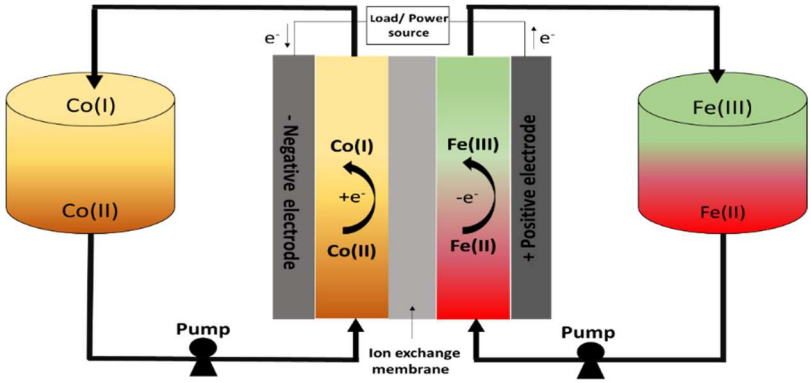

Fig.6.1 Schematic of a Co(II)/Co(I) and Fe(III)/Fe(II) based redox flow battery. The cell is shown under charge.

The electrochemical properties of a series of Iron and Cobalt complexes, based on chelate ligands, were explored with the aim of finding promising candidates for application in high voltage organic flow cells. The reported compounds were selected by considering the stability of the electrochemical response of the Fe(III)/(II) and Co(II)/(I) couples on carbon based electrodes and their solubility in a mixture of ethylene and propylene carbonates (EC:PC) chosen as low volatility and electrochemically stable solvents. The most promising compounds, which lead to limiting current of the order of 30 mA/cm^2 in thin layer cell, were also preliminarily tested in a lab. scale flow cell equipped with a Nafion membrane, where a good stability and reversibility in open circuit potential (≈ 1.9 V) and *ca.* 90 % coulombic efficiency were recorded. Nevertheless, the deterioration of membrane conductivity, resulting in energy conversion efficiency of *ca.* 20 %, was observed. A change of membrane characteristics should be considered to exploit the full potentiality of these redox mediators.

6.1 Introduction

As previously reported, since 1980s numerous chemistries have been explored and among them the aqueous vanadium-based batteries represent nowadays the state-of-the art for the market penetration [1-5]. Besides, aqueous batteries are not immune from concerns and problems, such as small potential window (1.23V) for water stability (which essentially coincides with the voltage delivered by the V(IV)→ V(V) and V(III)→ V(II) redox couples) and limited solubility of a variety of couples, which compromise their energy density and,

as a consequence, their efficiency [6-8]. Currently, first row transition metal complexes have been considered as redox active species in non-aqueous redox flow batteries (NA-RFB) with encouraging results [9]. The advantages to employ redox couples based on metal complexes are several, for instance the possibility to easily tune electrochemical properties by varying coordination sphere of transition complexes, the existence of wider stability windows in non-aqueous solvents and the chance to reach higher energy density and multiple electron transfer. The Earth-abundant metals, which are available at relatively low cost, comprise chiefly first row transition elements such as Mn [12], Fe [14,15,16,18] Co [15-18], Ni [14], Cr [10-11] and V [13]. To date, metal-complexes in non-aqueous RFBs do not compete with vanadium RFBs in term of long-term efficiency, and so additional work must be carried out. For what concerns cost, a combination of factors must be satisfied, such as: cell voltage towards 3 V, electrolyte cost below 5 $/kg, molecular weights of complexes below 200 g/mol [19]. Recent studies, aimed at increasing complex solubility, have functionalised the backbones of simple ligand structures, such as acetylacetonate or bipyridine, with polar moieties that possess more preferential solvent interactions [8]. However, there are few studies thus far which have modified the intrinsic ligand structure to customise the electrochemistry of the complexes, in order to increase the cell potential [8]. In this work we have explored the electrochemical properties of a series of cobalt (Co(II)/(I)) and iron complexes (Fe(III)/(II)) as triflate and tetrabutyl-ammonium salts, in order to couple solubility and reversible or *quasi*-reversible electrochemistry to the possibility of extracting large cell voltages. Co (II) to Co (I) reduction and Fe(II) to Fe(III) oxidation are centered on orbitals with prevailing metal character, thus avoids, unlike cathodic and anodic couples based on organic species, formation of organic radicals characterized by high reactivity, which can give rise to collateral reactions damaging the long-term chemical stability of redox species [20]. Furthermore, oxidative and reductive processes centered on metals do not involve breaking and formation of chemical bonds and are often kinetically fast mono-electronic processes, implying, in principle, reduced overvoltage during device charge and discharge. In order to find ligands suitable for use in redox flow batteries, it is interesting to note that there is a large synthetic library developed in recent years in the field of dye-sensitized solar cells, where both the chromophore and the redox mediator are often coordination compounds whose redox properties are tuned to optimize harvesting and energy conversion [21]. Synthetic simplicity and chemical stability have oriented us towards the preparation of polypyridine chelants derived by pyridine condensation, in particular, those with secondary amines or hetero-cycles were selected and substituted by alkyl- and aryl-groups. Co (II) or Fe (II) complexes can be generated by mixing appropriate Co (II) or Fe

(II) salts with stoichiometric ratios of monodentate, bidentate or tridentate ligands, or mixture of these. In particular, our work is focused on the study of **1**, **2**, **3** [22], **4** [23], **5** (Fig.6.3) Cobalt species used as negative couples and Iron(II) **6,7,8,9** [24] complexes as positive couples (Fig.6.4). 4-4' substituents of 2-2'-bipyridine were considered in order to cathodically shift the redox potential of Co(II)/Co(I) and in general, to tune the solubility in the organics. Moreover a cobalt hexadentate and a negatively charged heteroleptic complex were synthesized in order to test higher stability with respect to either ligand dissociation (**5**) or electrode passivation under negative polarization (**4**).

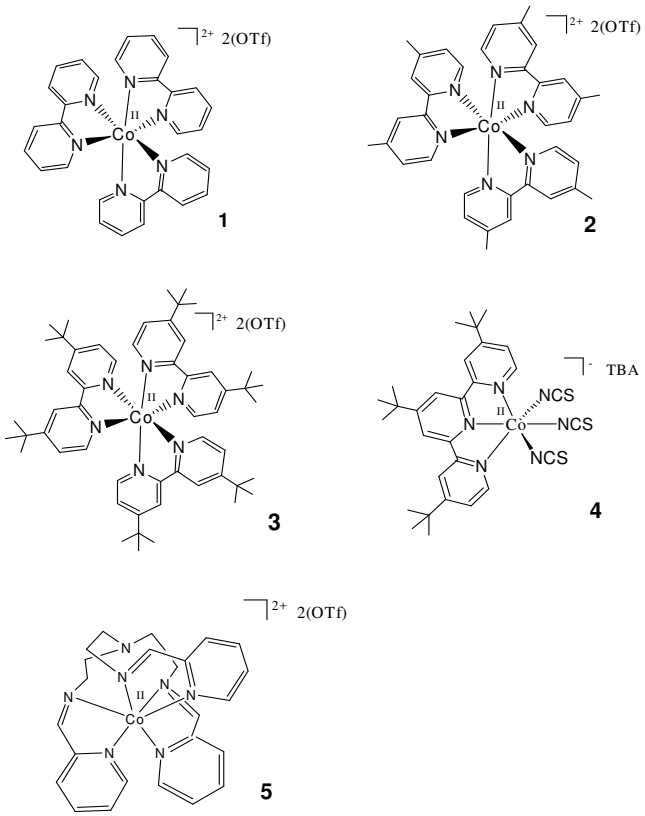

Fig.6.2 Co(II) complexes chosen for electrochemical testing (where TBA= tetrabutyl-ammonium ion).

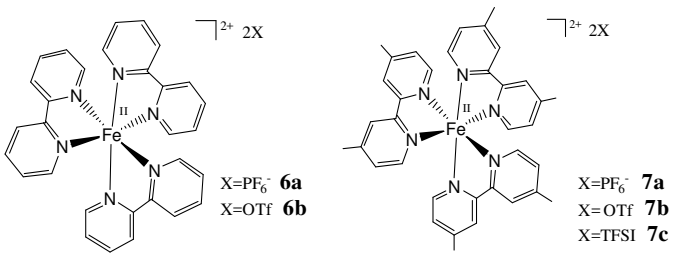

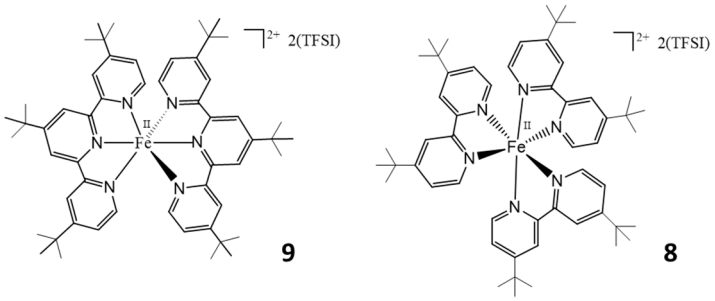

Fig.6.3 Fe(II) complexes chosen for electrochemical testing (where TFSI = Bis(trifluoromethane)sulfonimide anion).

6.2. Experimental section

6.2.1. Materials and Methods

All chemicals were Sigma Aldrich products and were used as received: Cobalt(II) carbonate hydrate ($CoCO_3$, ≥99.9%), triflic acid (HOTf, ≥99%), 2,2'-bipyridine (bpy, ≥99%), 4,4'-dimethyl-2,2'-bipyridine (dmb, 99%), 4,4'-di-*tert*-butyl-2,2'-bipyridine (dtb, 98%), ammonium Iron(II) sulfate hexahydrate ($(NH_4)_2Fe(SO_4)_2 \times 6(H_2O)$, 99.9%), 4,4',4''-tri-*tert*-butyl-2,2':6',2''-terpyridine (ttt, 95%), tetrabutylammonium hexafluorophosphate ($TBAPF_6$, ≥99%), nitrosyl tetrafluoroborate ($NOBF_4$, 95%), Sodium hydroxide (NaOH, ≥97%), tetrabutylammonium thiocyanate (TBANCS, 98%), lithium triflate (LiOTf, 99.9%), bis(trifluoromethane)sulfonimide lithium salt (LiTFSI, ≥95%), ammonium cerium(IV) nitrate (CAN, ≥98.5%), 3-4-ethylenedioxythiophene (EDOT, 97%). The following solvents were Sigma-Aldrich and were used as received: Diethyl ether (ACS reagent, ≥99%), Acetonitrile (AcN, for HPLC, gradient grade ≥99.9%), methanol (MeOH, anhydrous, 99.8%), Propylene carbonate (PC, reagent grade, 99%), Ethylene carbonate (EC, anhydrous, 99%), Acetone (for HPCL, ≥99.9%), Methanol-d (CD_3OD, ≥99.8 atom % D), Acetonitrile-d (CD_3CN, ≥99.8 atom % D), Chloroform-d ($CDCl_3$, ≥99.8 atom % D). The solvent mixtures AcN:PC and EC:PC were prepared by mixing respectively Acetonitrile and Propylene carbonate (1:1) and Ethylene carbonate and Propylene carbonate (1:1). Characteristic NMR spectra were obtained on Bruker Avance III 400 MHz (^1H) spectrometer. Chemical shifts (δ) of spectra are expressed in ppm relative to Me_4Si. Spectra were processed with MNOVA. Mass spectrometry was performed in ESI mode with a Finningan LCQ Duo Ion Trap (Capillary Temp: 250 °C, Infusion flow rate: 18 μL/min, Sheath gas flow rate: 20 AU), or with a Waters Micromass ZQ 2000 (Cone Temperature 110°C and desolvation Temperature of 130°C, Capillary voltage 2.30 KV, Cone Voltage 20 V, Extractor Voltage 3V and RF Lens Voltage 0.3V, Flow rate 295 L/hr) under positive/negative mode acquisition.

6.2.2 Electrochemical characterization.

Electrochemical studies on glassy carbon electrodes (Amel) were carried out by cyclic voltammetry (CV) and by Impedance spectroscopy (EIS) in a standard three-electrode nitrogen-purged cell with an Autolab PGSTAT302N potentiostat and with a standard calomel electrode as reference (Amel) and a Pt wire as auxiliary (Sigma-Aldrich). Impedance spectra were fitted with Z-View by using the electric equivalent reported in Scheme 6.1 where R1 is the serial Ohmic resistance (*Rs*), CPE1 is the constant phase element, R2 is the charge transfer resistance (R_{CT}) and Wo1 is the open Warburg element.

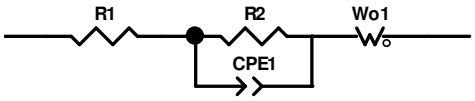

Scheme 6.1-Equivalent circuit for fitting the EIS data in three-electrode cell.

Electrochemical studies on carbon felts (Sigracell® GFD4.6 EA) were carried out by Chronoamperometry and by cyclic voltammetry in a standard three-electrode nitrogen-purged cell with an Autolab PGSTAT302N potentiostat and with a standard calomel electrode as reference (Amel) and a Pt wire as auxiliary (Sigma-Aldrich). Cyclic voltammetries were recorded at scan rates varying between 2mV/s and 200mV/s in a EC:PC + 0.1M LiOTf solution with dynamic IR-drop compensation and the redox couple concentration was 10^{-3} M. Oxidation-reduction cycles on a 10^{-3}M solution of complex **6b** were carried out in EC:PC + 1M LiOTf by chronoamperometry in a standard three-electrode cell with an Autolab PGSTAT302N potentiostat and with a standard calomel electrode as reference (Amel) and a Pt wire as auxiliary (Sigma-Aldrich), by employing a carbon felt working electrode (Sigracell® GFD4.6 EA) (1cm^2 Area).

6.2.3 Spectroelectrochemical characterization

Spectroelectrochemical measurements on Fe(III)/(II) were carried out in EC:PC + 1M LiOTf on a 10^{-3}M solution of complex **6b** in 1 cm path three-electrode quartz cell with an Autolab PGSTAT302N potentiostat and a JASCO V-570 UV–Vis spectrophotometer. In order to oxidize **6b,** a potential of 1.5V was applied for 500s and a potential of 0V was applied for 730s to reduce the oxidized species formed in the first potential step. A standard calomel electrode as reference (Amel), a Pt wire as auxiliary (Sigma-Aldrich) and a transparent ITO working electrode (Sigma-Aldrich) (2×0.5cm^2 Area) were employed.

6.2.4 Thin layer cell study

Impedance spectroscopy measurements (EIS), slow scan rate cyclic voltammetry and linear sweep voltammetry in symmetric (i.e. two identical electrodes) thin layer dummy cells having active area of 0.25 cm^2 sealed with a 25 μm inter-electrode spacing (Surlyn®, DuPontTM), were carried out with an Autolab PGSTAT302N potentiostat, employing two different kind of electrodes to study Fe(III)/(II) and Co(II)/(I) complexes. PEDOT (Poly(3,4-ethylenedioxythiophene)) films were electrodeposited [22] on FTO (Pilkington) to study the Fe(III)/Fe(II) couple while carbon nanohorns (CNH) (Carbonium s.r.l) based electrodes were spray deposited [26] on FTO to study Co(II)/Co(I). Contrary to PEDOT, which is insulating at cathodic voltages, nanohorn films present a large electroactivity window, which allows to intercept the Co(II)/Co(I) couple. EIS experiments were carried out at the equilibrium voltage potential (0 V) of Fe(III)/(II) couple and at the half wave potential (*ca.* -1.25 V) of the Co(II)/(I) couple. Impedance spectra were fitted with Z-View by using the electric equivalent reported in Scheme 6.2 where R1 is the serial Ohmic resistance (*Rs*), CPE1 is the constant phase element, R2 is the charge transfer resistance (R_{CT}) and Ws1 is the short Warburg element.

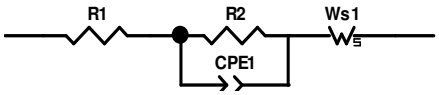

Scheme 6.2 Equivalent circuit for fitting the EIS data in symmetric thin layer cell.

6.2.5 Redox Flow Battery tests

Redox Flow Battery tests were carried out in collaboration with ENI Renewable Energy and Environmental R&D Center, in Novara, with an apparatus still described in Chapter 3. The two-compartment flow cell was assembled after purging both compartments under nitrogen flux; liquid flow rate of 45 ml/min was set up; the electrodes employed were two carbon-felts Sigracell® GFD4.6 EA and a Nafion 115 membrane has been used for separation. Before the tests in flow cell, the membrane was wetted with PC for 24 h, followed by 30 min of ultrasonic treatment.

6.2.6 XPS analysis

The XPS analysis was carried out with a PHI-5500 spectrometer with monochromator (Pass Energy= 58.7 eV; Step= 0.5 eV; Time x step= 0.10 s). Small membrane samples were inserted in a high vacuum (10^{-9} Torr) chamber and an electron gun was used as a neutralizer.

XPS analysis was carried out in collaboration with ENI Renewable Energy and Environmental R&D Center, in Novara.

6.2.7 Synthesis of $[Co(H_2O)_6](OTf)_2$

$[Co(H_2O)_6](OTf)_2$ was synthesized by a standard procedure reported in literature [24]: 3 g of $CoCO_3$ were suspended under magnetic stirring in 50 ml of distilled water and HOTf was added dropwise under pH-metric control (the pH was never lowered below 4.5). During the course of the reaction CO_2 evolved and the formation of a transparent pink solution of $[Co(H_2O)_6](OTf)_2$ was observed. The addition of acid ceased when no further evolution of CO_2 was observed. The solution was filtered to remove minor dark insoluble impurities and the solvent was evaporated under reduced pressure. The resulting hygroscopic solid was preserved in a desiccator.

6.2.8 Synthesis of complexes 1,2,3

Cobalt complexes **1**, **2** and **3** were synthesized according to a literature procedure [22] by mixing 1eq. of $[Co(H_2O)_6](OTf)_2$ salt with 3 eq. of the appropriate ligand (respectively 2,2'-bipyridine (bpy), 4,4'-dimethyl-2,2'-bipyridine (dmb), 4,4'-di-*tert*-butyl-2-2'-bipyridine (dtb)) in methanol solution. Solution was stirred for 15 minutes, and the final product was obtained by evaporation under vacuum. All complexes were purified by dissolving the solid in a minimum amount of acetonitrile, followed by precipitation with diethyl ether and drying at room temperature. Yield **1**: 89%; Yield **2**: 85%; Yield **3**: 86%. The diamagnetic oxidized form of the complexes (for ^{1}H-NMR characterization) was obtained by addition of a slight excess of $NOBF_4$ in acetonitrile followed by rotary evaporation of the solvent.

^{1}H-NMR (400 MHz) CD_3CN ,δ (ppm): $[Co(bpy)_3]^{3+}$: 8.68 (dd, 6H), 8.38 (m, 6H), 7.74 (m, 6H), 7.27 (d, broad, 6H); $[Co(dmb)_3]^{3+}$: 8.65 (d, 6H); 7.92 (dd, 6H); 7.4 (d, 6H); 2.48 (s, 18H); $[Co(dtb)_3]^{3+}$: 8.66 (d, 6H), 7.7 (dd, 6 H), 7.1 (d, 6 H), 1.5 (s, 54 H).

6.2.9 Synthesis of complex 4

Complex **4** was obtained by treating 1e.q of $[Co(H_2O)_6](OTf)_2$ with 1 eq. of 4,4',4''-tri-*tert*-butyl-2,2':6',2''-terpyridine (ttt) in acetone and by adding an excess of TBANCS (6eq.) [23] that was intentionally left to avoid Co-NCS dissociation in the operational cell. Solution was stirred for 15 minutes, and the final product was obtained by evaporation under vacuum. Yield: 70%. Co(III) for ^{1}H-NMR was prepared by addition of a slight excess of $NOBF_4$ in acetonitrile and evaporation of the solvent.

^{1}H-NMR (400 MHz) CD_3CN, δ (ppm): $[Co(ttt)(NCS)_3]$: 9.1 (s, 2H); 8.7 (s, 2H); 7.4 (d, 2H); 7.05 (d, 2H); 1.9 (s, 9H); 1.4 (s, 18H). ESI positive **4**: *m/z* = 242 $[TBA]^+$; 518 $[Co(ttt)(NCS)]^+$.

6.2.10 Synthesis of complex 5

Ligand (L^3) was sintetised by following a procedure reported in literature [27]. Corresponding Cobalt complex **5** was never reported and was prepared as follows: to 1eq. of ligand L^3 dissolved in methanol, 1eq. of $[Co(H_2O)_6](OTf)_2$ was added. The resulting solution was stirred for 15 minutes, and the final product was obtained by evaporation under vacuum. **5** was purified by dissolving the solid in a minimum amount of acetonitrile, followed by precipitation with diethyl ether. Yield: 75%. Co(III) was generated by addition of a slight excess of $NOBF_4$ in acetonitrile.

^{1}H-NMR (400 MHz) $CDCl_3$, δ (ppm): L^3: 9.56 (s, broad, 3H), 8.54 (d, 3H), 8.37 (m, 3H), 7.4 (m, 3H), 3.6 (t, 6H), 3.1 (t, 6H); CD_3CN, δ (ppm): $[Co(L^3)]^{3+}$: 8.71 (s, broad, 3H), 8.55 (m, 6H), 7.85 (m, 3H), 7.1 (d, broad, 3H), 3.3 (m, 6H), 2.5 (m, 6H). ESI positive **5**: *m/z* = 236 $[Co(L^3)]^{2+}$.

6.2.11 Synthesis of complexes 6a ,7a

Complex **6a** and **7a** were synthesized as PF_6^- salts for comparative purposes (solubility and electrochemical response) according to published reports [24]: the mixing of 1eq. of $(NH_4)_2Fe(SO_4)_2 \times 6(H_2O)$ dissolved in the minimum amount of distilled water with 3eq. of ligand (respectively 2,2'-bipyridine (bpy), 4,4'-dimethyl-2,2'-bipyridine (dmb)) afforded the desired compound. Stirring was continued for 15 minutes and complexes **6a** and **7a** were obtained by precipitation with NH_4PF_6 followed by filtration under vacuum. All complexes were purified by dissolving the solid in a minimum amount of acetonitrile, followed by precipitation with diethyl ether and drying at room temperature. Yield **6a**: 86%; Yield **7a**: 87%.

6.2.12 Synthesis of complexes 6b ,7b

$[Fe(H_2O)_6](OTf)_2$ salt was synthesized by adding to 1eq. of $(NH_4)_2Fe(SO_4)_2 \times 6(H_2O)$ dissolved in the minimum amount of distilled water, 2eq. of NaOH under N_2 atmosphere. After formation of a white precipitate ($Fe(OH)_2$), the addition of 2eq. of HOTf lead to the formation of $[Fe(H_2O)_6](OTf)_2$ as a pale green solution. Water was evaporated under vacuum and the solid was dissolved in methanol. Complexes **6b** and **7b** were obtained by adapting the procedure reported at *6.2.11* paragraph, mixing $[Fe(H_2O)_6](OTf)_2$ with 3eq. of ligand

(respectively 2,2'-bipyridine (bpy), 4,4'-dimethyl-2-2'-bipyridine (dmb)). Solution was stirred for 15 minutes, and the final product was obtained by evaporation under vacuum. All complexes were purified by dissolving the solid in a minimum amount of acetonitrile, followed by precipitation with diethyl ether and drying at room temperature. Yield **6b**: 75%; Yield **7b**: 74%.

^{1}H-NMR (400 MHz) CD_3OD ,δ (ppm): **6b** : 8.7 (d, broad, 6H), 8.2 (m, 6H), 7.5 (m, 12H); **7b** : 8.57 (s, broad, 6H), 7.25 (m, 12H), 2.6 (s, 18H).

6.2.13 Synthesis of complexes 7c ,8 and 9

Complex **7c, 8** and **9** were synthesized by adapting the procedure reported at *6.2.11*: 1eq. of $(NH_4)_2Fe(SO_4)_2 \times 6(H_2O)$ dissolved in the minimum amount of water was mixed in stoichiometric ratio with selected ligand (respectively 3eq. of 4,4'-dimethyl-2,2'-bipyridine (dmb), 3 eq. of 4,4'-di-*tert*-butyl-2,2'-bipyridine (dtb) and 2eq. of 4,4',4''-tri-*tert*-butil-2,2':6',2''-terpyridine (ttt)). Stirring was continued for 15 minutes, and complexes **7c**, **8** and **9** were obtained by precipitation with LiTFSI followed by filtration under vacuum. All complexes were purified by dissolving the solid in a minimum amount of acetonitrile, followed by precipitation with diethyl ether and drying at room temperature. Yield **7c**: 82%; Yield **8**: 80%: Yield **9**: 78%.

^{1}H-NMR (400 MHz) CD_3OD ,δ (ppm): **7c** : 8.58 (s, broad, 6H), 7.28 (m, 12H), 2.55 (s, 18H); **8**: 8.68 (s, broad, 6H), 7.58 (dd, 6 H), 7.27 (d, 6 H), 1.48 (s, 54 H); **9**: 9.2 (s, 4H), 8.8 (s, 4H), 7.27 (d, 4H), 6.9 (d, 4H), 1.9 (s, 18H), 1.3 (s, 36 H).

6.2.14 Synthesis of 6ox

6ox ($[Fe(bpy)_3](TFSI)_3$) was synthetized by adding to 1 eq. of **6b** in acetonitrile, an excess of CAN (2eq). The white precipitate ($[Fe(bpy)_3](NO_3)_3$) was centrifuged and washed several times in acetonitrile. Once dissolved the solid in water, **6ox** was precipitated with an excess of LiTFSI (4eq), as TFSI salt.

6.3. Results and Discussion

Co (II) or Fe (II) complexes can be easily generated by mixing appropriate Co (II) or Fe (II) salts with stoichiometric ratio of ligands. Iron complexes with several counter ions were synthesized in order to tune solubility. Indeed, complex solubility is affected by the nature of the counter ion, by the nature of peripheric pendants and by the charge of the metal complex, so significant variations of solubility can be expected within this series. Solubility tests have been carried out in different NA solvents as PC, AcN, AcN:PC and EC:PC, chosen

for their electrochemical stability window suitable for the use in redox flow batteries (see Tables 6.1 and 6.2).

Table 6.1 Cobalt complexes solubility

	PC	**EC:PC**
1	0.6M	0.68M
2	0.49M	0.53M
3	0.47M	0.5M
4	0.11M	0.15M
5	0.65M	0.7M

Table 6.2 -Iron complexes solubility

	AcN	**AcN:PC**	**PC**	**EC:PC**
7a	0.2M	0.23M	0.3M	0.32M
7b	0.32M	0.38M	0.46M	0.47M
7c	0.28M	0.3M	0.35M	0.37M
6a	0.24M	0.28M	0.3M	0.35M
6b	0.34M	0.48M	0.56M	0.62M
8	0.3M	0.4M	0.44M	0.46M
9	0.21M	0.25M	0.27M	0.3M

The most soluble anodic complex resulted **6b** with OTf as counter ion, reaching 0.62M solubility at room temperature. EC:PC has generally better solvent properties than PC alone probably due to higher polarity. TFSI anions also provide a satisfactory solubility, but generally it is about 20% lower than the equivalent OTf species. Both TFSI and OTf ensure a higher solubility than PF_6^-. A similar trend is found with the cobalt couples, among which **1** reached 0.68M and **5** 0.7M concentration in EC:PC with OTf as counter ion. A first electrochemical screening was carried out by cyclic voltammetry, recording Half-wave

redox potentials ($E_{1/2}$) referred to saturated calomel electrode (SCE) related to Fe(III)/Fe(II) and Co(II)/Co(I) redox couples. It is worth to note that this study was focused on the triflate salts of complexes **6** and **7** (**6b** and **7b**) due to their much higher solubility in EC:PC. Results are reported in Table 6.3. Nearly identical $E_{1/2}$ were observed in PC, AcN and AcN:PC. Cyclic voltammogramms of all complexes at glassy carbon (GC) working electrode (WE) show *quasi*-reversible processes associated to metal centered oxidation and reduction, with peak separation (ΔE (Epa-Epc)) in the range of 0.1 ÷ 0.12 V. Cobalt complexes CVs are characterized by a redox wave corresponding to the reduction of Co(II) to Co(I), with $E_{1/2}$ in the range of -0.98 ÷ -1.16 V vs SCE. The most negative $E_{1/2}$ is observed for **3**, probably due to the electron donating effect of the alkyl substituents. **2** displays a nearly identical $E_{1/2}$, consistent with the similar inductive effect of methyl vs. *tert*-butyl groups. CVs of the iron complexes are characterized by a monoelectronic redox wave corresponding to the oxidation of Fe(II) to Fe(III), with $E_{1/2}$ in the range of 0.8 ÷ 1 V vs SCE. From data reported in Table 6.3 it is clear that processes related to Co(II)/(I) and Fe(III)/Fe(II) species are energetically suitable to develop potential differences between 1.6V and 2V, if coupled in a redox cell (Fig.6.4). The highest thermodynamic potential of the charged cell would be expected by coupling **6b** and **3** reaching values close to 2.2 V.

Table 6.3 Electrochemical parameters extracted from CVs of 10^{-2} M Cobalt and Iron complexes in EC:PC + 0.1M LiOTf

	Co(II)/Co(I)			
	E_{pc}(V)	**E_{pa}(V)**	**$E_{1/2}$(V)**	**ΔE(V)**
1	-1.07	-0.97	-1.02	0.1
2	-1.2	-1.1	-1.15	0.1
3	-1.21	-1.1	-1.16	0.11
4	-1.03	-0.93	-0.98	0.1
5	-1.13	-1.01	-1.07	0.12
	Fe(III)/Fe(II)			
	E_{pc}(V)	**E_{pa}(V)**	**$E_{1/2}$(V)**	**ΔE(V)**
6b	0.93	1.03	0.98	0.1
7b	0.78	0.88	0.83	0.1
8	0.77	0.87	0.82	0.1
9	0.81	0.91	0.86	0.1

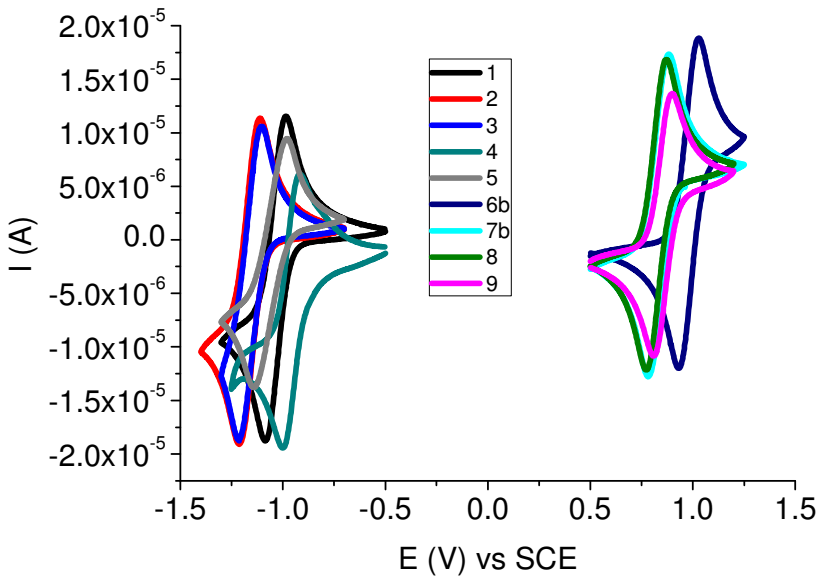

Fig.6.4 Cyclic voltammograms of 10^{-2}M Cobalt and Iron complexes in EC:PC + 0.1M LiOTf (scan rate: 10mV/s).

Preliminary stability tests were carried out by recording multiple cycling (100 scan) within -0.2/-1.3 V vs SCE for Co(II)/(I) and within 0.2/1.2 V vs SCE for Fe(III)/(II), at a glassy carbon WE, to screen the reproducibility of the electrochemical response of the selected series at carbonaceous interfaces. In order to stress electrochemical stability high concentrations (10^{-2}M) and slow scan rates (10mV/s) were selected, which are more sensitive to adsorbate formation on electrode surface. The anodic peak current (Ipa) was monitored as an indication of stability of the electrodic response upon subsequent scans. It can be appreciated, due to a continuous decrease of the peak current upon multiple cycles, that in AcN and AcN:PC cobalt complexes lead to electrode passivation, even when decreasing by an order of magnitude complex concentration (10^{-3}M) (Fig.6.5 a, b). Besides, in PC and EC:PC **1**, **3** and **5** show a substantially stable current, which indicates that the electrode surface does not reduce its electroactivity due to formation of adsorbates or electrostatic assemblies between the negatively charged surface and positively charged complexes (Fig.6.5 c,d) which lead to the blockage of the electron transfer. Among the analyzed cobalt complexes, **4** displays the most stable current up to 100 scans, consistent with the negative charge (varying between 2^- (Co(I)) and 1^- (Co(II)) which helps to avoid, through electrostatic repulsion, the formation of electrode adsorbates (Fig.6.5 c, d cyan line).

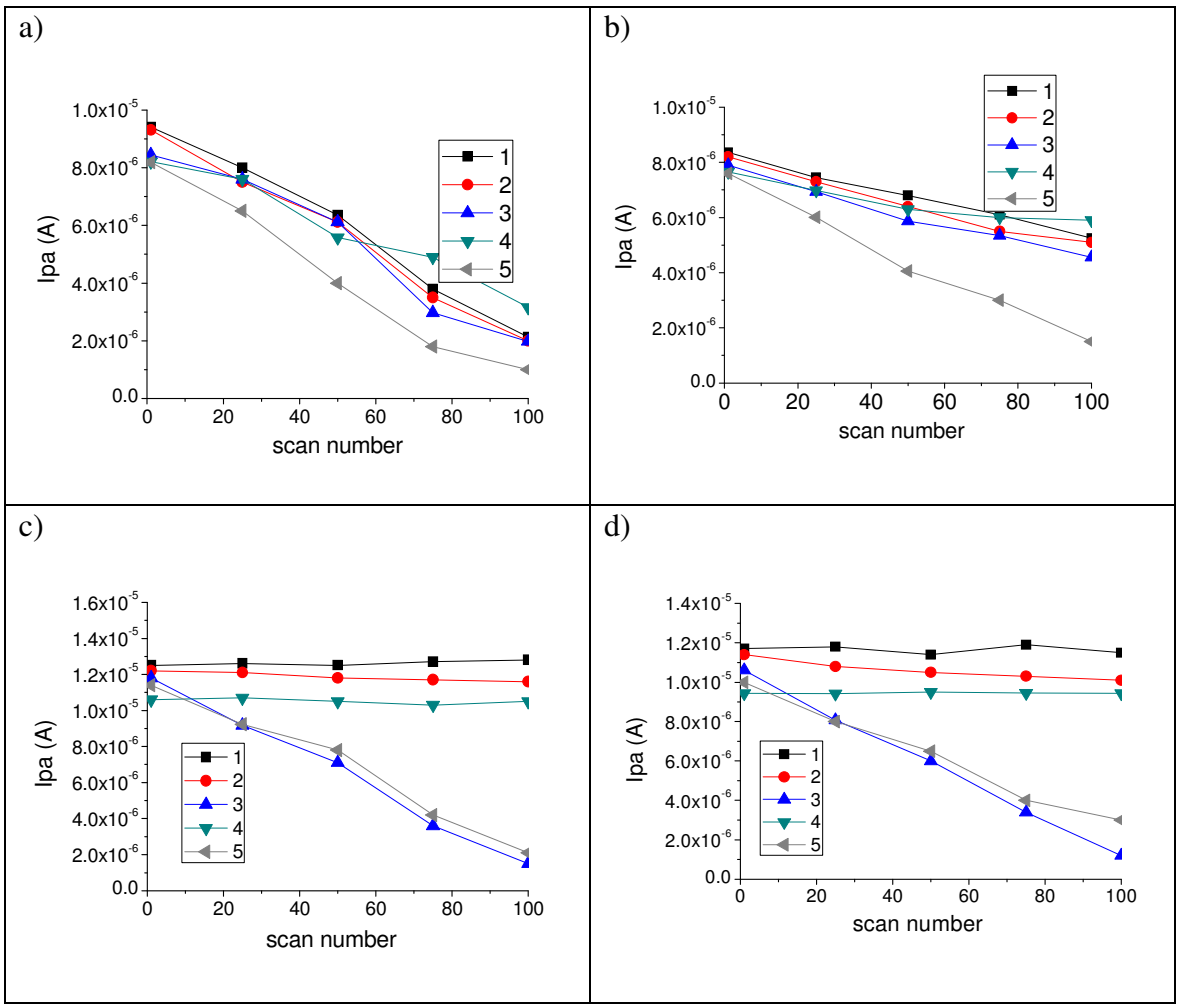

Fig.6.5 Anodic peak current of cobalt Complexes vs scan number in a)-AcN; b)-AcN:PC; c)-PC; d)-EC:PC; + 0.1M LiOTf. In a and b, cobalt complex concentration is 10^{-3} M (scan rate: 100mV/s). In c and d cobalt complex concentration is 10^{-2} M (scan rate: 10 mV/s).

It should be noted that the origin of the electrode passivation should not be related to an intrinsic chemical instability of the cobalt(I) complexes, since: i) no new redox waves resulting from possible decomposition products could be observed and ii) a simple cleaning of the electrode surface with alumina paste was able to fully restore the pristine electrochemical response (Fig.6.6)

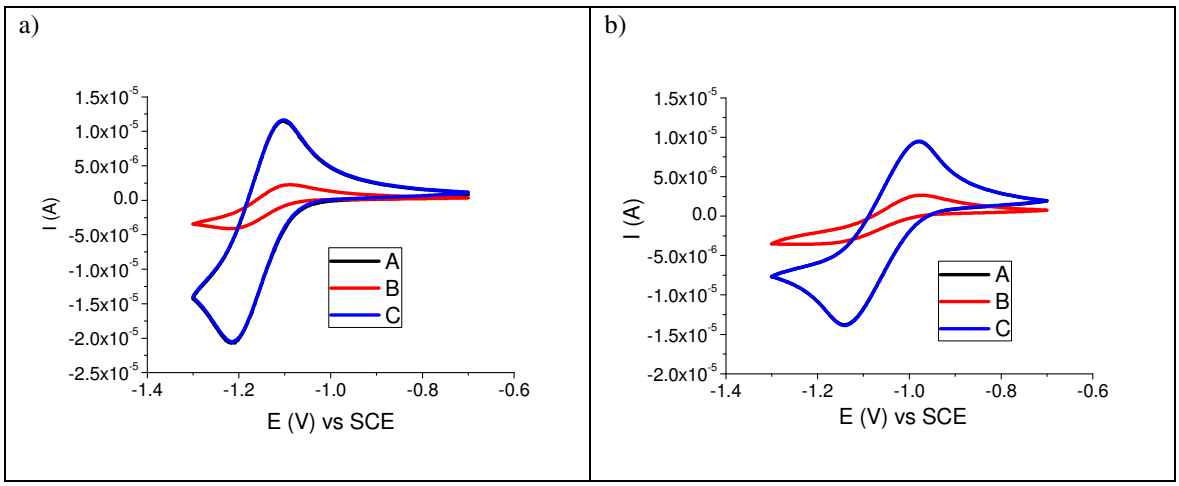

Fig.6.6 Cyclic voltammetries of a)- **3**; and b)- **5**; in EC:PC; + 0.1M LiOTf at A- t_0, B- after 100 scan, C- after cleaning the electrode surface with alumina paste. Cobalt complexes concentration is 10^{-2}M.

For what concern iron complexes, passivation is not observed in any of the selected solvents (Fig.6.7).

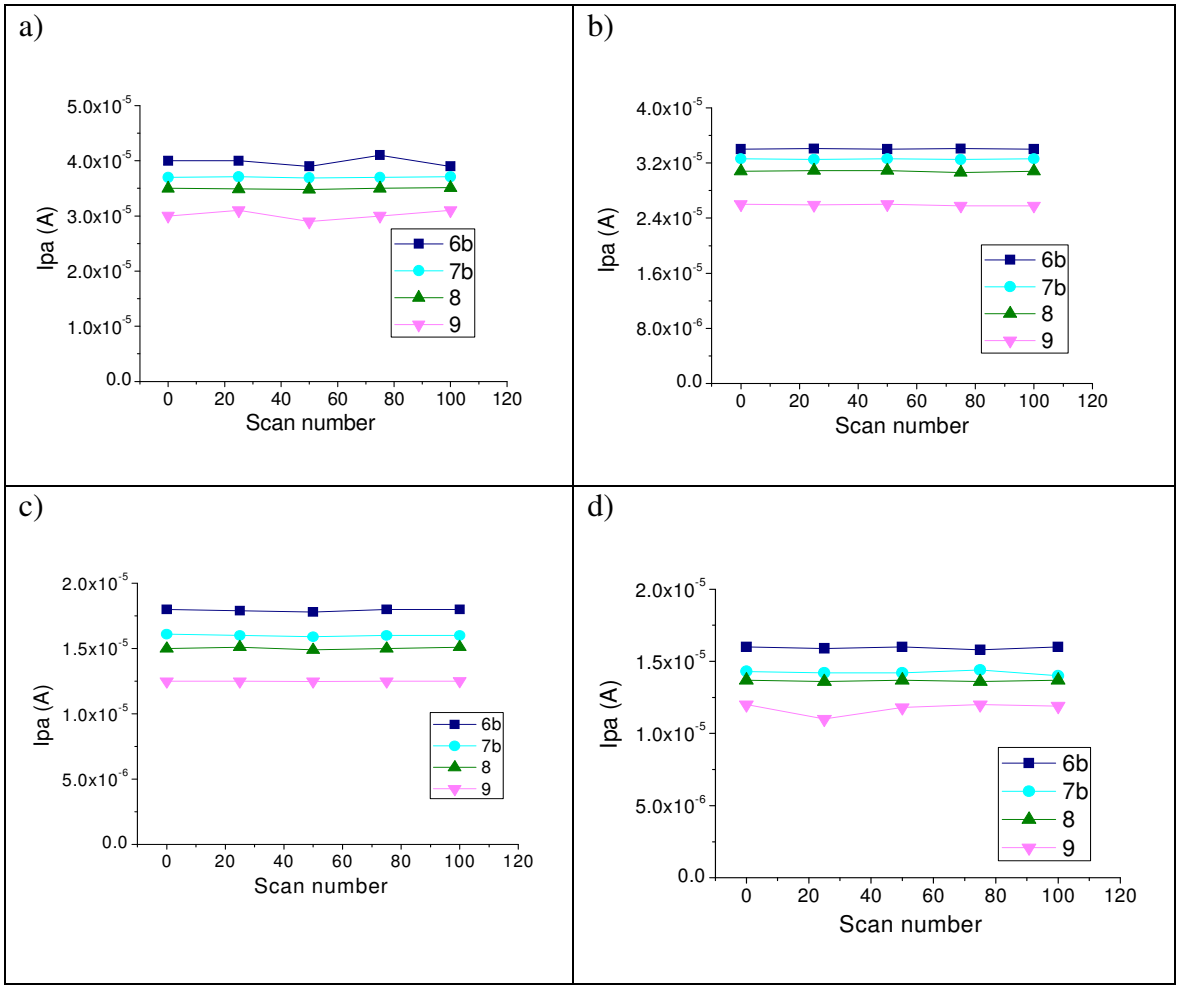

Fig.6.7- Iron complexes Anodic peak current vs scan number in : a)-AcN; b)-AcN:PC; c)-PC; d)-EC:PC; + 0.1M LiOTf. Iron complexes concentration is 10^{-2}M (scan rate: 10 mV/s).

In the light of the above, stability tests were performed on Co(II) complexes by employing carbon felt electrodes of the same type of those to be used in flow batteries, polarizing for 1h at a potential 300mV more negative than the $E_{1/2}$ of the selected Co(II)/Co(I) couple. These conditions are expected to be stronger than the ones adopted before, namely cycling, since static electrolysis allows to evaluate more properly redox couple stability and formation of secondary species as a result of side reactions accompanying electron transfer. It is worth to note that chronoamperometric tests confirm the generation of a stable current due to Co(I) formation in the case of **1,2** and **4** (Fig.6.8), besides cathodic current associated to complexes **3** and **5** decreases with time (Fig.6.8), which is very evident in the case of **3**, for which the decrease is one-half of the initial value, while **5** displays a much less evident drop during the first hour. In all cases, consistent with the preliminary screening at GC WE, CVs recorded after polarization do not reveal any response attributable to decomposition byproducts, possibly generated during 1hour long electrolysis. **1**, **2** and **4** (Fig.6.9 a, b, d) exhibit nearly overlapping voltammetric waves with the initial scan, while for **3** and **5** (Fig.6.9 c, e) the only consequence of carbon felt prolonged negative polarization is a decrease in the intensity of the voltammetric waves with respect to the reference initial scan.

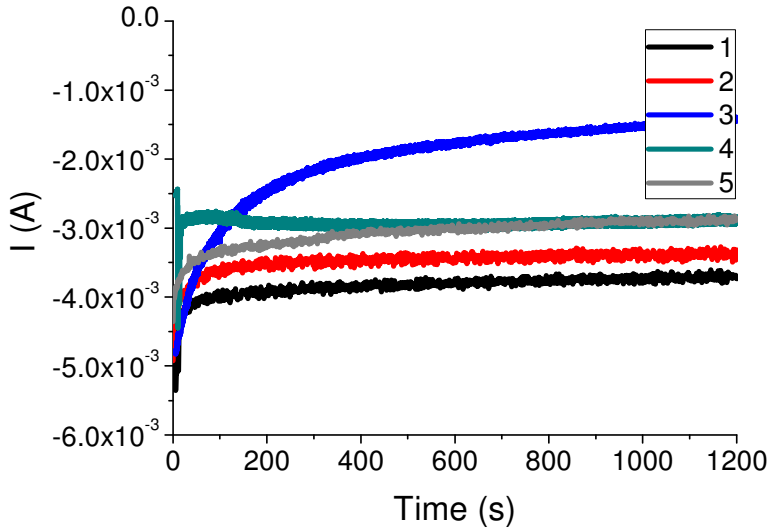

Fig.6.8-Chronoamperometries of 10^{-2}M Cobalt complexes in EC:PC + 0.1M LiOTf.

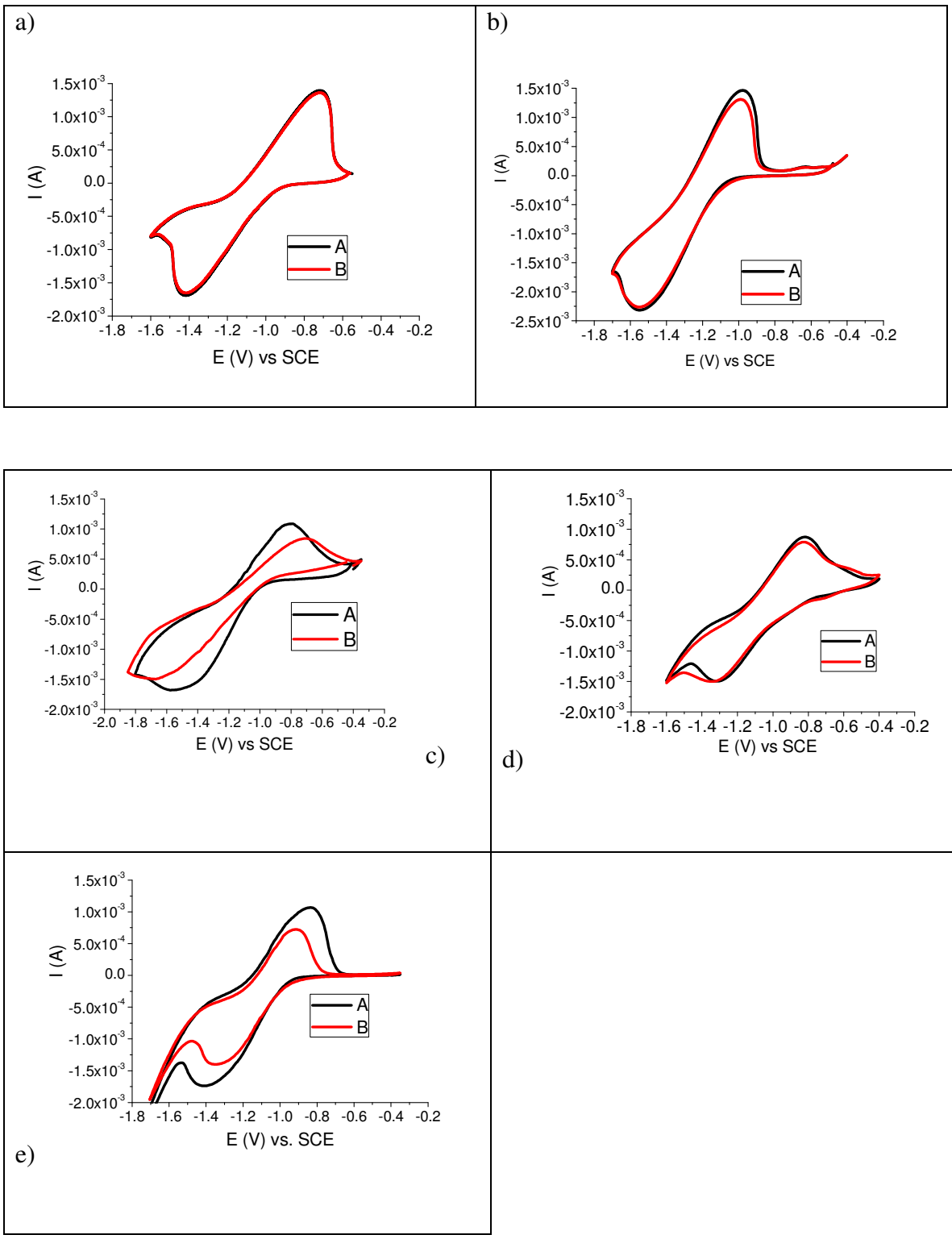

Fig.6.9 Cyclic Voltammetries of a)- **1** b)- **2** c)- **3** d)- **4** e)- **5** in EC:PC + 0.1M LiOTf at A- t_0 and B- after 1h of cathodic polarization. Cobalt complex concentration is 10^{-2}M.

Kinetic properties of Fe(III)/Fe(II) and Co(II)/Co(I) were screened both on carbon felt electrodes and on glassy carbon electrodes in EC:PC, which was found to be the best solvent for what concern Cobalt and Iron complexes redox stability and solubility. The EIS results (Fig.6.10) at glassy carbon of all complexes at their equilibrium potential could be modeled with a simple circuit comprising the electrochemical interface and the semi-infinite diffusion

element. In all cases the charge transfer arc is comparatively small with a charge transfer resistance which is about constant, of the order of 60-70 Ohm. Both in case of iron and cobalt the slowest couples are the *tert*-butyl substituted complexes (*i.e.* **3**, **8** and **9** bearing the dtb and ttt ligands). **5** displays also not ideal kinetics with respect to the unsubstituted polypyridine ones. The evaluation of its charge transfer properties is however complicated by the limited stability upon prolonged polarization. In all cases the major contribution to the electrode impedance arises from the diffusional contribution (Wo1-R) which is from 3 to 4 times larger than the charge transfer one. Diffusional resistive contributions of all complexes are comparable (Table 6.4).

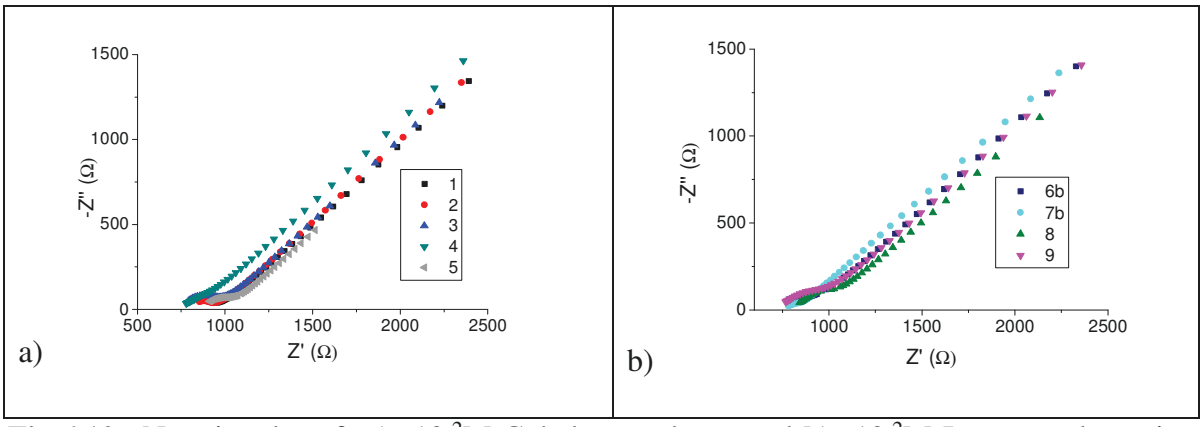

Fig.6.10 –Nyquist plot of **a)**- 10^{-2}M Cobalt complexes and **b)**- 10^{-2}M Iron complexes in EC:PC + 0.1M LiOTf

Table 6.4 Main resistive contributions in Cobalt and Iron based static three electrode cell.

	R_{CT} (Ω)	Wo1-R (Ω)
1	55	356
2	61	371
3	126	389
4	70	384
5	82	408
6b	50	366
7b	57	360
8	97	370
9	80	434

Kinetic properties were investigated on carbon felts by cyclic voltammetry since EIS experiments on these types of porous substrates were problematic due to exceeding data dispersion at low frequency. Apparent heterogeneous electron transfer rate constants (k_{heter}) (Table 6.5) of Co(II)/Co(I) and Fe(III)/Fe(II) species were obtained by plotting ln(Ip) vs E_p-$E_{1/2}$ as function of the scan rate [25] (Fig.6.11 b, Fig.6.12 b) (Eq.6.1) from the fits of the linear trait of the curve. While, diffusion coefficients (D_{red}) were calculated from the Randles-Sevcik equation [25] (Fig. 6.11 a, Fig.6.12 a) (Eq.6.2).

$$\ln(Ip) = \ln(0.227nFk_{heter}AC) + (\alpha nF/RT)(E_p-E_{1/2}) \quad \text{(Eq.6.1)}$$

$$Ip = (3.01 \times 10^5)\, n^{3/2}\, \alpha^{1/2}\, AD_{red}^{1/2}\, v^{1/2}\, C \quad \text{(Eq.6.2)}$$

Where n represents the number of exchanged electrons, C the bulk concentration of the electroactive species, Ep and $E_{1/2}$ the peak and the half wave peak potentials respectively, A the electrode surface area, and D_{red} the diffusion coefficient of the complexes when using anodic peak current. It is worth to notice that the electroactive area of carbon felt was estimated with a 10^{-3}M ferrocene standard from the Randles-Sevcik equation after determination of the ferrocene diffusion coefficient in EC:PC (D_{red} = 1.06×10^{-6} cm^2/s) and was found to be *ca.* 50cm^2. In general, the *quasi*-reversible behavior of all the redox couples was preserved with electron transfer constants of the order of $5\pm1\times10^{-4}$ cm/s, leading to equivalent kinetic overpotentials for the two families of iron and cobalt mediators. Also diffusion coefficients, about one order of magnitude lower than those reported in literature for acetonitrile [28] due to the superior viscosity of the EC:PC, are quite comparable, since values of the order of 8×10^{-7} were commonly found, consistent with the similar structure and coordination environment of these complexes. Thus, mass transport limitations should be equivalent at the anodic and cathodic compartments of the cell, favoring, in principle, cell balance. The symmetry factors (α), extracted from a Butler-Volmer analysis, considering a simple outer sphere electron transfer, are between 0.4 and 0.5, consistent with the symmetric shape of the voltammetric waves.

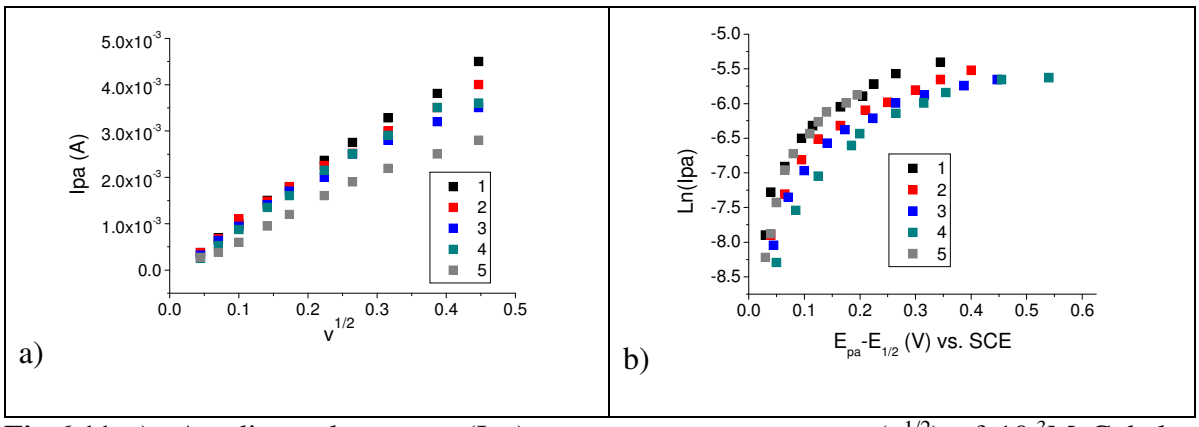

Fig.6.11 a)- Anodic peak current (Ipa) vs. square root scan rate($v^{1/2}$) of 10^{-3}M Cobalt complexes in EC:PC + 0.1M LiOTf b)- Natural logarithm of anodic peak current (Ln(Ipa)) vs. anodic peak potential(E_{pa}) minus half wave peak potential($E_{1/2}$) of 10^{-3}M Cobalt complexes in EC:PC + 0.1M LiOTf.

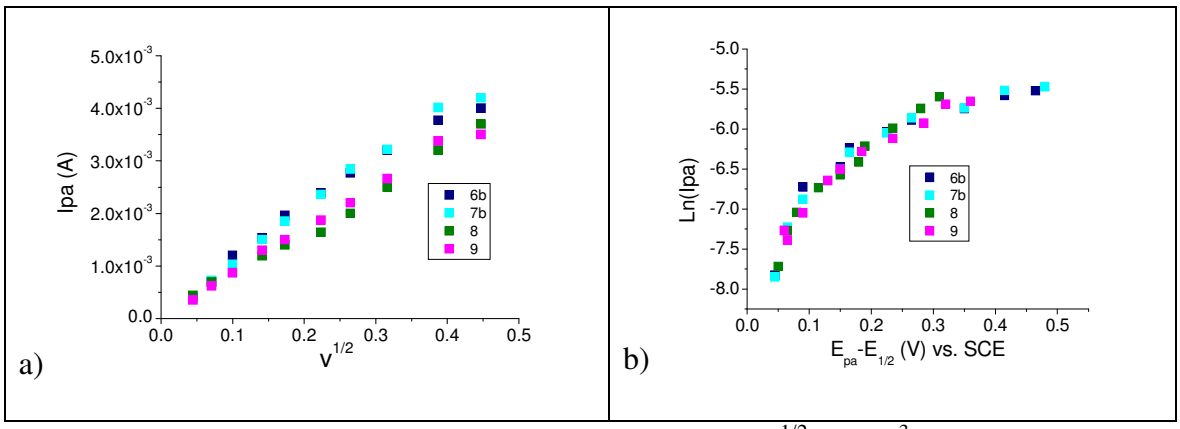

6.12 a)- Anodic peak current (Ipa) vs. square root scan rate($v^{1/2}$) of 10^{-3}M Iron complexes in EC:PC + 0.1M LiOTf b)- Natural logarithm of anodic peak current (Ln(Ipa)) vs. anodic peak potential(E_{pa}) minus half wave peak potentials($E_{1/2}$) of 10^{-3}M Iron complexes in EC:PC + 0.1M LiOTf.

Table 6.5 Diffusion coefficients (D_{red}) and heterogeneous electron transfer rate constants (k_{heter}) for cobalt and iron complexes.

	D_{red}(cm^2/s)	**k_{heter}(cm/s)**
1	8.47E-07	6.26E-04
2	8.07E-07	5.90E-04
3	7.88E-07	5.13E-04
4	6.95E-07	4.88E-04
5	5E-07	4.16E-04
6b	9E-07	5.34E-04
7b	8.9E-07	4.64E-04
8	7.17E-07	4.19E-04
9	6.9E-07	4.20E-04

6b and **1** were found to be the most promising complexes with respect to electrochemical kinetics, stability and solubility and will be thus used for the further studies approaching application in a real flow battery. Indeed, complex **5**, which reaches solubility of ca. 0.7M did not display the best response stability at glassy carbon and carbon felt working electrodes and the other suitable complex **4,** for what concern electrochemical stability, presents a solubility of 0.15M. Before testing in a lab. scale flow cell, the absorption characteristics of the redox couples were evaluated since the possibility of tracking the charge state of the battery via an independent method, like optical spectroscopy, is a fast way to assess chemical changes occurring during the redox reactions. Co(II) complexes do not display strong absorption characteristics nor diagnostic fingerprints, indeed electronic absorption spectra of Co(II) complexes, show weak featureless transitions, namely d-d forbidden transitions at wavelengths > 400 nm, with maximum molar extinction coefficients of *ca.*700 M^{-1} cm^{-1}(Fig.6.13 a) and the transitions are only marginally modified by the change in the redox state from Co(II) to Co(I) and from Co(II) to Co(III). By contrast, the electronic absorption spectra of Fe(II) complexes, present MLCT transitions at wavelengths in the range of 500-600 nm, with higher molar extinction coefficients of *ca.* 10000 M^{-1} cm^{-1} (Fig.6.13 b).

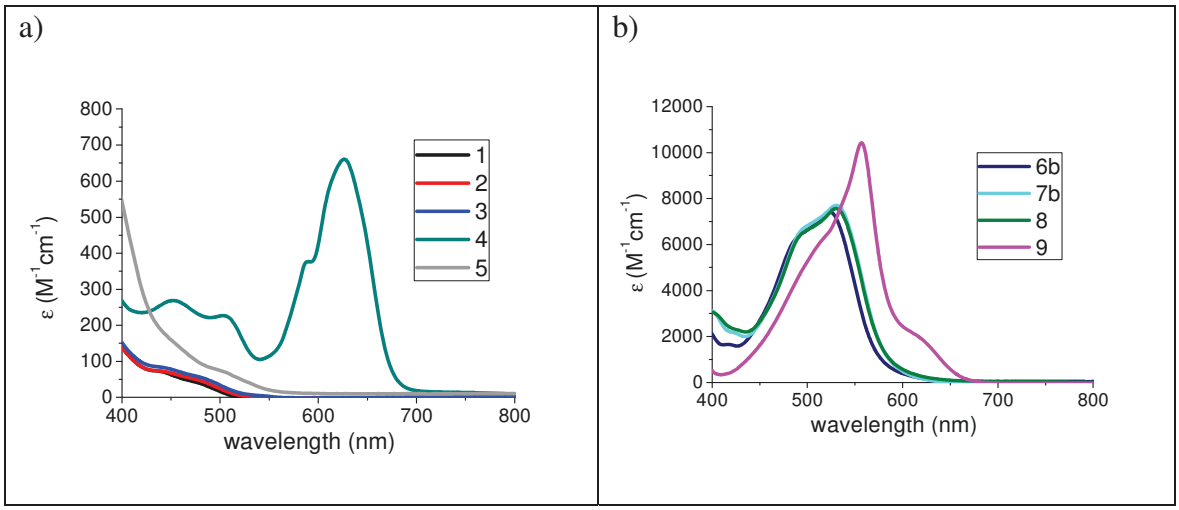

Fig.6.13 Extinction coefficient spectra of **a)**- Cobalt complexes and **b)**- Iron complexes

6b, which was found to be the most promising Iron complex for the employment in redox flow battery, was chemically reduced and oxidized to explore the possibility of monitoring independently iron-based cell. It is worth to note that is very easy to follow **6b** charge and discharge, thanks to the bleaching of the MLCT band at 525nm, after oxidation (Fig.6.14 a). A similar behavior extends to complexes **7b** (Fig.6.14 b) and **9** (Fig. 6.14 c).

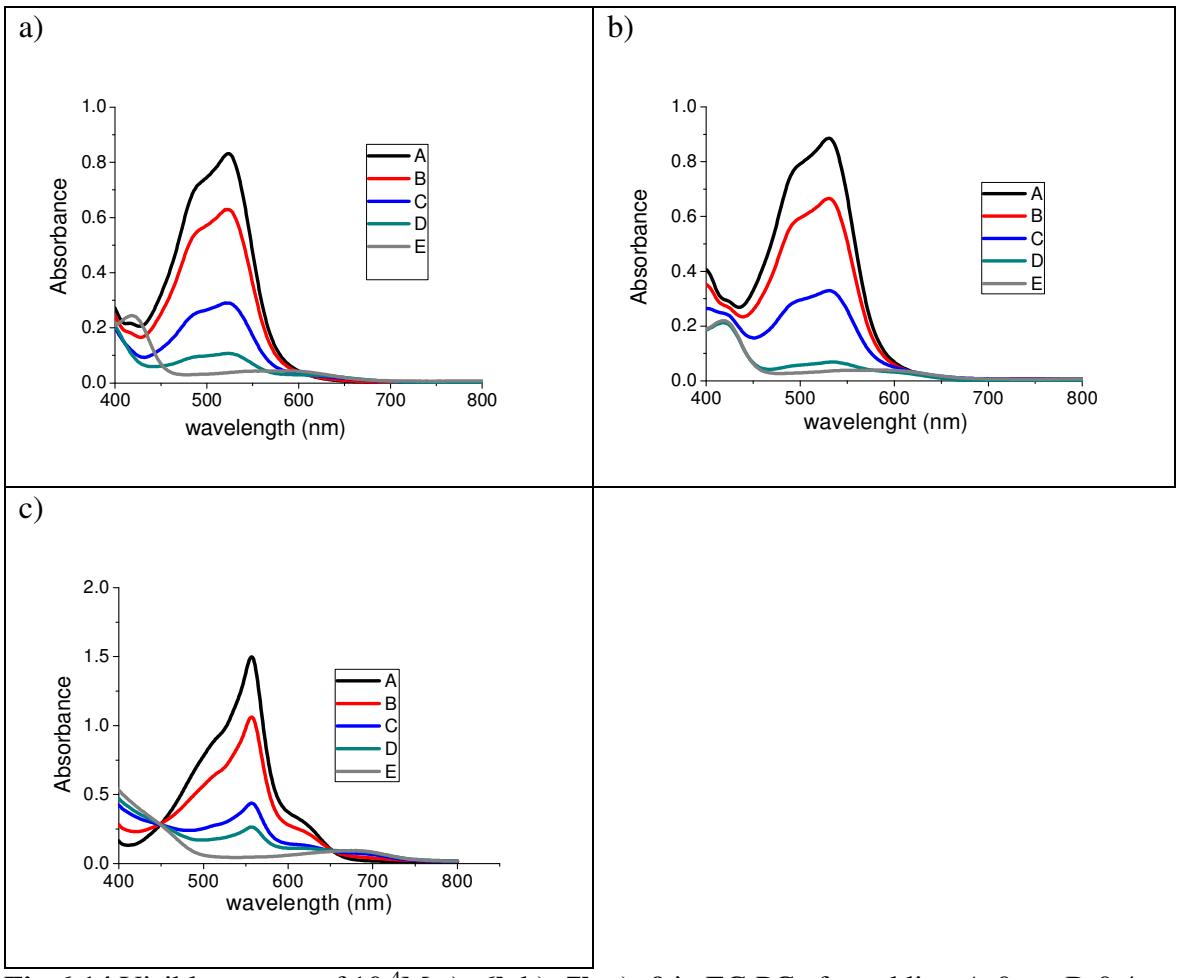

Fig.6.14 Visible spectra of 10^{-4}M a)- **6b** b)- **7b** c)- **9** in EC:PC after adding A-0 eq. B-0,4eq. C-0,8eq. D-1,2 eq. E-1,4eq. of CAN (cerium ammonium nitrate).

Chemical reversibility of Iron complex **6b** was confirmed upon electrochemical oxidation-reduction cycles at constant potential in EC:PC. These Cycles were carried out at +1.5V vs SCE, until attainment of a spectrophotometric steady state where the complete bleaching of the MLCT band at 525 nm was observed (Fig.6.15 B), whereas the reduced state was regenerated at 0 V showing its complete restoration (Fig.6.15 C).

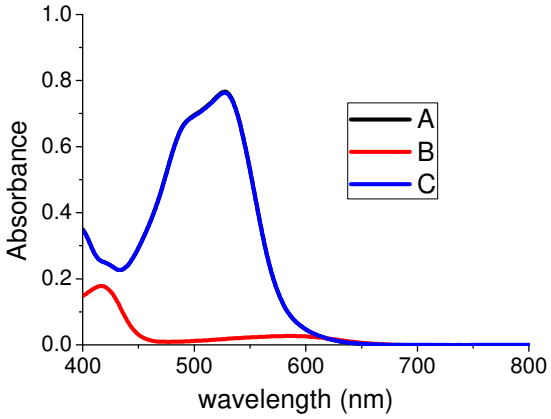

Fig.6.15 Visible spectra of 10^{-4}M **6b** in EC:PC at A-t_0; B- after 1.5V vs SCE polarization; C- after 0V vs SCE polarization.

Furthermore, the storage of the oxidized form of iron for several days without observing chemical decomposition was proved: according to spectrophotometric evidence, Fe(III) **(6ox)** was preserved in EC:PC (Fig.6.16) for 30 days, without significant changes during this time.

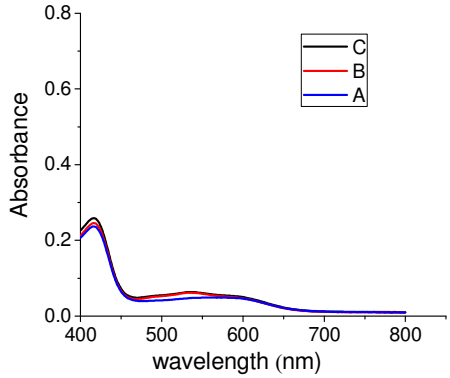

Fig.6.16 Visible spectra of 10^{-4}M **6ox** in EC:PC at A- t_0 B- after 15 days C- after 30 days.

In the end, the reversibility of the iron Fe(III)/(II) (**6b)** couple was further spectroelectrochemically corroborated by reproducible spectral variations at 525 nm upon fast potential cycling (500 s oxidation at 1.5 V vs SCE and 730 s reduction at 0 V vs SCE) (Fig.6.17).

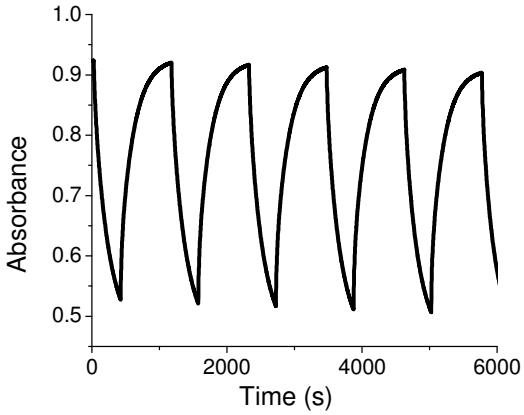

Fig.6.17 Absorbance at 525nm vs time of **6b** during cyclical oxidation and reduction steps.

Finally, **1** and **6b**, the most promising complexes in terms of solubility and electrochemical stability, were examined in a symmetric thin layer cell, to investigate the i-V behavior of these couples in conditions of optimized mass transport, made possible by the use of an inter-electrode spacing of *ca.* 25 μm, and in concentrations relevant to the possible application in the flow battery (*i.e* from 0.1M to 0.5M). EC:PC in the presence of 1 M LiOTf, was the electrolyte of choice for all these studies. In the case of the anodic couple, PEDOT was selected for its generally good electroactivity and for its ease of electrodeposition to yield mechanically stable thin films. The resulting J-V curves are shown in Fig.6.18a, where it can be appreciated the attainment of limiting current densities varying between 32 and 26 mA/cm^2, depending on Fe(II) concentration. The reduction in limiting current by moving from 0.1 to 0.5 M is consistent with the increase in viscosity of the solution due to the augmented amount of dissolved redox mediator. This leads to a decrease in the diffusion coefficient D, evaluated from limiting current J_L, expressed as $J_L = \frac{(2nFCD)}{L}$,where L is the thickness of the spacer and C is the concentration of the redox couple, from *ca.*1E-06 cm^{2}s^{-1} to 6E-07 cm^{2}s^{-1} at [Fe^{2+}]=0.5. It is worth to notice that diffusion coefficients found are in perfect agreement with the one evaluated from cyclic voltammetry tests (*i.e* 8.47E-07). We also note that there is a concentration interval (0.2 M-0.4 M) where the enhanced viscosity is balanced by the increased concentration of the redox active species resulting to nearly constant limiting current densities. This suggests the possibility of increasing the cell energy density and capacitance, by acting on the redox mediator concentration, without negatively affecting its maximum current. EIS provides deeper insight of the overall electrochemical processes, by resolving charge transfer and mass transfer processes in the frequency domain (Fig.6.18 b). It can be appreciated that the Nyquist plots recorded at the equilibrium voltage (0 V) are dominated by the diffusion of the redox couple, while the charge transfer arc is so

small to be essentially unobservable under these conditions, confirming the fast electron transfer on PEDOT. It means that even under very small overvoltage (10 mV perturbation) mass transport is the limiting process for these redox couples. The decreasing slope of the J-V curves when moving from 0.1 to 0.5 M is thus well explained by the increasing diffusional arc, whose projection on the real axis (Ws-R) varies progressively from ca. 15 Ohm at 0.1 M to ca. 100 at 0.5 M (Table 6.6).

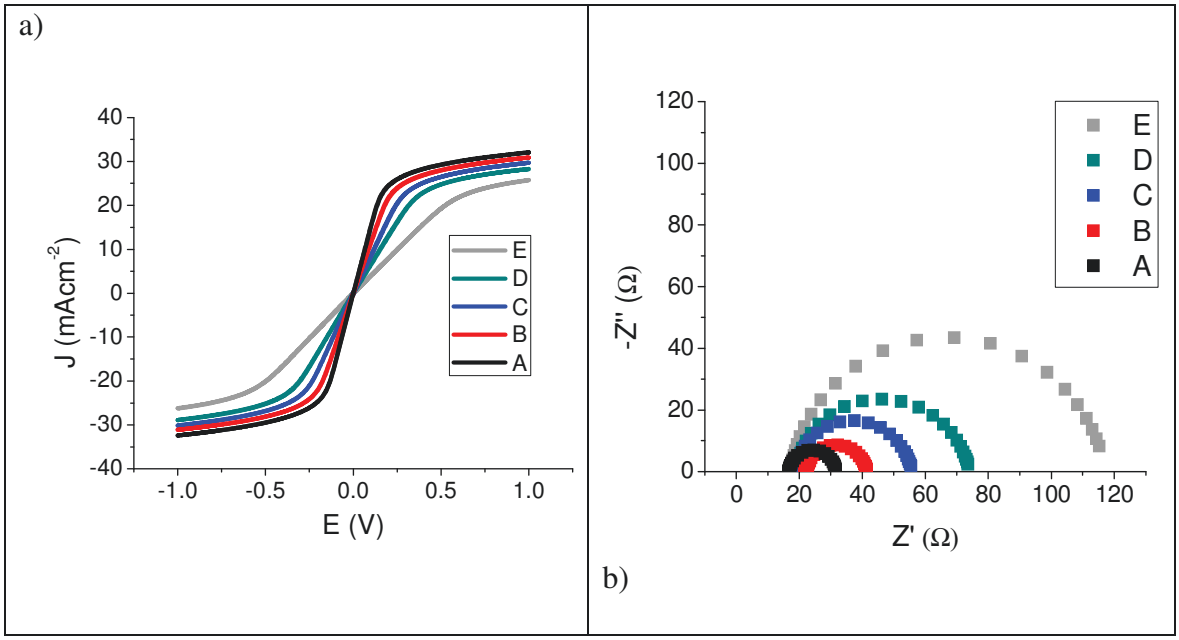

Fig.6.18 a)Slow scan rate linear sweep voltammetry of **6b** complex in thin layer dummy cell in EC:PC + 1M LiOTf at different concentrations (-A: 0.1M – B: 0.2M – C: 0.3M – D: 0.4M – E: 0.5M).b) Nyquist plot of **6b** complex in a two-electrode cell in EC:PC + 1M LiOTf at different concentrations (-A: 0.1M – B: 0.2M – C: 0.3M – D: 0.4M – E: 0.5M).

Table 6.6 Kinetics data and Fitting parameters for **6b** (Rs = serial ohmic resistance; Ws-R = Warburg element projection on real axis)**.**

	J_L(mA/cm^2)	**D (cm^2/s)**	**Rs (Ω)**	**Ws-R (Ω)**
0.1M	32.15	4.16E-06	16.7	14.85
0.2M	30.71	1.99E-06	22.07	18.9
0.3M	29.88	1.29E-06	18.96	36.66
0.4M	28.24	9.15E-07	18.91	55.12
0.5M	25.57	6.62E-07	17.25	99.67

An analogous preliminary characterization was carried out for **1**, with two electrodes made of single-wall CNH, spray-deposited on FTO, in EC:PC (1:1) + LiOTf 1M, at different cobalt concentrations (0.1-0.4M). Voltammetric scans to identify the entire electrochemical region

associated with cobalt redox states are reported in Fig.6.19a, where the subsequent processes Co(III)→Co(II) and Co(II)→Co(I) (with $E_{1/2}$ = -1.25 V) are shown. Despite the greater variability of spray deposited NH substrates with respect to electrodeposited PEDOT, we were able to individuate the best performance at [Co(II)]=0.4 where a limiting current density of the order of 30mA/cm^2 at *ca.* -1.5 V was observed, which matches well the limiting anodic current that could be delivered by anodic Fe(III)/(II) compartment. Cobalt diffusion coefficients of 6±2E-07 cm^{2}s^{-1} , similar to iron, were indeed found, in agreement with the analogous molecular structure. EIS studies confirm a dominant role of the diffusion, whose arc is the predominant feature of the Nyquist plot. Consistent with the steep slope of the Co(II)/(I) process, the diffusional arcs reach amplitudes lying between 31Ω and 23 Ω (Fig.6.19b). This might be related to the wider electroactive area of NHs with respect to PEDOT.

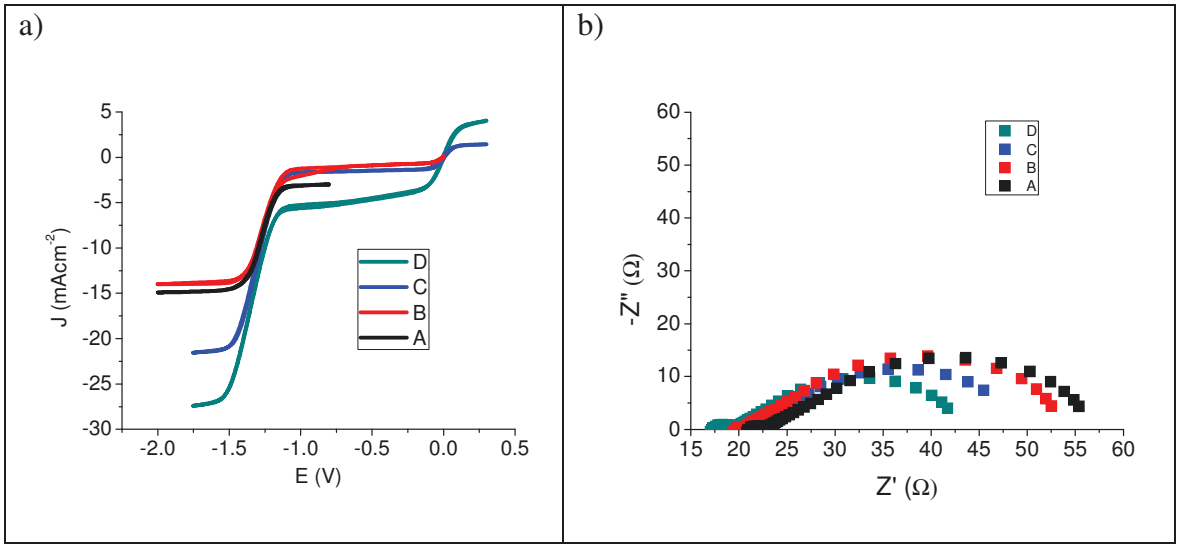

Fig.6.19 a) Slow scan rate cyclic voltammetry of **1** in thin layer dummy cell in EC:PC + 1M LiOTf at different concentrations (-A: 0.1M – B: 0.2M – C: 0.3M – D: 0.4M). b) Nyquist plot of **1** complex in a two-electrode cell in EC:PC + 1M LiOTf at different concentrations (-A: 0.1M – B: 0.2M – C: 0.3M – D: 0.4M – E: 0.5M).

Table 6.7 Kinetics data and Fitting parameters for **1**.

	J_L(mA/cm^2)	D(cm^2/s)	Rs (Ω)	R_{CT} (Ω)	Ws-R (Ω)
0.1M	14.30	3.87E-7	21.15	0.58	30.89
0.2M	14.90	4.07E-7	19.92	0.25	32.58
0.3M	21.45	7.83E-7	19.98	0.39	27.04
0.4M	26.74	8.35E-7	17.49	1.8	22.92

Furthermore, no loss in electroactivity nor appearance of electroactive decomposition byproducts were observed upon repeated cyclings (Fig 6.20 a) and 24h rest of the cell

(Fig.6.20 b), confirming the stability of Co(II)/(I) response on carbon substrates even under concentrations suitable for the application in a real cell, *i.e* 0.4M and 0.3M respectively. It is worth to notice that there is a slight increase in the total cell resistance after 24h, which is, however, attributable to the ohmic resistance (*Rs*), which has a variability of a few ohms (typically 1-5) related to metal / FTO contact (Fig 6.20 c).

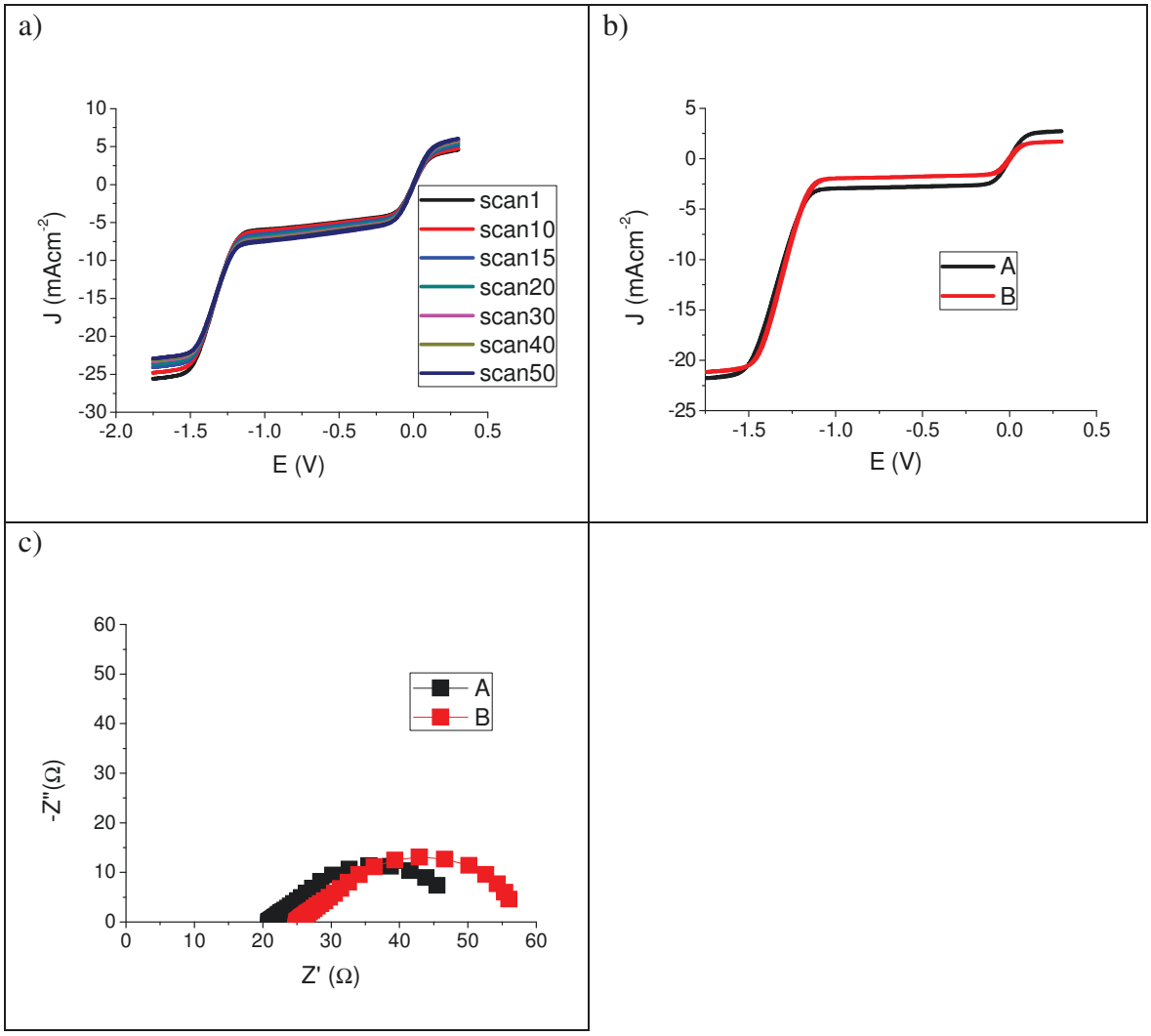

Fig.6.20 Slow scan rate linear sweep voltammetry in a two-electrode cell of a) 0.4M **1** in EC:PC (1:1) + 1M LiOTf upon repeated cyclings and of b) 0.3M **1** in EC:PC (1:1) + 1M LiOTf at A- t0 B- after 24h .**c)-**Nyquist plot of 0.3M **1** in EC:PC + 1M LiOTf at A- t_0 B- after 24h

In the light of the above, we can state that the comparison between Fe(III)/(II) and Co(II)/(I) couples provides promising expectations for the coupling of these two complexes in liquid battery for energy storage. Therefore, a two-compartment flow cell was assembled, with **1** and **6b** (Fig.6.21), to preliminary evaluate in lab. scale the efficiency of the whole system.

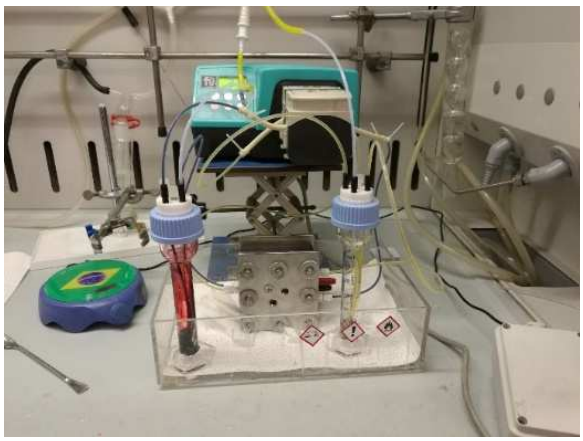

Fig.6.21 Flow cell assembling with small tanks.

A first screening was carried out by setting the potentials at +2.5 V during charge and +0.6 V during discharge, with **6b** 0.1M, **1** 0.1M and LiOTf 0.4M respectively (Fig.6.22). It is worth to note that after charging, a stable open circuit voltage (OCV) equal to 1.9 V was obtained in agreement with the theoretical expectation. Within the first 7 cycles, spanning a time interval of 35000 s, the cell behavior is fairly reproducible. Besides, a reversible drop of current for each cycle (*i.e* from 10 mA to 3 mA) is observed and the current recorded is significantly lower than the one reached in thin layer cell. These phenomena should be probably due to the increase of cell size and the insertion of a membrane.

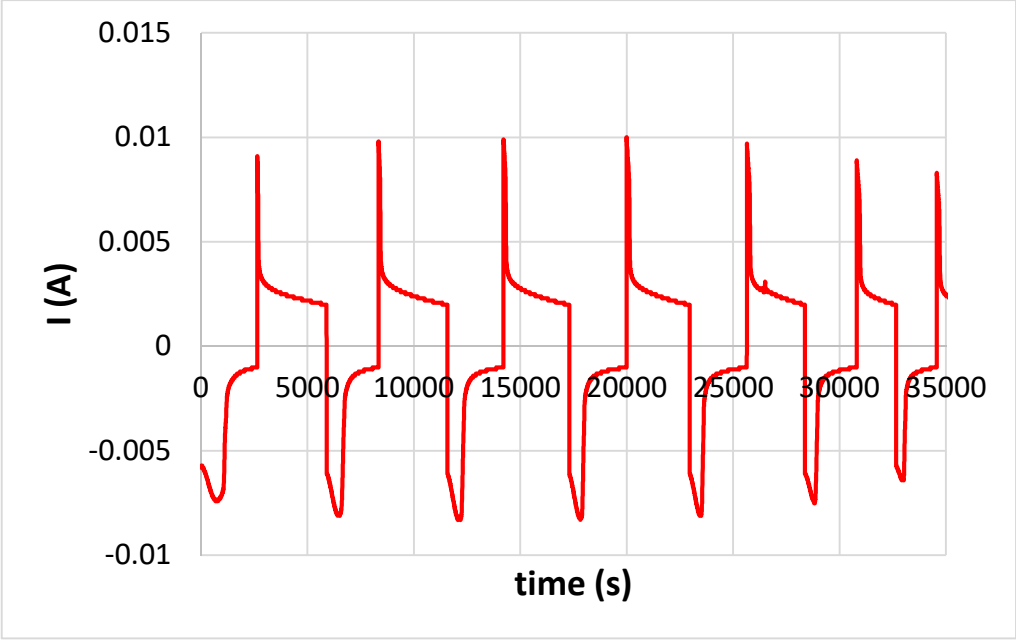

Fig.6.22 Potentiostatic cycles with **6b** 0.1M, **1** 0.1M and LiOTf 0.4M.

In this experimental set, 14 cycles of charge/discharge were collected to get some performance data such as electrode polarization, exchanged charges and efficiency. Data in

Fig.6.23 show a low electrode polarization, a noticeable charge loss with time, *i.e* 75% after 8h, a good coulombic efficiency (*ca.* 90%) and Voltaic and Energetic efficiencies around 20 %.

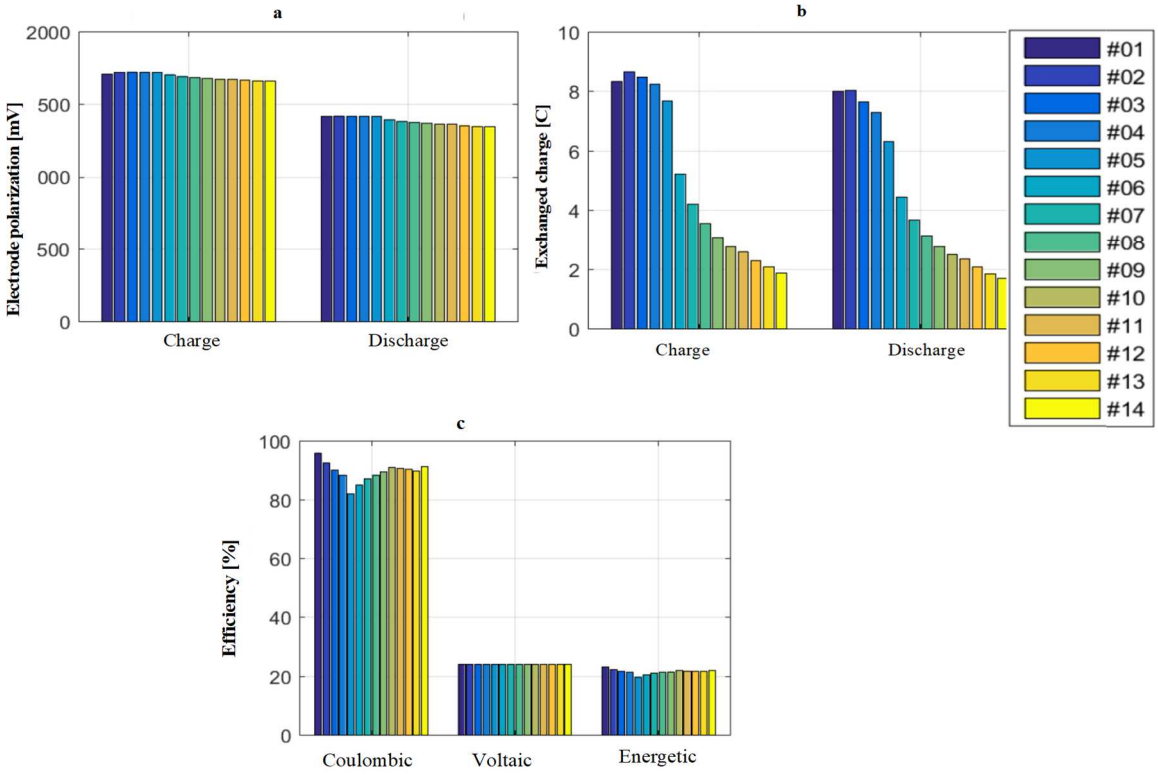

Fig.6.23 a) Polarization data; b) Exchanged charges; c) Efficiency for 14 cycle operation.

Charge loss with time seems not due to either side reactions or redox couples' instability, rather should be reasonably due to a reduced ionic transport, caused by a permanent adsorption of OTf-anions on membrane surface. Indeed, contrary to expectation, a current decrease (Fig.6.24, curve C) is well noticed when the concentration of LiOTf was increased to 1 M, despite better electrolyte conductivity. This means that the system has potential to be used in a cyclable flow battery but an immobilization of LiOTf may occur during cycling because of the high affinity between OTf-anions and acidic groups on Nafion membrane.

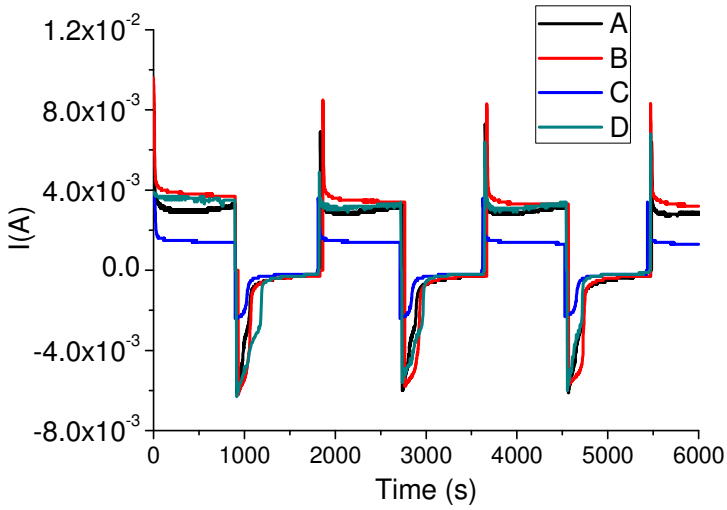

Fig.6.24 Potentiostatic cycles with different ratios of **6b** : **1** : LiOTf. A) 0.1:0.1:0.4. B) 0.2:0.2:0.2. C) 0.1:0.1:1.0. D) 0.2:0.2:0.4.

Galvanostatic cycles were recorded by using the same flow cell, with the most promising active species concentration (see fig.6.24), namely **6b** 0.2 M, **1** 0.2M, LiOTf 0.2 M. The experimental conditions were set as charging current at 4 mA with voltage limit at 2.7 V and discharging current at - 4 mA with voltage limit at 0.2 V. The feasibility of galvanostatic cycles in flow cell is shown in Fig.6.25. In this experimental condition 20 charge/discharge cycles have been collected, giving more than 90% of coulombic efficiency, but maintaining only 20% of voltaic and energetic efficiencies.

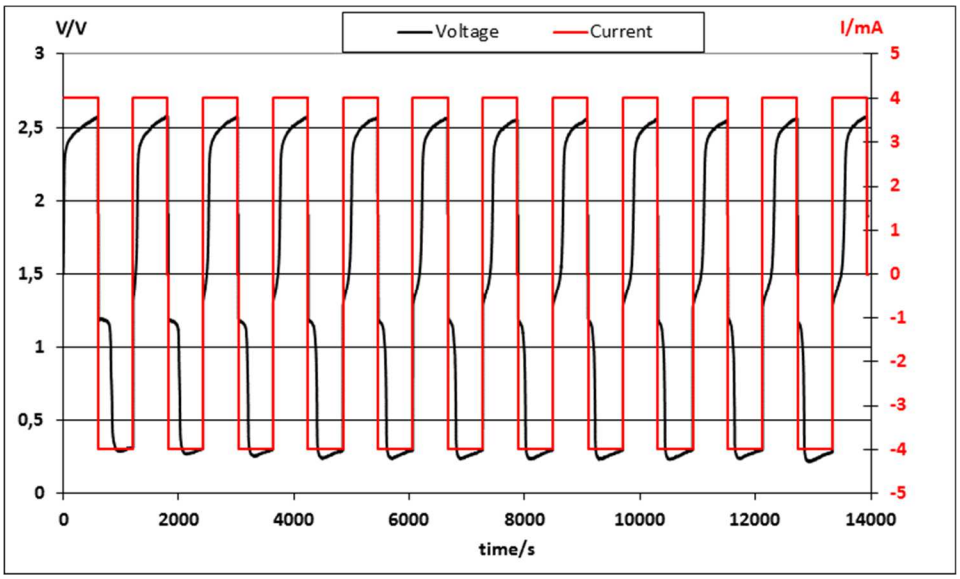

Fig.6.25 Galvanostatic cycles

In order to investigate the origin of deterioration of membrane conductivity, XPS measurements were carried out on both membrane sides, which resulted identical in

chemical composition: no metals have been revealed in the surface, even though the technique sensivity is quite high, indicating that the redox active complexes were not retained within the membrane, and did not concur to its clogging. Beside, the elemental semi-quantitative analysis, performed by survey rough data with Shirley baseline subtraction, shows that after discharging the membrane is covered by additional chemical species (F, O, S), clearly due to the presence of triflate anions attached to the surface.

Atomic Conc. (%)	**C 1s**	**F 1s**	**O 1s**	**S 2p**
Nafion new	78.7	13.5	6.8	0.3
Nafion discharged	37.8	51.1	8.4	1.4

Table6.8 XPS survey data

6.4 Conclusions

A series of Co(II) and Fe(II) polypyridine complexes as trifilate and TFSI salts were explored with the aim of evaluating their chemical and electrochemical characteristics for application in the framework of redox flow batteries. Among the explored series the best results were observed with complexes **6b** and **1** which couple solubility > 0.6 M in EC:PC and chemical stability upon slow rate potential cycling and potentiostatic electrolysis with diffusion limited electron transfer processes. The exploitation of Co(II)/(I) and Fe(III)/(II) states allows to obtain open circuit voltages close to 2 V, with the delivery of limiting current of the order of 30 mA/cm^2 when the mass transport conditions are optimized. Furthermore, the employment of Iron complexes, such as **6b**, with strongly colored MLCT states offers in addition the possibility of monitoring the charge state of the battery via fast optical methods. Given these promising properties, selected Iron and Cobalt couples, **6b** and **1**, were tested in lab. scale organic redox flow batteries, finding a stable OCV of *ca.* 1.9 V, in agreement with thermodynamic expectations. The possibility of obtaining charge/discharge cycles have been demonstrated both in potentiostatic and galvanostatic conditions. Besides, a decrease of performance with time was observed and was explained with a diminution in ion exchange properties of the Nafion membrane which displays a strong affinity for the adsorption of anions. The research is now directed towards the development of different supporting electrolytes and to the evaluation of different ionic exchange membranes.

6.5 References

1) Q. Huang, W. Huang, Y. Kim, Chempluschem 2015, 80, 312;

2) G. Kear, A.A. Shah, F.C. Walsh, Int. J. Energy. Res. 2012, 36, 1105;

3) E. Wesoff, J.S. John, Largest capacity Flow Battery in North America and EU is on-line and commissioned. http://www.greentechmedia.com/ articles/read/Largest-Capacity-Flow-Battery-in-NorthAmerica-and-EU-is-Online-and-Commiss;

4) M.A. Miller, A. Bourke, N. Quill, et al., Journal of the Electrochemical Society 2016, 163, A2095;

5) M. Skyllas-Kazacos, F. Rahman, J. Power Sources 2009, 189, 1212;

6) F.C. Walsh, P. Leung, X. Li et al., RSC Adv. 2012, 2, 10125;

7) S. Eckroad, Palo alto, CA: Electric Power Research Institute 2007, 1014836;

8) C.G. Armstrong, K.E. Toghill, J. Power Sources 2017, 349, 121;

9) Y. Huang, S. Gu, Y. Yan, S.F. Yau Li, Current Opinion in Chemical Engineering 2015,8 , 105;

10) Q. Liu, A.A. Shinkle, Y. Li et al., Electrochem. Commun. 2010, 12, 1634;

11) P. J. Cabrera, X. Yang, J.A. Suttil,,R.E.M. Brooner, L.T. Thompson, M.S. Sanford, Inorg. Chem., 2015, 54 , 10214;

12) A.E. Sleightolme, A.A., Shinkle, Y. Li et al., J. Power Sources, 2011, 196, 5742;

13) Q. Liu, A.E. Sleightolme, A.A. Shinkle, et al., Electrochem. Commun., 2009 ,11 , 2312;

14) J. Mun, M.J. Lee, J.W. Park, et al., Electrochem. Solid. St., 2012, 15, A80;

15) M.-S. Park, N.-J. Lee, et al., ACS. Appl. Mater. Interfaces 2014, 6, 10729;

16) Yu Ding et al., Energy Environ. Sci. 2017, 10, 491;

17) X. Xing, D. Zhang, Y. Li, J. Power Sources 2015, 279, 205;

18) X. Xing, Y. Zhao, Y. Li, J. Power Sources 2015, 293, 778;

19) R.M. Darling, K.G. Gallagher, J.A. Kowalski S. Ha, F.R. Brushett, Energy Environ. Sci. 2014, 7, 3459;

20) T. Ayers, S. Scott, J. Goins, Inorganica Chimica Acta 2000, 307, 7;

21) C.A. Bignozzi, R. Argazzi, R.Boaretto et al., Coordination Chemistry Reviews 2013, 257, 1472;

22) S. Carli, E. Busatto, S. Caramori, et al., J. Phys. Chem. C. 2013, 117, 5142;

23) L. Casarin, W.B. Swords, S. Caramori et al., Inorg. Chem. 2017, 56, 7324;

24) S. Cazzanti, S. Caramori, R. Argazzi, C.M. Elliot, C.A. Bignozzi, J. Am. Chem. Soc. 2006, 128, 9996;

25) F. Ghamouss, R. Pitson, F. Odobel et al., Electrochimica Acta 2010, 55, 6517;

26) S. Carli, L. Casarin, Z. Syrgiannis, et al., ACS Appl. Mater. Interfaces 2016, 8, 146404;

27) S. Mandal, D.K. Seth, P. Gupta, Polyhedron 2012, 31, 167;

28) T.J. Nelson, T.J. Amick, C.M. Elliott, J. Phys. Chem. C. 2008, 112, 18255;

CHAPTER 7. PERYLENE AGGREGATES ON SnO_2 AND ON Sb-DOPED SnO_2: CHARGE TRANSFER DYNAMICS RELEVANT TO SOLAR FUEL GENERATION.

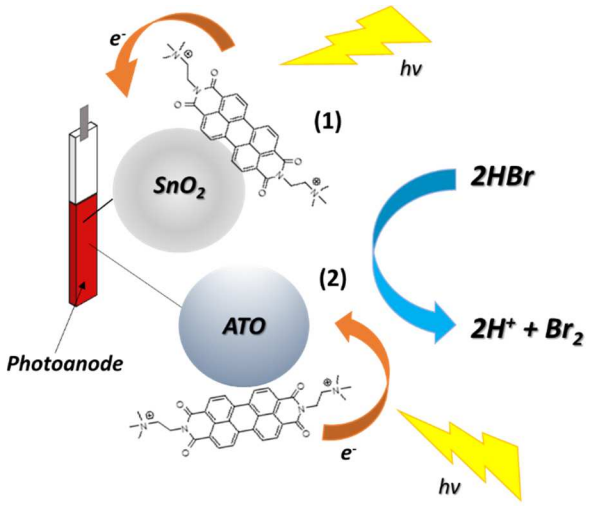

Fig.7.1 Schematic representation of the perylene/SnO_2 (**1**), perylene/ATO photoanodes (**2**), for HBr splitting.

This chapter will report on the possibility to combine wide band gap semiconductors like SnO_2 and Sb-doped SnO_2 (ATO) with perylene (PDI)-based aggregates to find an efficient nanostructured photoanode for photoelectrochemical solar fuel generation. A detailed analysis of semiconductor properties was carried out in order to understand interfacial energetics, charge separation and charge transfer dynamics. An interesting behaviour associated to Sb-doped SnO_2 was found. Indeed, due to Sb doping, ATO showed a significant density of deep intra band states, which are absent in pure SnO_2. The presence of these states, whose occupancy varies with the applied potential, plays a substantial role in tuning the efficiency of photoinduced charge separation and collection of ATO-PDI system. The role of surface states seems to be much less pronounced in PDI/SnO_2 electrodes but still an influence of the pH on the charge injection and collection efficiency of SnO_2-PDI photoanodes was observed through an evaluation of the incident photon-to-current conversion. This suggests that in such systems the energy of the semiconductor states can be tuned independently from the molecular levels, allowing to improve the photoanode quantum yield in the case of poorly reducing excited states.

7.1. Introduction

As previously reported in Chapter 2, during recent years the possibility to convert solar energy into chemical bonds that can serve as solar fuels was explored [1-2]. The employment of dye-sensitized photoelectrodes [3-4], *i.e.* wide band gap semiconductors in which a suitable molecular dye was adsorbed, was considered to carry out water splitting [5] or water oxidation combined with CO_2 reduction [6,7] which are among the most attractive reactions, given the importance of the products as alternative fuels. Furthermore, another method to produce solar fuels is through hydrohalic acid (HX) splitting. Like water splitting, HX splitting is the concurrent reduction of H^+ to H_2 and oxidation of X^- to X_2. In particular, photoinduced HBr splitting represents an interesting approach since its products H_2 and Br_2 can be used in redox flow batteries to generate electricity [8-10]. Most of the research work in this field concerns the design and the optimization of the photoanode, since a molecular level approach, to carry out either water or HBr splitting, requires a significant control over photophysical and electrochemical properties of the dye and the semiconductor material [11-12]. The main problem is the development of visible absorbing sensitizers, having sufficient driving force to carry out both charge injection into the semiconductor conduction band and hole (*h*+) transfer to water oxidation catalysts [13] (needed to lower the kinetic barrier for multi-electron transfer). Even in the case of kinetically more facile reactions, like bromide oxidation, strongly oxidizing ground states are required to produce Br_2 at a reasonable rate, storing > 1 eV/molecule. A huge series of metal complexes or organic molecules [14] was employed during recent years in conjunction with metal oxides like as TiO_2 or WO_3. Usually the absorber is linked to semiconductor surface with an anchoring group, and the bond with the surface is either ester-like or a coordination type with both binding modes co-existing depending on adsorption conditions and surface heterogeneity. Besides, in recent times dye-semiconductor interactions based on π-stacking/hydrophobic [15-16] forces were reported. Following this latter example, in this chapter we will investigate charge injection and collection in two different semiconductor surfaces on which a cationic perylene based dye ([(*N,N'-bis*(2-(trimethylammonium)ethylene)-perylene-3,4,9,10-tetracarboxylic acid *bis*-imide)]$(PF_6)_2$, namely PDI (Fig.7.2)) was adsorbed.

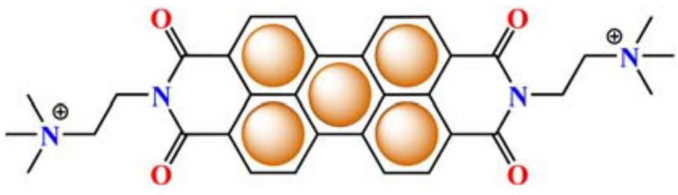

Fig.7.2 Schematic structure of the dicationic PDI dye.

The most interesting advantage coming from the use of a dye-semiconductor system based on hydrophobic interactions is given by the surface binding type, which does not suffer the hydrolytic cleavage of the covalent link generally reported in the case of carboxylic or phosphonic bonds at pH above 5 [17]. In this latter case, special surface treatment procedures are required to further stabilize the binding of carboxylate or phosphonate groups with the surface, typically consisting in ALD deposition of thin layers of inert metal oxides to protect the anchoring site from the access of the solvent. The specific perylene was chosen because it presents a thermal and photochemical stability, furthermore its energetics perfectly matches with the thermodynamic requirements for driving demanding oxidation reactions [18-20]. Indeed, PDI, characterized by a planar geometry of the aromatic core (Fig.7.3), shows a calculated HOMO-LUMO energy gap of *ca.* 2.5eV with a E^0_{red}/E^0_{ox} potential oxidative enough (~1.9 V *vs* NHE from DFT calculation) to drive most of the oxidation reactions proposed in most photoelectrochemical solar fuel formation processes [16]. On the contrary, the redox potential of its excited state (E^0*/E^0_{ox}) is scarcely reducing (-0.4 V *vs* NHE from DFT calculation) [16], consequently only semiconductors with conduction bands (CB) more positive than this value can be efficiently coupled with this dye.

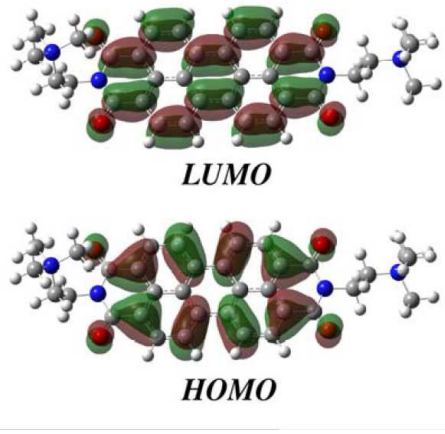

Fig.7.3 Optimized geometries and frontier molecular orbitals of PDI used in semiconductor sensitization, computed at DFT level in AcN (The DFT functional employed for calculation is reported in ref.[16]) .

Semiconductors of election were SnO_2, which presents a suitable thermodynamic to promote electron collection as previously reported [16], and the equivalent antimony doped (ATO), which was chosen to improve electron collection. Due to the rather high availability of tin, tin dioxide (SnO_2) is one of the most extensively studied transparent conducting materials. Prepared in the form of dense films, it is polycrystalline with a rutile (cassiterite) type of structure in the space group $P4_2/mnm$ [21-23], isostructural to TiO_2. SnO_2 exhibits a band gap of ~3.8eV [21] and is an n-type semiconductor, which is a result of the non-

stoichiometry, or in particular of the oxygen deficiency. In order to increase the conductivity of SnO_2, various dopants have been used up to now. In antimony doped tin oxide (ATO) the conductivity of SnO_2 is increased by substituting tin (Sn^{4+}) with antimony ions in a higher valence state than tin, namely Sb^{5+} [24-25]. The dopant atoms, Sb, sit on the Sn sites in the lattice and bring one electron more into the host lattice forming a shallow donor level close to the conduction band. Thus the donation of this electron induces an increase in conductivity [21]. The influence of the amount of incorporated antimony on the structural and electrical properties of the ATO was intensively studied by several authors and highest conductivity was obtained for dense ATO films [26-31], of the order of 1×10^3 S/cm, when the films contain 7 mol % of antimony. It is worth to notice that at high enough doping levels a degenerate semiconductor is obtained displaying metallic properties like an electrical conductivity which only weakly depends on temperature. These observations are in accord with quantum mechanical calculations of the electronic structure of highly Sb-doped SnO_2, showing that the antimony ions lead to a partially filled free-electron-like impurity band in the band gap of tin dioxide [39]. Furthermore, doping of tin oxide with antimony modifies the conduction band leading to a shift in the optical absorption edges to higher energies with increasing charge carrier concentration. This type of behaviour is known as the Burstein-Moss effect [21]. Herein, we will investigate both SnO_2 and ATO properties and charge transfer, collection dynamics as substrates for dye sensitization by molecular aggregates (SnO_2-PDI, ATO-PDI), demonstrating their capabilities to transfer photogenerated h^+ to sacrificial species like HBr. Furthermore, in conjunction with a suitable catalysts, these systems are able to carry out water oxidation as well [16]. A particular emphasis is given to the description of the interfacial energetics and to the characterization of the charge transfer dynamics from the fs to the ms time domain.

7.2 Experimental section

7.2.1 Materials and Methods

SnO_2 colloidal solution (15% in water) and 10% Sb-doped SnO_2 (50% in water) were purchased from Alfa Aesar. Polyethyleneglycol bisphenol A epichlorohydrin copolymer 15000 - 20000 Dalton, 70% perchloric acid ($HClO_4$), ≥99% glacial acetic acid, absolute ethanol, spectroscopic grade acetonitrile (AcN), ACS grade ≥99.8% 2-propanol, perylene-3,4,9,10-tetracarboxyldiimide, quinoline, N,N'-dimethylethylenediamine, methyl iodide, ammonium haxafluorophosphate (NH_4PF_6), sodium perchlorate ($NaClO_4$), 48% hydrogen bromide (HBr), sodium bromide (NaBr) and Alconox® were purchased from Sigma Aldrich.

Milli-Q water was obtained using a Millipore apparatus, equipped with 0.22 µm filters. TEC 8 Fluorine-doped Tin Oxide (FTO) conductive glass slides were obtained from Pilkington. Unless otherwise stated, all reagents were used as received. UV-Vis absorption spectra were measured with a JASCO V-570 with a bandwidth of 2 nm. AFM images were collected using a Digital Instruments Nanoscope III scanning probe microscope (Digital Instruments, CA). The instrument was equipped with a silicon tip (RTESP-300 Bruker) and operated in tapping mode. Surface topographical analysis of raw AFM images was carried out with NanoScope analysis 1.5 program.

7.2.2 Synthesis of [(N,N'-bis(2-(trimethylammonium)ethylene)-perylene-3,4,9,10-tetracarboxylic acid bis-imide)]$(PF_6)_2$, PDI

PDI was synthesized by M. Prato group at the University of Trieste following a procedure reported in literature [32], starting from the corresponding bis-iodide salt. For the exchange of the counterion, the precursor was solubilized in H_2O and saturated aqueous solution of NH_4PF_6 was added. The required material was precipitated after stirring for 1 hour and collected by filtration, followed by washing with water and MeOH. The resulting solid was dried under vacuum to afford the product as red powder. Yield was 84%. ^{1}H-NMR and ^{13}C-NMR were in agreement with results reported in literature. ESI *m/z*: 852.60 $[PDI\cdot(PF_6)_2]^-$, 281.5 $[PDI]^{2-}$; $\varepsilon(\lambda)$ [M^{-1} cm^{-1}]: 9650 (465 nm), 25750 (485 nm), 40450 (521 nm).

7.2.3 Preparation of SnO_2 and Sb-doped SnO_2 colloidal paste

Colloidal SnO_2 was prepared following a literature procedure [16]: 2.1 ml of glacial acetic acid were added to 50 ml of SnO_2 colloidal solution in order to favour nucleation and growth of larger SnO_2 particles. The mixture was vigorously stirred for 2 hours to avoid gelation and excessive thickening of the gel. The colloidal suspension was autoclaved in oven at 220°C for 12 hours. After cooling at room temperature, 3.5 g of polyethyleneglycol bisphenol A epichlorohydrin copolymer (Carbowax) were added to the resulting white paste, followed by magnetic stirring for 6 hours, to allow a complete dissolution of the copolymer and homogenization with the SnO_2 colloid. Sb-doped SnO_2 paste was prepared following the same procedure, from the commercial colloidal dispersion.

7.2.4 Preparation of SnO_2 and Sb-doped SnO_2 (ATO) powders

SnO_2 and Sb-doped SnO_2 powders were synthesized from colloidal paste by following the same procedure. Before the addition of Carbowax, the colloid was evaporated to dryness.

Subsequently, the solid obtained was heated to 550 °C for 30 min leading to the synthesis of the crystalline powder.

7.2.5 Sensitization of SnO_2 and Sb-doped SnO_2 (ATO) powders

SnO_2-PDI and ATO-PDI powders were prepared by dipping in a 1mM PDI acetonitrile solution for *ca.* 1h (*i.e.* 10mg SnO_2/ATO in 10mL PDI solution) under magnetic stirring. Afterwards each suspension was centrifuged and the surface modified semiconductor powder was collected and dried under vacuum.

7.2.6 Preparation of the photoanodes

FTO cleaning was performed by sonicating the slides in Alconox® solution for 10 minutes and in 2-propanol for further 10 minutes. SnO_2 paste, prepared by following the procedure reported above, was diluted (1:2) by adding milliQ water, then deposited *via* spin coating (6 s at 600 rpm, 20 s at 2000 rpm) onto cleaned FTO slides and annealed at 550°C for 30 min. Colloidal Sb-doped SnO_2 (ATO) paste was spin coated onto cleaned FTO slides by employing the same conditions described for SnO_2. Colloidal ZrO_2 was prepared and deposited onto FTO following a literature procedure [33].

7.2.7 Sensitization of photoanodes

Electrodes were dipped in a 1mM acetonitrile (AcN) solution of PDI (Fig.7.4), until surface saturation of the dyes was reached (*ca.* 1h). The sensitized photoanodes were then rinsed with acetonitrile and dried under an air flow.

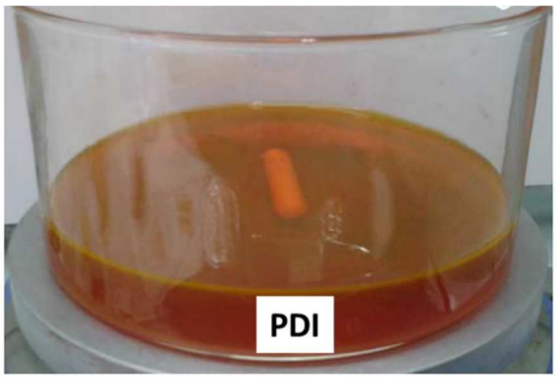

Fig.7.4 10^{-3} M AcN solution of PDI (shoot by Dr. Federico Ronconi).

7.2.8 Electrochemical characterization

Cyclic Voltammetry (CV) measurements (scan rate 10mV) were carried out on a PGSTAT302N potentiostat in a three-electrode nitrogen-purged cell, using SCE (Amel) and Pt (Sigma-Aldrich) wire respectively as the reference and the counter electrode. Unless

otherwise stated, all the potential values are given versus the SCE reference electrode. Different electrolytes were employed, containing several $HClO_4$ concentrations in order to tune pH (10^{-3}M $HClO_4$, 0.1 M $NaClO_4$ (pH3); 0.1M $HClO_4$ (pH1)).

7.2.9 Photoelectrochemical characterization

Photoelectrochemical measurements were carried out on a PGSTAT302N potentiostat in a three-electrode configuration, using SCE and Pt wire respectively as the reference and the counter electrode. A LOT-Oriel solar simulator, equipped with an AM 1.5 G filter, was used as the illumination source, and set to 0.1 W/cm^2 incident irradiance power by means of a Power Meter (Newport 1918-C). *J-V* curves, recorded at 10 mV/s scan rate, were repeated by cycling the photoanodes until an overlapping response upon subsequent scans (stationary state) was achieved. *J-V* curves under shuttered illumination were acquired by manually chopping the excitation source. Unless otherwise stated, all the potential values are given versus the SCE reference electrode. Incident photon-to-current conversion efficiency (IPCE) was measured in a three-electrode configuration under the monochromatic illumination generated by an air cooled Luxtel 175 W Xe lamp, coupled to an Applied Photophysics monochromator. The resulting photocurrent, recorded at the constant potential of 0.8 V *vs* SCE, was measured by a PGSTAT302N potentiostat. Different electrolytes were employed, containing the same sacrificial agents, namely Br^-, and different amounts of Hbr and of NaBr in order to tune pH and to keep constant Br^- concentration, respectively.

7.2.10 Zeta potential measurements

Zeta potential measurements were carried out at Paris Lodron University in Salzburg in collaboration with Prof.T.Berger. SnO_2, ATO, SnO_2-PDI, ATO-PDI suspensions in water were prepared by dissolving 1mg of the corresponding powder in 10mL of water. Zeta potential measurements on suspensions were carried out with a Malvern Zetasizer Nano ZSP ZEN560A. The zeta potential was calculated from the electrophoretic mobility using the Smoluchowski approximation. The applied voltage on the disposable folded capillary zeta cell was 40 V. To ensure an appropriate dispersity of the suspensions for the zeta potential measurements, an ultrasonic finger UP200St (Hielscher Ultrasonics GmbH) was used for typical irradiation times of 10 min while the sample dispersion was cooled in an ice bath for temperature control. To investigate the impact of the pH value on the dispersion stability, the suspensions were adjusted to different pH using two solutions of perchloric acid (0.1M $HClO_4$; 0.01M $HClO_4$).

7.2.11 Spectroelectrochemical characterization

Spectroelectrochemical measurements were performed at Paris Lodron University in Salzburg in collaboration with Prof.T.Berger. Spectroelectrochemical measurements on SnO_2 and ATO thin films before and after dye adsorption were carried out with a Keithley potentiostat and a Perkin Elmer Lambda 750 spectrophotometer connected to an integrating sphere in a 1 cm path three-electrode nitrogen-purged quartz cell, using SCE (Amel) and Pt wire (Sigma-aldrich) as the reference and the counter electrode, by applying the potential step progressively from 1.2V to -0.3V and from 1V to -0.3V for unsensitized and sensitized substrates respectively. Absorbance recorded by applying 1.2V for unsensitized and 1V for sensitized subastrates was set as baseline. It is worth to notice that all UV-Vis/NIR-spectra recorded represent the difference of the Kubelka-Munk function of spectra taken either at 1.2V or 1V. Spectroeclectrochemical measurements on PDI were carried out with an Autolab PGSTAT302N potentiostat and a JASCO V-570 UV–Vis spectrophotometer in a 1 cm path three-electrode quartz cell, employing SCE (Amel) and Pt wire (Sigma-Aldrich) respectively as the reference and the counter electrode. Both ITO electrode and ZrO_2-PDI electrode were employed as working electrodes.

7.2.12 Stationary emission spectra

Stationary emission spectra were measured with an Edinburgh Instruments FLS 920 spectrofluorimeter, equipped with a double emission monochromator. The photoanodes were placed in a dedicated film holder equipped with a micrometric mechanical regulation stage. In order to attain a good reproducibility, the maximum emission intensity was optimized before collecting the spectrum by tuning the angle between the electrode, the excitation beam and the emitted light reaching the detector. The S/N ratio was optimized by summing 10 subsequent scans with 1 nm wavelength step and a bandwidth ($\Delta\lambda$) of 4 nm. Spectra were corrected for the photomultiplier (R928P-Hamamatsu) response by using a factory built calibration file. Excitation was set to the absorption maximum of the sensitized thin films (485 nm). Background subtracted spectra were corrected for the LHE at the excitation wavelength (λ_{exc}).

7.2.13 Photocurrent Transient measurements

Photocurrent Transients were collected by irradiating the samples with the 532 nm harmonic of a nanosecond Nd:YAG laser (Continuum Surelite II), attenuated by several neutral filters to yield an intensity of 0.6 mW/cm^2. Sensitized photoanodes were placed in a three-compartment cell and immersed in 0.1 M HBr (pH 1). An additional continuous white light

bias was provided (when needed) by a LOT-Oriel solar simulator (equipped with an AM 1.5 G and a 435 nm cut-off filters) calibrated to 0.14 W/cm^2 intensity. Polarization of the photoanode was achieved using an EcoChemie PGSTAT302N potentiostat and the current response was sampled at 10^{-4} s intervals.

7.2.14 Nanosecond Transient Absorption spectroscopy

Kinetic evolution of the absorption feature at 550 nm for ATO-PDI immersed in 0.1 M NaClO4 (pH 3) was observed with an apparatus decribed in Chapter8,[16] by averaging the transient signal over 60 laser pulses at 532 nm. The kinetic trace, having an amplitude of *ca.* 1 mΔOD, was corrected for the baseline due to the monochromatic (550 nm) probe pulse averaged over 60 shots and then smoothed and fitted with a monoexponential function to calculate the charge-separated state lifetime.

7.2.15 Femtosecond Transient Absorption spectroscopy

Femtosecond Transient Absorption (TA) measurements were carried out on a pump-probe setup fed by 100-fs, 2-kHz repetition rate Ti:sapphire system (Libra, Coherent) with a central wavelength of 800 nm. The pump pulses were obtained by second-harmonic generation on a 100-μm, Type I β-barium borate crystal of a home-built infrared optical parametric amplifier (OPA). The so-generated pulses had a duration of ~70 fs and a centre wavelength of 485 nm. The energy was adjusted to 20 nJ, providing a fluence of $8x10^{-6}$ J/cm^2 on the sample. The probe pulses were obtained by white-light generation on a 3-mm thick calcium fluoride crystal, with a spectrum spanning from 350 to 700 nm. The transmitted probe beam was dispered in a spectrometer (SP2150 Acton, Princeton Instruments) and detected using a linear image sensor driven and read out by a custom-built board from Stresing Entwicklungsbüro. The differential transmission (ΔT/T) was then measured as a function of probe wavelength and pump−probe delay. For all the experiments reported in this paper pump and probe had perpendicular polarizations; a cross-polarizer was placed in front of the detector to avoid scattered light from the pump.

7.3 Results and Discussion

SnO_2 and ATO (Sb-doped SnO_2) powders were prepared from the colloidal paste by a simple procedure (see Experimental section). At an antimony doping of ca. 10 mol % Sb/(Sb+Sn), bluish ATO nanoparticles were formed; the colour appears to be due to a free charge carrier absorption in the material. [27]. At the very beginning a first screening was carried out by determining experimentally the electrophoretic mobility of the suspension of both SnO_2

and ATO powders in water before and after PDI adsorption. An electric field was applied across the dispersion to measure zeta potential, which is a key indicator of the stability of dispersions. Indeed, the magnitude of zeta potential indicates the degree of electrostatic repulsion between adjacent, similarly charged particles [34-35]. Furthermore, the electrical charge of the particles was measured as a function of pH, showing a really different behaviour between the undoped and the Sb doped semiconductors. SnO_2 and ATO present, before titration, a zeta potential of *ca.* -30mV, which indicates that the suspensions are stable, namely the repulsion between particles in solution is strong enough to avoid Van Der Waals interactions and hence coagulation. While SnO_2 reaches the isoelectric point at pH values around 3-4 [35], the doped one is not affected within this pH window by the increase of ionic strength showing a quite stable zeta potential in the range examined (Fig.7.5). This alteration of the surface charge is probably due to replacement of the surface Sn atoms by Sb ones, since a different surface charge of the particles originates by the presence of Sb^{5+}, leading to increased acidity of the surface OH groups. Furthermore, shift of isoelectric point is a mark of Sb percentage, since it varies as a function of doping: for Sb concentrations >10%, such as in the present case, it is supposed to be equal to *ca.* 2, according to literature reports [37-38], consistent with nearly constant ζ found in our case. Semiconductor functionalization with the dicationic dye, PDI, leads to a significant zeta potential shift of ATO towards a positive value (with an overall variation ≥ 30mV within the pH interval under consideration), indicating a change of the surface charge of the particles upon PDI adsorption. PDI adsorption on ATO powders seems to be more efficient, probably due to a more negative and constant electrical charge of ATO particle surface.

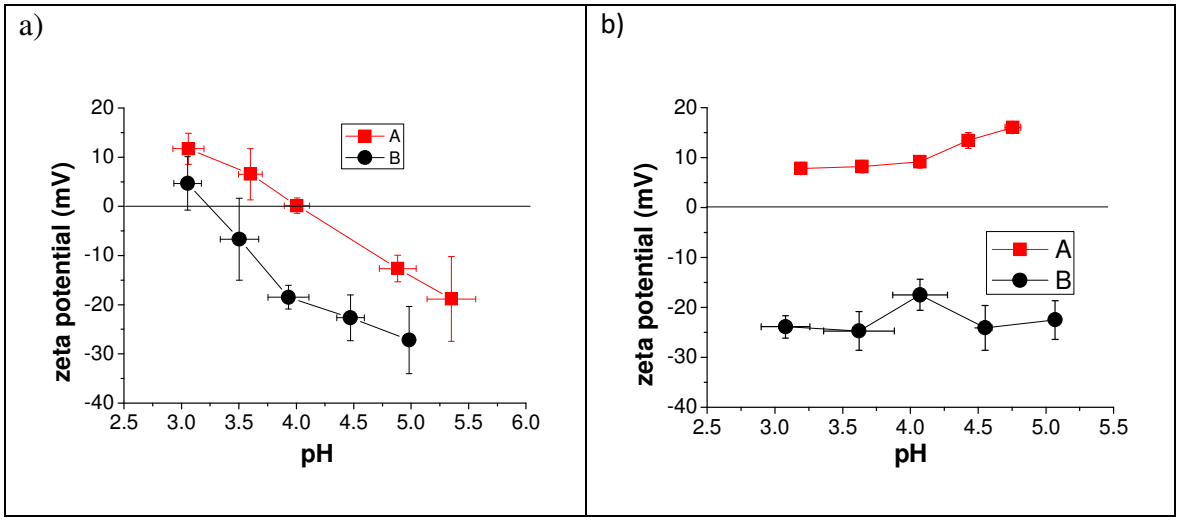

Fig.7.5 Zeta potential vs. pH of **a)**- SnO_2-PDI (A) and SnO_2(B) and **b)**- ATO-PDI (A) and ATO (B)

Colloidal dispersions of the two semiconductors were deposited onto conductive fluorine-doped tin oxide (FTO) electrodes, resulting in quite uniform nanostructured films consisting of particles with diameters of 100-120 nm and 60-70 nm respectively for ATO, and SnO_2, as confirmed by atomic force microscopy (AFM) measurements (Fig.7.6, Fig.7.7 respectively).

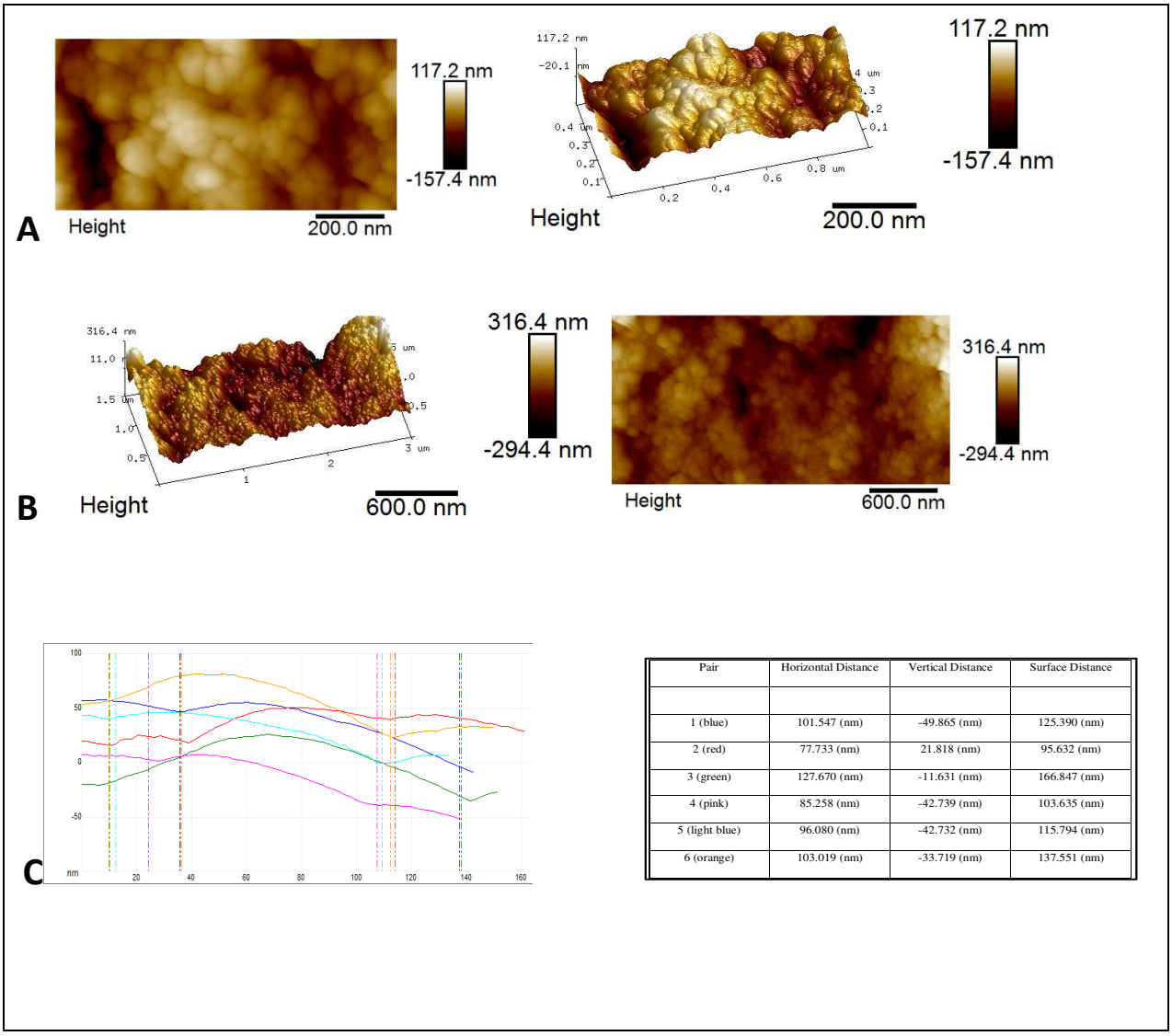

Fig.7.6 AFM images of the nanostructured semiconductors deposited onto FTO. A-B) ATO, 1 and 3 μm scan size respectively.

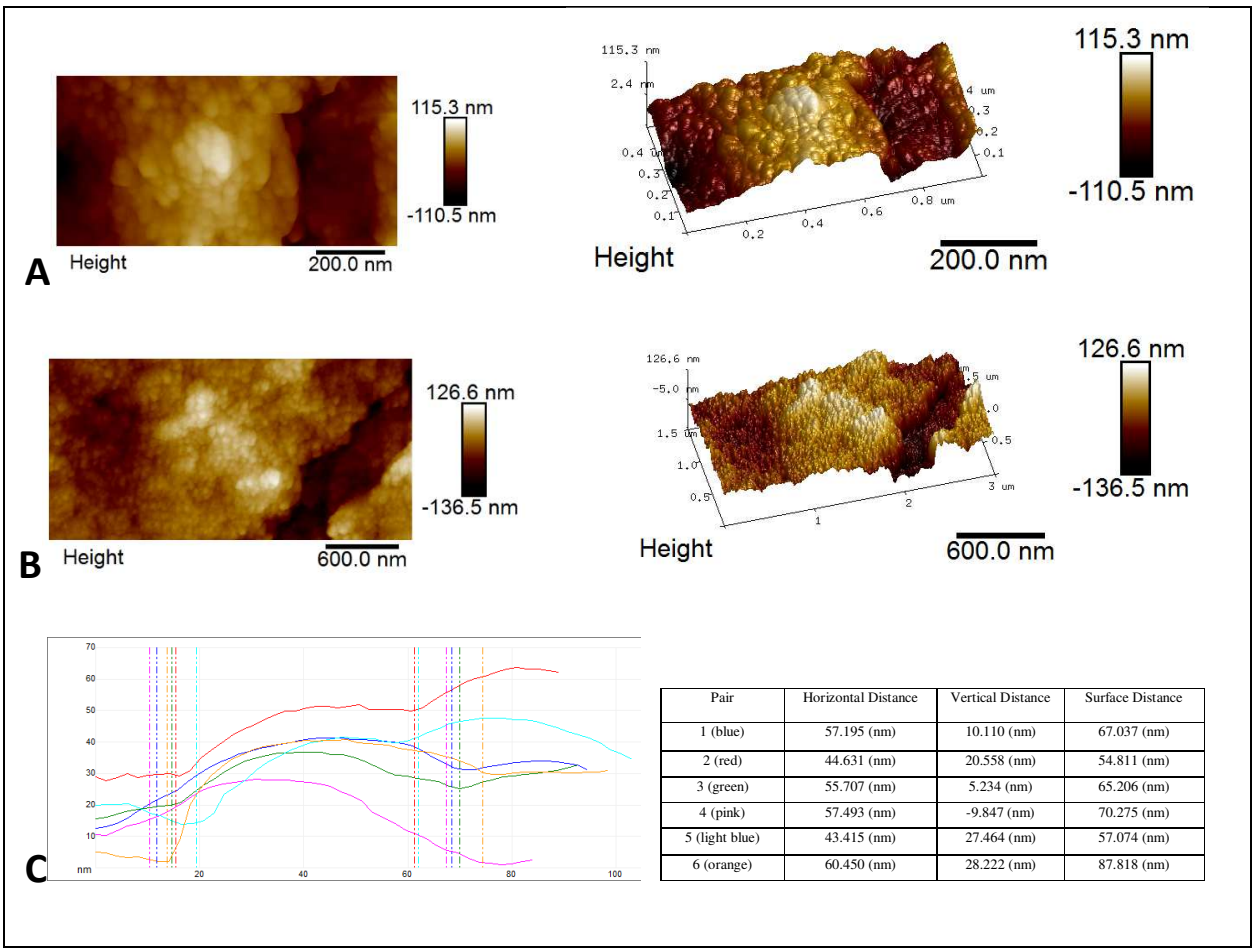

Pair	Horizontal Distance	Vertical Distance	Surface Distance
1 (blue)	57.195 (nm)	10.110 (nm)	67.037 (nm)
2 (red)	44.631 (nm)	20.558 (nm)	54.811 (nm)
3 (green)	55.707 (nm)	5.234 (nm)	65.206 (nm)
4 (pink)	57.493 (nm)	-9.847 (nm)	70.275 (nm)
5 (light blue)	43.415 (nm)	27.464 (nm)	57.074 (nm)
6 (orange)	60.450 (nm)	28.222 (nm)	87.818 (nm)

Fig.7.7 AFM images of the nanostructured semiconductors deposited onto FTO. A-B) SnO_2, 1 and 3 μm scan size respectively

The sensitization of the photoelectrodes has been revealed by UV-Vis spectroscopy (Fig.7.8 a). As shown in Fig.7.8 SnO_2-PDI presents a higher dye uptake with respect to the doped substrate, contrary to zeta potential evidence, since the surface properties of powders (*i.e.* particle size, porosity) are not identical with respect to those of the films. The spontaneous adsorption of the perylene diimide dye onto the surface of the semiconductors is mainly due to the precipitation of both crystalline and amorphous domains, forming H-aggregates via *pi*-stacking, as evidenced by the intensity reversal of the vibronic 0−0 and 0−1 bands in the absorption spectrum of ATO-PDI with respect to that of PDI in solution (Fig.7.8 b).

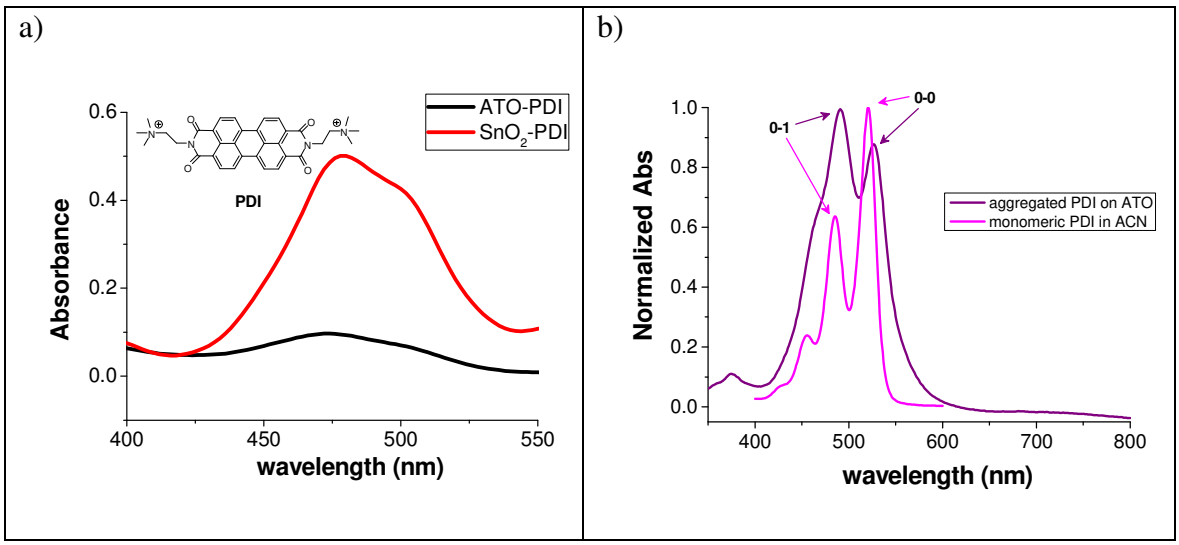

Fig.7.8 a) Visible spectra of the PDI-sensitized photoanodes ; b) Normalized absorption and emission spectra of PDI aggregates deposited onto ATO compared to those of PDI in AcN solution.

Cyclic voltammetries of SnO_2 and ATO before and after dye adsorption were carried in order to investigate the impact of dye adsorption on the interfacial energetics. CVs on SnO_2 and ATO (Fig.7.9) were recorded by varying the potential window. Various scans were performed by progressively extending the potential window towards negative values, in order to explore the region of appearance of the reductive current which determines the filling of empty states close to the conduction band (CB) edge, having *ca.* 0.2 V onset potential (E_{onset}) at pH 1 for both semiconductors. The discharge, observed when the potential progresses toward more negative values (from 0V vs SCE to -0.3V vs SCE), is due to further CB population. Moreover, ATO shows a broad anodic wave between 0.2 and 0.8 V, determined by the charge extraction from a distribution of intraband-gap states (ISs) as a consequence of Sb doping.

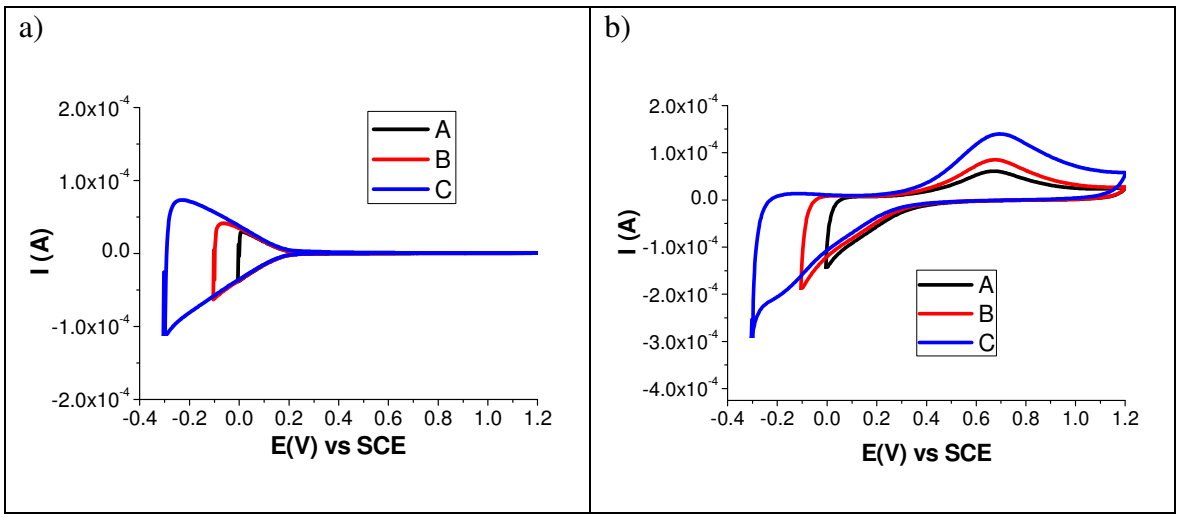

Fig.7.9 Dark cyclic voltammetry traces of **a)** SnO_2 recorded between A- 1.2V/0V; B-1.2V/-0.1V; C-1.2V/-0.3V; **b)** ATO recorded between A- 1.2V/0V; B-1.2V/-0.1V; C-1.2V/-0.3V in $HClO_4$ 0.1M (pH1).

SnO_2-PDI (Fig.7.10 a) onset potential shift associated to dye absorption can be estimated of *ca.* 5mV, in perfect agreement with zeta potential measurements (See Fig.7.5 a). Furthermore, in both dyed photoanodes a sharp cathodic process whose threshold appeared at -0.3V, was observed, and tentatively assigned to dye reduction (Fig.7.10 b, Fig.7.11,b).

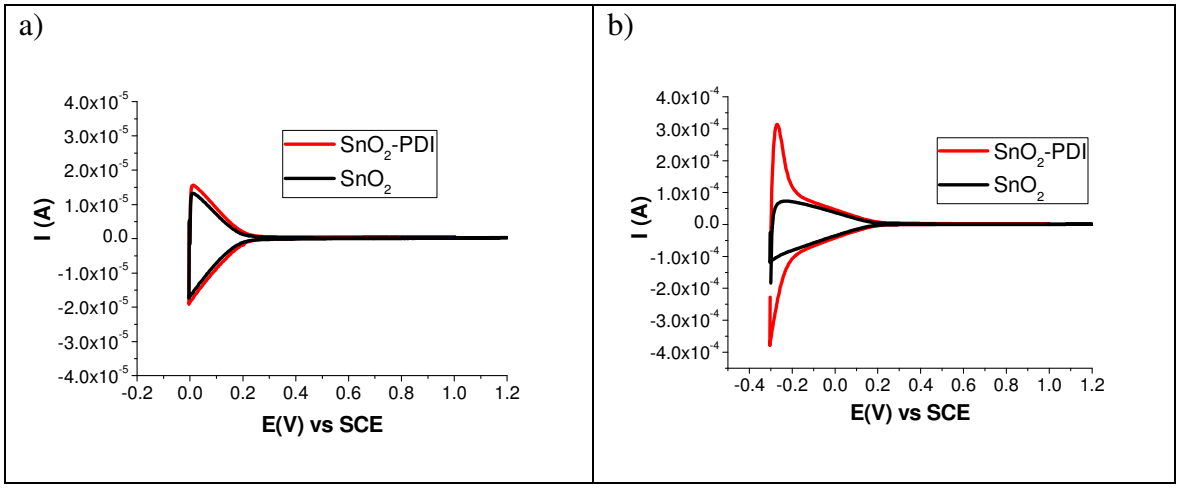

Fig.7.10 Dark cyclic voltammetry traces of SnO_2 and SnO_2-PDI recorded between **a)** 1.2V/0V; **b)** 1.2V/-0.3V in $HClO_4$ 0.1M (pH1)

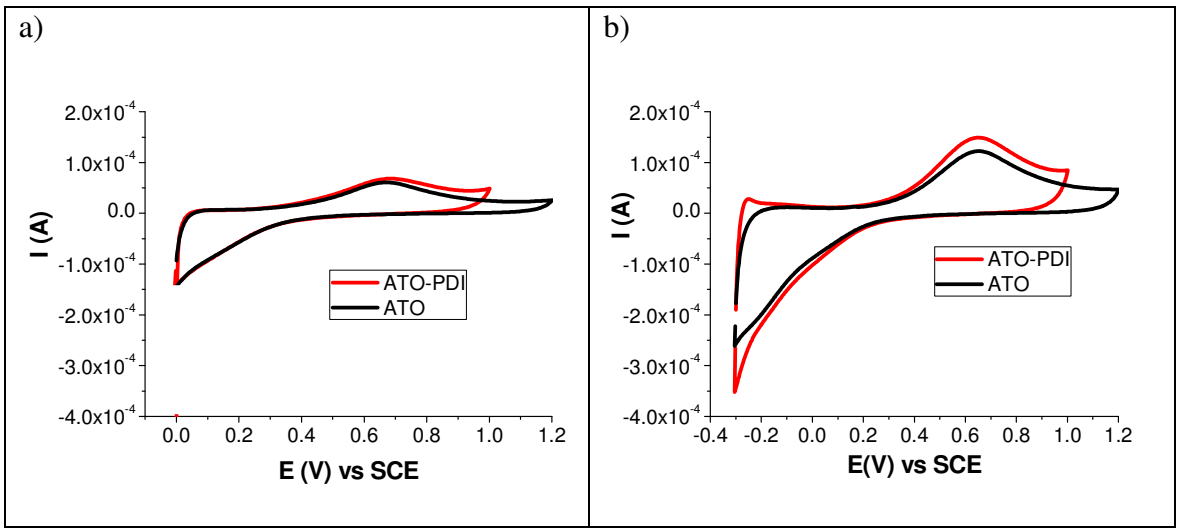

Fig.7.11 Dark cyclic voltammetry traces of ATO and ATO-PDI recorded between **a)** 1.2V/0V; **b)** 1.2V/-0.3V in $HClO_4$ 0.1M (pH1)

The presence of a wide energy distribution of intraband-gap states (ISs) in ATO due to Sb doping was confirmed by spectroelectrochemical analysis. Potential-dependent optical absorption spectra of nanostructured SnO_2 and ATO electrodes in aqueous electrolyte at pH1 are shown in Fig.7.12. The reference spectrum was recorded by polarizing at +1.2 V both electrodes. A bleach at wavelengths shorter than 400 nm and an increase in absorption at longer wavelengths are observed upon application of more negative potentials. These optical changes are caused by an increase in the concentration of conduction band electrons in the nanostructured films. The increase in absorbance at ~1300nm is due to absorption by free conduction band electrons, *i.e.* Drude absorption, while the bleach at ~280nm is due to occupation of conduction band levels by electrons, giving rise to an apparent increase in the bandgap, *i.e.*a Burstein shift. It is worth to note that, while in SnO_2 optical changes can be intercepted by applying +0.2V (*i.e.* SnO_2 E_{onset} potential) (Fig.7.12 b), in the doped substrate ATO, absorption bleach and increase begin to be significant at the application of +1.1 V, showing a continuum associated to donor levels below the conduction band (ISs) (Fig.7.12 c).

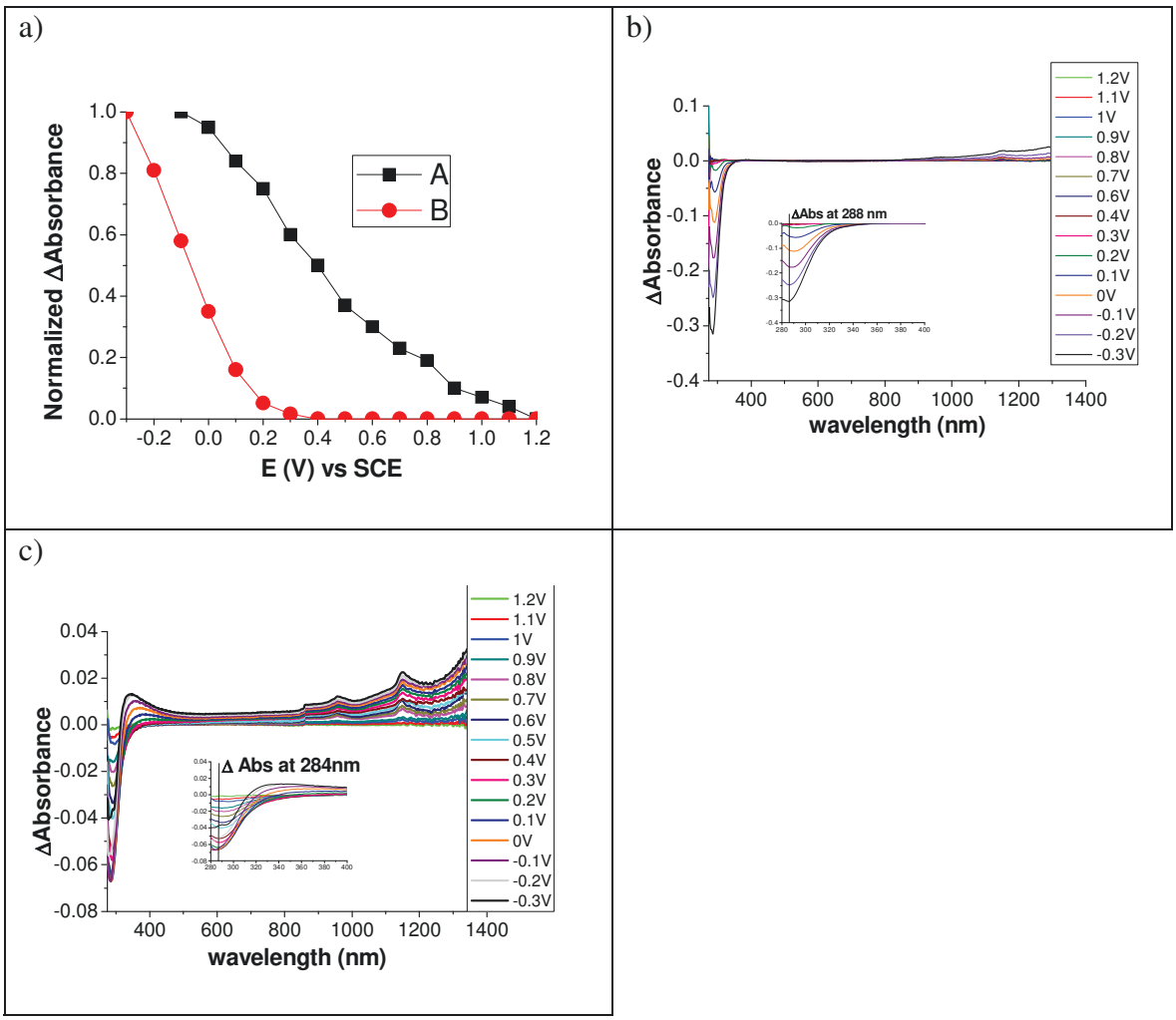

Fig.7.12 a) Normalized ΔAbsorbance A- at 284nm of ATO, B- at 288nm of SnO_2 vs. applied potential in $HClO_4$ 0.1M (pH1); **b)** Absorption spectra of SnO_2 as a function of applied potential in $HClO_4$ 0.1M (pH1). Spectra are recorded after polarization for 1 min at the indicated applied potential. Spectra from +1.2 V to -0.3V in 0.1 V intervals were recorded. The spectrum measured at +1.2 V has been subtracted. Zoom of the region up to 400nm (inset); **c)** Absorption spectra of ATO as a function of applied potential in $HClO_4$ 0.1M (pH1). Spectra are recorded after polarization for 1 min at the indicated applied potential. Spectra from +1.2 V to -0.3V in 0.1 V intervals were recorded. The spectrum measured at +1.2 V has been subtracted. Zoom of the region up to 400nm (inset);

The same results were achieved by recording potential-dependent optical absorption spectra of SnO_2-PDI and ATO-PDI (Fig.7.13), highlighting the behaviour of Sb-doped based semiconductor, connected to ISs presence, previously found. In both substrates the bleaching of the dye was appeared at 450nm and a strong absorption, that should be associated to dye reduction, was individuated by applying -0.3V, consistent with the faradaic process detected by CVs analysis. It is worth to notice that SnO_2-PDI spectra between 450 and 1400 nm was multiplied *per* 3 to better underline the spectral changes associated to the dye reduction.

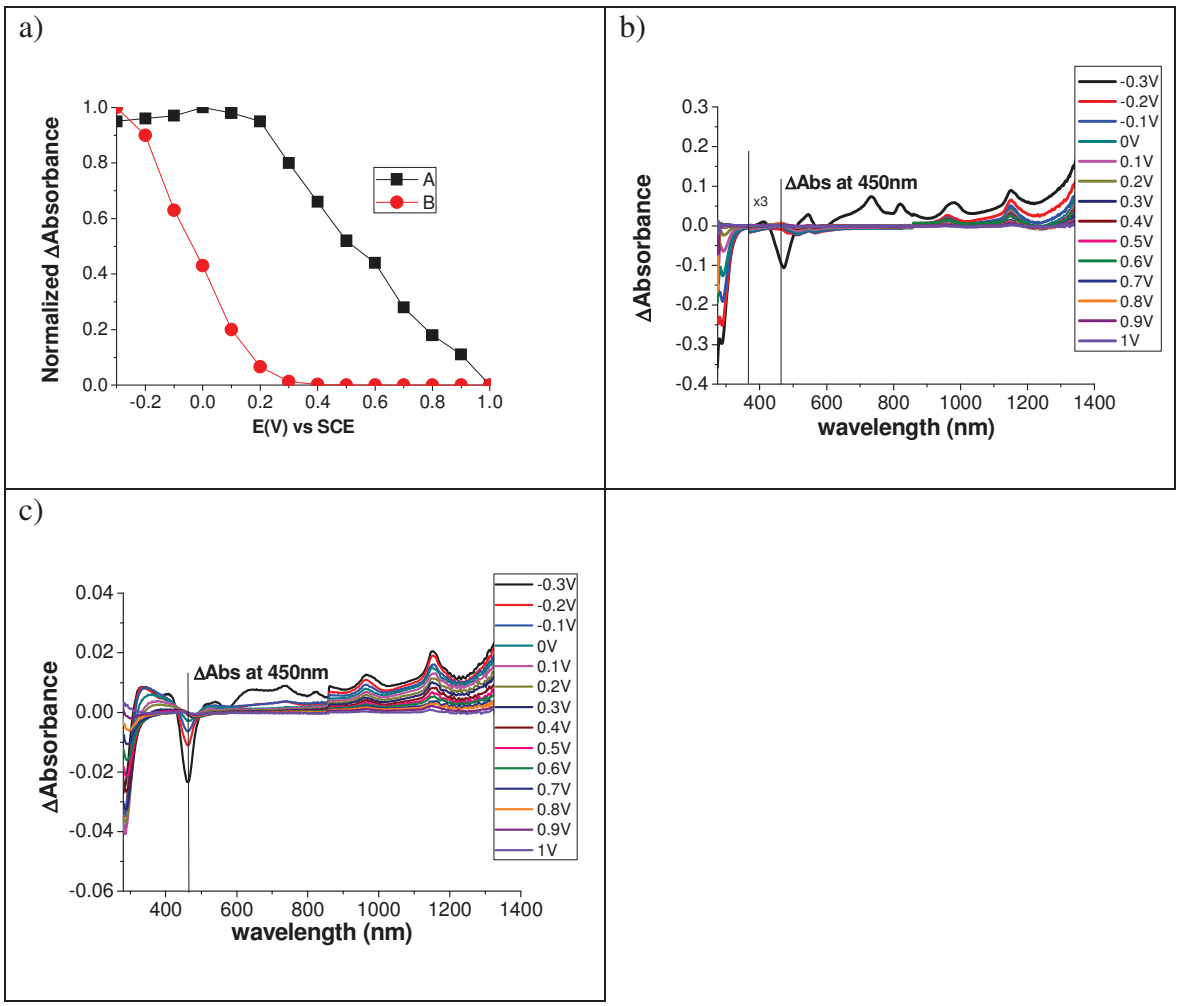

Fig.7.13 a) Normalized ΔAbsorbance A- at 284nm of ATO-PDI, B- at 288nm of SnO_2-PDI vs. applied potential in $HClO_4$ 0.1M (pH1); **b)** Absorption spectra of SnO_2-PDI as a function of applied potential in $HClO_4$ 0.1M (pH1). Spectra are recorded after polarization for 1 min at the indicated applied potential. Spectra from +1V to -0.3V in 0.1 V intervals were recorded. The spectrum measured at +1V has been subtracted; **c)** Absorption spectra of ATO-PDI as a function of applied potential in $HClO_4$ 0.1M (pH1). Spectra are recorded after polarization for 1 min at the indicated applied potential. Spectra from +1V to -0.3V in 0.1 V intervals were recorded. The spectrum measured at +1V has been subtracted;

To confirm the assignment of the spectral signature appearing at -0.3 V to dye reduction, spectroelectrochemical experiments on PDI in solution and on an electrochemically inert substrate (ZrO_2) were undertaken. In this latter case reduction occurs by charge hopping from the FTO, being ZrO_2 an insulating material at the potentials of interest. It is worth to notice that the fingerprint of reduced PDI in solution (Fig.7.14 a) shows the bleach of the vibronic bands of the ground state in a range between 450 and 530 nanometers followed by a 550 nm absorption. Upon reduction of the PDI aggregates adsorbed on ZrO_2, the vibronic structure is clearly lost, consistent with the ground state absorption, and a featureless bleaching band centred at *ca.* 480 nm, accompanied by the simultaneous increase of a band

at *ca.* 580nm band, is observed (Fig.7.14 b). This fingerprint agrees with the spectral variations observed on SnO_2 and ATO at potentials more negative than -0.3 V.

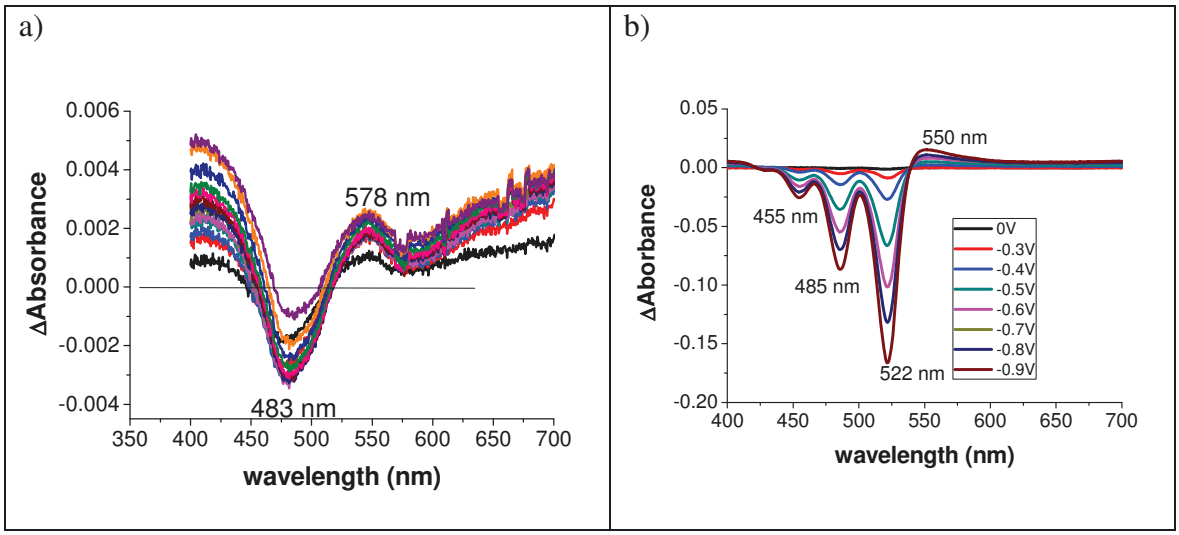

Fig.7.14 a) Absorption Spectra of ZrO_2-PDI at -0.3V in $NaClO_4$ 0.1M (pH3). 13 scans are reported. The spectrum recorded without applying potential has been subtracted; **b)** Absorption Spectra of PDI as a function of applied potential in AcN, $TBAPF_6$ 0.1M. Spectra from 0V to -0.9V were recorded. The spectrum recorded without applying potential has been subtracted.

In order to screen the charge separation and collection ability of the different dye-sensitized photoanodes and to understand the rule of ATO ISs in these dynamics, photocurrents were recorded during the irradiation of PDI-sensitized photoanodes with AM 1.5 G light (Fig.7.15 a). Bromide (0.1 M HBr, pH 1) was selected as sacrificial agent, since it represents a redox couple with a significantly positive oxidation potential (E^0 = 1.07 V *vs* NHE), and dark current contributions only after 1.2 V *vs* NHE. At potentials >0.65 V, the ATO-PDI electrode outperforms SnO_2-PDI, yielding up to 1 mA/cm^2 net photocurrent at 1 V, while SnO_2-PDI gave plateau values of ca. 0.1 mA/cm^2. However, the ATO-based photoanodes show a retarded photoanodic onset (*ca.* 0.65 V), probably due to the presence of the intra-bandgap states as explained above, that constitute recombination centres. Incident photon to current efficiency (IPCE) curves of the PDI-based photoanodes are reported in Fig.7.15 b, where the action spectra are consistent with the corresponding absorption spectra of the thin films (Fig.7.8), confirming the involvement of the PDI molecules in the process of photoconversion. Furthermore, the IPCEs follow, as expected, the J-V curves trend, with the maximum values registered for ATO-PDI (*ca.* 8% at 490 nm).

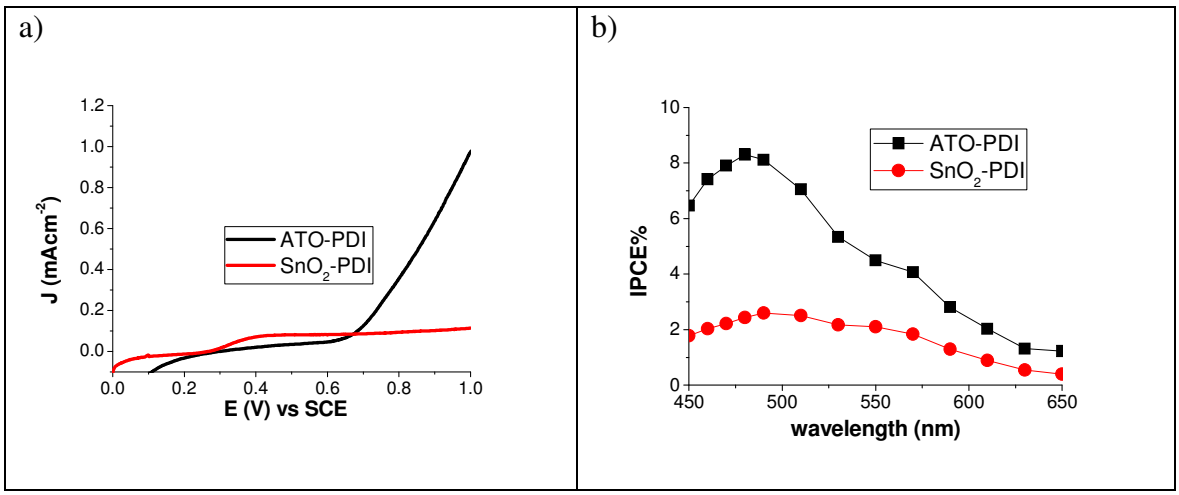

Fig.7.15 a) Steady state J-V curves of the PDI-sensitized photoanodes in 0.1 M HBr (pH 1); 10 mV/s scan rate; 0.1 W/cm^2 AM 1.5 G illumination; **b)** IPCE curves for the PDI-sensitized photoanodes recorded at 0.8 V in 0.1 M HBr (pH 1).

The first indication of a better charge separation on ATO is gained by the comparative measurement of the static emission quenching of PDI loaded on the different semiconductor thin films. Static emission spectra of the PDI-sensitized photoanodes consisted of a broad emission band, centred at 680 nm, most probably due to the formation of excimer-like states on the surface. The strongest quenching of the emitting PDI* is observed in the case of ATO (Fig.7.16).

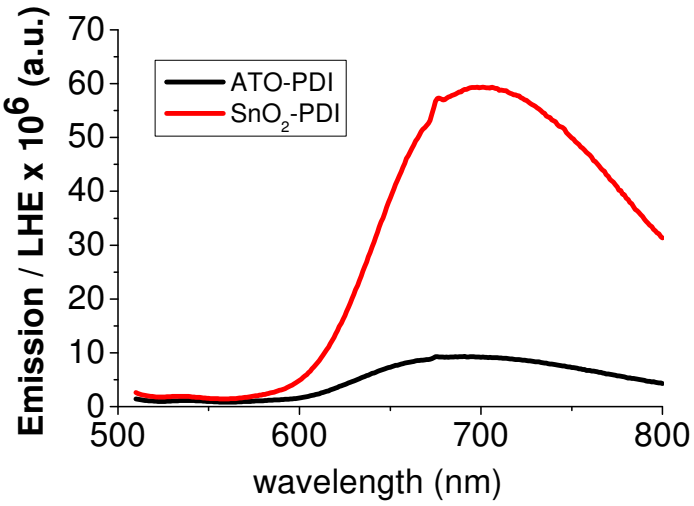

Fig.7.16 Emission spectra of the PDI-sensitized photoanodes. Average of two different electrodes. λ_{exc} = 485 nm.

Furthermore, a deeper understanding of the charge separation dynamics on ATO is gained by the study of photoanodic transients generated by nanosecond laser excitation (7 ns Full Width at Half Maximum, 532 nm), obtained by recording the photocurrent response with fast (10^{-4} s sampling) chronoamperometry experiments in 0.1 M HBr, pH 1. Photoanodic

transients recorded at different applied potentials, both in the presence and in the absence of white light bias, are reported in Fig.7.17 for ATO-PDI and in Fig.7.18 for SnO_2-PDI : after the laser pulse, a sharp rise is observed, due to both charging of the interface and instantaneous electron injection and collection.

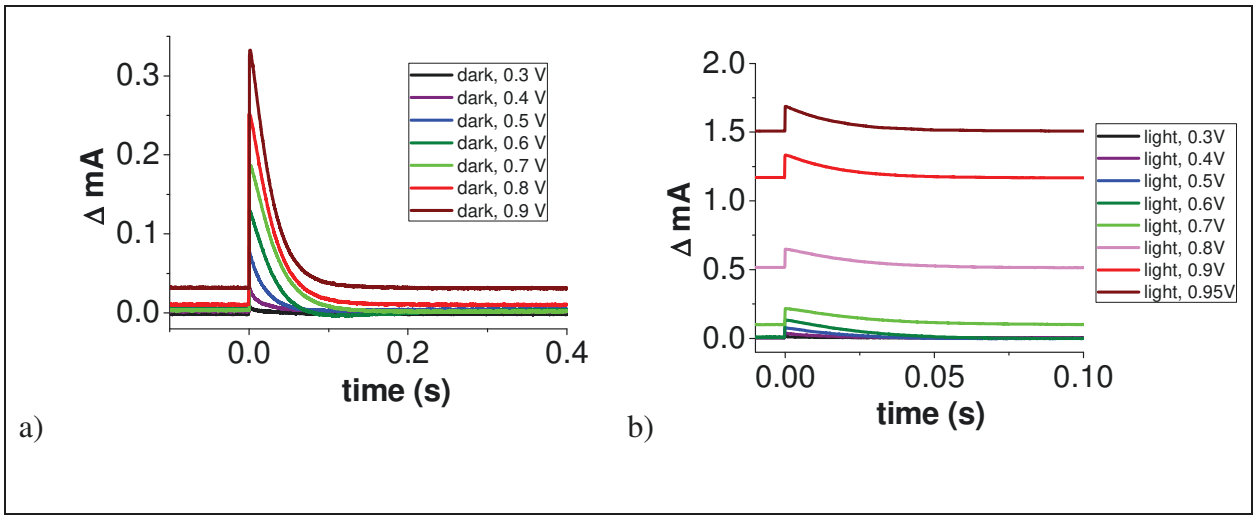

Fig.7.17 Photocurrent transient decays registered after the 532 nm laser excitation (0.6 mW/cm^2 intensity) under different applied bias for ATO-PDI in the absence (**a**) or in the presence (**b**) of an additional white light illumination (0.14 W/cm^2 intensity). In 0.1 M HBr, pH 1.

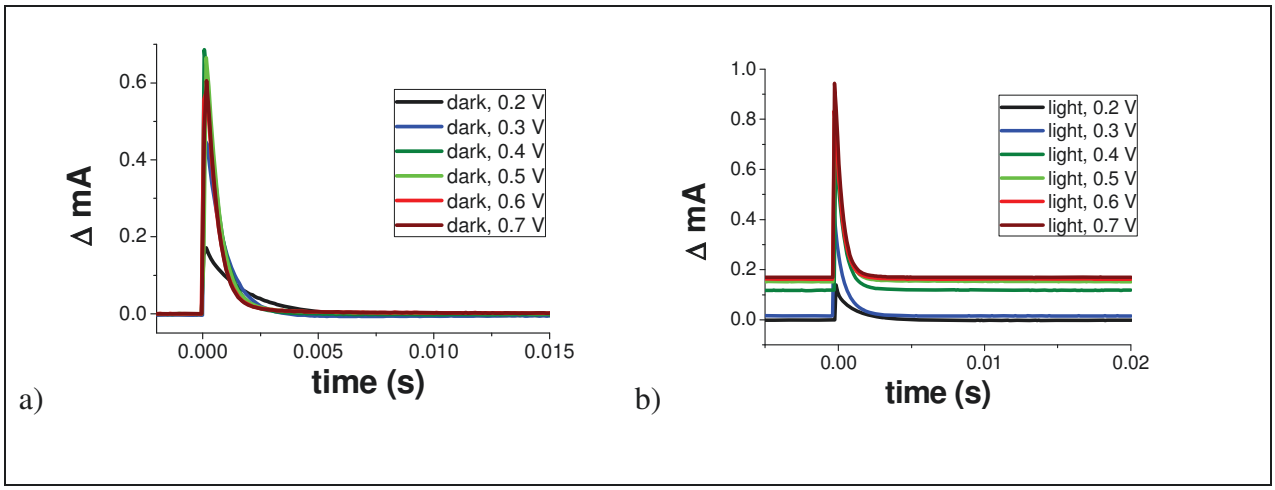

Fig.7.18 Photocurrent transient decays registered after the 532 nm laser excitation (0.6 mW/cm^2 intensity) under different applied bias for SnO_2-PDI in the absence (**a**) or in the presence (**b**) of an additional white light illumination (0.14 W/cm^2 intensity). In 0.1 M HBr, pH 1.

In all the cases the photocurrent transients show multiexponential decay kinetics, which were, for mathematical convenience, satisfactorily fitted with a biexponential function. The shape of the photoanodic transient is determined by the collection of the electrons which are generated within the film by the laser pulse and diffuse/migrate to the electron collector. If part of these electrons recombine, the photocurrent transient will be shorter in time and

less intense. Its area (i.e. the collected photocharge) will thus decrease when the efficiency of the recombination channels increases.

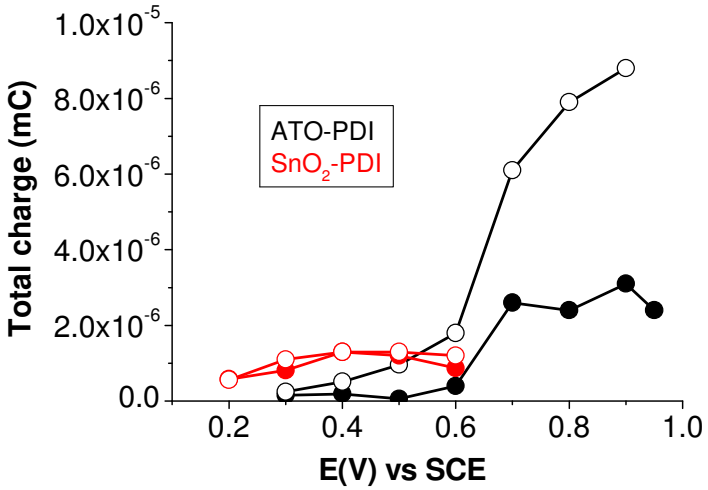

Fig. 7.19 Total collected charge as a function of the applied bias for the dye-sensitized photoanodes under pulsed 532 nm laser excitation (0.6 mW/cm^2) in the absence (empty markers) or in the presence (full markers) of white light illumination (0.14 W/cm^2). In 0.1 M HBr, pH 1

From the integration of the photocurrent transients (Fig.7.19), we can thus obtain the collected photocharge, as shown in Fig.7.19. The highest collected photocharge values are indeed observed for ATO-PDI at > 0.65 V applied bias, consistent with the steady state J-Vs, suggesting that the intraband states (ISs), once emptied by the applied potential, favour charge separation and collection. This affirmation is corroborated by the analysis of ATO-PDI's decay traces at different applied potentials: at 0.3 V (Fig.7.20 a), the ISs are completely filled, resulting in photoanodic transients having a small amplitude with a comparatively short lifetime, while at 0.5 V, the ISs are only partially filled, thus the amplitude of the transient increases, but a slow negative component appears, indicative of trap-mediated recombination (fig.7.20 b). At 0.8 V in the dark, the ISs population is largely reduced and empty states may behave as electron acceptors, whereas the applied bias accelerates charge collection over recombination (Fig.7.20 c). As a consequence, the collected charge is increased by a factor of 8. It is worth to notice that, under steady state illumination at 0.8 V, a partial ISs filling occurs, as the result of electron injection from PDI molecules excited by the additional white light. This condition results in a reduced amplitude of the laser induced transient, as well as of the collected photocharge, suggesting that the control of the ISs occupation may allow to tune the injection quantum yield by PDI*.

Conversely, the results obtained for SnO_2-PDI point to a much less relevant effect of ISs in controlling the charge separation dynamics as we supposed above.

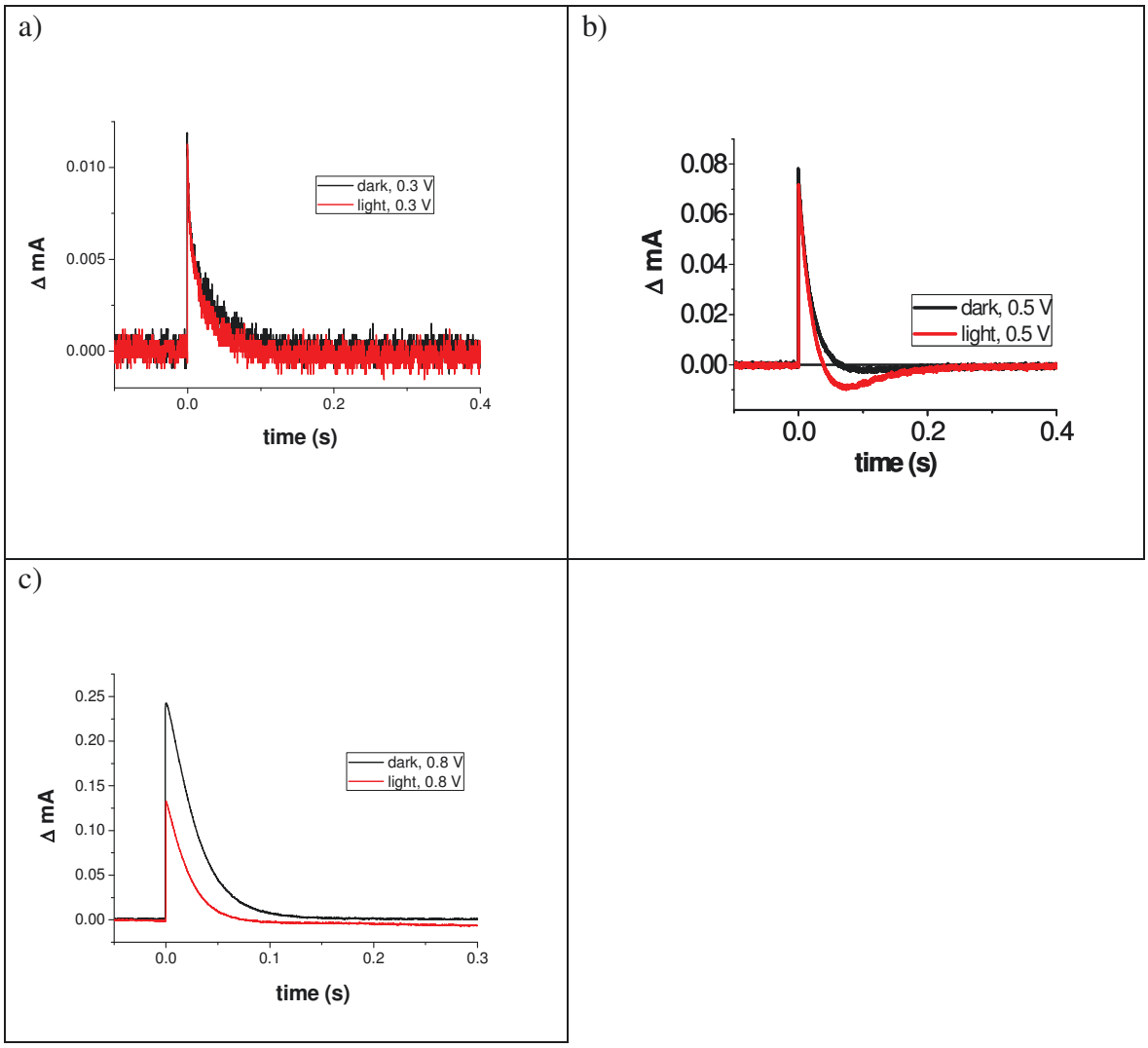

Fig.7.20: Photocurrent transient decays (black traces) of ATO-PDI after 532 nm laser excitation (0.6 mW/cm^2 intensity) under **a)** 0.3 V **b)** 0.5 V and **c)** 0.8V applied bias. Red traces represent the laser induced transients in the presence of continuous white light illumination of 0.14 W/cm^2 intensity. In 0.1 M HBr, pH 1**.**

In order to gain more insights on the charge injection dynamics, we have performed femtosecond transient absorption (TA) spectroscopy experiments, using 485 nm pump pulses, resonant with the PDI ground state absorption. These measurements where performed in collaboration with the group led by Prof. G. Cerullo at the Politecnico of Milan. Figure 7.21 shows the differential transmission (ΔT/T) spectra of PDI adsorbed on the inert substrate ZrO_2.

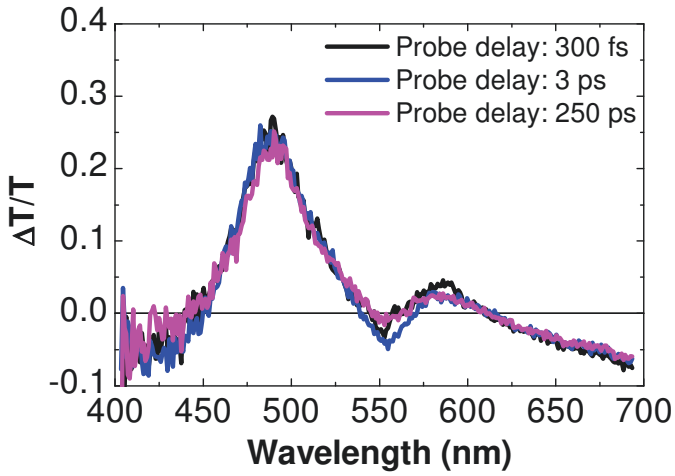

Fig.7.21 Transient absorption spectra of PDI-sensitized ZrO_2;

We observe a positive band at 485 nm, assigned to the photobleaching (PB) of the PDI ground state, a red-shifted positive band in the 570-610 nm range, assigned to the stimulated emission (SE) from the PDI* excited state, and a broad photoinduced absorption (PA) band, which we call PA1, at $\lambda > 620$ nm, also assigned to the PDI* excited state. On the other hand, the TA spectra measured for the dye-sensitized semiconductors in the same conditions (Figures 7.22) showed, along with the ground state bleaching (GSB) at 485 nm and the broad PA1 band at $\lambda > 620$ nm, an additional PA band at 550 nm, which we call PA2, overlapping with and quenching the SE signal. We assign the PA2 band to the SC(e^-)-PDI(+) charge separated state generated, on the ultrafast timescale, by electron injection from the dye into the semiconductor.

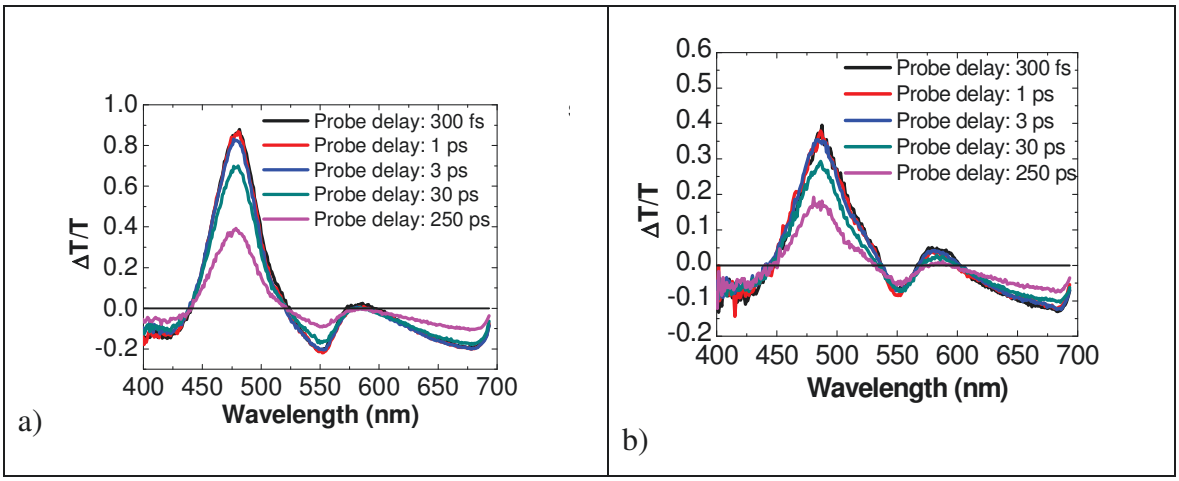

Figure 7.22 Transient absorption spectra of PDI-sensitized ATO (**a**) and SnO_2 (**b**). Femtosecond laser pulse at 485 nm.

Multi-exponential fits of the TA dynamics at different probe wavelengths over the first picosecond are shown in Figure 7.23, and the corresponding time constants are summarized

in Table 1. We observe that, while the GSB and the PA1 bands show rise times essentially limited by the *ca.* 45 fs instrumental resolution, the PA2 band shows a fast but resolved build-up. This indicates that at least a fraction [40] of the dye population is able to inject into ATO on time scales of 173 ± 8 fs, while a longer value (362 ± 12 fs) was observed for SnO_2-PDI. These evidences confirm that, even under open circuit conditions, ATO is the best substrates for the efficient PDI* quenching by electron transfer, probably due to the electrical charge of the ATO nanoparticles (see zeta potential measurements) which favours the coupling with the dicationic dye, and, as a consequence, charge injection. Despite the intense pump fluence typical of femtosecond experiments, charge recombination was long-lived, and the SC(e−)-PDI(+) state recovered with a lifetime of several tens of picoseconds (174 ± 2 ps for ATO and 165 ± 3 ps for SnO_2 respectively, see Table 1) to achieve a constant ΔT/T amplitude maintaining, in all cases, *ca.* 50% of the initial value. Such residual component of the charge-separated state survives far beyond the time scale of the pump probe experiment (300 ps), thus confirming the successful competition between charge separation and recombination within PDI-sensitized interfaces.

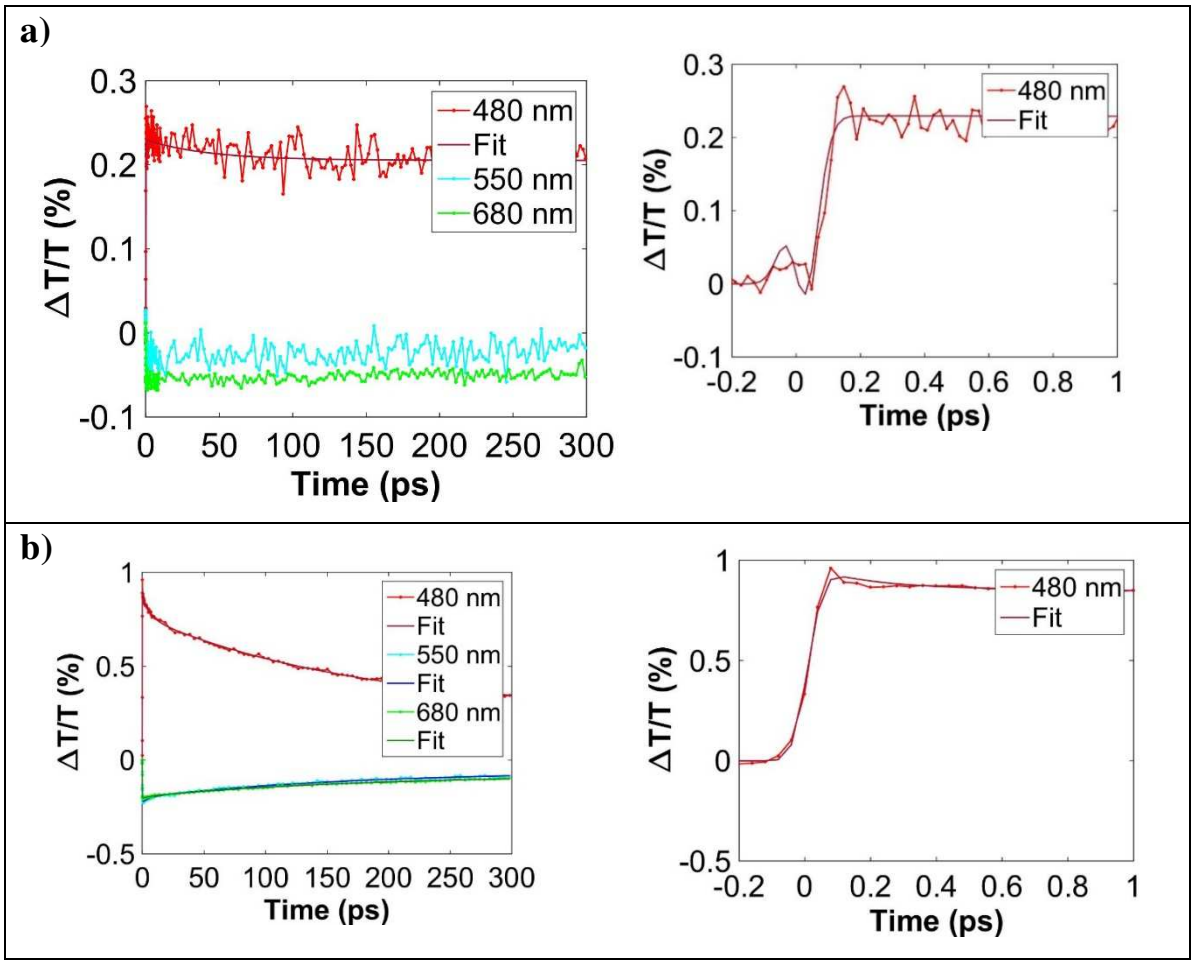

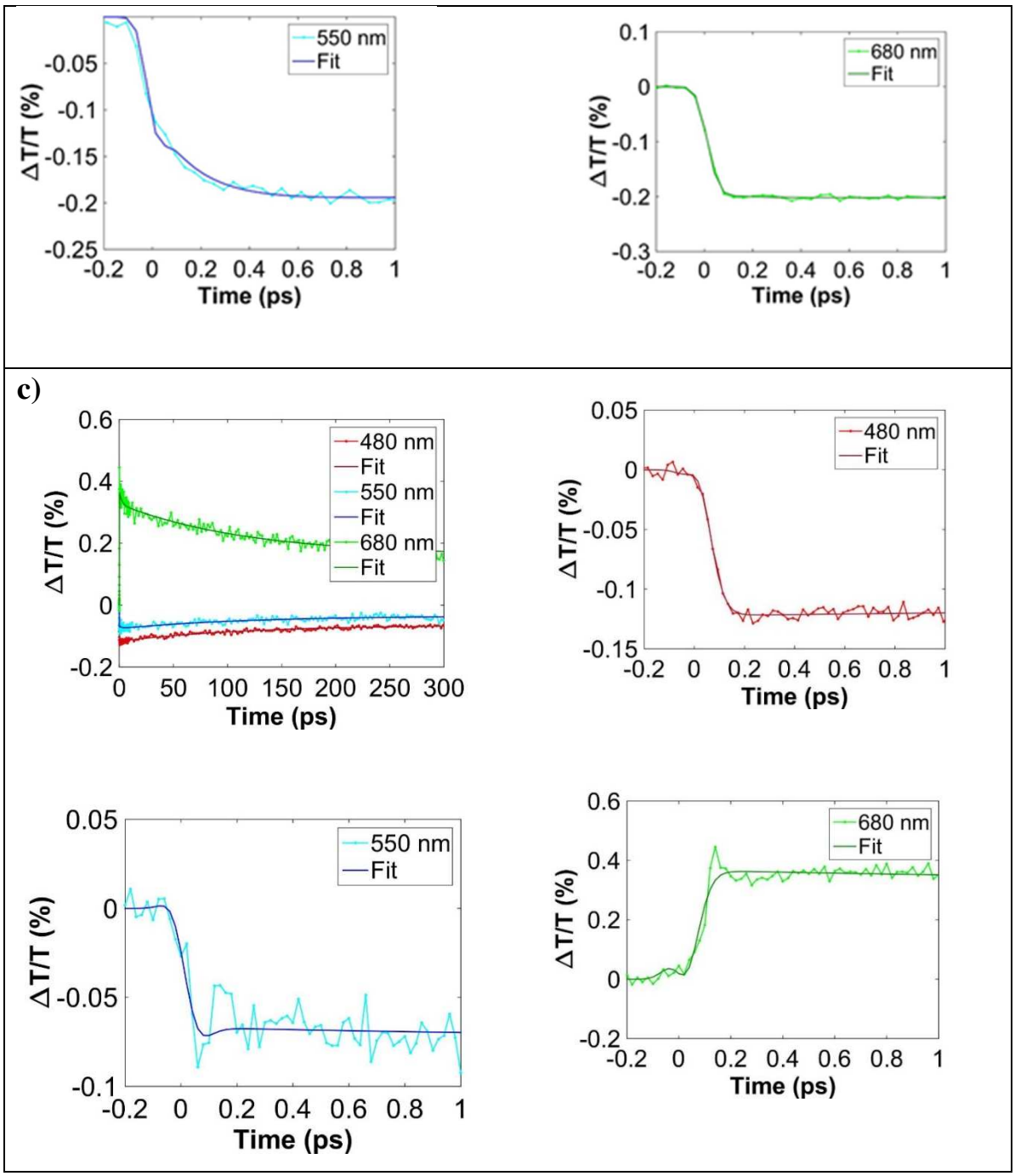

Fig.7.23 Decay traces and corresponding fittings (in the range 0-300 ps) for the 480, 550 and 680 nm features observed for the dye-sensitized ZrO_2 (**a**), ATO (**b**) and SnO_2 (**c**) after the femtosecond laser excitation at 485 nm. The corresponding fittings in the < 1000 fs range are also reported.

Table1 Time constants associated to the formation and recombination of the charge separated species CB(e-)-PDI(+) after the femtosecond laser excitation of the PDI-sensitized photoanodes.

	550 nm initial rise, *i.e.* **CB(e-)-PDI(+) formation**	**550 nm decay,** *i.e.***CB(e-)-PDI(+) recombination**
ATO-PDI	τ = 173 ± 8 fs	τ = 174 ± 2 ps
SnO_2-PDI	τ = 362 ± 12 fs	τ = 165 ± 3 ps

Transient measurements in the nanosecond−microsecond time scale are also consistent with the formation, upon 532 nm excitation, of the long-lived charge-separated state on ATO-PDI, absorbing at 550 nm. From the corresponding kinetic trace (Fig.7.24), we evidenced that the ATO(e−)-PDI(+) state is characterized by a *ca.* 4 μs lifetime and undergoes to a partial recovery (ca. 50%) in the explored 20 μs time scale, thus allowing for the exploitation of the strongly oxidizing species to trigger multielectronic redox chemistry.

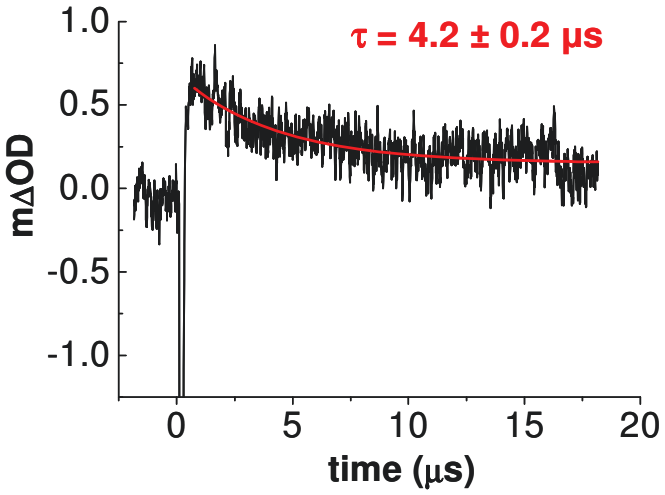

Fig.7.24. Kinetic evolution of the absorption feature at 550 nm (due to the ATO(e^-)-PDI(+) charge separated state) after the nanosecond laser excitation at 532 nm; 1.48 kV laser pump; average of 60 laser shots, corrected for the pulser baseline; 5 s delay; 350 Ω impedance (300 ns pulse time base). In 0.1 M $NaClO_4$ pH 3.

Furthermore, the influence of pH on semiconductor and on semiconductor/dye system properties was investigated by recording cyclic voltammetry and potential-dependent optical absorption spectra. Studies were conducted at pH3, for both ATO and SnO_2, in order to

compare results with the ones previously obtained at pH1. Under less acid conditions the CVs shift to more negative potentials. The shape, however, remains essentially the same and the shifts are consistent with a Nernstian shift of 59 mV per pH unit (Fig.7.25 a, b). In perfect agreement with CV measurements, the bleach of the absorbance at ~280nm (Fig.7.25 c, d), related to electronic occupation of empty states close to the conduction band , presents the same potential shift per pH unit.

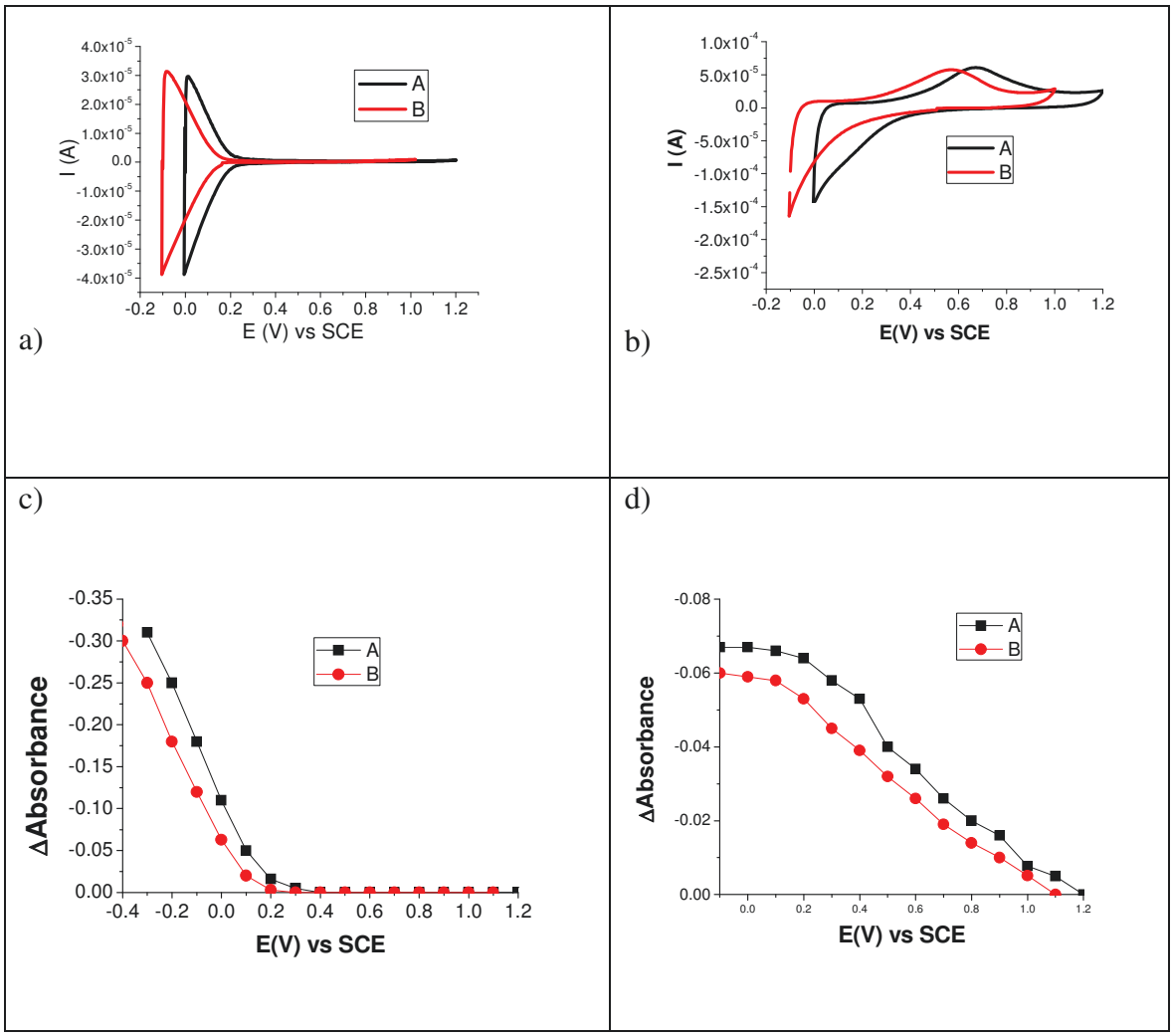

Fig.7.25 a) Dark cyclic voltammetry traces of SnO_2 in A- $HClO_4$ 0.1M (pH1), B- $NaClO_4$ 0.1M, $HClO_4$ 10^{-3}M (pH3); **b)** Dark cyclic voltammetry traces of ATO in A- $HClO_4$ 0.1M (pH1), B- $NaClO_4$ 0.1M, $HClO_4$ 10^{-3}M (pH3); **c) Δ**Absorbance at 288nm of SnO_2 vs. applied potential in A- $HClO_4$ 0.1M (pH1), B-$NaClO_4$ 0.1M, $HClO_4$ 10^{-3}M (pH3); **d) Δ**Absorbance at 284nm of ATO vs. applied potential in A- $HClO_4$ 0.1M (pH1), B-$NaClO_4$ 0.1M, $HClO_4$ 10^{-3}M (pH3).

Moreover, dye reduction takes place at the same potential identified at pH1 (*i.e* -0.3V), revealing that the dye energetics are substantially unaffected by pH, as shown in Fig.7.26 where CVs on SnO_2-PDI (Fig.7.26 a), spectroelectrochemical results obtained on SnO_2-PDI

and ATO-PDI, upon interception of the dye reduction process at -0.3V (Fig. 7.26 b, c) are reported .

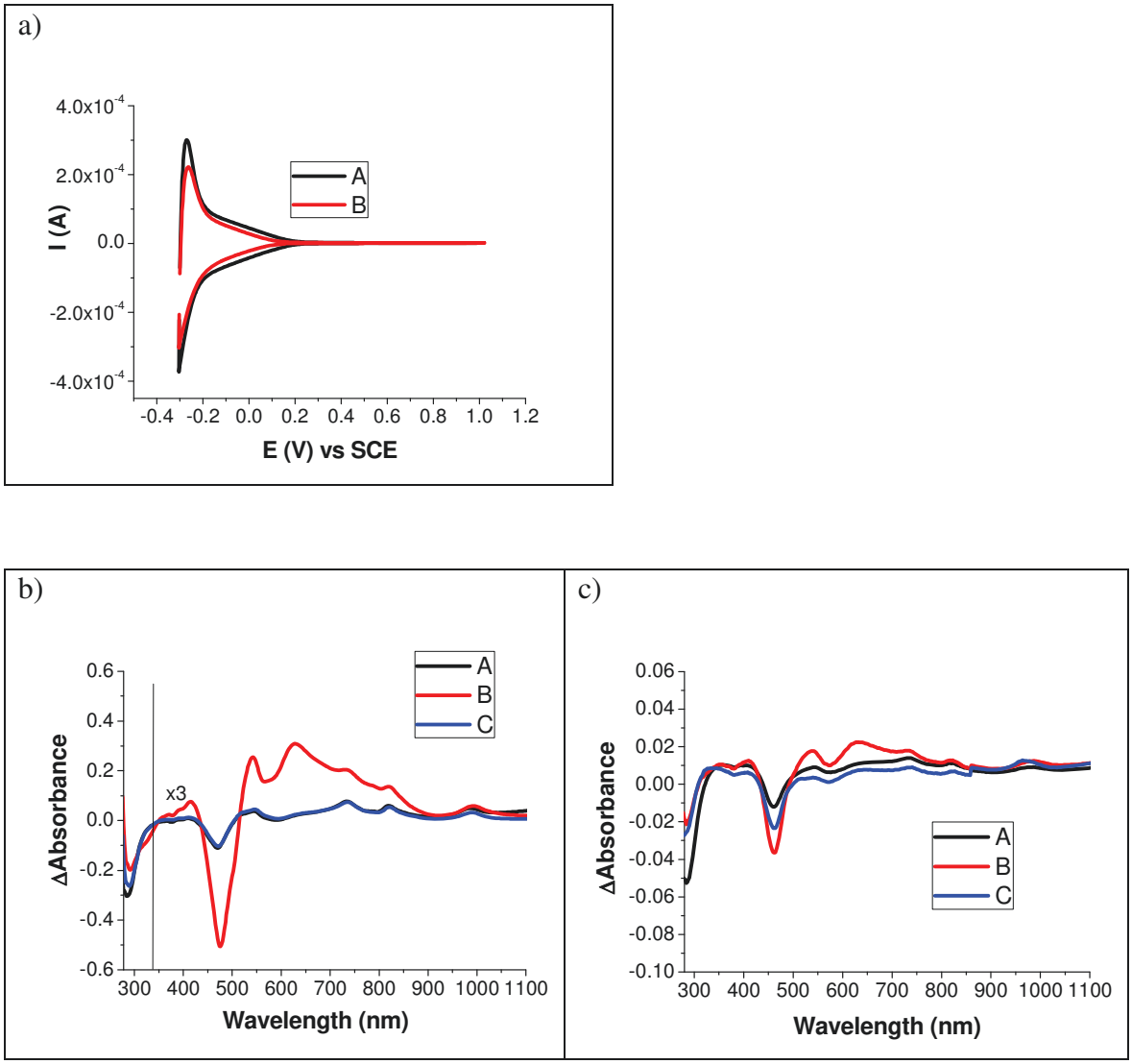

Fig.7.26 a) Dark cyclic voltammetry traces of SnO_2-PDI in A- $HClO_4$ 0.1M (pH1), B- $NaClO_4$ 0.1M, $HClO_4$ 10^{-3}M (pH3); **b)** Absorption spectra of SnO_2-PBI recorded by applying A- (-0.3)V in $HClO_4$ 0.1M (pH1); B- (-0.4)V in $NaClO_4$ 0.1M, $HClO_4$ 10^{-3}M(pH 3); C- (-0.3)V in $NaClO_4$ 0.1M, $HClO_4$ 10^{-3}M(pH 3). Spectra are recorded after polarization for 1 min at the indicated applied potential. The spectrum measured at +1V has been subtracted. **c)** Absorption spectra of ATO-PBI recorded by applying A- (-0.3)V in $HClO_4$ 0.1M (pH1); B- (-0.4)V in $NaClO_4$ 0.1M, $HClO_4$ 10^{-3}M(pH 3); C- (-0.3)V in $NaClO_4$ 0.1M, $HClO_4$ 10^{-3}M(pH 3). Spectra are recorded after polarization for 1 min at the indicated applied potential. The spectrum measured at +1V has been subtracted.

pH variation can thus provide a means to tune the semiconductor energy levels independently by those of the sensitizer, allowing to optimize interfacial charge separation, at least in the case of a poorly reducing excited state like those of aggregated PDI. In order to validate this possibility, photocurrents of SnO_2-PDI were recorded by employing, as electrolytes, three solutions with different $[H^+]$: 0.1M NaBr, 0.1M $HClO_4$, 0.9M $NaClO_4$

(pH1); B- 0.1M NaBr, 10^{-3}M $HClO_4$ 1M $NaClO_4$ (pH3); C- 0.1M NaBr, 1M $HClO_4$ (pH0). It is worth to note that the bromide concentration and ionic strength, were kept constant to avoid any current increase because of the enhancement of sacrificial agent concentration in solution or other spurious effects possibly related to the different solution conductivity on the photocurrent . We also emphasize that the analysis was not carried out on ATO based photoanodes, given that ATO-PDI charge collection is governed by the presence of deep ISs as previously demonstrated by photoanodic transient measurements, but on simple SnO_2 whose CB states are only moderately positive with respect to the excited state oxidation potential of the dye. The driving force for the electron transfer from the PDI aggregates' excited state to the SnO_2 CB (ΔG_{ET}) can be estimated by $\Delta G_{ET} = -e(|E^*_{ox}|-|E_{onset}|)$, giving values for SnO_2-PDI at pH0, at pH1 and at pH3 respectively of *ca.* -0.56eV, -0.5eV and -0.4eV, taking into account that SnO_2 E_{onset} varies from *ca.* 0.26V at pH0 to 0.2V at pH1 and 0.1V at pH3. SnO_2-PDI at pH0 outperforms the results obtained in the other solutions, yielding up to 0.2 mA/cm^2 net photocurrent at 0.8V, a doubled intensity with respect to the other two cases (Fig.7.27 a). IPCE curves are in perfect agreement with steady state measurements, showing a photo to current conversion of *ca.* 4% at pH0 (Fig.7.27 c).

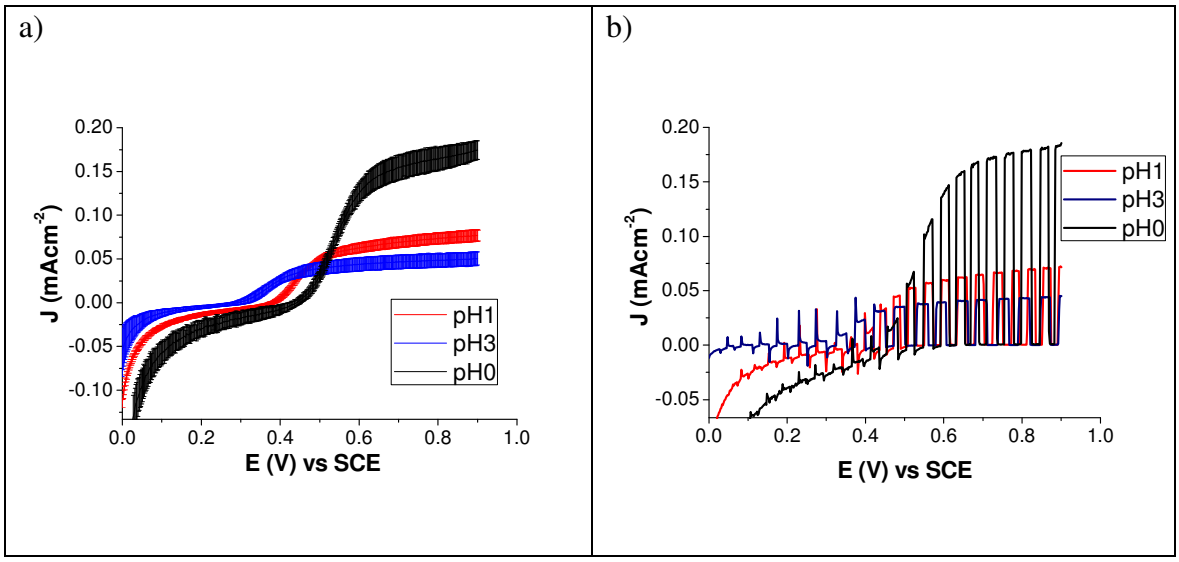

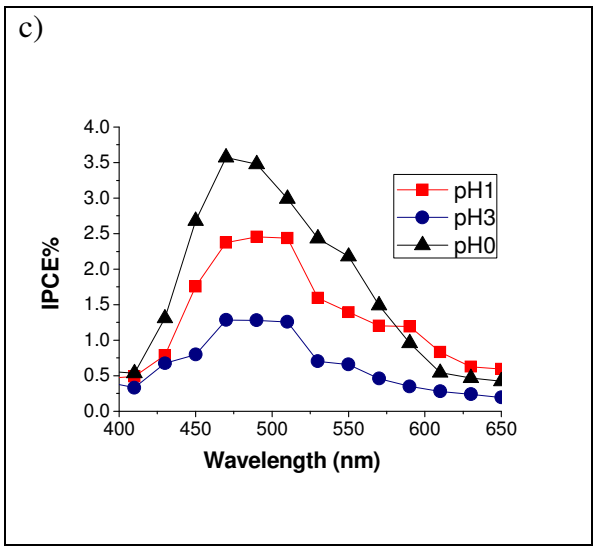

Fig.7.27 a) Statistic on steady-state *J-V* curves of SnO_2-PBI at several pH ; **b)** Light-dark curves of SnO_2-PDI at several pH; **c)** IPCE curves of SnO_2-PDI recorded at 0.8 V at several pH.

Rate constant associated to electron transfer, *i.e* electron injection from PDI* to SnO_2 CB, can be expressed by the Marcus equation:

$$k_{et} = \upsilon_N k_e e^{-\frac{\Delta G^*}{kT}} \qquad \text{(Eq.4.1)}$$

where k and T are the Boltzmann constant and the absolute temperature, respectively. υ_N is the nuclear frequency factor, and κ_e is the transmission coefficient, a parameter expressing the probability of the system to evolve from the reagent to the product configuration. ΔG^* is the activation energy and can be estimated by the equation:

$$\Delta G^* = \frac{(\Delta G^0 + \lambda)^2}{4\lambda} \qquad \text{(Eq.4.2)}$$

where $\Delta G°$ is the free energy variation accompanying the process, while λ is the reorganization energy and represents the energy necessary to transform the nuclear configurations of the reactant and of the solvent to those of the products. Given ΔG_{ET} values previously calculated, photocurrent trend as a function of pH should follow Marcus theory, showing a Gaussian shape. However, the trend recorded is exponential (Fig.7.28), suggesting that efficiency decrease obtained by increasing pH cannot be ascribed only to a decrease in the charge injection rate, but is probably explained by an increase in the efficiency of recombination phenomena, as we can estimate from the transients recorded at several pH in light-dark measurements (Fig.7.29).

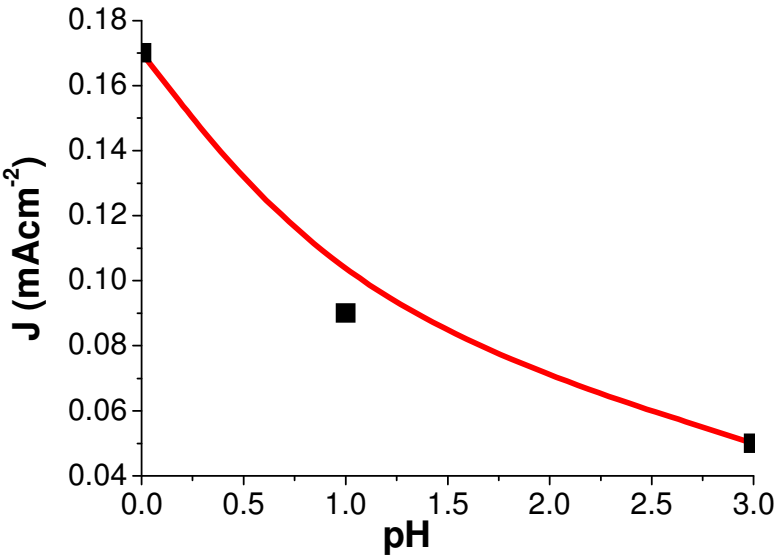

Fig.7.28 SnO_2-PDI current density recorded at 0.8V as a function of pH.

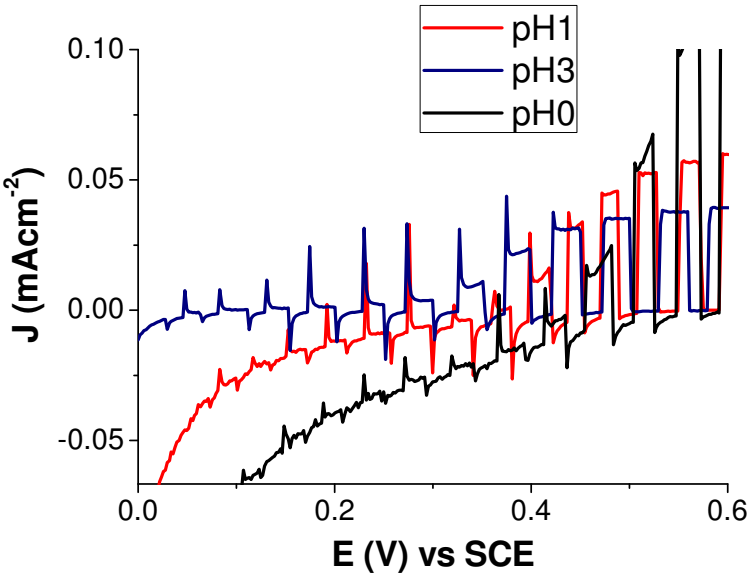

Fig.7.29 Light-dark curves of SnO_2-PDI at several pH.

7.4 Conclusions

The present chapter is focused on the study of photoanodes for molecular level solar fuel generation in aqueous environment. The exploitation of hydrophobic interactions to form robust perylene diimide-based molecular aggregates constitute an interesting solution to overcome the hydrolytic cleavage usually observed with conventional linkers in a wide pH range. In the case of photoactive molecular aggregates, charge injection occurs by a traveling excited state (exciton) which separates at the interface between the molecule and the semiconductor. Excited state directionality nor electronic coupling are in this case ideal for efficient charge injection, and different materials and working conditions should be explored to optimize the efficiency of charge separation. In the present work a characterization of the interfacial proprieties of PDI modified SnO_2 and Sb-doped SnO_2 (ATO) was carried out with the aim of finding substrates with an optimized charge collection ability. The investigation of incident photon-to-current efficiency revealed that ATO outperforms the previously reported SnO_2, despite their similarity in conduction band energetics. A more careful exploration of their interfacial energetics reveals however that the occupancy of intrabandgap states (ISs) on ATO plays a significant role in tuning photoinduced charge separation and collection, resulting in a *ca.* four times photoanodic current for photoelectrochemical bromide oxidation with respect to SnO_2. Finally, SnO_2 photocurrent dependence on pH was investigated, observing a significant increase of the photoanode performance with respect to pH, successfully demonstrating the possibility of tuning the energetics of shallow surface states independently by those of the dye sensitizer. However, the incremental improvement does not seem to be related uniquely to an increase in the charge injection rate, but also to an improved electron collection which is achieved at high proton concentration. The disappearance of transient recombination features in region of the photoanodic onset is consistent with such interpretation. .

7.5 References

1)N.S. Lewis, D.G. Nocera, *Proc. Natl. Acad. Sci. U. S. A.* **2006,** *103*, 15729;

2) N.S. Lewis, Research opportunities to advance solar energy utilization. *Science* **2016,** *351*, 1920;

3) L. Alibabaei, et al. *Proceedings of the National Academy of Sciences* **2013**, *110*, 20008;

4) Y.Gao, X.Ding, J.Liu, L. Wang, Z.Lu, L.Li, L.Sun, *Journal of the American Chemical Society* **2013**, *135*, 4219;

5) Y.Tachibana, L.Vayssieres, J.R.Durrant, *Nat. Photonics* **2012,** *6*, 511;

6)T. Arai, S. Sato, T. Kajino, T. Morikawa, *Energy Environ. Sci.* **2013,** *6*, 1274;

7) G.Sahara, H.Kumagai, K.Maeda, N.Kaeffer, V.Artero, M.Higashi, R.Abe, O. Ishitani, *J. Am. Chem. Soc.* **2016,** *138*, 14152;

8) B. Mei, G.Mul, B.Seger, *Adv. Sustain. Syst.* **2017**, *1*, 1600035;

9) V. Livshits, A.Ulus, E.Peled, *Electrochem. Commun.* **2006***, 8,* 1358;

10) K.T.Cho, P.Ridgway, A.Z.Weber, S.Haussener, V.Battaglia, V.J.Srinivasan, V. J., *Electrochem. Soc*. **2012**, *159*, A1806*;*

11) A.K. Vannucci, L.Alibabaei, M.D.Losego, J.J.Concepcion, B.Kalanyan, G.Parsons, T.Meyer, J. *Proceedings of the National Academy of Sciences* **2013**, *110*, 20918;

12) Y.Gao, L. Zhang, X.Ding, L.Sun, *Physical Chemistry Chemical Physics* **2014**, *16*, 2008;

13) J.R. Swierk, T.E. Mallouk, Design and development of photoanodes for water-splitting dye-sensitized photoelectrochemical cells. *Chem. Soc. Rev.* **2013,** *42*, 2357;

14) Z.Yu, F.Li, L.Sun, L.,Recent advances in dye-sensitized photoelectrochemical cells for solar hydrogen production based on molecular components. *Energy Environ. Sci.* **2015,** *8*, 760;

15) Mishra, A., Fischer, M. K., Bäuerle, P., *Angew. Chem. Int. Ed.* **2009,** *48*, 2474;

16) F.Ronconi, Z.Syrgiannis, A.Bonasera, M.Prato, R.Argazzi, S.Caramori, V.Cristino, C.A. Bignozzi, *J. Am. Chem. Soc.* **2015,** *137*, 4630;

17) K.Hanson, M.K. Brennaman, H.Luo, C.R.Glasson, J.J.Concepcion, W.Song, T.J.Meyer, *ACS Appl. Mater. Interfaces* **2012,** *4*, 1462;

18) C.Li, H.Wonneberger, *Adv. Mater.* **2012,** *24*, 613;

19) F.Würthner, C.R.Saha-Möller, B.Fimmel, S.Ogi, *Chem. Rev* **2016,** *116*, 962;

20) J.T.Kirner, J.Stracke, et al. *ACS Applied Materials & Interfaces* **2014**, *6*, 13367;

21) M.Batzill, U.Diebold, *Progr. Surf. Sci.* **2005**, *79*, 47;

22) L.Abello, B.Bochu, A.Gaskov, S.Koudryavtseva, G.Lucazeau, M.Roumyantseva, *J. Solid State Chem.* **1998**, *135*, 78;

23) M.Acciarri, C.Canevali, C.M. Mari, M.Mattoni, R.Ruffo, R.Scotti, F.Morazzoni, D.Barreca, L.Armelao, E.Tondello, E.Bontempi, L.E.Depero, *Chem. Mater.* **2003**, *15*, 2646;

24) K.L. Chopra, S.Major, D.K. Pandya, *Thin Solid Films* **1983**, *102*, 1;

25) T.Minami, Semicond. Sci. Technol. **2005**, *20*, S35;

26) M.Guglielmi, E.Menegazzo, M.Paolizzi, G.Gasparro, D.Ganz, J.Pütz, M.A.Aegerter, L.Hubert-Pfalzgraf, C.Pascual, A.Durán, H.X. Willems, M. Van Bommel, L.Büttgenbach, L.Costa, *J. Sol-Gel Sci. Technol.* **1998**, *13*, 679;

27) T.Nutz, M.Haase, *J. Phys. Chem. B* **2000**, *104*, 8430;

28) T.Nutz, et al., M., *J. Chem. Phys.* **1999**, *110*, 12142;

29) V.Geraldo, L.V.A Scalvi, P.N. Lisboa-Filho, C.Morilla-Santos, *J. Phys. Chem. Solids* **2006**, *67*, 1410;

30) B. Grzeta, E.Tkalcec, C.Goebbert, M.Takeda, M.Takahashi, K.Nomura, M.Jaksic, *J. Phys. Chem. Solids* **2002**, *63*, 765;

31) V. Müller, M.Rasp, G.Štefanić, J.Ba, S. Günther, J.Rathousky, M.Niederberger, D.Fattakhova-Rohlfing, *Chem. Mater.* **2009**, *21*, 5229;

32) F.Rigodanza, E.Tenori, A.Bonasera, Z.Syrgiannis, M.Prato, *Eur. J. Org. Chem.* **2015,** *2015*, 5060;

33) A.Orbelli Biroli, F.Tessore, M.Pizzotti, C.Biaggi, R.Ugo, S.Caramori, A.Aliprandi, C.A. Bignozzi, F. De Angelis, G.Giorgi, *J. Phys. Chem. C* **2011,** *115* , 23170;

34) N.S Levov, V.Rodrigez-Santiago, et al. *Langmuir* **2009**, 25, 8101;

35) N.Li, Q.Meng, N.Zhang, *Particuology*, **2014**, *17*, 49;

36) R.Greenwood, K.Kendall, *Journal of the European Ceramic Society*, **1999***, 19,* 479;

37) D.A.H Hanaor, M.Michelazzi, C.Leonelli, C.C.Sorrell, *Journal of the European Ceramic Society*. **2012** *32*, 235;

38) M. Müller, M.Rasp, et.al, *Small*, **2010**, *6*, 633;

39) M.Haase, et at., *J. Phys. Chem. B* **2000**, *104*, 8430;

40) M.J.Griffith, K.Sunahara, P.Wagner, K.Wagner, G.G.Wallace, D.L.Officer, A.Furube, R, Katoh, S,Mori, A.J. Mozer, *Chem. Commun.* **2012,** *48*, 4145;

CHAPTER 8. EXPERIMENTAL SECTION

In this chapter the electrochemical, photoelectrochemical and spectroscopic methods employed in this thesis work will be described. The outlined techniques summarized below were essential in order to fully characterize the studied systems, like new electrode materials and molecular systems, in solution or attached to a surface.

8.1 Spectroscopic characterization

8.1.1 Stationary emission/absorption techniques

UV-visible spectroscopy measurements were performed in this thesis work to investigate the spectral profile of sensitizers, redox couples and electrodes, using for the most part of the experiments a double beam *JASCO V-570* spectrophotometer, bandwidth of 2 nm, equipped with a W/I2 (for NIR/vis, from 2500 nm to 400 nm) and a H2/D2 (for UV, from 400 nm to 200 nm) lamps. For the molecules studied in this thesis, absorption measurements were achieved with standard quartz cuvettes of 1.0 cm optical path (dyes, redox couples in solution), or with transparent sensitized electrodes (dyes adsorbed on semiconductor). The absorbance (A) of a sample at a specific wavelength is calculated from its transmittance (T) according to equation 8.1:

$$A(\lambda) = -\log T(\lambda) \qquad \text{Eq.8.1}$$

where $T = I/I_0$, with I_0 and I being the incident and transmitted radiant intensity. An important parameter that can be extracted is the molar extinction coefficient (ε), which is obtained by the Lambert-Beer's law:

$$A = \varepsilon C l \qquad \text{Eq.8.2}$$

where C is the molar concentration of the species and l is the path length. For optical diluted solutions, the absorbance can be correlated to the concentration of the absorbing species through Eq.8.2. The Lambert-Beer law can be applied also for species adsorbed on semiconductor thin film, through the Eq.8.3:

$$A = 1000\Gamma\varepsilon \qquad \text{Eq.8.3}$$

where Γ is the adsorbed species surface concentration (mol/cm^2) and 1000 is the volume conversion factor.

Photoluminescence and excitation spectra were recorded on an *Edinburgh Instruments FLS 920* fluorescence spectrometer, equipped with a double emission monochromator, Xe lamp (450 W, excitation range from 230 nm to 1700 nm) as excitation source and a *R928P-Hamamatsu* photomultiplier tube as detector. Standard quartz cuvettes, with 1.0 cm optical path, or sensitized thin film electrodes were employed. A photoluminescence measurement consists in the detection of the intensity of the emitted light by a sample at different wavelengths (in general in the UV/visible range) upon excitation at a fixed λ. By the intersection of normalized absorption and emission spectra, of a generic molecule, it is possible to calculate the zero-to-zero spectroscopic energy ($E^{0\text{-}0}$), relative to the energy gap between the HOMO-LUMO molecular orbitals.

$$E^{0\text{-}0} = \frac{10^7}{\lambda^{0\text{-}0}[\text{nm}] \times 8066\ [\text{cm}^{-1}]} \qquad \text{Eq.8.4}$$

where $\lambda^{0\text{-}0}$ is the intersection wavelength and 8066 is the energy conversion factor.

Spectroelectrochemistry

This technique consists in the collection of absorption spectra while applying a potential to the studied system. For example, it was employed in this thesis work to monitor the absorbance of electrons in SnO_2 and ATO, changing as their concentration changes under increasingly negative potential, in the context of a detailed dye/semiconductor study conducted at Paris Lodron University in Salzburg. Steady-state UV-vis absorption spectra were recorded with a *Perkin Elmer Lambda 750* spectrophotometer, at room temperature, concomitant with bulk electrolysis of a standard three-electrodes cell. External biases were applied to the thin films before and after sensitization, deposited on a FTO substrate working electrode, positioned in a 1 cm cuvette. A *Keithley* potentiostat was employed. Each potential step was held for around 2 to 3 minutes until the spectrum was invariant with time and the next potential was applied. A Pt wire counter electrode and an SCE reference were employed.

8.1.2 Time-resolved absorption techniques

Electron transfer dynamics at the semiconductor/dye/electrolyte interface were studied mainly by time-resolved absorption measurements. These techniques can be distinguished on the basis of the investigated time domain (*i.e.* Nanosecond/Femtosecond transient absorption spectroscopy). Following the excitation pulse, a population of excited dye molecules able to inject charge into the semiconductor is created. The output is usually

expressed as ΔOD, where A* and A_0 are the absorbance of the transient species and the ground state respectively:

$$\Delta OD(\lambda, t) = A^{*}\text{-}A_0 \qquad \text{Eq.8.5}$$

By considering Equation 8.5 and the Lambert-Beer law in Equation 8.2, it is thus possible to calculate the concentration ΔC of the photogenerated transient species if the molar extinction coefficient is known (Eq.8.6):

$$\Delta OD(\lambda, t) = \Delta\varepsilon\Delta Cl \qquad \text{Eq.8.6}$$

$$\Delta C = C^{*}\text{-}C_0 = C_0 e^{-\frac{1}{\tau}}\text{-}C_0 \qquad \text{Eq.8.7}$$

From ΔOD, using the Equation 8.6, where C* and C_0 are respectively the molar concentration of the molecules at excited state and at ground state, it is possible to determinate the lifetime (τ) of the light excited species. It is worth to notice that the parameter l, correlating ΔOD and ΔC, is not strictly the optical path of the cell, but rather the real fraction of the solution in the cell, which is pumped by the excitation source and analysed by the light probe.

Nanosecond transient absorption spectroscopy

The electron injection is much faster (fs-ps) than the time resolution of the nanosecond transient absorption spectroscopy technique, so that a population of oxidized dye molecules is instantaneously created. The decay of the oxidized dye absorption recorded in various conditions gives information about the efficiency of dye regeneration and about the dynamics of electron recapture. Transient measurements at the university of Ferrara were performed with a custom laser spectrometer (a schematic representation is given in Figure 8.1) comprised of a *Continuum Surelite II Nd:YAG* laser (1064 nm, FWHM = 6-8 ns), equipped with frequency doubled (532 nm), tripled (355 nm), or quadrupled (266 nm) options, an *Applied Photophysics* Xe light source, including a *mod.720* 150 W lamp housing, a *mod. 620* power controlled lamp supply, and a *mod. 03-102* arc lamp pulser. Laser excitation is provided at 90° with respect to the white light probe beam. This latter is controlled by means of an *Oriel 71445* shutter, which opens only for ca. 100 ms during the measurements, thus preventing continuous irradiation of the sample. Light transmitted (transient absorption measurements) by the sample is focused onto the entrance slit of a 300 mm focal length *Acton SpectraPro 2300i* triple grating, flat field, double exit monochromator equipped with a photomultiplier tube detector *Hamamatsu R3896*, used for kinetic studies at fixed *λ*, and a *Princeton Instruments PIMAX II* gated intensified CCD

camera, used for spectral detection at fixed time-delays, employing a *RB Gen II* intensifier, a *ST133* controller and a *PTG* pulser. Signal from the photomultiplier is processed by means of a *LeCroy 9360* (600 MHz, 5 Gs/s). Excitation source, lamp and shutter are computer-controlled by a *LabVIEW National Instruments* software routine. It is worth to notice that appropriate cut-off and neutral filters can be added to eventually reduce the energy of the excitation or analysis light.

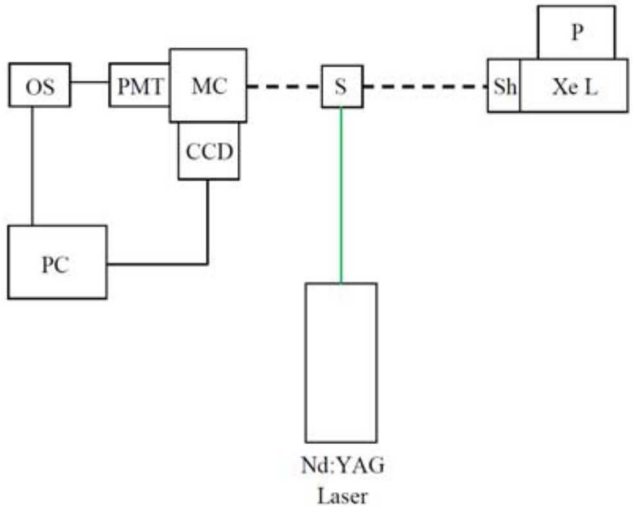

Fig.8.1 Schematic layout of the Nanosecond Laser Flash Photolysis setup: green line, excitation beam; black dashed line, white light probe beam; Xe L, xenon arc lamp; P, Xe lamp pulser; Sh, shutter; S, sample; MC, monochromator, PMT, photomultiplier tube; CCD, CCD camera; OS, oscilloscope; PC, personal computer.

Femtosecond transient absorption spectroscopy

To investigate ultrafast processes taking place in the sub-nanosecond timescale, like the electron injection driven by the dye photoexcitation, an investigation was conducted in Milan in collaboration with Prof. G.N.Cerullo [1]. The employed femtosecond transient absorption (TA) spectrometer is based on an amplified Ti:sapphire laser (Coherent Libra), generating 2-mJ, 100 fs pulses at 800 nm wavelength and 2-kHz repetition rate. A 300-μJ fraction of the pulse energy is used for the experiments, and is split into two beams. The first beam feeds an optical parametric amplifier, generating tunable pump pulses in the visible with ~70-fs duration; the second beam is focused in a CaF2 crystal, generating a broadband white-light continuum (WLC) spanning the visible range (370-750 nm) and used as a probe. To avoid optical damage, the CaF_2 plate is slowly scanned in the beam focus. Pump and WLC probe pulses are non-collinearly focused on the sample and the transmitted probe, spatially selected by an iris, is sent to a silicon spectrometer capable of single-shot detection at the full 2-kHz repetition rate of the laser. The pump is modulated by a mechanical chopper at 1 kHz and the differential transmission spectra, defined as $\Delta T/T = (T_{pump\ on} - T_{pump\ off})/T_{pump}$

$_{off}$, are recorded as a function of probe wavelength and delay. Chirp-free ΔT/T maps by using a home-made dechirping algorithm.

8.2 Electrochemical/ Photoelectrochemical characterization

8.2.1 Cyclic Voltammetry/Linear sweep voltammetry

In order to obtain experimental information on the redox properties of the investigated systems, potentiodynamic electrochemical methods, such as cyclic voltammetry (CV) and linear sweep voltammetry (LSV) have been used. These techniques are based on the possibility of studying electron transfer reactions between an electrode and a molecule in solution. By applying a variable external voltage, it is possible to tune the virtual Fermi level of the electrode (a metal or more generally a conductor) thus allowing a "communication" with the electronic levels of the molecules in solution. This communication consists in a chemical reaction of the molecules in solution undergoing either oxidation (anodic process) or reduction (cathodic process), which is detected as a current. Considering a general reduction reaction ($A_{OX} + ne- \rightarrow A_{RED}$), occurring at the interface between the electrode and the solution, in order to measure a current, it is necessary that A_{OX} reaches the electrode and accepts electrons (*e*-) from it. Therefore, the electron transfer process at the interface is controlled by two kinetic factors: *a)* the rate of diffusion (v_d) of A_{OX} to the electrode/solution interface and *b)* the rate of electron exchange (v_e) between the electrode and A_{OX}. For simple electron transfer reactions is often encountered the situation $v_e >> v_d$, therefore the observed current is only dependent on the diffusion process of the analyte to the electrode. In CV a voltage (*E*) is applied between the working electrode and the counter electrode (measured with respect to the reference electrode) and varied as a function of time (Fig.8.2A). A current at each potential value is achieved and the result is a cyclic voltammogram, plot of *i* vs. *E* (Fig.8.2B).

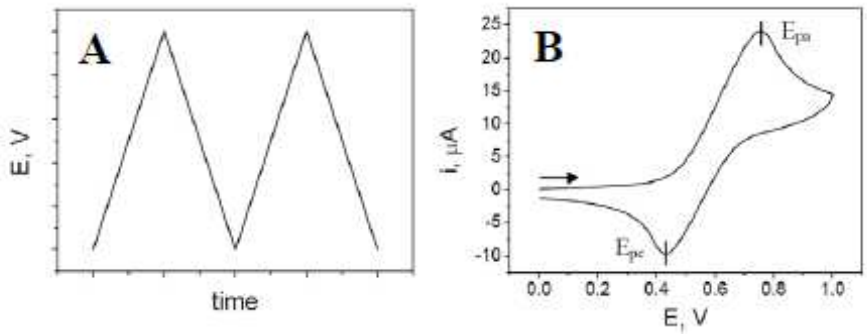

Fig.8.2 Cyclic voltammetry: (A) variation of the potential *E* as a function of time (two cycles); (B) example of the resulting cyclic voltammogram.

In CV the voltage is varied linearly with time (*t*), without illumination by a solar source (only electrochemical measurements), from an initial potential to a final potential followed by the opposite path, with scan rate preset at the beginning of the experiment. Instead, in LSV the potential variation is performed only in one way (anodic or cathodic), representing half of the total CV, and if is registered under illumination by Sun simulator, the change of *i* switching from light to dark is achieved. In Fig.8.2B a typical CV behavior is reported representing the plot of *i* vs. *E*, in which two main features can be distinguished. Upon anodic scan (*i.e.* from negative to positive potentials) a positive wave is observed, ascribable to the oxidation of the analyte at the electrode/solution interface, featuring an anodic peak potential E_{pa}. Upon reversed scan (cathodic scan) a negative wave with a cathodic peak potential E_{pc} is detected, due to the reduction process. Important information can be obtained by CV, for example about thermodynamic properties of the investigated system. In fact, if the redox process is reversible the cathodic and anodic peak potentials should follow the Equation 8.8 (true for only monoelectronic processes):

$$\Delta E = E_{pa} - E_{pc} = 0.059V \qquad \text{(Eq.8.8)}$$

Where E_{pa} and $E_{pc}$are the anodic and cathodic maximum peak potentials. This value represents the reversibility of an electrochemical reaction, which decreases with increasing *ΔE*. Another parameter extractable from CV measurements is the half-wave potential ($E_{1/2}$):

$$E^0 \approx E_{1/2} = \frac{E_{pa}+E_{pc}}{2} \qquad \text{(Eq.8.9)}$$

which indicates an estimate of the formal potential E^0 of a redox couple involved in an electron transfer process. CV and LSV measurements were carried out with a PC interfaced *Eco Chemie Autolab/PGSTAT302N* potentiostat workstation controlled by *GPES*. For photoelectrochemical experiments (only LSV) the same apparatus was coupled with a solar simulator (AM 1.5 G illumination): to experimentally characterize DSPECs, functionalized semiconductor photoanodes were used as working electrodes, with a saturated calomel electrode (SCE from Amel) as reference and a platinum wire (Pt from Sigma-Aldrich) as counter; while to experimentally characterize DSSCs, linear sweep voltammetry (LSV) measurements were conducted by connecting the electrical terminals of the potentiostat to the photoanodic and cathodic solar cell components, and an external potential ranging from 0 up to the open circuit voltage (Voc) was applied.

8.2.2 Electrochemical Impedance spectroscopy

Electrochemical impedance spectroscopy (EIS) measurements provide data on both electrode capacitance and charge transfer kinetic, giving valuable mechanistic information. The main advantage of EIS is the possibility to use a simple electronic model to represents an electrochemical cell, due to the analogy between electrode interfaces, where electrochemical reactions occur, and electric equivalent circuits, consisting in specific combination of resistors and capacitors. It is possible to use the alternate current (AC) circuit theory to characterize the electrochemical system (*i.e.* reaction mechanisms, charge transfer kinetics, physical properties), due to the correlation of its impedance behaviour with one or more equivalent circuits, simply extracting numerical values by fitting the experimental data from the circuit model. During EIS experiments, a time-dependant signal, usually a sinusoidal perturbation of the constant bias potential (E) with frequency f ($0.01\ \text{Hz} < f < 100$ MHz), is applied to the working electrode and the photocurrent (under illumination), or simply the current (in dark conditions), is registered. The excitation signal, imposed to the electrochemical cell, is typically a small potential (1 mV - 10 mV), so the response will be pseudo-linear, resulting in a sinusoidal i behaviour at the same frequency of the sinusoidal E applied, but shifted in phase. By varying the excitation frequency, processes with different time constants can be resolved. It should be noted that electrochemical cells are in general not linear: in fact, doubling the voltage will not necessarily double the current, but they can be considered pseudo-linear focusing on a small portion of the J-V characteristics (Fig.8.3). The further analysis of the frequency dependant response, using an electronic model, can separate the different aspects of charge transport, charge trapping and charge transfer at the interface with electrolyte.

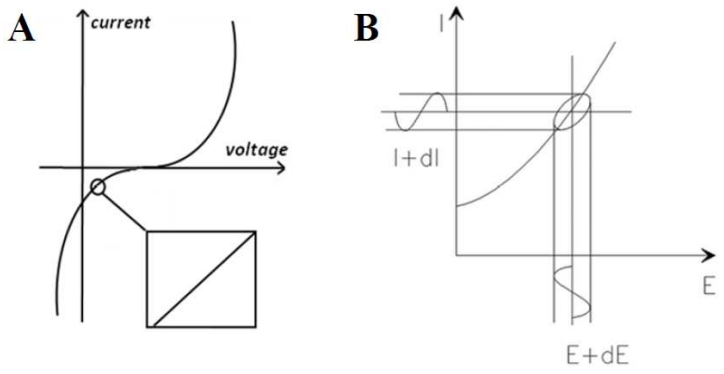

Figure 8.3 (A) E_t vs. I_t curve showing pseudo-linearity for little potential perturbation. (B) Graphical interpretation of the "Lissajous figure".

The excitation signal, expressed as function of time, has the form of Eq.8.10:

$$E_t = E_0 \sin(\varpi t) \quad \text{(Eq.8.10)}$$

where E_t is the potential at time t, E_0 is the amplitude of the signal and ω is the radial frequency, related to the frequency expressed in hertz (f) by Equation 8.11:

$$\varpi = 2\pi f \quad \text{(Eq.8.11)}$$

In a linear system, the response signal, I_t is shifted in phase (φ) and has a different amplitude than I_0:

$$I_t = I_0 \sin(\varpi t + \phi) \quad \text{(Eq.8.12)}$$

The term *impedance (Z)* denotes the opposition to the flow of electrons and so, in analogy to Ohm's law, it can be written as:

$$Z = \frac{E_t}{I_t} = \frac{E_0 \sin(\varpi t + \phi)}{I_0 \sin(\varpi t + \phi)} \quad \text{(Eq.8.13)}$$

Reporting the sinusoidal signal E_t on the x-axis of the *J-V* plot and the sinusoidal response I_t on the y-axis, the result is an oval known as "Lissajous Figure" (Figure 8.3B), the first accepted method for impedance measurements. Using the Euler's relationship:

$$e^{j\phi} = (\cos\phi + j\sin\phi) \quad \text{(Eq.8.14)}$$

the impedance can be also represented as a complex number:

$$Z(\varpi) = Z_0 e^{j\phi} = Z_0(\cos\phi + j\sin\phi) \quad \text{(Eq.8.15)}$$

(j is used by electrochemists instead of i to define $\sqrt{-1}$ to avoid confusion with the current symbol i). Impedance represents thus a more general concept of the resistance defined by the classical Ohm's law: in AC circuits, also capacitors and inductors impede the flow of electrons through the circuit rather than resistors. Let us consider, for example, a simple circuit composed by a resistor in series with a capacitor represented in Figure 8.4.

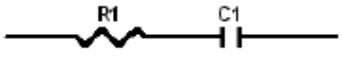

Fig.8.4 Simple electrical circuit composed by a resistor (R) in series with a capacitor (C).

The total impedance of the circuit (Z_{tot}) is given by the sum of the single contributions, Z_R and Z_C for the resistor and the capacitor respectively.

$$Z_{tot} = Z_R + Z_C = R\text{-}jX_C \quad \text{(Eq.8.16)}$$

where R is the classic Ohm resistance and X_C is the capacitive reactance. Notice that the impedance of a resistor is equal to the resistance value: it is independent from frequency and it has no imaginary component because there is no phase-angle shift between the voltage and the current flowing through the resistor (Fig. 8.5). With only a real impedance component, the current through a resistor stays in phase with the voltage across the resistor. Capacitors have instead only an imaginary impedance component because the current through a capacitor is phase shifted by 90 degrees with respect to the voltage, as can be demonstrated from Equation 8.17. The capacitors impedance decreases as the frequency is raised. The impedance of elements in parallel is instead the inverse of the sum of the inverse of impedances.

$$I = C\frac{dE}{dt} = C\frac{d(E_0 \sin(\varpi t))}{dt} = \varpi C \cos(\varpi t) = \frac{E}{X_C}\sin(\varpi t + \frac{\pi}{2}) \qquad \text{(Eq.8.17)}$$

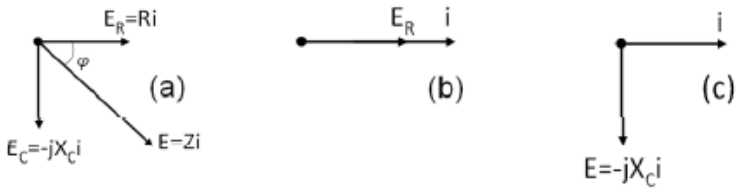

Fig.8.5 Vector representation of the relation between the applied potential and the flowing current (a) in the circuit represented in Figure 8.4, (b) in a resistor and (c) in a capacitor. In a resistor, the phase angle between the potential applied and the current is 0 degrees, so the two vectors are coincident. In a capacitor, the angle is 90 degrees and, reporting the current on the x-axis, the capacitive vector has an imaginary part for convention because coincident with the y-axis.

A common way to plot impedance data is the Nyquist plot, where the real part of the impedance is plotted on the x-axis while the imaginary part is plot on the y-axis. In this plot, the y-axis is negative, and each point corresponds to the impedance at one frequency. The major shortcoming of this representation is that looking at it is not possible to know at which frequency corresponds a single data point. The Bode plots allow to gain this kind of additional information by plotting the logarithm of the frequency on the x-axis and both the absolute values of the impedance ($|Z|=Z_0$) and the phase-shift angle (φ) on the y-axis. In Figure 8.6 Nyquist and Bode plots for a circuit comprised of a resistor and a capacitor in parallel are reported.

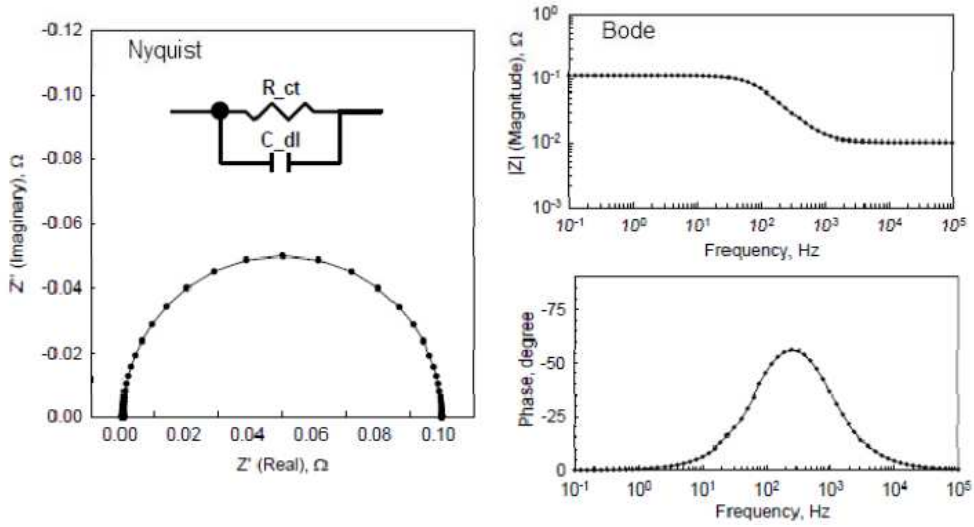

Fig.8.6 Nyquist (left) and Bode (right) plots for the reported RC circuit.

Once an experiment is complete, the raw data at each frequency measured consist of the real and imaginary component of both the voltage applied and the current generated. From these data it is possible to compute the phase shift (φ) and the total impedance (Z) for each applied frequency, as well as many other impedance functions. An important step in the elaboration process is the choice of the correct circuital model that well describes the system under investigation and then the interpretation of the values related to physical and chemical properties of the system. EIS measurements are usually repeated for different E values, in order to describe the system in the full potential range. Although the circuital elements have a detailed mathematical description, their physical interpretation, and so their association at the different electrode interfaces, is probably the most challenging part of the experiment. The physical description of the most common circuital elements is listed below.

- Resistor (R): it can be associated to limitation of electronic conductivity inside the bulk of the material, charge transfer through interfaces and also resistance due to the solution or to the set-up employed for the measurements.

- Capacitor (C): it represents the charge accumulation at the interfaces where a double layer is formed.

- Constant Phase Element (CPE): it represents an interface that acts as a non-ideal capacitor showing a strong dependence to the frequency; this behaviour is probably due to high porosity or non-homogeneity of a surface that generate charge dissipation processes that are not described by an ideal capacitor.

- Warburg element (W): it describes diffusive phenomena inside the solution of redox species that are generated on the working electrode.

In the present thesis EIS was mainly employed to investigate electronic and ionic processes occurring in DSSC. Analysis of the EIS spectrum of a DSSC, which is fitted by means of an appropriate equivalent circuit representing the physical system under study, provides information about several important charge transport, transfer, and accumulation processes in the cell. The DSSC contains three spatially separated interfaces formed by FTO/TiO_2, TiO_2/electrolyte, and electrolyte/counter electrode-FTO. In the dark under forward bias, electrons are injected in the conduction band of the TiO_2 nanoparticles and their motion is coupled to that of the electron donor and acceptor ions in the electrolyte. Illumination gives rise to new redox processes at the TiO_2/dye/electrolyte interface, comprising electron injection from the photoexcited sensitizer, recombination with the parent dye, and regeneration of the sensitizer. If a potential correspondent to the open circuit condition is applied to an operative DSSC under illumination, the measurement output has generally the aspect reported in figure 8.7. The resulting Nyquist diagram typically features three semicircles that, in the order of increasing frequency, are attributed to the Nernst diffusion within the electrolyte (Z_D), the electron transfer at the oxide/electrolyte interface (Z_{TiO2}), and the redox reaction at the platinum counter electrode (Z_{CE}) [2]. Correspondently, the Bode phase plot shows three characteristic frequency peaks.

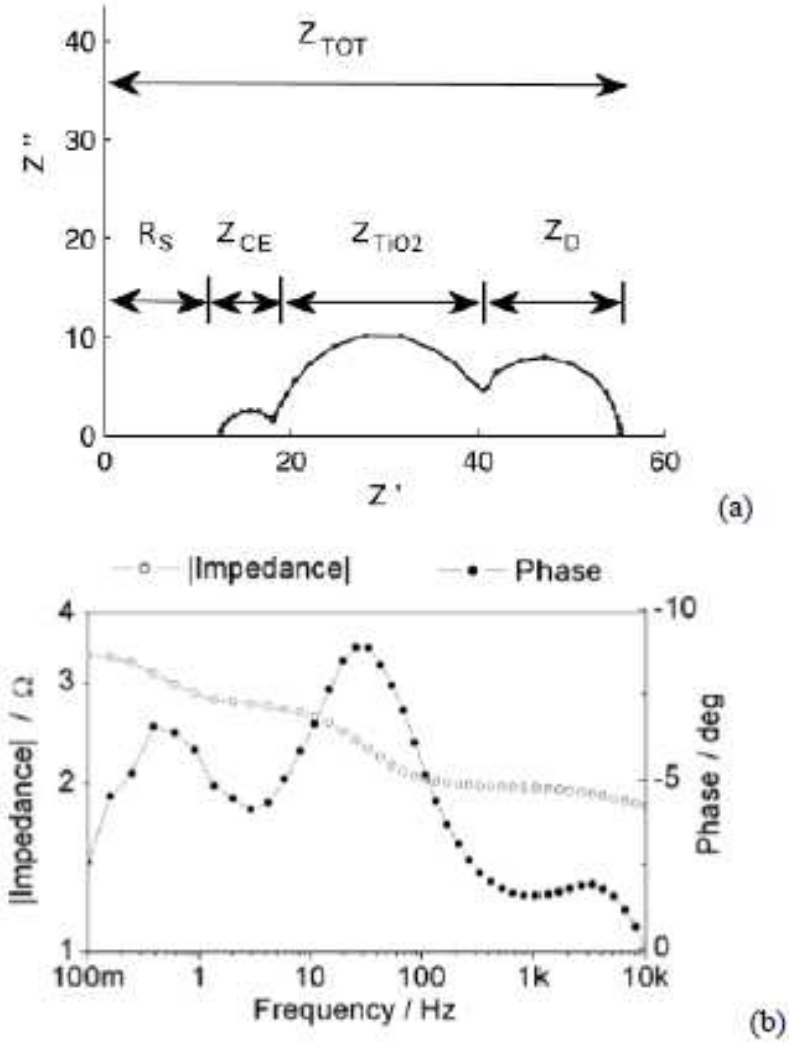

Fig.8.7 General electrical impedance spectrum of a dye-sensitized solar cell under open-circuit condition and 0.1Wcm^{-2} bias illumination, in the form of Nyquist (a) and Bode (b) plots.

If a low potential, closer to the short-circuit condition, is applied, the impedance of the TiO_2/dye/electrolyte interface becomes very high, since TiO_2 is rapidly depleted by electrons which are drawn to the back contact. To adequately fit the obtained measurement outcome, an equivalent circuit such as that reported in fig.8.8 is generally used.

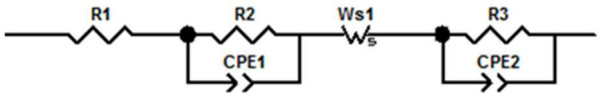

Fig.8.8 Electrical circuit model used to fit experimental EIS data of a DSSC under illumination

where R1 is the series ohmic resistance (namely *Rs*), representing the sum of the bulk electrolyte, substrate, and electric contacts resistances; the parallel combination of R2 and

CPE1 represents the resistance to charge transfer on TiO_2 (namely R_{CT}); Ws represents the short Warburg diffusion element, whose projection on the real axis gives the diffusional resistance of the redox couple in the electrolyte (namely, R_D); and the parallel combination of R3 and CPE2 stands for the resistance to charge transfer to the counter electrode (R_{CE}). The interfacial double layer capacitance is replaced by a constant phase element (CPE) to account for the deviation from an ideal capacitor, arising from the non-homogeneity of the rough, porous electrodes surfaces involved, and causing a flattening of the Nyquist plot semicircles.

Alternatively, in the present thesis EIS was also employed to carry out analysis on thin layer dummy cells, made of two facing counter electrodes. This measurement produces a voltammogram in which the slope of the linear interval, centered on the origin, is inversely proportional to the charge transfer resistance at the electrode surface, and the reached limiting current represents the highest current obtainable in the presence of the specific cathodic material and electrolyte combination employed. EIS technique was carried out applying a potential in the dark, producing a Nyquist diagram consisting in two semicircles centered on the real axis (Fig.8.9). The smaller one at higher frequencies is ascribed to the charge transfer resistance at the counter electrode, whereas the largest at lower frequencies is attributed to the redox electrolyte diffusion resistance.

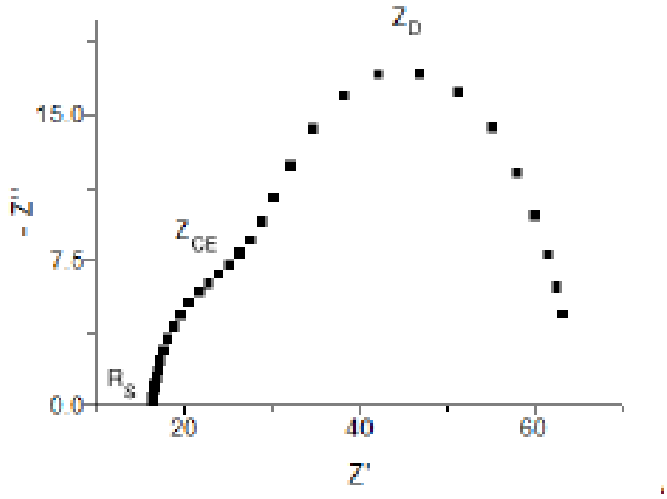

Fig. 8.9 Nyquist plot of a dummy cell made of PEDOT and $[Co(bpy)_3](OTf)_2$ electrolyte, measured at 0V under dark.

The equivalent circuit used to model this EIS spectrum is reported in fig.8.10, where the counter electrode/electrolyte interface global impedance is represented by the parallel combination of a charge transfer resistance (R2) and a costant phase element (CPE), in series

with respect to a ohmic resistance and a Warburg element identifying the electrolyte diffusion.

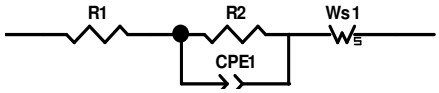

Fig.8.10 Electrical circuit model used to fit experimental EIS data of a thin layer cell under dark

8. 3 References

1) T. Virgili , G. Grancini , E. Molotokaite , I. Suarez-Lopez , S. K. Rajendran , A. Liscio , V. Palermo , G. Lanzani , D. Polli , and G. Cerullo *Nanoscale*, **2012**,*4*, 2219;

2) R. Kern, R. Sastrawan, J. Ferber, R. Stangl, J. Luther, *Electroch. Acta* **2002,** 47, 4213;

APPENDIX A

a)

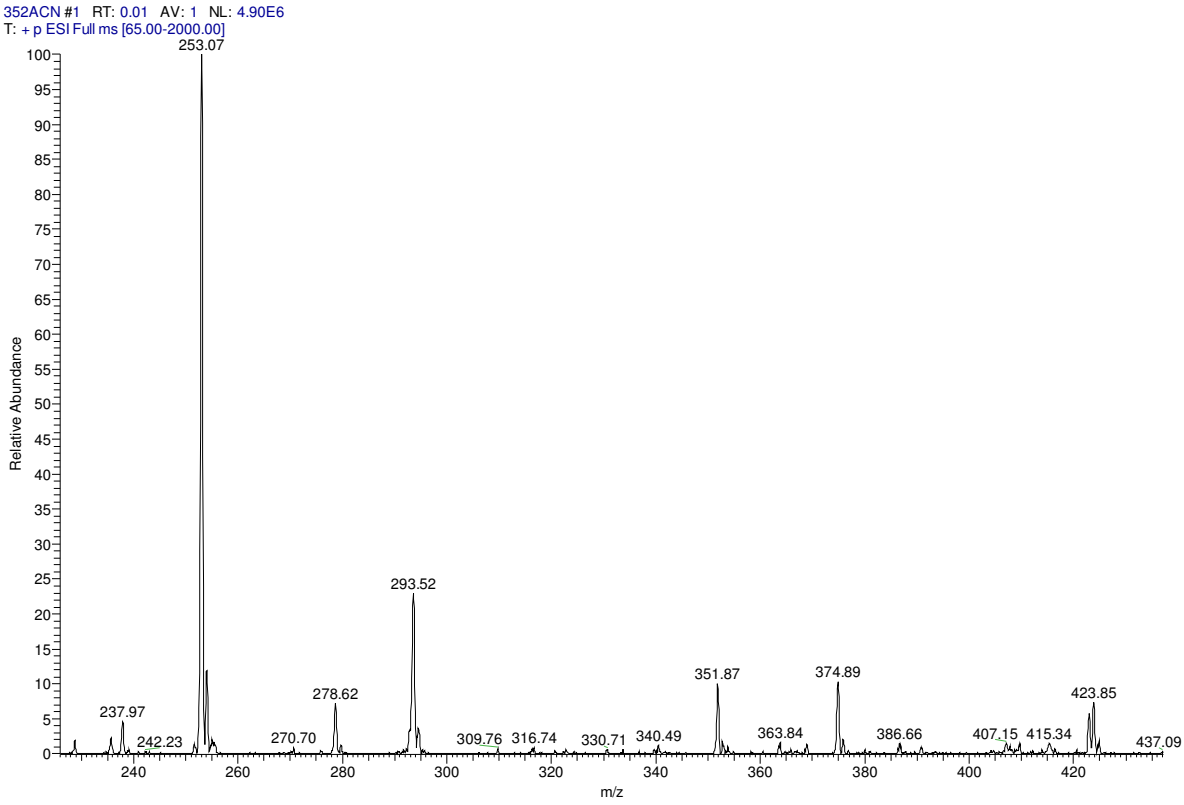

b)

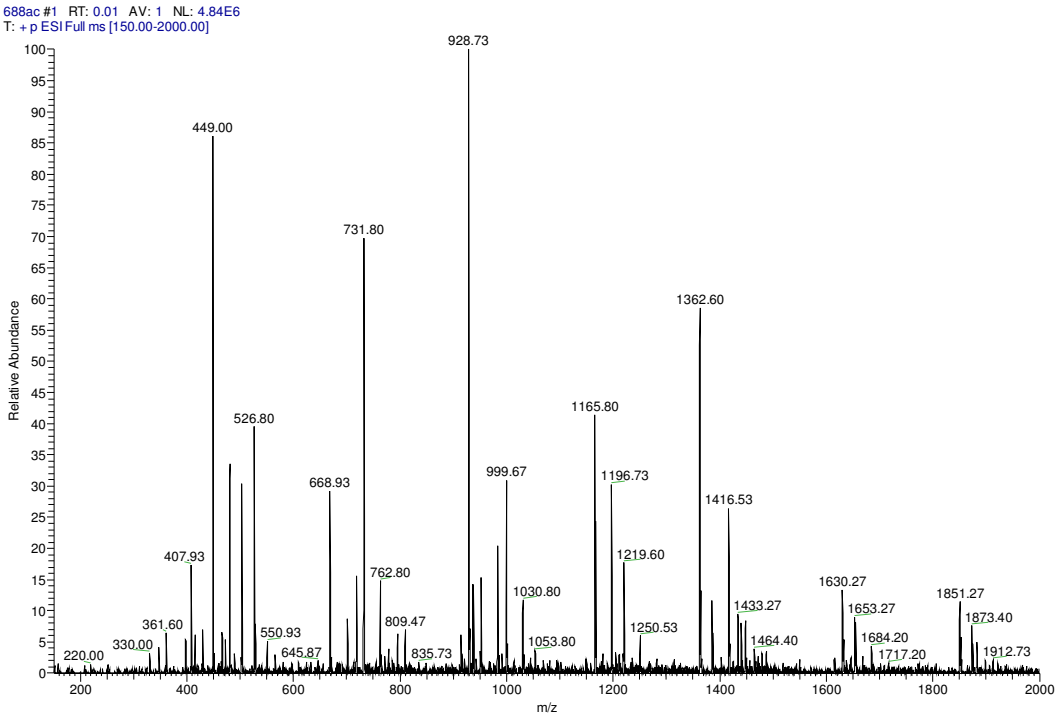

c)

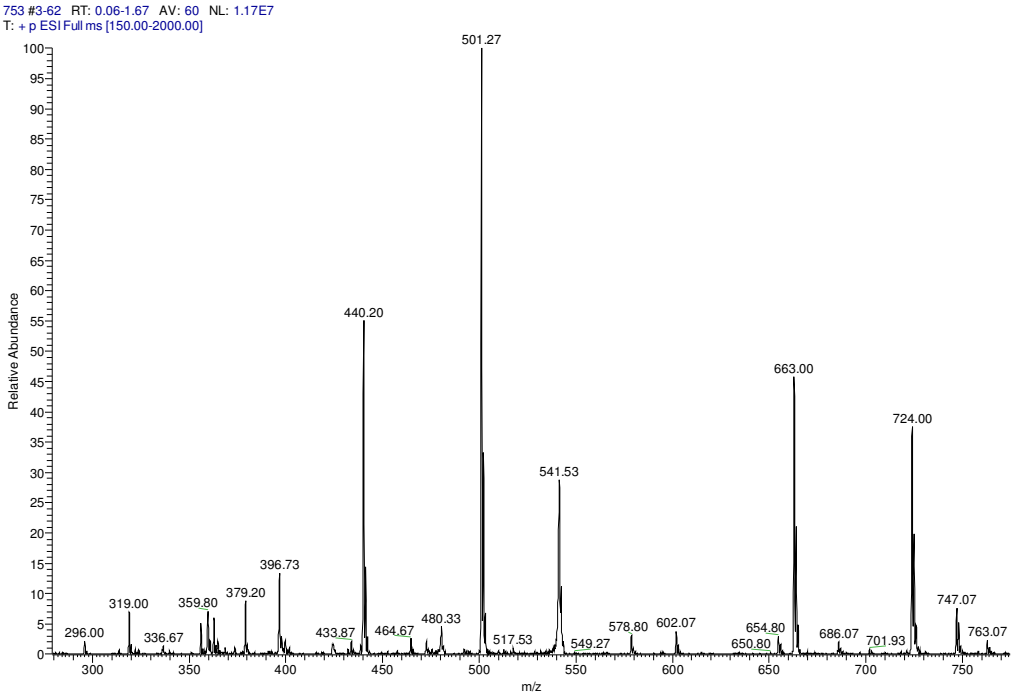
753 #3-62 RT: 0.06-1.67 AV: 60 NL: 1.17E7
T: + p ESI Full ms [150.00-2000.00]
Relative Abundance
m/z
501.27
440.20
663.00
724.00
541.53
396.73
319.00
359.80
379.20
747.07
296.00
336.67
433.87
464.67
480.33
517.53
549.27
578.80
602.07
654.80
650.80
686.07
701.93
763.07

d)

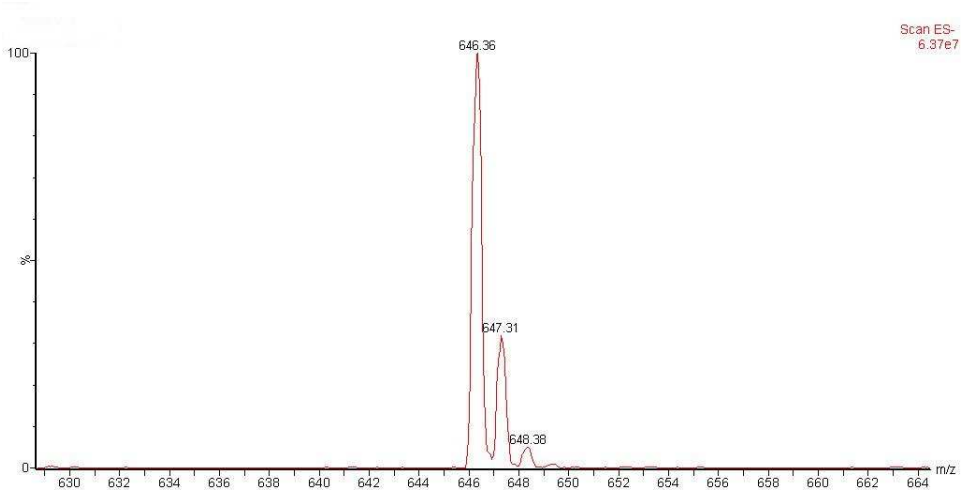
Scan ES-
6.37e7
%
m/z
646.36
647.31
648.38

e)

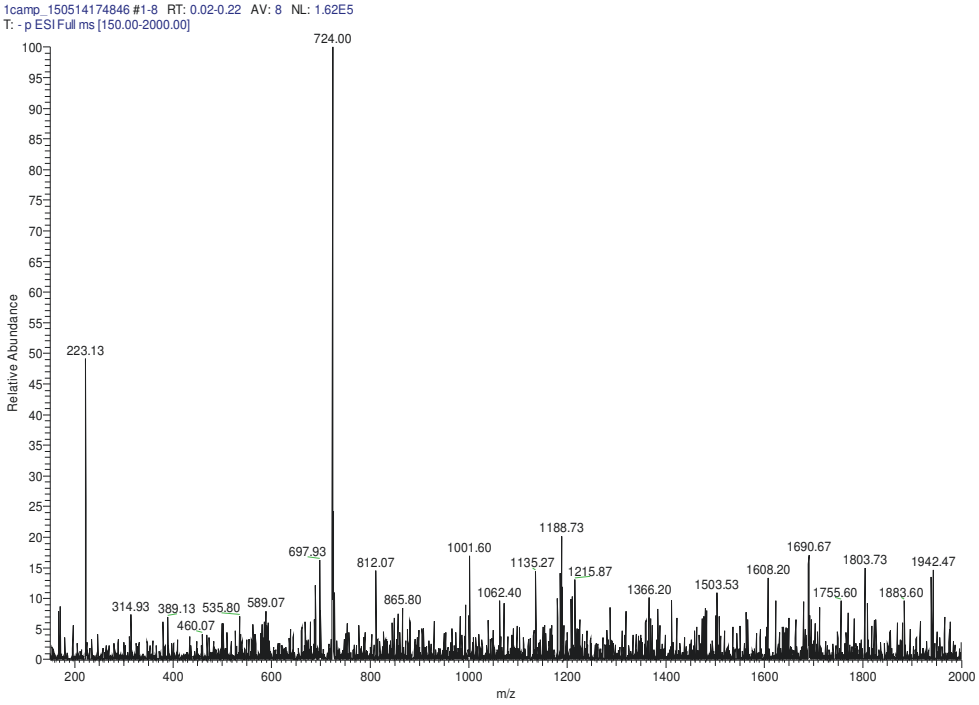

Fig.A1 ESI mass of 1 (**a**), 2 (**b**), 3 (**c**), 4(**d**), 5(**e**).

Table A1a. Crystallographic Data for *fac*-[Mn(CF2)$_3$] (complex **2**).

Compound	*fac*-[Mn(CF2)$_3$] (complex **2**)
Formula	Mn(III)$C_{30}H_{21}F_6O_6$
M	646.41
Space group	*R-3*
Crystal system	Trigonal
a/Å	18.583(1)
b/Å	18.583(1)
c/Å	14.503(1)
α/°	90.00
β/°	90.00
γ/°	120.00
U/Å^3	4337.3(4)
Z	6
T/K	295
D_c/g cm^{-3}	1.485
F(000)	1968
μ(Mo-Kα)/mm^{-1}	0.537
Measured Reflections	3905
Unique Reflections	2071
R_{int}	0.0210
Obs. Refl.ns [I≥2σ(I)]	1496
θ_{min}- θ_{max}/°	4.39 – 27.00
hkl ranges	-23,23;-20,20;-15,18
R(F^2) (Obs.Refl.ns)	0.0505
wR(F^2) (All Refl.ns)	0.1513
No. Variables/Restraints	130/0
Goodness of fit	1.046
$\Delta\rho_{max}$; $\Delta\rho_{min}$ /e Å^{-3}	0.295; -0.327
CCDC Deposition N.	1421029

Table A1b. Selected bond distances and angles (Å and degrees).

	fac-[Mn(CF2)$_3$] (complex **2**)
Distances	
Mn1-O1	1.978(2)
Mn1-O2	1.995(2)
Angles	
O1-Mn1-O2	89.17(8)
O1-Mn1-O1’	90.48(8)
O1-Mn1-O2’	91.57(9)
O1-Mn1-O2”	177.92(8)
O2-Mn1-O2’	88.79(8)
O2-Mn1-O2”	91.57(9)

a)

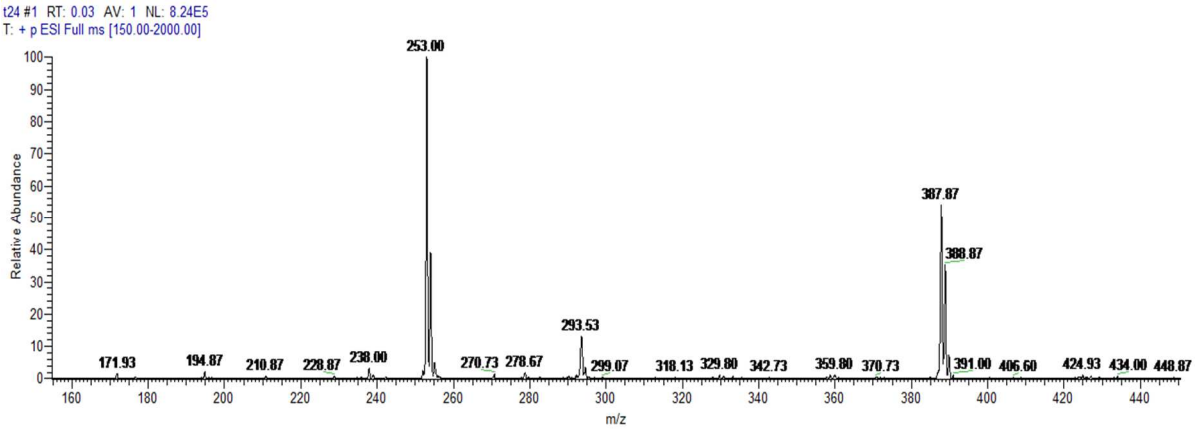

b)

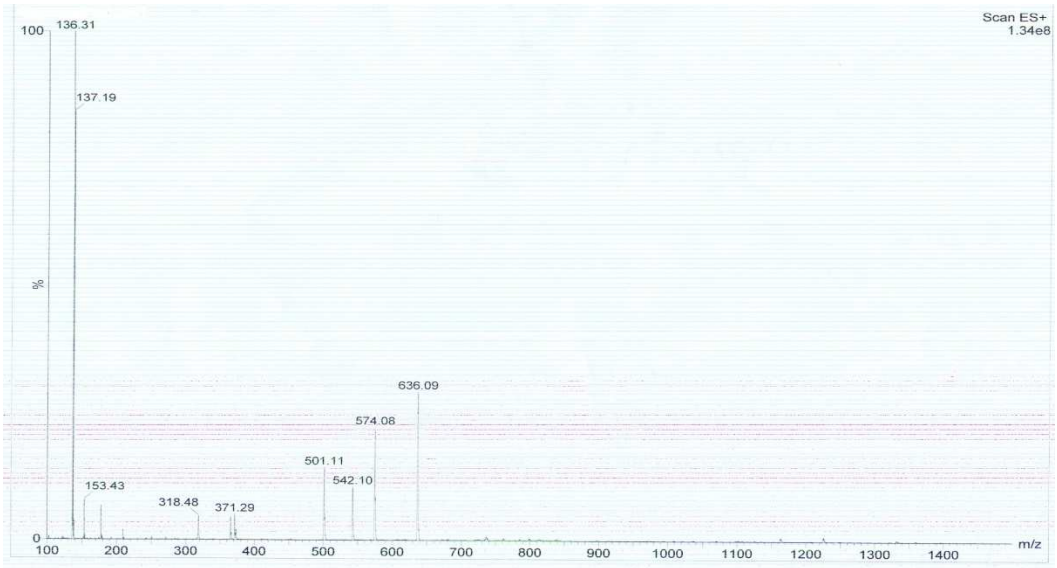

Fig.A2 ESI mass of 1(**a**) and 3(**b**) after the addition of TBP.

Table A2a. Crystallographic Data for *trans*-$[Mn^{III}(acac)_2TBP_2]ClO_4$.

Compound	*trans*-$[Mn^{III}(acac)_2TBP_2]ClO_4$
Formula	$[Mn(III)C_{28}H_{40}N_2O_8]^+ \bullet [ClO_4]^-$
M	623.01
Space group	*C2/c*
Crystal system	Monoclinic
a/Å	16.325(1)
b/Å	17.663(1)
c/Å	12.491(1)
α/°	90.00
β/°	115.434(10)
γ/°	90.00
U/Å^3	3252.7(4)
Z	4
T/K	295
D_c/g cm^{-3}	1.272
F(000)	1312
μ(Mo-Kα)/mm^{-1}	0.534
Measured Reflections	5347
Unique Reflections	2838
R_{int}	0.0785
Obs. Refl.ns [I≥2σ(I)]	1742
θ_{min}- θ_{max}/°	3.26-25.00
hkl ranges	-19,19;-20,20;-14,14
R(F^2) (Obs.Refl.ns)	0.0841
wR(F^2) (All Refl.ns)	0.2813
No. Variables/Restraints	220/21
Goodness of fit	1.034
$\Delta\rho_{max}$; $\Delta\rho_{min}$ /e Å^{-3}	0.519;-0.513
CCDC Deposition N.	1421030

Table A2b. Selected bond distances and angles (Å and degrees).

	trans-$[Mn^{III}(acac)_2TBP_2]ClO_4$
Distances	
Mn1-O1	1.924(3)
Mn1-O2	1.915(4)
Mn1-N1	2.290(4)
Angles	
O1-Mn1-O2	92.24(16)
O1-Mn1-O1'	180.00
O1-Mn1-O2'	87.76(16)
O2-Mn1-O2'	180.00
O1-Mn1-N1	89.15(16)
O1-Mn1-N1'	90.85(16)
O2-Mn1-N1	90.60(16)
O2-Mn1-N1'	89.40(16)
N1-Mn1-N1'	180.00

Table A3a. Crystallographic Data for *trans*-$[Mn^{II}(CF2)_2TBP_2]^0$.

Compound	*trans*-$[Mn^{II}(CF2)_2TBP_2]^0$
Formula	$Mn(II)C_{38}H_{40}F_4N_2O_4$
M	719.66
Space group	*C2/c*

Crystal system	Monoclinic	
a/Å	18.2229(9)	
b/Å	19.0407(10)	
c/Å	11.7031(7)	
α/°	90.00	
β/°	115.785(2)	
γ/°	90.00	
U/Å^3	3656.4(3)	
Z	4	
T/K	295	
D_c/g cm^{-3}	1.307	
F(000)	1500	
μ(Mo-Kα)/mm^{-1}	0.422	
Measured Reflections	5464	
Unique Reflections	3172	
R_{int}	0.0265	
Obs. Refl.ns [I≥2σ(I)]	2230	
θ_{min}- θ_{max}/°	3.53– 25.00	
hkl ranges		-21,21;-21,22;-13,13
R(F^2) (Obs.Refl.ns)		0.0750
wR(F^2) (All Refl.ns)		0.2310
No. Variables/Restraints		239/19
Goodness of fit		1.129
$\Delta\rho_{max}$; $\Delta\rho_{min}$ /e Å^{-3}		0.400; -0.384
CCDC Deposition N.		1421031

Table A3b. Selected bond distances and angles (Å and degrees).

	trans-[Mn^{II}(CF2)$_2$TBP$_2$]^0
Distances	
Mn1-O1	2.156(4)
Mn1-O2	2.128(2)
Mn1-N1	2.271(6)
Mn1-N2	2.325(6)
Angles	
O1-Mn1-O2	85.34(11)
O1-Mn1-O1'	177.09(18)
O1-Mn1-O2'	94.69(11)
O2-Mn1-O2'	178.96(16)
O1-Mn1-N1	91.45(9)
O1-Mn1-N2	88.55(9)
O2-Mn1-N1	89.48(8)
O2-Mn1-N2	90.52(8)
N1-Mn1-N2	180.00

a)

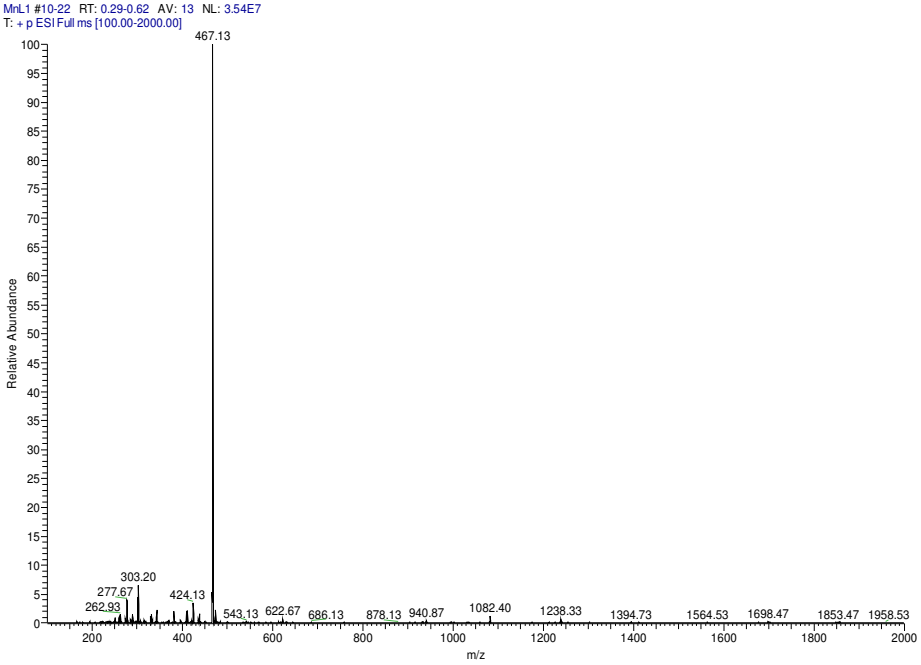

b)

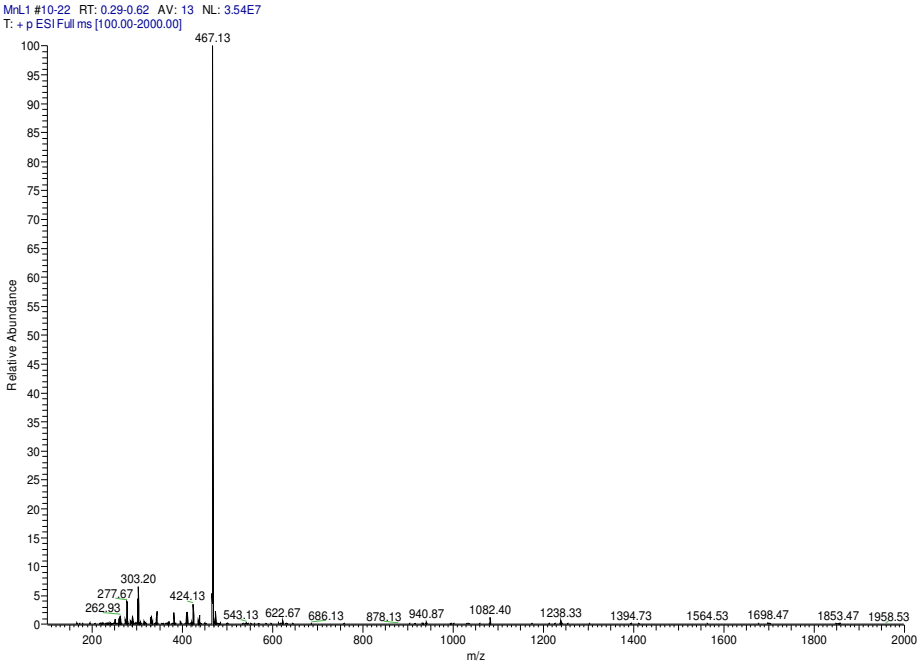

Fig.A3 ESI mass of 6 before (**a**) and after (**b**) the addition of TBP.

LIST OF PUBBLICATIONS and POSTER PRESENTATIONS

Elisabetta Benazzi, Mirko Magni, Alessia Colombo, Claudia Dragonetti, Dominique Roberto, Stefano Caramori, Carlo Alberto Bignozzi, Roberto Giannuzzi, Roberto Grisorio, Gian Paolo Suranna, Maria Pia Cipolla, and Michele Manca: "Bis(1,10-phenanthroline) copper complexes with tailored molecular architecture: from electrochemical features to application as redox mediators in dye-sensitized solar cells".
Electrochimica Acta, **2018**.
Manuscript submitted.

Laura Meda, Fabio Oldani, Gabriella Tozzola, Stefano Caramori, Elisabetta Benazzi, Vito Cristino and Carlo Alberto Bignozzi: "Searching for new redox-complexes in organic flow batteries".
Solid state Ionics, **2018**, *317*, pp 142-148.

Elisabetta Benazzi, Vito Cristino, Stefano Caramori, Laura Meda, Rita Boaretto and Carlo Alberto Bignozzi: "Electrochemical characterization of Polypyridine Iron (II) and Cobalt (II) complexes for organic redox flow batteries".
Polyhedron, **2018**, *140*, pp 99-108.
DOI: 10.1016/j.poly.2017.12.001.

Alessia Colombo, Gabriele Di Carlo, Claudia Dragonetti, Mirko Magni, Alessio Orbelli Biroli, Maddalena Pizzotti, Dominique Roberto, Francesca Tessore, Elisabetta Benazzi, Carlo Alberto Bignozzi, Laura Casarin, and Stefano Caramori: "Coupling of Zinc Porphyrin Dyes and Copper Electrolytes: A Springboard for Novel Sustainable Dye-Sensitized Solar Cells".
Inorg. Chem., **2017**, *56* (22), pp 14189–14197.
DOI: 10.1021/acs.inorgchem.7b02323.

Serena Berardi, Vito Cristino, Martina Canton, Rita Boaretto, Roberto Argazzi, Elisabetta Benazzi, Lucia Ganzer, Rocío Borrego Varillas, Giulio Cerullo, Zois Syrgiannis, Francesco Rigodanza, Maurizio Prato, Carlo Alberto Bignozzi, and Stefano Caramori: "Perylene Diimide Aggregates on Sb-Doped SnO_2: Charge Transfer Dynamics Relevant to Solar Fuel Generation".
J. Phys. Chem. C, **2017**, *121* (33), pp 17737–17745.
DOI: 10.1021/acs.jpcc.7b05928.

Stefano Carli, Laura Casarin, Zois Syrgiannis, Rita Boaretto, Elisabetta Benazzi, Stefano Caramori, Maurizio Prato, and Carlo Alberto Bignozzi: "Single Walled Carbon Nanohorns as Catalytic Counter Electrodes for Co(III)/(II) Electron Mediators in Dye Sensitized Cells".

ACS Appl. Mater. Interfaces, **2016**, *8* (23), pp 14604–14612.
DOI: 10.1021/acsami.6b03803.

Stefano Carli, Elisabetta Benazzi, Laura Casarin, Tatiana Bernardi, Valerio Bertolasi, Roberto Argazzi, Stefano Caramori and Carlo Alberto Bignozzi: "On the stability of manganese tris(β-diketonate) complexes as redox mediators in DSSCs".
Phys. Chem. Chem. Phys., **2016**, *18*, pp 5949-5956.
DOI: 10.1039/C5CP05524E.

Poster Presentation at "EnerCHEM 2016", **February 2016**, Firenze (FI), title: *"Manganese Complexes as Redox Mediators in Dye Sensitized Solar Cells"*

,